4-Dimensional Printing and Characterization of Net-Shaped Porous Parts Made from Magnetic Ni-Mn-Ga Shape Memory Alloy Powders

by

Matthew Caputo

Submitted in Partial Fulfillment of the Requirements

for the Degree of

Doctor of Philosophy

in the

Materials Science and Engineering

Program

YOUNGSTOWN STATE UNIVERSITY

May, 2018

4-Dimensional Printing and Characterization of Net-Shaped Porous Parts Made from
Magnetic Ni-Mn-Ga Shape Memory Alloy Powders

Matthew Caputo

I hereby release this dissertation to the public. I understand that this dissertation will be made available from the OhioLINK ETD Center and the Maag Library Circulation Desk for public access. I also authorize the University or other individuals to make copies of this dissertation as needed for scholarly research.

Signature:

Matthew Caputo, Student Date

Approvals:

Dr. *C. Virgil Solomon*, Dissertation Advisor Date

Dr. Pedro Cortes, Committee Member Date

Dr. Tim Wagner, Committee Member Date

Dr. Donald Priour, Committee Member Date

Dr. Brett Conner, Committee Member Date

Dr. Salvatore A. Sanders, Dean of Graduate Studies Date

Abstract

Ferromagnetic shape memory alloys (FSMA's) are known to produce large strains in the presence of magnetic fields. Amongst the FSMA's near stoichiometric Ni_2MnGa alloys present copious conceivable applications such as actuators and sensors due to these large magnetic field induced strains (MFIS's). Albeit, the large MFIS's are often observed in single crystals; which are difficult to manufacture and possess limited ductility. Recent investigations of polycrystalline Ni-Mn-Ga foams are reported to exhibit comparable MFIS's to those reported for single crystals. Therefore the ability to increase the MFIS in Ni-Mn-Ga alloys is envisioned through the introduction of pores in the microstructure. However, the manufacturing is difficult for all the above-mentioned Ni-Mn-Ga materials. Moreover, current techniques lack the ability to manufacture complex geometries.

Additive Manufacturing (AM) via binder jetting is a method for producing porous near net shaped components utilizing micrometer sized material. This research investigates an additive manufacturing route of producing functional net shaped parts from pre-alloyed magnetic shape memory Ni-Mn-Ga powders. Three types of Ni-Mn-Ga powders were used in this investigation: spark eroded in liquid nitrogen (LN_2), spark eroded in liquid argon (LAr), and ball milled (BM). Additive manufacturing via powder bed binder jetting, also known as 3D printing (3DP) was used in this research due to the ability to control part porosity and the possibility to obtain complex shaped parts from Ni-Mn-Ga alloys. The fourth-dimension (4D) is created by the predictable change in 3D printed part configuration over time as the result of shape-memory functionality. Powder characterization techniques including packing density measurements, size distribution

analysis, and binder saturation experiments were conducted on the powders to obtain optimized printing parameters, respectively. The optimum layer thickness and binder saturation range was determined as 80 – 110 μm, and 110 – 250 %, respectively. Binder jetting of Ni-Mn-Ga powders followed by curing and sintering proved successful in producing net shaped porous structures (spring-like, 3-D hierarchical lattice structures, etc.) with suitable mechanical strength. Parts with porosities between 24.08 % and 73.43 % (1.164 g/cm^3 to 6.35 g/cm^3) have been obtained by using powders with distinct morphologies.

The printed and sintered Ni-Mn-Ga parts undergo reversible martensitic transformations during heating and cooling, which is a prerequisite for the shape memory effect. Thermo-magneto-mechanical trained 3D printed parts obtained from ball milled Ni-Mn-Ga powders showed reversible magnetic-field-induced strains (MFIS's) of up to 0.01%. Binder jetting additive manufacturing is a viable technology in solving the design issues of functional parts made of Ni-Mn-Ga magnetic shape-memory alloys (MSMA).

Acknowledgements

First, I would like to express my everlasting gratitude to my dissertation advisor, Dr. C. Virgil Solomon. During my time in your lab you have pushed me far from my comfort zone and ultimately taught me how to be a scientist, engineer, and a professional. Thank you for all your time, patience, guidance, and effort during my doctoral education.

Next, I would like to thank the members of my dissertation committee, Dr. Pedro Cortes, Dr. Donald Priour, Dr. Tim Wagner, and Dr. Brett Conner. Thank you all for assisting in my dissertation research.

My dearest respect and recognition is for Dr. Ami Berkowitz and the Center for Memory and Recording Research at the University of California San Diego. Without Dr. Berkowitz, a large portion of this work would not have been possible.

I wish to express my sincere thanks to Dr. Chunfei Li and the Department of Chemistry Mathematics & Physics at Clarion University.

I am very thankful for my best friends and colleagues Shaikh "Tofa" Hossain and Elizabeth Zell. In addition, I want to extend my thankfulness to my fellow graduate students; in particular the following group members, Rafaela Vannutelli, Tim Daugherty, and, Eric Myers as well as non-group members, Brian Fredrick, Sanjay Shrestha, Mike "Juice" Juhasz, George Kubas, Kyle Myers, Ram Gullapalli, Manush Prame and Travis Kneen. Along with anyone else that has helped along the way. I would also like to thank Meera Maxy for all of her help; she has been a great friend.

Dr. Matt Willard and Mr. Anthony Martone representing the Materials Science & Engineering Department at Case Western Reserve University also have my gratitude.

I am deeply grateful to the Department of Mechanical, Industrial and Manufacturing Engineering at YSU, and to Dr. Hazel Marie, the Department Chair.

I would like to express my appreciation and acknowledgments to the Micron School of Engineering and the Magnetic Materials Lab at Boise State University. Furthermore, I want to thank Dr. Peter Müllner, Dr. Paul Lindquist, and Mr. Andrew Armstrong for all their help and support during my visit to Boise State University.

I acknowledge the help received from both the Center for Excellence in Materials Science and Engineering and the Center for Innovation in Additive Manufacturing at YSU. I would like to express my gratitude for the help and guidance I received from Mr. Jay Wargacki on preforming the additive manufacturing research. I also want to thank the faculty and staff in the Department of Chemistry at YSU, specifically, Lisa Devore, Ray Hoff, and Dr. Matthew Zeller who never hesitated to help when I needed it.

To my friends and family, specifically my parents, I cannot express how grateful I am for all your support and guidance throughout life. This achievement would not be possible without you. To my sister Giaona, you have never failed to put a smile on my face during any difficulty; because I have you, I will always have a friend.

Lastly, to my fiancée Madeline, I want to thank you for always being there for me. I appreciate all your support during the past four years and am excited to see where our future takes us. You'll always be my babe over there, I love you!

List of Acronyms

CAD – Computer Aided Design

SMA – Shape Memory Alloy

SME – Shape Memory Effect

MFIS – Magnetic Field Induced Strain

RMT – Reversible Martensitic Transformation

AM – Additive Manufacturing

3DP – 3D Printing

LAr – Liquid Argon

LN_2 – Liquid Nitrogen

BM – Ball Milled

T_{As} – Austenitic Start Temperature

T_{Af} - Austenitic Finish Temperature

T_{Ap} - Austenitic Peak Temperature

T_{Ms} - Martensitic Start Temperature

T_{Mf} – Martensitic Finish Temperature

T_{Mp} – Martensitic Peak Temperature

SE – Secondary Electron

BSE – Back Scatter Electron

EDS – Electron Dispersive Spectroscopy

DIC – Differential Interference Contrast

MSME – Magnetic Shape Memory Effect

SEM – Scanning Electron Microscope

FIB – Focused Ion Beam

TEM – Transmission Electron Microscope

Table of Contents

List of Figures

List of Tables

1. Purpose

Over the course of history, the evolution of metals and alloys has been paramount during any specific era in history. Earliest accounts of humans utilizing metal reports the use of small amounts of gold, discovered in Spanish caves during the Paleolithic period (40,000 BC) [1]. Copper, tin, silver, and meteoric iron have also been discovered in intrinsic form, and initially allowed for limited metal working for earlier cultures [2]. In the bronze and iron ages, alloying was introduced for the first time, creating stronger metals as well as demonstrating a significant technological shift. From here, other metallurgical techniques such as forging, and smelting began to evolve for more prominent uses of metals and alloys. Considering the above-mentioned techniques along with other advancements in science and technology, a deeper understanding of the microstructural and processing techniques was evident. These effects were related to the materials behaviors, thus fundamentally creating the field of materials science and engineering, which has radically improved since the bronze and iron ages. Through combining the understanding of material properties and technological developments, the capability to engineer various material properties such as, mechanical, thermal, and electrical, for plethora of applications has been achievable by means of new alloys and/or composites.

Modern day applications have an everlasting demand for lighter, stronger materials with tailored properties that can address structural requirements and provide additional engineering functionality (actuation, sensing, etc.). Through this, functional materials, a new branch of materials have been explored and developed. Materials that produce actuations convert a signal, such as electrical response, into a mechanical output while materials with sensing capabilities convert a mechanical response into an electrical signal (i.e. voltage) output. These functional materials generally exhibit a mechanical response when subjected to external energy sources, like thermal gradients, electrical signals, and magnetic fields. Functional materials typically respond to these energy sources one or more orders of magnitude greater than non-functional materials. Some examples of functional materials include piezo-electrics and electro-strictives, piezo-magnetics, magneto-strictives and shape memory alloys. These functional materials can be sub-divided into active materials that produce either direct or indirect coupling responses. Piezo-ceramics, piezoelectric polymers, magneto-strictive ceramics, shape memory alloys and magnetic shape memory alloys are examples of materials that exhibit direct coupling [3]. It can be conferred based on this, either mechanical or non-mechanical reactions serve as inputs, while the other serves as an output. Materials such as electro-rheological fluids (ERF) and magneto-rheological fluids (MRF) classify as indirect couplings. The indirect active materials lack reciprocity.

The suitability of functional materials with direct coupling responses for actuator/sensing applications depends on several factors. Two key design drivers are the actuation energy density (work output per unit volume) and the actuation frequency of the material [3]. Functional materials that possess both high energy density and high actuation frequency are superlative candidates. Figure 1.1 and Figure 1.2 compare the energy density and actuation frequency for common functional materials. The energy density in Figure 1.1 is denoted by the dotted lines and is defined as the product of the actuation strain and stress, while assuming actuation is occurring at a constant stress.

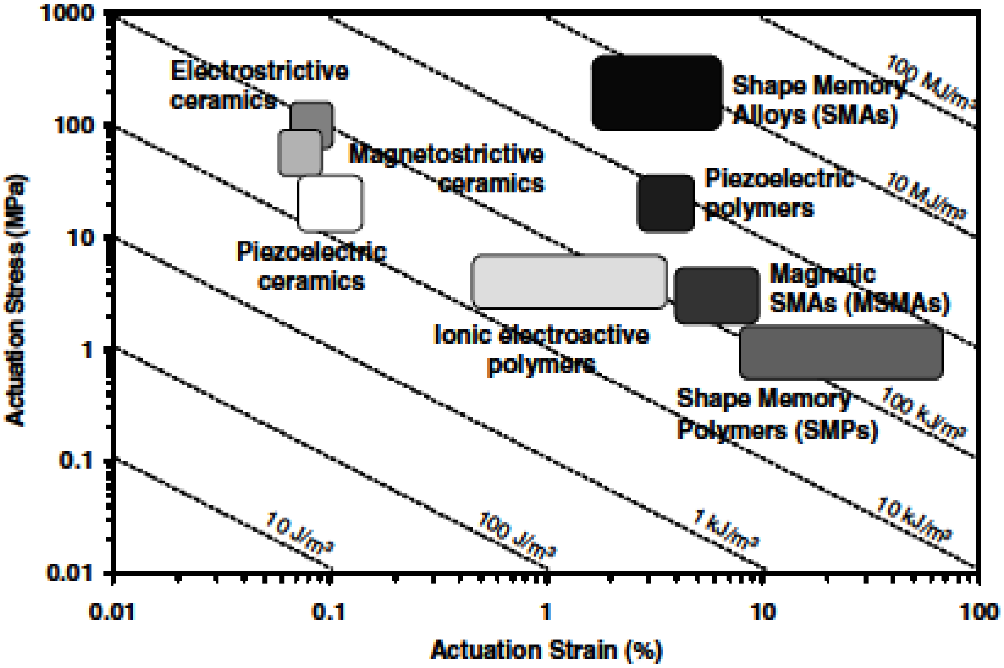

Figure 1.1: Energy density versus actuation strain, as well as actuation stress for various functional materials with direct coupling [3]. Reprinted with permission from Springer Nature, see Appendix A.

Shape memory alloys (SMA's) are a particular class of functional materials that possess the ability to recover their shape when heat is applied, and a specific temperature is reached. In addition, when the shape memory alloy experiences applied loads, and the specific temperature is achieved, the result produces the actuation energy density, as displayed in Figure 1.2. Furthermore, under specific conditions shape memory alloys have the potential to absorb and disperse mechanical energy due to a reversible hysteretic shape change under externally applied mechanical cycling. As previously stated, the characteristics shape memory alloys possess have made this functional material very promising for actuator/sensing applications as well as impact absorbing and vibration damping purposes. However, thermally activated shape memory alloys operate with low frequencies, Figure 1.2. Certain shape memory alloys have the capability to operate at higher response frequencies; in particular, this is achievable through the use of magnetic shape memory alloys (MSMA's).

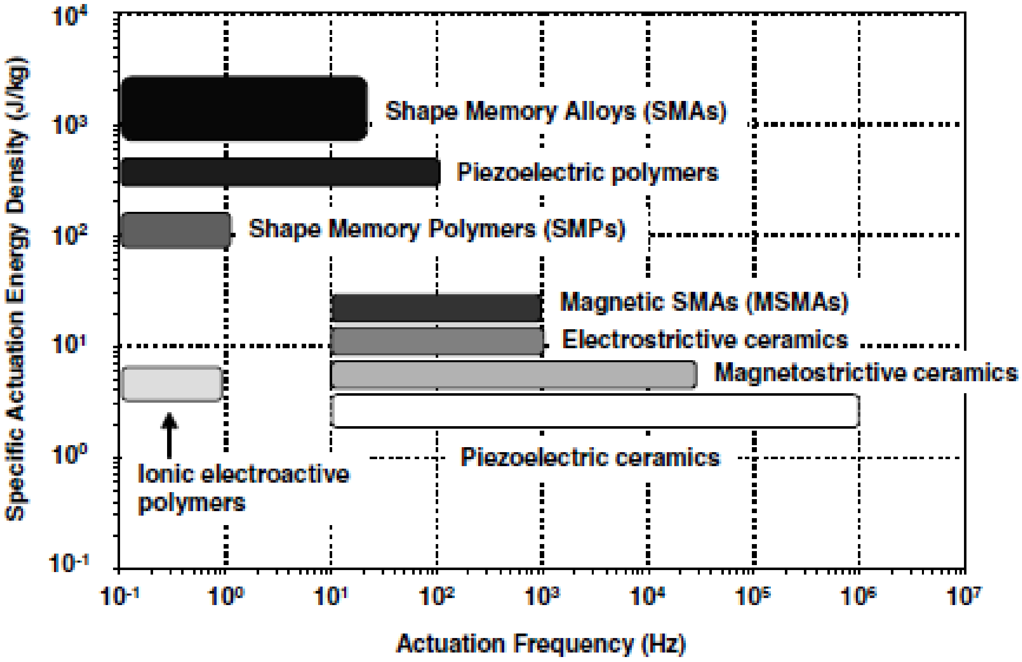

Figure 1.2: Actuation frequency diagram comparing frequency ranges and energy density for various direct coupling functional materials [3]. Reprinted with permission from Springer Nature, see Appendix A.

Ternary ferromagnetic Ni-Mn-Ga (nickel-manganese-gallium) Heusler structured alloys are a distinct magnetic shape memory alloy. Ni-Mn-Ga alloys have attracted a lot of scientific and engineering interest over the last two decades due to large magnetic field induced strains (MFIS) reported in single crystals [4]. Ni-Mn-Ga alloys possess the ability to produce large reversible deformations due to a phenomenon called the reversible martensitic transformation (RMT). A large magnetic induced deformation is demonstrated in Figure 1.3. The left photo shows a Ni-Mn-Ga single crystal and the right photo displays a 5% shear strain relative to the unchanged variant sample. The driving force for the reversible martensitic transformation in Ni-Mn-Ga alloys is typically an external magnetic field, albeit heat and/or an applied load can be a mechanism for activation. In this particular example, an applied magnetic field of 4 kOe was imposed in order to activate the crystallographic reorientation. This reversible magnetic field induce strain (MFIS) is often referred to as the magnetic shape memory effect (MSME). Moreover, the actuation frequency of magnetic shape memory alloys are orders of magnitude higher than the traditional shape memory alloys, as observed in Figure 1.2.

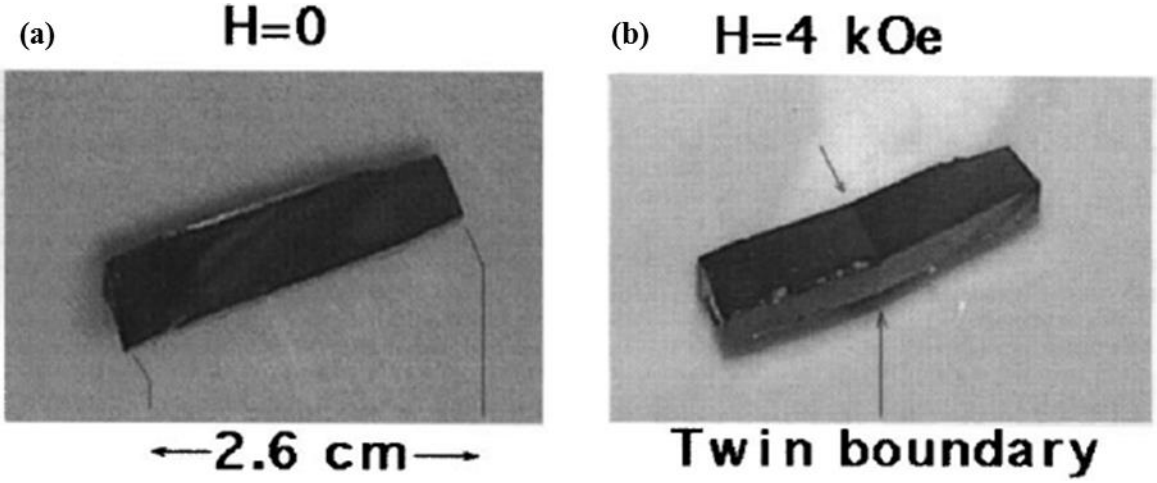

Figure 1.3: (a) Ni-Mn-Ga single variant sample with no applied external magnetic field; (b) The same sample with a 6° kink at a twin boundary introduced by application of a field of 4 kOe [5]. Reprinted with permission from AIP Publishing LLC, see Appendix A.

However, one major drawback for both single and polycrystalline Ni-Mn-Ga alloys are poor mechanical properties, principally limited ductility, subsequently restricting engineering applications. Moreover, the MFIS effect is significantly reduced in bulk polycrystalline Ni-Mn-Ga, compared to the single crystals. The best MFIS for a polycrystalline Ni-Mn-Ga alloy was reported to be 0.5% in trained samples containing 5M martensite [6, p.]. One paper reports a slightly higher MFIS in polycrystalline Ni-Mn-Ga, of 1% [7]. Several technological solutions have been proposed to address the weaknesses of Ni-Mn-Ga materials. In one method, bulk composite materials have been synthesized by mixing Ni-Mn-Ga powders with PVDF polymer [8]. Although the Ni-Mn-Ga-polymer composite showed improved mechanical properties, the MFIS effect was still poor, compared with single crystal Ni-Mn-Ga, in the range of 0.35% [8]. A different approach involves fabrication of Ni-Mn-Ga metallic foams by using ceramic preforms with bimodal pore-size distributions [9]. The bimodal cast metallic foams demonstrated an initially reported unstable 8.7% MFIS during thermal cycling, and later a stable 4.4 - 5.1% MFIS. The 8.7% MFIS is comparable to the 9.5% MFIS reported in oriented bulk single crystal Ni-Mn-Ga [10], [11]. According to Müllner *et al* [12], porosity increases MFIS in polycrystalline Ni-Mn-Ga by reducing the effect of constraints imposed by grain boundaries, thus enabling twin boundary motion. Based on these reports, it seems that porous Ni-Mn-Ga shows both improved mechanical properties and relatively large MFIS, compared to the bulk polycrystalline material, and could be suitable for some engineering applications. However, large and complex shaped Ni-Mn-Ga parts are difficult to be produced using the above mentioned metal foam replication technology.

Complex shape parts made out of porous material can be readily obtained using additive manufacturing (AM) methods. Moreover, material porosity (void size and distribution) can be controlled in additive manufacturing processes. Additive manufacturing is a relatively new method of engineering that produces near net shape components, one layer at a time, based on a computer aided design (CAD). AM methods can be classified in terms of the material feed stock, energy source, build volume, etc. [13]. Based on material feed stock, AM manufacturing systems are classified in: (i) powder bed systems, (ii) powder feed systems, and (iii) wire feed systems. Bonding sources for AM systems are: binder jetting, electron beam, laser beam, etc. The AM system used in this project is a powder bed, binder jetting system, typically known as three dimensional printing (3DP). 3DP resembles ink-jet printing, but with multiple passes to build the materials upwards into a three-dimensional form. An illustration of this process can be observed in Figure 1.4. 3DP has been successfully used in manufacturing net-shape components from various materials, including metals, polymers and ceramics [14]. In the case of binder jetting technique, the 3D printed parts are produced with an intrinsic porosity due to the nature of the process [15]. The porosity can be controlled by printing and post-printing parameters such as powder morphology and packing density, particle size distribution, sintering temperature and sintering time, see Figure 1.4. Therefore, it seems that binder jetting technology might be well suited to manufacture net shaped Ni-Mn-Ga parts having both adequate mechanical strength and required porosity for producing large MFIS.

All manufacturing techniques require a source material, and unlike traditional methods, additive manufacturing systems typically use wires and/or powders. Binder jetting additive manufacturing systems typically use micro-meter sized powders (20 – 100 μm) as feed stocks. For this reason, powder selection is a crucial parameter for the binder jetting process. In this research, three different Ni-Mn-Ga based powders have been used for 3D printing. Two of these powders were produced using spark erosion in different dielectric liquids [16]–[21]. See section 4.1.1 for a more detailed explanation about the synthesis of these powders. The third powder used in this research was produced from Ni-Mn-Ga ingots by ball milling. All three powders possess different chemical compositions, morphologies, and overall powder characteristics. Moreover, each powder requires specific printing parameters such as binder saturation, layer thickness, and speed of layer deposition. Furthermore, the final part will have individualized features as well as functional properties, for instance reversible martensitic transformation temperatures.

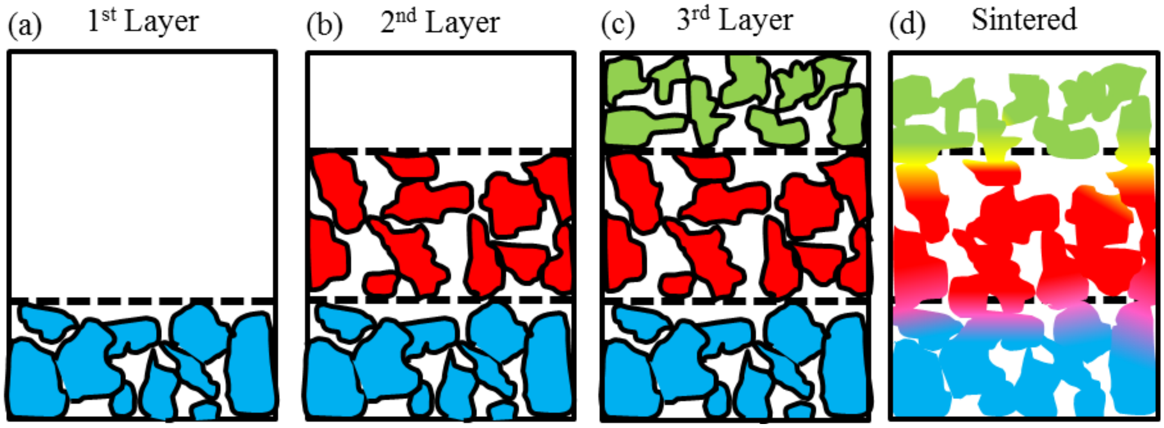

Figure 1.4: Illustration of the binder jetting process. Powderous material is deposited layer by layer, (a) first layer, (b) second layer, (c) third layer, until part geometry is completed. Afterwards, a sintering process (d) is conducted to solidify neighboring powders.

Many modern technologies need transducing materials which combine high force, fast dynamic responses, and large strains during actuations [22]. The functionality of these materials is based on physical mechanisms responsible for the electric, magnetic, or thermal energy transformations into mechanical work, which produce the actuation [22]. The reverse of this action is used for sensing purposes. The efficiency of above-mentioned materials determines the scope of engineering applications.

The rise in MFIS in off-stoichiometric Ni-Mn-Ga alloys is fitting for many actuation and sensing applications including but not limited to, thin film actuators, magnetocaloric effects, and energy harvesting. Traditionally, parts made of shape memory alloys are difficult to manufacture and are limited to a few techniques such as; hot pressing, hot isostatic, hot extrusion, metal injection, and mechanical alloying [23]. These forms of manufacturing produce unwanted stable secondary phases and can only fabricate simple geometries [24]. Utilizing binder-jet AM, complex near net shaped components can be manufactured while controlling metallic phases by using pre-alloyed powders. The purpose of this research is to produce 3D printed functional parts with a desired geometry, known phase and reversible martensitic transformations, that exhibits ferromagnetic shape memory behavior.

The objective of this work is to manufacture parts with complex geometry from Ni-Mn-Ga powders using binder jetting AM technique and to investigate the shape memory characteristics of the 3D printed parts. The long-term goal of this work is envisioned as the successful production of actuators and sensors made of Ni-Mn-Ga, using additive manufacturing technology. Included in this work is information regarding the synthesis, processing, manufacturing, mechanical, chemical, and physical properties, reversible martensitic transformation behavior, and functionality of 3D printed Ni-Mn-Ga alloys.

2. Additive Manufacturing and Shape Memory Alloys

2.1 Additive Manufacturing

Additive manufacturing (AM) is a semi-automated engineering process that is utilized to produce near net shaped components, based on a computer-aided design (CAD). AM has significantly evolved from rapid prototyping to traditional manufacturing techniques. In the 1980's AM was used to produce prototypes for evaluation during product development stage. Subsequently, AM has advanced to be recognized for seven different categories of manufacturing by means of liquid and solid phase materials [25]. These seven categories of AM include: material extrusion, powder bed fusion, material jetting, directed energy deposition, sheet lamination, vat photo-polymerization, and binder jetting. There are clear advantages while utilizing AM that include: waste reduction, relatively fast production time, automated manufacturing, ability to readily modify part geometries, as well as diversify materials [26]. Furthermore, industrial interest considers three main advantages against subtractive manufacturing: (1) AM removes customary restrictions thus enabling design freedom for innovative products [27], (2) Profit space for manufacturers can be increased by reducing supply chain of fabrication [28], and (3) AM is a sustainable method of manufacturing; potentially reducing environmental impacts that normal manufacturing produces [29]. Moreover, AM can produce near net shaped parts with high aspect ratios, often with better resolutions than rapid prototyping systems (RP) [30]. This offers a unique opportunity to create shapes that are difficult or impossible by common manufacturing techniques.

Although many advantages are apparent, the disadvantages are mutual. Interdisciplinary research has been conducted on AM of both, inorganic materials (including metals, ceramics), and organic materials (polymers) [31]–[36]. Furthermore, optimization and method of 3D printing varies with material, resulting in extensive research tailored to one process and one material. Moreover, once the optimized method of AM and parameters have been determined, it is often the case the material properties are less desirable compared to their traditionally manufactured counterparts. The material properties are often weakened due to defects such as porosities, which can be modified using an infiltration process [37]. Another drawback for laser additive systems such as selective laser sintering (SLS) and selective laser melting (SLM) is the inability to reuse powder [38]. The use of high powered laser systems creates debris, such as carbon and oxides that redeposit on the surface of the surrounding powders. The presence of these contaminants makes the used powders unrecyclable.

2.1.1 Binder Jetting Additive Manufacturing

Additive manufacturing of metals typically uses powder bed systems. Three common methods for printing metallic powders include selective laser sintering (SLS), selective laser melting (SLM), and binder jetting (known as 3D printing). SLM and SLS use a high-powered laser system to fuse powder together, layer by layer, resulting in a near fully dense component. Albeit, binder jetting AM uses a binder, deposited layer by layer to adhere powders resulting in a porous structure. A schematic of the binder jetting process is shown in Figure 2.1, portraying the process of building vertically, layer by layer, until complete. Parts, after printing via binder jetting, are dubbed "green part" and typically are 30%-75% volume powder, 10% volume binder, while the rest is void space [39]. Binder jetting was selected for the AM of Ni-Mn-Ga powders to achieve levels of porosity comparable to those foams aforementioned. To date, this is the only research that focuses on the binder jetting of Ni-Mn-Ga material. Therefore, creating the template for 3D printing of Ni-Mn-Ga materials is broken into three steps: (1) powder formulation, (2) selection of binder, (3) and specification of printing parameters.

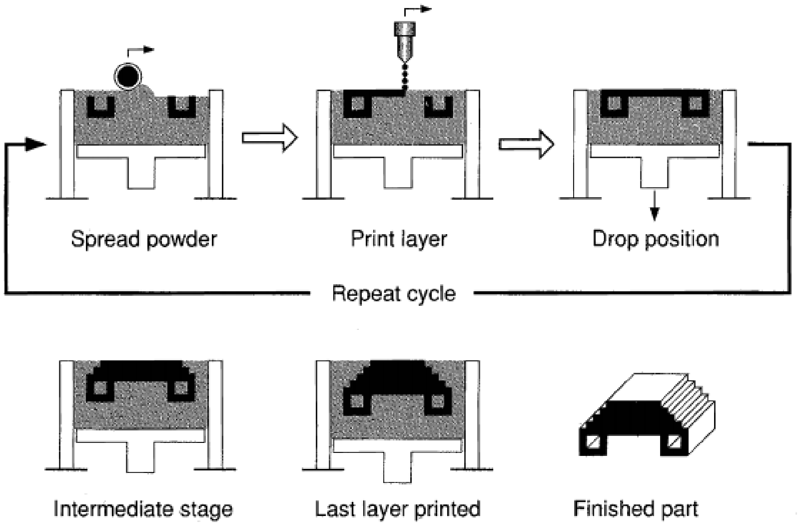

Figure 2.1: Schematic of the binder jetting AM process [40]. Reprinted with permission from Elsevier, see Appendix A.

Current binder jetting technology uses a process that evenly distributes powder from the powder bed onto the build bed. This powder is spread using a rotating roller or traversing blade. As seen in Figure 2.1, after the layer of powder is spread, binder is deposited on the powder, based on a computer aided design, subsequently adhering particles together. Next, the build bed is lowered, based on the layer thickness of the build, and powder once again is spread onto the build bed. This process is repeated, layer by layer, until the part is complete.

After printing, the green parts need to be separated from the surrounding powder. Although before depowdering, green parts should undergo a drying or curing process to eliminate excess liquid in the part and ensure that all intended binding agent is contributing to green part strength. In systems that use plaster or cement based binding agents, a curing step is crucial because additional strength can be obtained via drying [41]. In the case of some organic binders' strength can be increased by curing, thus further polymerizing the binder. Curing of organic binders can be done using specific methods such as vacuum, heating, increases in pressure and exposure to visible light [42].

Depowdering is the next step after curing the 3D printed parts, if the binder jetting method is used. The goal of this step is to retrieve the now cured parts from the build bed without producing a failure, such as a fracture, in the material. For this, excess powder needs to be removed, typically done by brushing or blowing powder from the surface of the part. Parts with intricate or convoluted geometries are more difficult to depowder; although vacuuming or vibrating the samples usually suffice.

The two most common post processing steps of 3D printed parts using the binder jetting process are sintering and infiltration. These steps can increase the strength of a part considerably. In the case of infiltration, bulk properties can be affected. In most cases, first step sintering results in a shrinkage between 1.5 – 2 % due to neck formation between particles [36]. Attempts have been made to sinter to a fully dense state; for instance when green part density is approximately 60 %, a greater than 15 % linear shrinkage was reported [43]. A step involving the surrounding 3D printed parts with higher sintering temperature materials, typically ceramics, is called settering. Settering is particularly useful for binders that thermally degrade. As a result, there is minimal binding to the part prior to the onset of a particle sintering. Albeit, settering has limitations during the sintering of high shrinkage samples since surrounding supports resist dimensional changes [36].

There are several major sintering parameters: material selection, particle size, sintering time, and sintering temperature. The printing process is dependent upon the first two parameters, while the latter two parameters are independent of the 3D printing process. All materials have specific sintering conditions based on physical properties. Examples of this are ceramic materials, such as silica, that can be sintered in air while most metals cannot because of oxidation. Nevertheless, using various particle sizes, coatings, and sintering aids and/or inhibitors, the sintering can be controlled, even over the processing of powder formulation. Metals in particular, have considerable flexibility during the sintering process. For example, materials with different liquid and solidus temperatures can be readily sintered, producing different densification ranges dependent upon the systems temperature [44]. Sintering temperatures of inorganic materials such as metals can be altered by introducing refractory materials. As an example, chromium electroplated on steel and intentional oxidation of stainless steel between 400 °C - 700° C [36]. Aiding the sintering of ceramics tends to be more challenging, although sintering aides such as tetraethylorthosilicate (TEOS) can be added to benefit the sintering. When added, TEOS melts at a temperature lower than the sintering temperature of the ceramic, flowing to the surfaces of the particulates, and enables sintering via surface tension manipulation [42].

Infiltration is the next most common post processing step. Infiltration can assist in achieving high densities for binder jetting 3D printed parts without high dimensional shrinkage sintering [45]. The infiltration process depends on a material to melt at lower temperatures than the base material, and impregnate void space in the 3D printed components. This process can be done at high and/or low temperatures but is reliant on the infiltrant and binding agent. The only constrain in the infiltration process is that the infiltrant must melt at a lower temperature than the solidus transition in the base material. If this constraint is not met, the base material could lose structure and spatial resolution [43]. There are few exceptions to this which occur when powder is coated in high temperature materials such as carbon coated ceramics. Therefore, during infiltration only the coating interacts with the infiltrant [46]. Desired characteristics for infiltrants include; low viscosity, sufficient fluidity, and low contact angles. All of these traits enhance the infiltration process by enabling flow through pores [47]. An example of the infiltration process is displayed in Figure 2.2 where a backscatter secondary electron (BSE) image of a 3D printed stainless steel component infiltrated with brass is presented.

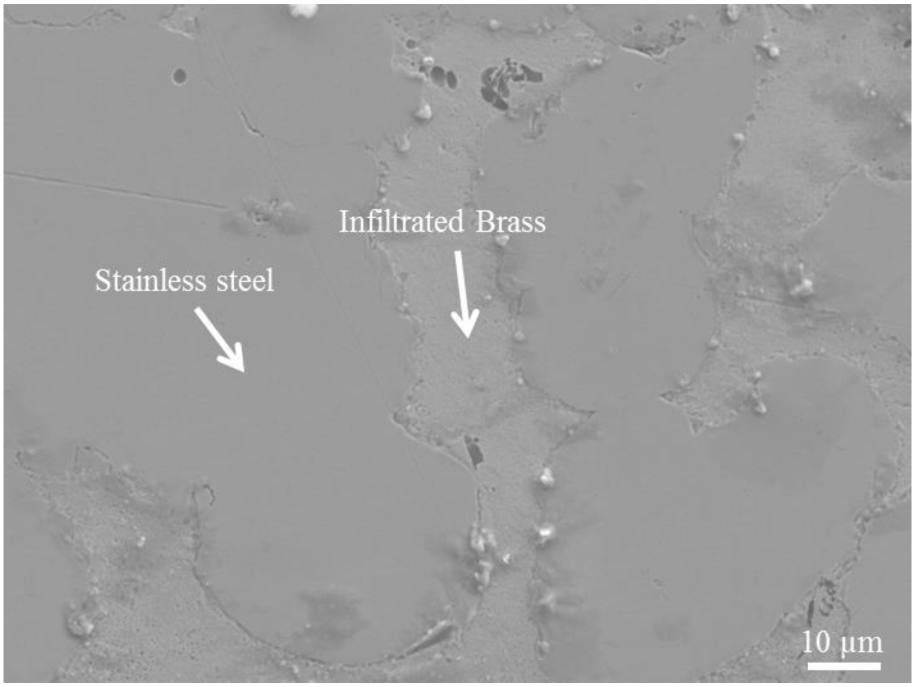

Figure 2.2: BSE micrograph of 3D printed stainless steel infiltrated with brass.

During the infiltration post processing, low temperature infiltrants are favored, mostly because the phase of the matrix material will not be affected. These infiltrants include molten wax, varnish, lacquer, cyanoacrylate, polyurethane, and epoxy [41]. Infiltration is most commonly done via dipping the 3D printed component, albeit parts can also be infiltrated by aerosolizing the infiltrant and spraying the part [48].

High temperature infiltration requires control over the composition and infiltrant as well as the thermal processing [30]. High temperature infiltration usually refers to temperatures 20 – 50 °C above the melting temperature of the infiltrant [39]. Furthermore, the part must be held isothermally until complete infiltration is achieved. In high temperature infiltration, the infiltrant is typically an alloy. It must be noted that these molten alloys can produce secondary metallic phases during infiltration. Alloy separation problems can be eliminated using a process called gating, which consists of mechanically separating the infiltrant from the part until complete melting of the infiltrant has occurred [43]. In most cases, infiltration is used to create composites, but it is possible to create homogenous metallic parts. Homogenous metals can be created using metal melting point depressants (MPD) to create a lower melting temperature phase of bulk powder, infiltrating the part, then heating the part at an elevated temperature to allow MPD to diffuse into the powder, thus homogenizing the part [43]. In order to evade premature solidification, the rate of which the infiltration occurs can be increased by inherently increasing particle size, increasing surface tension, decreasing infiltrant viscosity and solid diffusivity [49].

Infiltration is the final step for processing of 3D printed metallic parts. Additional steps can be performed to complete fabrication, although these are considered external to the core development of a new 3D printing materials system.

2.1.2 Powder Formulation

The powder formulation process includes material selection, particle sizing, additive selection, and deposition optimization. Powder formulation is generally the first step for a 3D printing process. This is primarily because after printing, majority of part volume will be of the selected powder. With that being said, a major advantage in the additive manufacturing process is there are no limitations on material selection. Any material that can be deposited in the micrometer order of magnitude can be 3D printed using the binder jetting technique. Therefore, the most important property when selecting a material is depositability. A materials ability to be deposited primarily depends on size and morphology of the powder. While powders can be deposited in the dry or wet state, each process has acceptable particle size range. Powder size distributions are commonly considered to be either large (>20 μm) or small (<20 μm) [30]. Particle that are considered large are typically deposited as dry, while small powders (<5 μm) can be deposited wet or dry. Ultra-fine particles (<1 μm) tend to agglomerate due to van der Waal's forces [50]. Humidity also effects the spreading of ultra-fine particles, and together with van der Waal interactions causes spreading to be challenging. Ultra-fine particles can therefore be deposited as a slurry, typically when the average particle size is below 5 μm [51]. For both dry and wet deposition methods, particle size has greater significance over particle shape.

Particle morphologies are grouped in two types: spherical and anisotropic. Spherical powders, for instance, are favored for dry deposition due to better depositability due to lower coefficients of friction [52]. Particles with faceted feature and/or anisotropic morphologies tend to endure high coefficients of friction which subsequently lower the depositability/spreadability. Albeit due to the anisotropic morphology, powders tend to pack at higher efficiencies when compared to spherical counterparts.

The particle size and morphology affect both the printing process and final 3D printed part. The referred parameters of processing and printing includes: sinterability, pore size, surface area, surface roughness, and minimum feature size. Powders classified as small have potential advantages of increased sinterability, lower surface roughness, smaller minimum feature size and thinner layer thicknesses [50]. Larger particles have much better flowability; therefore, tend to spread much easier. Large powders have lower surface area per volume, as well as larger pores to facilitate fluid migration [43], [53]. The drawback is the fact that the largest powder establishes a minimum layer thickness. Powder system containing a varying distribution of particle sizes, such as bimodal or multimodal offer the above-mentioned advantages of both small and large sized particles. In particular, large powders allow powder mixtures to be spread easily using larger layer thicknesses, while the smaller particles fill intrinsic sites, subsequently increasing density [44]. The use of bimodal powders systems containing large and small particles has been successfully implemented to increase part density of coarse bronze powders in green part state; increasing from 59.3% density as monomodal powders, to a 73.2% dense system with the addition of 31% volume of fine copper powders [44].

In addition, the powder depositability, printing behavior, part characteristics, as well as post processing parameters can be affected by introducing additives to a 3D printed part in the bulk state. For instance, dry powder deposition can benefit from a solid lubricant in low weight percentages (1 – 2 wt%) [45] or by coating the surfaces of the powder to reduce friction coefficients [54]. The above-mentioned part properties can be affected via the addition of long fibers, constrained by the layer thickness, to reinforce the final part strength. The addition of fiber, approximately half the size of the layer thickness can be added to increase dimensional stability [55]. These materials being added to the additive manufacturing process include but are not limited to: polymers, ceramics, graphite, and fiberglass [53]. Albeit, the addition of these materials often limits part properties such as packing density and flowability due to increases in internal friction. Other additives affect the post processing of 3D printed parts, for example, oxygen getters placed in the sample to reduce oxygen content during the sintering of metallic powders [56], [57]. Nevertheless, additives should mix coherently with base powder to prevent the creation of uncontrolled inhomogeneity in the final system.

2.1.3 Binder Selection

There are many studies on binder selection, due to the important role of the binder on adhering particles and layers together in the green stage, prior to post processing. For the selection of a binding agent two common methods are considered: in liquid and in bed [30]. The liquid binder contains all components for binding and it is deposited as a liquid directly on the powder. This method binds a large variety of powders, but often disrupts the printing process due to binder congestion in print head nozzles [58], [59].

The in-bed component is mixed with the powder and binding occurs when it interacts with the deposited liquid. This method of binding requires an additional step during powder formulation, but it allows the use of a more reliable liquid during the 3D printing.

While selecting a binder, the residuals on the material post printing should be considered. A fugitive binder leaves little or no residue after processing but requires that the powder be bound by heat treatment [30]. If heating of the binder is required to achieve full strength for adhesive purposes, the materials phase transformation must be lower than the curing temperature. An example of this has been reported for colloidal silica converting to pure silica [60]. Examples of fugitive binders include chloroform and biodegradable polyesters [61]. Other binders can leave excess that contributes partially or fully to the final strength. These types of binders include inorganics such as aluminum nitrate, plasters and cements [62], [63]. These binders are self-binding since the hydration activates the setting agent.

Powder binding for the 3D printing process commonly uses nine different methods for adhering particle together which include: organic liquids, in bed adhesives, hydration systems, acid/base systems, inorganics, metal salts, solvents, phase changing materials, and sintering aids/inhibitors [30].

Organic liquid binders serve as a resourceful binding agent. Organic binders bind a large variety of powder materials and in addition, thermally decompose leaving little to no residue. These binders include but not limited to: butyral resins [64], polymeric resins [41], along with polyvinyl based materials [45]. The most concerning issue when using organic based binders is a fear of clogging nozzles in the print head which occurs when the liquid adhesive dries during/after deposition [65]. Most organic binders are dissolvable in water solutions and also thermally depredate in the range of 200 °C – 300 °C [66], but carbohydrate based binders are reported to contribute to part strength even when temperatures are close to solidus temperatures for some metals [39].

The binder loaded binding agent is an adhesive, in the bed, liquid that cohere powders after an interaction with an aqueous deposited liquid. Examples of in bed binder loaded materials are maltodextrin [67] and sucrose [60]; which dissolve when liquid penetrates the bed, or spread in a localized area. Afterwards, as volatile components of the binding agent evaporate, powders are held together [60]. In bed binders should possess the following characteristics for optimized bindability: highly soluble in the deposited liquid, low viscosity when dissolved, low hydroscopicity, as well as high bonding strength [55]. Binder loaded adhesives can be in particulate form or coated on the powderous material. Similar to organic binders, the in bed methods are not material specific [52] and tend to depredate as temperature increases.

The next method of binding to be discussed is the hydration system, which is another methodology that uses the in-bed system to adhere particles. This process relies on bulk materials that bind when introduced to a wetting source. Similar to in bed adhesives, hydration based systems use simple wetting liquids, such as water based solutions. Common materials that utilize the hydration method include plasters [41] and cements [53]. These materials have the advantage of well-known properties, such as strength.

Acid-base systems rely on the controlled interaction of two components to imitate binding and can be used to bind most materials [68]. For instance, acid and base electrolyte coatings of polyvinyl pyrrolidone on the surface of powder result in strong bonding between particulates after activated water. Furthermore, this process leaves little residue after thermal treatment [68]. One alternative method involves printing one component in liquid form into a powder containing the second component, therefore depositing one component in each liquid or placing the components in a bed and initiates the reaction via solvent. In addition to the above-mentioned, the acid-base method of binding allows for a combination of other binding systems. The combination of acid base and plaster binders has been also reported [69].

Inorganic binders are typically incorporated into the final part and are often silicate based materials [51]. Most commonly chosen is colloidal silica due to its ability to easily be manipulated as a stabilized solution (pH 9 – 9.5). When this solution is printed onto a powder bed which contains an acid or is exposed to gaseous carbon dioxide, the pH drops resulting in a colloid gel, ultimately bonding surrounding powders [60]. Post processing of this colloid gel results in the deposition of silica that is residual, but adds to part strength [64]. Using a different approach, inorganic binders can be deposited by solid material into a print bed by printing precursors or solid dispersions [70]. An example of this method has been reported [62], where aluminum nitrate was used and decomposes to alumina, through dissolving by means of deionized water. Based on this, solids can be deposited directly in dispersions with oxides, such as alumina, which can be surface treated to form stable aqueous suspensions that can be used directly in the printing process [71]. This deposited material will not behave as a binding agent at first, although after subsequent steps such as, heating, melting, converting, or sintering, the material will bond adjacent particles.

The next method of binding is particularly popular with metallic powders because two of the previously mentioned binding methods require material to be deposited into the powder bed. Metallic salts inherently bind powders together when the molten salts dry and salts recrystallize. Furthermore, this method can be used with any powderous material, as long as it is insoluble in the molten salt solution [36]. If desired, the molten salt, when crystallized, can be thermally reduced to a pure metal. The result of which is an additional metal in the system, which acts as a binder and/or additional source for compounding. Although, the base material should endure the heat treatment required to reduce the salt. Another method of binding with the use of metallic salts involves a salt displacement reaction. During this, bulk powder is dissolved into a salt solution and metal, from the salt, and deposits on the surface of the powder. This then dries in salt form and can be reduced to metal via heat treating [36]. The metallic salt binding method can be utilized both in bed as well as in liquid systems. The use of silver nitrate and copper sulfate to plate steel powder, resulting in copper covered steel has been reported [36].

The non-binder approach involves a solvent being deposited onto polymer-based powders. Afterwards, the solvent dissolves part or nearly all the particles that come into contact with the solvent. Therewith, the solvent evaporates, and the polymer precipitates, causing the polymer powders to connect [70]. This method has been reported to successfully bind biodegradable polyesters with chloroform [61], as well as PLLGA salt mixtures [72]. In addition to this, multi-solvent solutions can be employed in order to balance strong binding solvents, subsequently reducing part warpage, which occurs in low vapor pressure solvents due to slower evaporations [52]. One major advantage of using a non-binding method is no compositional change is produced from the presence of the solvent, and leaves little to no residue via evaporation.

Phase changing materials as binders can be used with most powders, although this process limits the potential post processing temperatures of the printed components [30]. An example of this is a solid ambient temperature material with low melting point is deposited onto a powder bed then heated, melts therefore penetrating the surrounding adjacent powder [51]. Once ambient temperature is achieved, the molten material solidifies and holds surrounding powders in place. The only notable limitation using this method is post printing heating treatments are limited based on the phase changing binder.

The last method of binder usage in the additive manufacturing process involves the use of sintering aids and/or inhibitors. The basis of this method relies on locally controlling the thermal behaviors of the powder, and ultimately controls the sintering via addition of various materials. This has been reported by selectively depositing metal flakes on a powder bed and with the use of induction heating; producing anisotropic melt pools that can selectively bound regions of powder within the bed [73]. A related approach involves the case where inhibitor materials, such as, reflective materials, heat isolators, sintering inhibitors and chemical oxidizers are introduced to select areas. These materials can inhibit the sintering potentials with the benefit of only requiring deposition at part boundaries. Albeit in most cases the entire powder bed is affected, meaning either the powders sinter or they become contaminated [74].

2.1.4 Printing Parameters

The major printing parameters for binder jetting AM are layer thickness, binder saturation, and speed of layer deposition. The layer thickness used during 3D printing is based on the maximum particle size of the powder; such that the maximum particle size should not exceed the layer thickness. Common layer thicknesses are chosen by slightly exceeding the maximum particle size. If the particle size is larger than the layer thickness, it will cause abrasions on each layer, ultimately compromising the final shape and reducing the strength in the green stage.

Binder saturation is typically chosen as a percentage value and is based on the packing density of the powder being printed. Optimal binder saturation creates strong bonds between particles and ensures the integrity of pre- and post-cured printed parts. On the other hand, too high saturation produces lateral binder spreading which translated into poor dimensional tolerance of the printed part. On the other side, if an insufficient amount of binder is deposited, powders within each layer will not adhere to each other causing the part in the green stage to fail.

Packing density is based on the morphology and size of the powder. The packing density ultimately determines the binder saturation value. Packing density is defined as the percentage of the air space volume between powder particles that is occupied by a binder volume [75]. For example, if a powder has a packing efficiency of 60%, the binder saturation amount should be sufficient to fill the remaining 40% of void space. The packing density also has a large influence on the density of the finished part, unless infiltration methods are employed.

2.1.5 Sintering

Sintering is a thermal process that utilizes Fick's laws of diffusion [76] via the mass transfer of atoms from adjacent particles to ultimately form a solid object. This sintering process subsequently leads to improved strength due to the binding of neighboring particles. The term 'sintering' for binding particles was first reported by White & Shremp [77] which had been used to describe ceramic particle bonding with reference to beryllia heated under different conditions. An example of sintering can be seen in Figure 2.3 where Ni-Mn-Ga adjacent powders have been sintered, indicated by the connecting channels from nearby particles, known as necking. In order to explain these changes induced by heat, sintering theories emerged to provide a mathematical collection of key parameters including: particle size, heating rate, dwell temperature, and dwell time. In addition to this, the physical properties of the materials being sintered were considered, due to specific characteristics such as, surface energy, atomic size, activation energy for diffusion, and crystal structure.

Sintering can be categorized into three types; solid state sintering of crystalline materials (SSS), liquid phase sintering of crystalline materials (LPS), and solid state sintering of amorphous materials [78]. Regardless of the type of sintering, the product of each is bonding between particles and densification of close-packed components. Sintering causes grain growth and subsequently densification which substantially influences the microstructure and density. Though, these influences are insignificant during initial stages of SSS. In amorphous materials, exchange between particles occurs from viscous flow without boundary between particles.

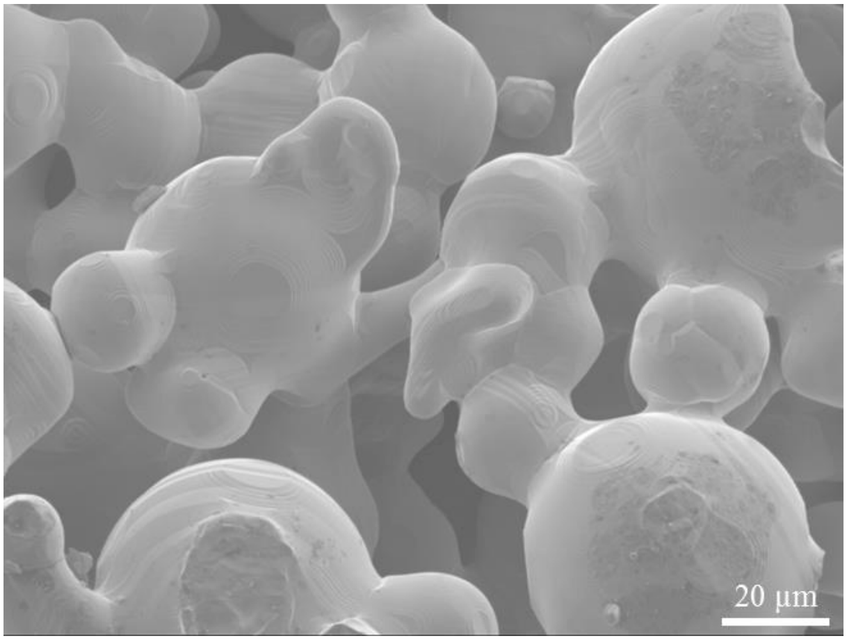

Figure 2.3: Ni-Mn-Ga powders displaying typical sintering morphology.

In is worth noting, sintering of materials will result in a relative density. These densities are measured in mass per unit volume (g/cm^3, kg/m^3). The density of the sintered material depends on the physical properties and changes during sintering/densification. Therefore, it is common to measure the degree or percentage of sintering. However, theoretical densities correspond to a full dense/pore free solid. Naturally, a fraction or density percentage is most commonly used for comparing density after sintering with theoretical density. The language used to quantify density for porous parts in this document are percentage values (%) and/or relative density. In addition, the densities of porous parts are reported in terms of mass per unit volume measurements.

Moreover, sintering can be sub-divided into three intersecting stages; initial, intermediate, and final [79]. These stages are based on the connectivity of the solid and porous phases [80]. Initial stages of sintering are classified via bonding between neighboring particles with formation and significant growth of necking but limited densification. In the initial stage, the solid and porous phases are connected. Considerable densification occurs during the intermediate stage. The final stage corresponds to the solid phase being connected but the porous phase is isolated. For crystalline materials, the final stages can produce significant grain growth and microstructural evolution.

Mechanisms of SSS and LPS sintering can be described via the transport of material from an atom source to an atom sink site by means of detachment of an atom from the source towards the sink (diffusion) and attachment of atoms to the sink (interface reaction). As a result, kinetics of bonding, densification, and grain coarsening must be governed by either diffusion or interfacial reactions. However, it is commonly accepted that for densification and grain growth in crystalline materials, diffusion governs the kinetics of the system [79]. For the most part, this assumption has been found to be valid only for crystalline materials with atomically disordered interfaces.

Since this research focuses only on one type of sintering, namely solid state sintering of crystalline materials (SSS), a thorough description of this method, and its mechanisms along with classical models will be discussed. The above mentioned models and descriptions began in the middle of the 20th century first by Frenkel [81] and later Pines [82]. These models describe the sintering process as viscous flow and vacancy flow, which were reported to lead to a reduction of free surface energy and served as the basis for many subsequent models. Afterwards, several kinetic models were developed to define the three stages in the SSS processes. One of which is the classical description of bonding and densification [78].

The classical description of bonding and densification reports the driving force for material transport stems from the difference of the chemical potentials. This particular model assumes the transfer of material occurs under curved surfaces, specifically spherical particles [83], [84]. Due to the chemical potential difference, atoms transport to necks between particles from grain boundaries as well as the spherical particle surfaces. Here, the necking acts as the sink in bonding and densification, while particle surfaces act as atom sources. Diffusion drives material from the surface of powders to the neck surface therefore, redistribution of material on the surface of the particles causes necking without densification. This situation is illustrated in Figure 2.4 In the case of material diffusing from grain boundaries; densification occurs and is accompanied by the bonding caused due to shrinkage of particles.

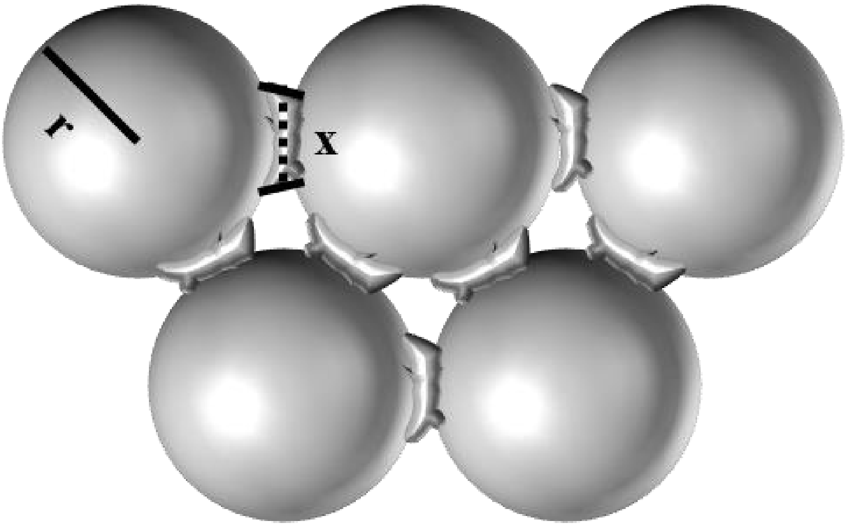

Figure 2.4: An example of impeccable sintering conditions involving isotropic particles having radius, r, and neck diameter, x.

Certain cases of diffusion, or the rate of material transport from source to site (i.e. grain boundary or particle surface to neck surface) has been described mathematically for isotropic spherical particles as [83]:

$$\frac{dV}{dt} = JAV_m = \left(-\frac{D}{RT}\nabla\sigma\right)AV_m \tag{2.1}$$

where V is the volume of material diffused to the neck from the particle (either grain boundary or surface), t represents the time sintered, D is the diffusional coefficient, R is the universal gas constant, T is absolute temperature (in Kelvin), σ represents a stress gradient, A is the diffusional area, and V_m is the molar volume.

During initial stages of sintering via neck growth the ratio of x/2r ~ 0.2, where x is the neck diameter and r is the particle radius (see Figure 2.4). For these particular instances, equations to describe the kinetics of diffusion can be derived from Equation 2.1. The general expression to describe sintering of aspherical particles during the initial stage is, [78]:

$$\left(\frac{x}{2a}\right)^n = F(T) * \left(\frac{1}{a^{n-m}}\right)t \tag{2.2}$$

As mentioned previously, x is the neck diameter and r is the particle radius, n and m are exponents dependent upon the transport mechanisms and atom sources, the function F (T) is temperature dependent and includes the diffusion coefficient, as well as the absolute temperature.

The intermediate and final stages of sintering can be mathematically described by simplifying and representing the microstructure as channel shaped connected pores along grain edges and corners [85]. As mentioned earlier, intermediate and final stages of sintering primarily contribute to densifications. The mechanisms for these stages are grain boundary diffusion along with lattice diffusion from neighboring grain boundaries to the pore surfaces [85]–[88]. A kinetic equation for the intermediate and final stages of sintering for spherical particles can also be derived from Equation 2.2:

$$\frac{1d\rho}{\rho dt} = \frac{K_1(1-\rho)^k}{G^m\rho} \tag{2.3}$$

In this expression, ρ is the relative density, K_1 is a constant of various parameters including diffusion coefficient, surface energy, temperature and molar volume, k and m are exponents based on transport paths and G is the grain size.

2.2 Shape Memory Alloys

2.2.1 History and Applications of Shape Memory Alloys

Martensite in steels was first discovered by Adolf Martens in the 1890's, which was a leading step for the discovery and explanation of the martensitic transformation. The martensitic transformation was perhaps the most widely studied metallurgical phenomenon during the early 1900's [3]. For example, martensite observed in Fe (iron) and C (carbon) systems was established as an irreversible martensitic transformation during this period.

The shape memory effect, due to the reversible martensitic transformation, was first reported by Chang and Reed in 1951 while experimenting with Au-Cd alloys [89]. Chang and Reed reported a material when deformed at a low temperature, and then heated, recovered the original shape; later termed one way shape memory effect. Soon after, the pseudo-elastic (super-elastic) shape memory effect was reported when a deformation occurred in a SMA in the high temperature austenite phase. An immediate recovery of the deformation was noticed. These effects weren’t publicized until 1963 when Buehler *et al* [90] discovered the same effect in NiTi (nickel-titanium) alloys. It was reported that NiTi possessed good mechanical properties that were comparable with some metals used for various engineering applications [91]. Shortly after the term “NiTiNOL” was created in honor of NiTi’s discovery at Naval Ordnance Laboratory (NOL).

Since then, a significant amount of interdisciplinary research has been invested into SMA’s due to their unique properties of remembering the original shape. In 1965 Wang *et al* [92] reported the addition of a third metallic element such as Co (cobalt) or Fe to the NiTi system caused significant decreases in the reversible martensitic transformation temperatures. This new series of alloys inspired commercial shape memory applications, such as Cryofit, which has been used as pipe couplings for F-14 fighter aircraft [93], [94]. These transformation temperatures were so low it has been reported that Cryofit had to be ship in liquid nitrogen to prevent martensitic phase transformations. Additional research lead to the discovery of NiTiNb alloys in 1989, which were much easier to work with due to larger thermal hysteresis along with newly found applications; damage repair and nuclear reactor repair [95].

Since the initial discovery of NiTi shape memory alloys, many commercial applications have been developed based the material properties. These applications are most notably biomedical applications beginning in the 1970's, and heart stents in the 1990's. In addition to these, NiTi has been used for actuation under high temperature operating conditions, aerospace, and oil industries have also utilized the high temperature shape memory effect characteristics. Additional applications for shape memory alloys include, but are not limited to, medical implants, optometry eye-glass frames, pipe-couplings, actuators in electrical appliances, automobile industry, guidewires, and micro-actuators, including thin-films [96]. Furthermore, alloys that exhibit the shape memory effect under the presence of an external magnetic fields have also been investigated, generating high actuation frequencies and large strains due to the magnetic shape memory effect [4], [97].

2.2.2 Reversible Martensitic Transformations

The shape memory effect is a manifestation of a crystalline phase transformation known as martensitic phase transformation. The martensitic phase transformation is a reversible solid-to-solid diffusionless process that occurs between two phases: martensite (low temperature phase) and austenite (high temperature or parent phase). This diffusionless transformation occurs by shear distortion of the lattice structure, as a result of atom shifts from their original position. Moreover, the reversible martensitic transformation is a necessary condition for the shape memory effect. The phase transformation mechanism is driven by temperature in traditional shape memory alloys. On the other hand, in the case of ferromagnetic shape memory alloys phase transformations are driven by external magnetic fields, as well as change in temperature and/or an applied stress. Reactions from martensite to austenite are endothermic and correspondingly, austenite to martensite is exothermic. This being established, it can be reputed the crystal structure of the martensitic phase is one of low symmetry (i.e. tetragonal, orthorhombic, monoclinic) compared to that of austenite phase, which is typically cubic. These distinct phases are illustrated in Figure 2.5.

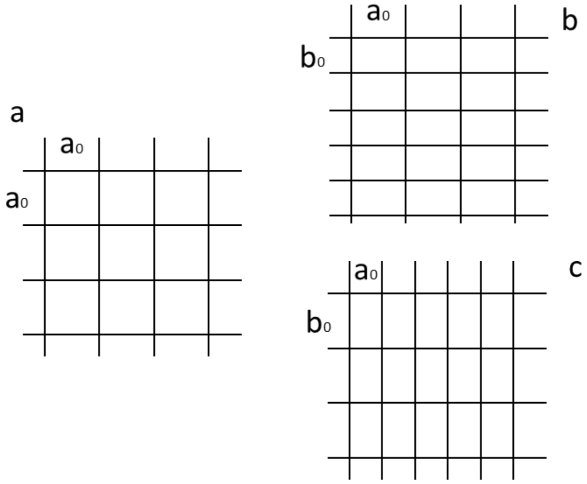

Figure 2.5: Schematic illustration of the martensitic phase transformation: (a) austenite; (b), (c) variants of martensite.

The deformation strain that occurs in the lattice during reversible martensitic transformations can easily be quantified using continuum mechanic techniques. For this, an austenite body occupying region A is considered in three-dimensional space as displayed in Figure 2.6. Choosing a reference plane, such as in Figure 2.6, we can describe any point in body A as;

$$X = \begin{pmatrix} x_1 \\ x_2 \\ x_3 \end{pmatrix} \tag{2.4}$$

Considering a homogenous linear deformation on the body A in the X_1 direction, any point can now be described as a function of X such that;

$$Y(x) = \begin{pmatrix} y_1(x) \\ y_2(x) \\ y_3(x) \end{pmatrix} \tag{2.5}$$

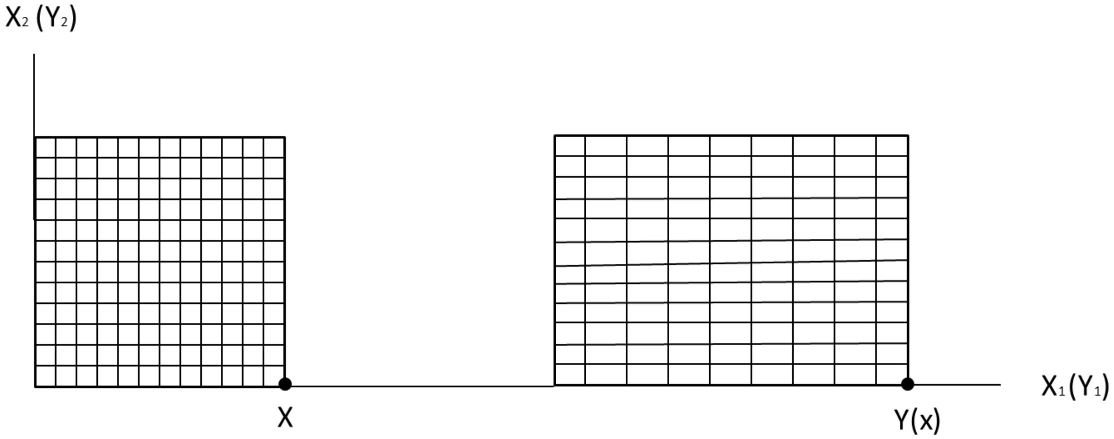

Figure 2.6: Example of a homogenous deformation. The reference configuration on the left deforms to the deformed configuration on the right.

The ability to quantify the deformations caused by heat, stress, or external magnetic fields allows the measure of strain (in percentage) with respect to each driving mechanism.

2.2.3 Shape Memory Effects

The shape memory effect describes the outcome of restoring a plastic deformation to its “original” position. In section 2.2.2, it was established this phenomenon is due to the reversible martensitic transformation; which is the phase transformation between martensite and austenite. In order to fully understand the three shape memory effects, the basis of the transformation must be elaborated upon at the atomic level. Therefore, the nature of crystal twinning will be introduced.

Twinning in a crystallographic domain occurs during crystal growth when a nucleating crystal is subjected to stress or temperature/pressure conditions that are dissimilar to original growth conditions [98], [99]. Multifarious atoms can impose the matrix material’s atomic positions during solidification, subsequently forming twin boundaries. The formation of twinning results in two separate crystals that share the same lattice positions, in terms of symmetry, resulting in separate crystals with a plethora of configurations. An illustration of crystallography of martensitic transformation at the atomic scale and its relationship as a function of deformation and temperature is displayed in Figure 2.7.

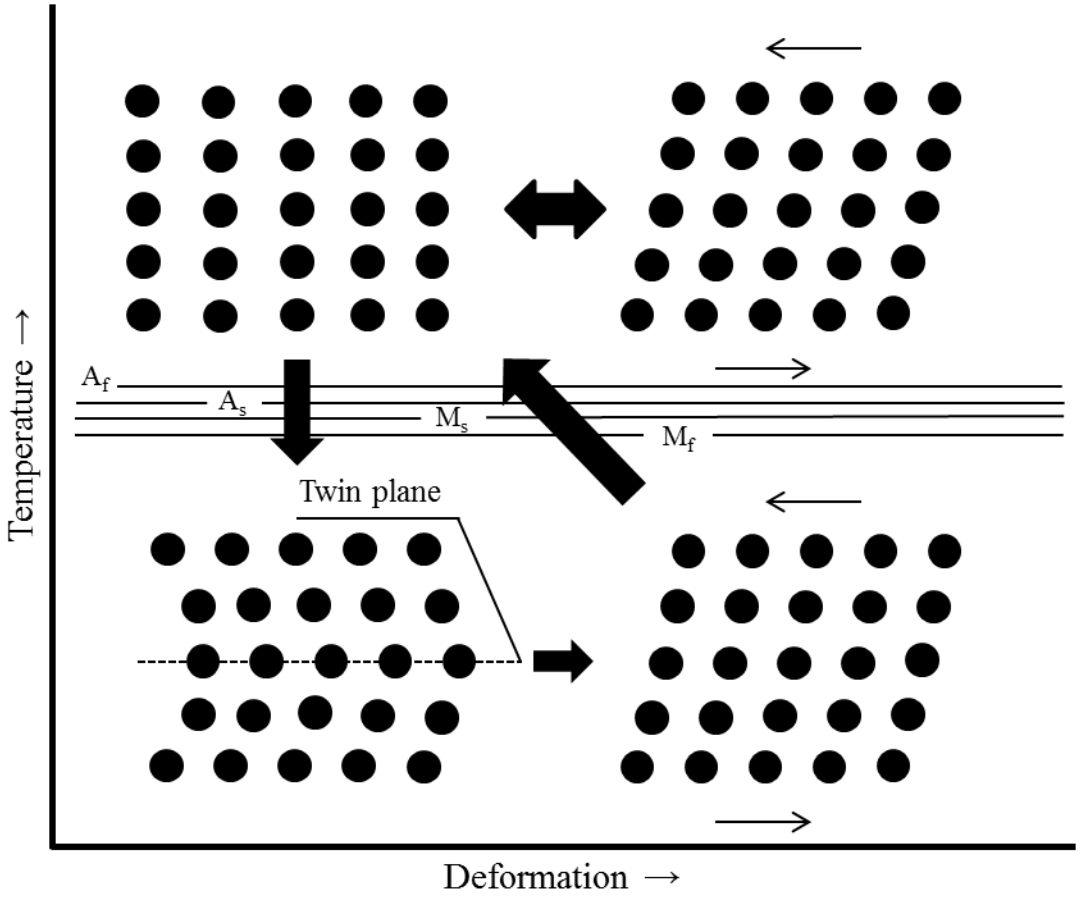

Figure 2.7: Illustration of the twin variant relationship between temperature and deformation.

In order to elaborate Figure 2.7, assume the material in reference is a single crystal shape memory alloy with one twin variant (bottom right). Next, assume the single crystal is in the martensitic phase and a stress, large enough to deform the twin is applied. The result of this deformation causes the martensite to inelastically deform, prompting the martensite to reorient, based on the stress applied (bottom left). Now consider the situation where heat (above the austenitic finish temperature) is applied to the inelastically deformed single crystal. As the temperature of the material increases, beginning with the austenitic start temperature, the deformed martensite begins to shift, ultimately forming the austenitic structure, as depicted in Figure 2.7 (top left). It is worth noting, during this transformation the atoms have shifted. The shifting of the atoms on the atomic scale compensates for the macroscale deformation (localized strain) on the single crystal, resulting in the recovery of the deformation and subsequently returns to the original state of the material. This effect is termed the one way shape memory effect, or often referred to as the thermoelastic martensitic transformation. The thermos-elastic stress - strain behavior is depicted in Figure 2.8, left side, as indicated by the martensitic phase.

The next shape memory effect that will be discussed is known as pseudo-elasticity or super-elasticity in other terminology. For this, consider a single crystal shape memory alloy that possesses the austenitic phase at ambient temperatures. This circumstance is depicted in Figure 2.7, top left. Now, consider a stress that is quasi-statically applied to the single crystal. As the stress increases, the austenitic single crystal experiences elastic deformation, until the transformation stress is reached. Upon reaching the transformation stress, the formation of stress-induced martensite begins. Once the stress induced martensite is reached, the material continues to strain at a constant stress. The removal of the load causes the stress induced martensite to return to the high temperature austenitic phase, coherently restoring any deformation imposed on the body. The stress – strain relationship of these two shape memory effects are illustrated in Figure 2.8. Notice, the loading path does not coincide with the unloading path between both cases. The unloading path plateaus, for the austenitic phase, at lower stresses compared to the loading cycle. This is due to stress differences between the M_f and A_s, and M_s and A_f consequently forming a hysteresis loop.

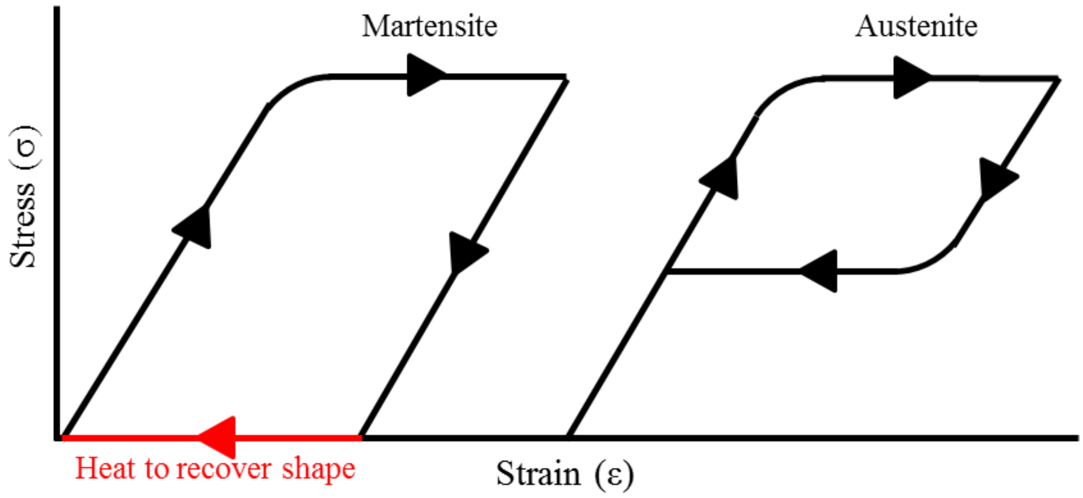

Figure 2.8: Representative stress – strain curves for shape memory alloys in the martensitic (left) and austenitic (right) phases, illustrating one way shape memory effect and pseudo-elastic effect, respectively.

The third and final shape memory effect is not intrinsic in nature, unlike the one way shape memory effect and pseudo-elasticity. The two way shape memory effect has the capability to remember a particular shape in the martensitic phase under certain conditions. The one way shape memory effect and pseudoelasticity only possess the ability to remember a shape in the austenitic phase. Albeit, through specific thermo-mechanical treatments known as “training”, the two way shape memory effect is achievable. Two way shape memory effect refers to reversible and spontaneous shape changes in shape memory materials through thermal cycling, such as heating and cooling. The previously mentioned thermo-mechanical trainings affect the material on the atomic scale. Plastic deformation exerted on the material in the martensitic phase cause dislocations in order to accommodate the applied stresses. These dislocations exist in the parents' phase, even through heating to austenite. This creates a stress-biased martensite; which is paramount for stimulating two way shape memory effects.

Only two of the three shape memory effects were investigated in this research: the one way shape memory effect and pseudoelasticity. These effects were achievable through heating the sample above the austenitic finish temperature, as the composition of the alloys were attuned to possess martensite at ambient temperatures. In a particular case, it was observed the Ni-Mn-Ga alloys in this researched possessed a mixture of austenite and martensite at room temperature

2.2.4 Current Research on Shape Memory Alloys Made by Additive Manufacturing

Attempts of binder-jet additive manufacturing of shape memory alloys powders have been reported by Lu & Reynolds [100], where TiNiHf gas atomized powders were printed in 3D fine mesh structures. They studied the influence of two printing parameters, layer thickness and binder saturation with varying particle size, on the dimensional quality and mechanical strength of the printed part. It was reported that at the same layer thickness, breaking strength increases with binder saturation level up to 170%. And at the same binder saturation, 35μm layer thickness is the optimal parameters for the TiNiHf fine mesh structures. Lu *et al* [100] investigated the 3D printing (3DP) of TiNiHf shape memory alloys embedded in a glass matrix. They reported the optimum 3DP parameters for successfully achieving shape memory effect on the printed part. The printed part showed reversible thermoelastic martensitic transformation, which is a prerequisite for shape memory effect.

In other work, attempts of 3D printing the well-known super-elastic shape memory nitinol (NiTi) using a laser based rapid manufacturing (LRM) system were conducted [23]. Three compositions of nitinol ($Ti_{55}Ni_{45}$, $Ti_{50}Ni_{50}$, $Ti_{45}Ni_{55}$) were ball milled and laser printed on a Ti substrate. Surface morphology, composition, micro-mechanical properties and phase presence were studied and compared to traditionally manufactured samples. Their results show micro-segregation in the alloys, as confirmed by EDS and XRD. DSC results reveal slight endothermic and exothermic heat flow, implying reversible martensitic transformations. The micro-hardness values reported were larger in 3D printed alloys, compared to the as-melted alloys. Nevertheless, successful attempts of additive manufacturing shape memory alloys are recorded.

Attempts to predict mechanical properties of the porous Ni-Ti alloys have been explored using mathematical investigation based on experimentally obtained material properties [101]. In their work, Zhao *et al* [101], were able to simulate three piecewise linear portions of compressive testing using a simple model.

3. Ni-Mn-Ga Alloys & Associated Magnetic Properties

3.1 History of Ni-Mn-Ga

Ni-Mn-Ga is a well-known ternary ferromagnetic shape memory Heusler alloy. The ferromagnetic shape memory effect was discovery in 1996 by Ullako *et al* [4] through showing a 0.2% magnetic field induced strain (MFIS) in a [001] crystallographic direction of an unstressed Ni_2MnGa single crystal. This magnetically induced strain is compared to other functional materials such as piezo-electrics and Terfenol-D, which only show magneto-strictive strains on the order of 0.1% and 0.2%, respectively [102], [103]. Since the aforementioned, a significant amount of interdisciplinary research has been conducted towards the Heusler alloy. Ten years after the discovery the number of publications on Ni-Mn-Ga alloys increased exponentially, as shown in Figure 3.1, [22].

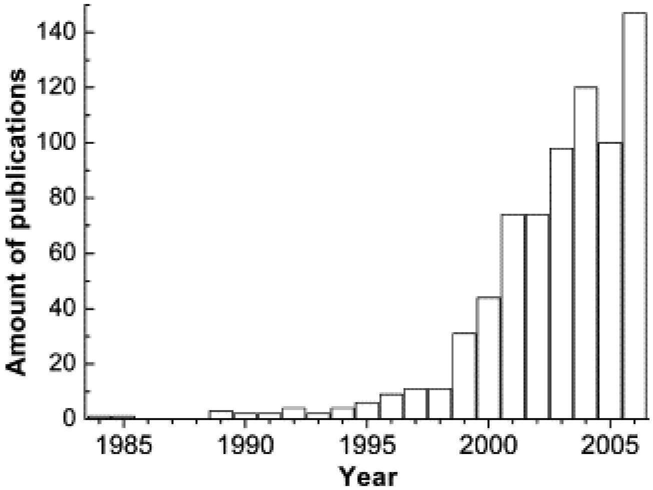

Figure 3.1: Diagram showing world-wide research of Ni-Mn-Ga alloys by number of publications per year from 1984 to 2006 [22]. Reprinted with permission from Elsevier, see Appendix A.

Subsumed in those publications a few major discoveries have been reported. One of which was in 2000, by Murray *et al* [104] where an off stoichiometric $Ni_{47.}4Mn_{32.1}Ga_{20.5}$ single crystal produced a 6% field induced strain at ambient temperature. Succeeding the 6% strain, in 2002 Sovinov *et al* [10] discovered a remarkably large, 9.5% MFIS. In their study, a single crystal of $Ni_{48.8}Mn_{29.7}Ga_{21.5}$ was prepared by induction melting high purity elements and grown into single crystals. It was reported, the crystal structure of the off stoichiometric Heusler phase was responsible for the large field induced strain. Chmielus *et al* [9] later formed thin-walled foam structures by melting ingots of $Ni_{52.0}Mn_{24.4}Ga_{23.6}$ and $Ni_{52.3}Mn_{23.9}Ga_{23.8}$ and casting them into bimodal sized ceramic preforms resulting in 62% porous metallic sponges. Magneto-mechanical testing showed the polycrystalline ferromagnetic shape memory alloy (FMSA) foams produced an 8.7% MFIS. In addition to the investigation of the bimodal Ni-Mn-Ga metallic foams, the effects of porosity on the MFIS were also examined by Witherspoon *et al* [105]. In their study, it was shown that increasing porosity in three foams enhanced the magnetic shape memory effect (MSME). Nonetheless, the metallic foam approach shows a viable method to produce polycrystalline Ni-Mn-Ga alloy that display relatively high magnetic shape memory effects; in the order of 1.3 %, for a 75 % porous foam. The reported magnetic field induced strains in bimodal metallic foams are well above the reported 0.12 % for monomodal counterparts [105]. Moreover, the magnetic field induced strains in the bimodal polycrystalline foams are well above reported 0.3 % MFIS's for directional solidified polycrystalline Ni-Mn-Ga samples.

Nevertheless, the above-mentioned reports show sufficient evidence that porous polycrystalline Ni-Mn-Ga alloys can produce remarkable MFIS's when compared to fully dense samples. With that being said, the interest in producing porous Ni-Mn-Ga alloys has become of attention, especially with new manufacturing methodologies such as additive manufacturing.

3.2 Ferromagnetism

Ferromagnetics, such as iron, cobalt, nickel and their alloys, demonstrate very particular magnetic behaviors. Exchange forces in ferromagnetics are quantum mechanical phenomenon's which occur in relative orientation to the spin directions of two electron moments. In ferromagnetic materials, parallel alignment of these coupled electrons cause "moments" resulting in large net magnetization (M), even in the absence of magnetic fields. Distinct characteristics of ferromagnetics are their spontaneous magnetization and the existence of magnetic ordering temperature. A typical magnetization process for a ferromagnetic material is illustrated in Figure 3.2.

Figure 3.2 (a) represents a ferromagnetic material in absence of an external magnetic field. When a magnetic field is applied (b), magnetic moments begin to grow in the direction of the field due to the reorientation of the electron spins; although the field magnitude is insufficient to fully saturate every dipole. When the field strength is increased (c), the spin directions reorient to form moments parallel to the field direction, relative to some degree (θ). If field strength continues to increase, the ferromagnetic material will reach a saturation point (M_s) at a given field (H_s), (d). The saturation magnetization is the maximum induced magnetic moment that can be obtained in a magnetic field H_s, beyond this no further increase in magnetization occurs. Furthermore, saturation magnetization is an intrinsic property, independent of particle size but heavily dependent upon temperature.

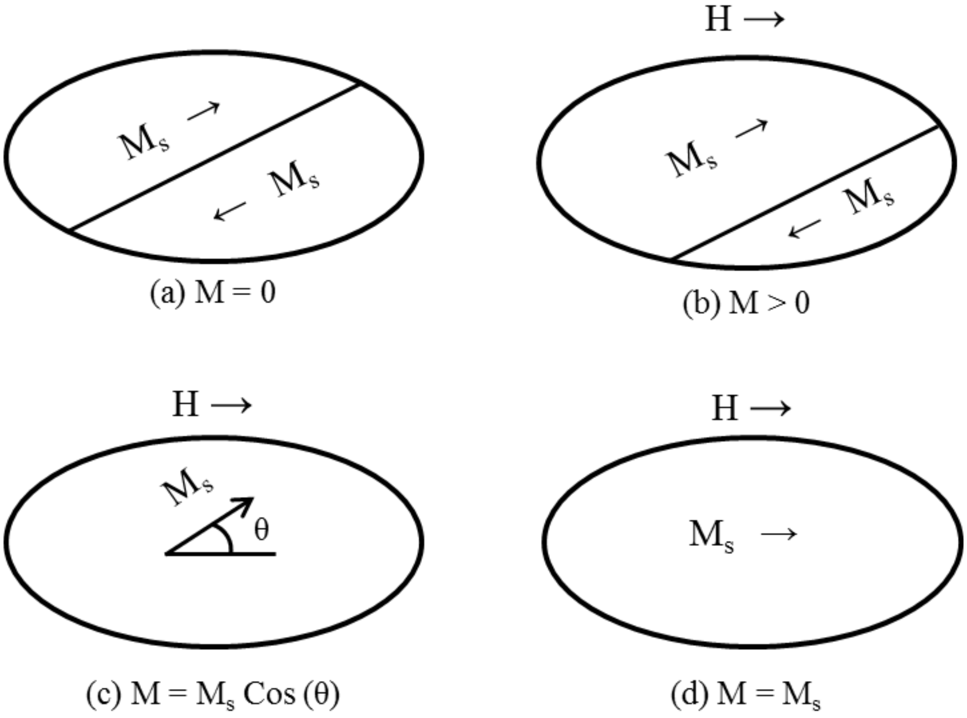

Figure 3.2: The magnetization process in a ferromagnetic material.

When a ferromagnetic material is magnetized in one direction, it will not return to zero magnetization when the applied external magnetic field is removed. For this, a magnetic field applied in the opposing direction is necessary. If an alternating field is applied to the ferromagnetic material, its magnetization will respond in a particular way, called a hysteresis loop [106]. This magnetization phenomenon is depicted in Figure 3.3. As shown in Figure 3.3 (a), the initial magnetization follows a non-linear curve when magnetized from a relative zero-field value. This curve follows an increase in magnetization until magnetic saturation (M_s) is achieved at a field value (H_s), (b). At this point, approximately all the magnetic domains are aligned, resulting in a net direction with respect to the applied field. The next step in the magnetic loop measurement is to remove the magnetic field, to attain a zero field value, (c). When the field reaches zero, the ferromagnetic material loses saturation although retains some degree of magnetization. The residual magnetization at zero field is termed "positive" remanence (M_r) [107]–[109]. As the field begins to reverse direction and magnitude, the effect on magnetization decreases to a zero value (d), at the "negative" coercive field value ($-H_c$). As the magnitude of the field is increased in the opposing direction (e), the ferromagnetic material experiences an additional "negative" saturation point ($-M_s$), at a field value ($-H_s$). Once again, switching the field direction and decreasing the magnitude (f), results in relative decreasing magnetization until the field reaches a zero value, in which a "negative" remanence saturation ($-M_r$) is retained. As the field continuously increases, a zero magnetization is again reached at a similar "positive" coercive field strength ($+H_c$). Further increase of magnetic field will result in M_s at H_s, as shown in (b).

The mechanisms responsible for the particular magnetic behavior in ferromagnetics are the motion of magnetic domain walls and the rotation of the magnetic moments. The magnetic domains can be envisioned as discrete volumetric regions with unidirectional magnetic moments. The magnetic domains are separated by coexisting domain walls. The domains and wall movement are the cause for the specific ferromagnetic behavior, producing the hysteresis during magnetization. When the direction of magnetization is uniform, domains with a magnetic moment more or less parallel to the magnetic field grow via domain wall motion albeit, by the expense of less parallel surrounding magnetic moments. In the case that the external magnetic field strength increases to the M_s, the magnetic moments belonging to favored magnetic domains will rotate until parallel with the external magnetic field, if misaligned.

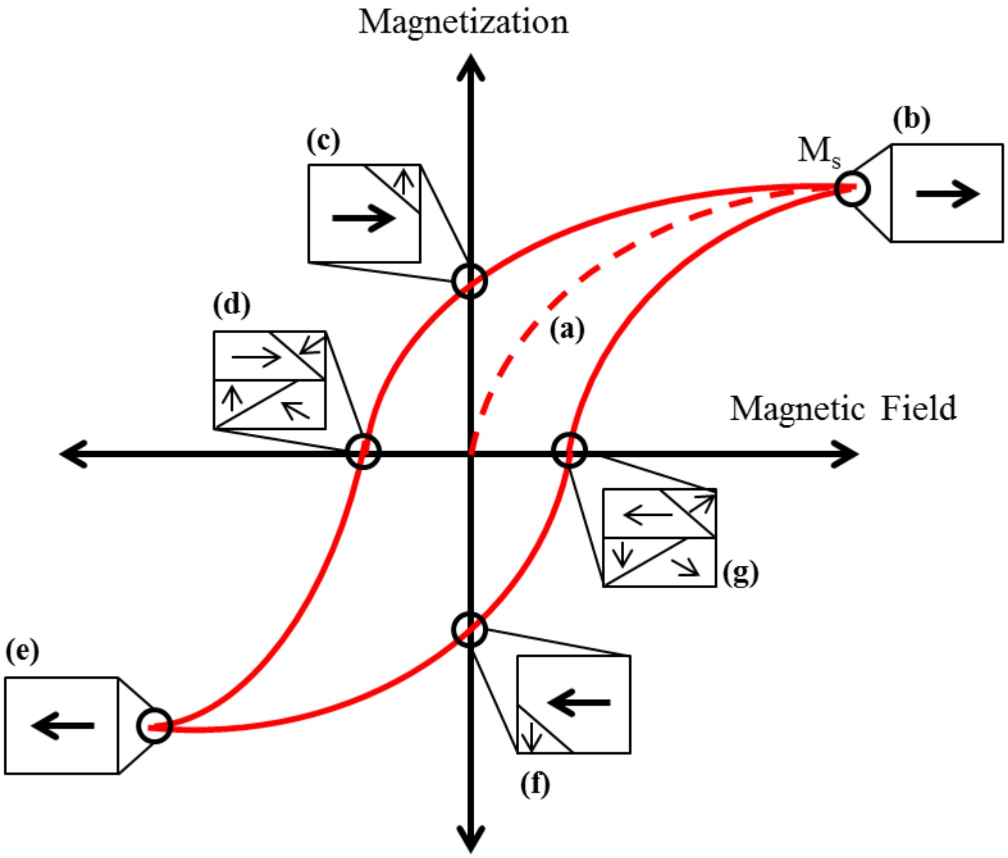

Figure 3.3: Typical magnetization hysteresis of a ferromagnetic material.

Ferromagnetic materials can result from spontaneous alignment of the dipole moment of atoms, without the presence of an external magnetic field, as shown in Figure 3.4 (a). As mentioned previously, the magnetization in ferromagnetics is heavily dependent upon temperature. This relationship is shown schematically, where the saturation magnetization of a ferromagnetic material decreases with increasing temperature. According to the Curie-Weiss law, this describes the magnetic susceptibility for ferromagnetic materials, the inverse magnetic susceptibility increases above the Curie temperature [110]. This relationship is described in Equation 3.1 (Curie-Weiss law) where X is the magnetic susceptibility of a ferromagnet in the paramagnetic region above the Curie point, C is a material dependent Curie constant, T is the absolute temperature is Kelvins, and T_c is the Curie temperature of the ferromagnetic material, in Kelvins.

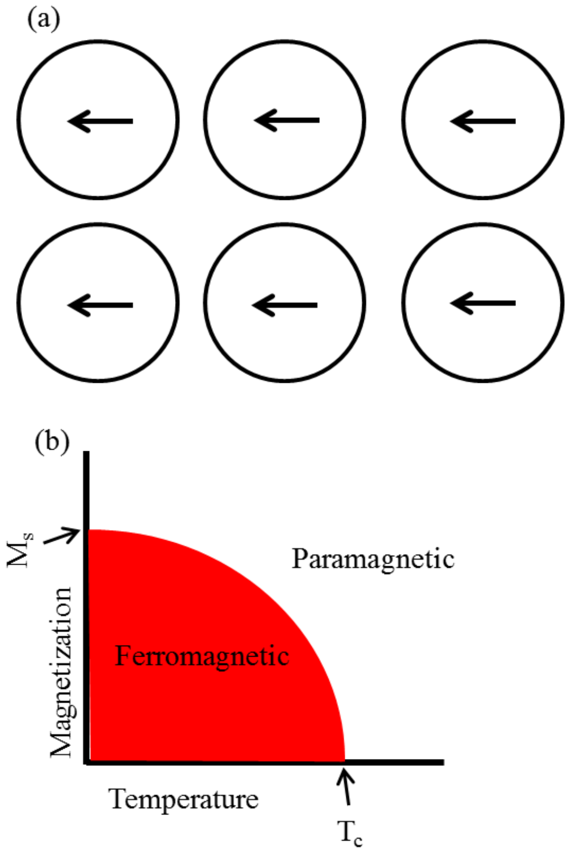

Figure 3.4: Illustrations representing the magnetic properties of ferromagnetic materials. (a) Magnetic moment behavior in ferromagnetic materials in absence of an external magnetic field; (b) Temperature dependence of magnetization for ferromagnetic materials.

$$X = \frac{C}{T - T_c} \tag{3.1}$$

As temperature in a ferromagnetic material increases, subsequently surpassing the Curie temperature, a second order phase transformation occurs, producing a paramagnetic material.

3.3 Paramagnetism

Paramagnetic materials such as magnesium (Mg), molybdenum (Mo), lithium (Li), and tantalum (Ta), are materials that possess minor (positive) susceptibility to magnetic fields. These materials are faintly attracted by means of magnetic field and unlike ferromagnetic materials, once the field is removed, magnetization returns to a net-zero value. The difference between ferromagnetic and paramagnetic materials is conveyed when atomic spins are investigated. Paramagnetic material properties are due to the presence of unpaired electrons. The unpaired electrons result in randomly oriented magnetic moments, which become more aligned in the presence of an external magnetic field. As discussed in section 2.3.2, the magnetic susceptibility is governed by the Curie-Weiss law, therefore heavily dependent upon temperature. As temperature increases, it becomes exponentially difficult to align the magnetic moments for paramagnetic materials. The susceptibility versus temperature relationship of a paramagnetic material is graphically shown in Figure 3.5 (a).

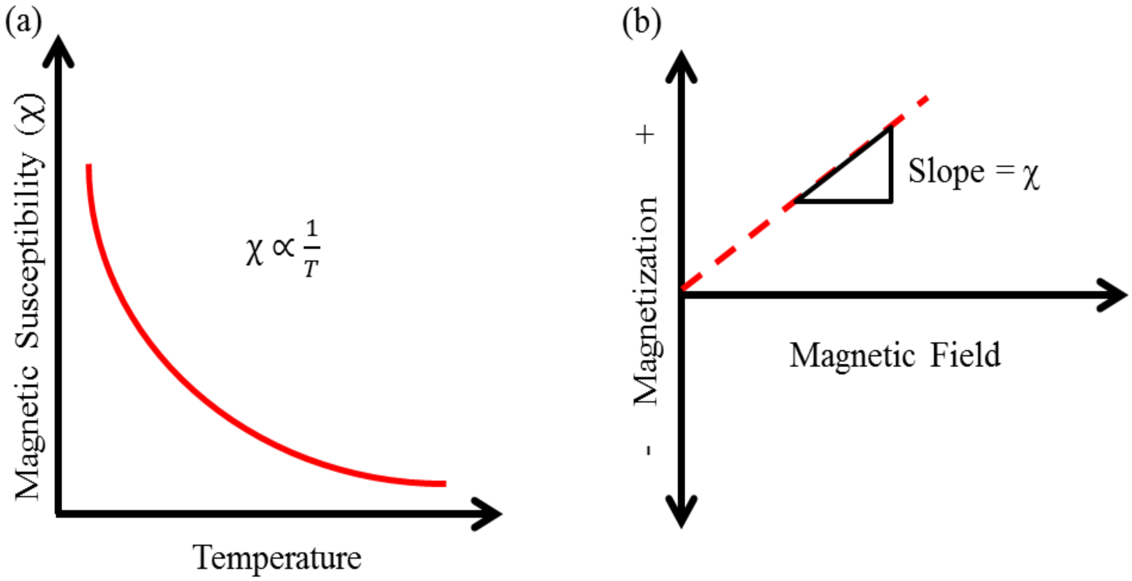

Figure 3.5: (a) Typical magnetic susceptibility versus temperature behavior for a paramagnetic material. (b) Typical magnetization versus magnetic field relationship for a paramagnetic material. The slope of the M vs H is the magnetic susceptibility at a specific temperature.

To determine the magnetic susceptibility of a paramagnetic material, magnetization measurements with increasing field strength is necessary. Since, the magnetic susceptibility is dependent on temperature; an individual measurement is conducted for a specific temperature. The result of this is illustrated in Figure 3.5 (b), where the slope of these measurements produces the magnetic susceptibility.

3.4 Crystal Structure of Ni_2MnGa and Near Stoichiometric Alloys

Fredrick Heusler, a German engineer and chemist, was the first to discover Heusler materials such as Cu_2MnAl, which later was determined to possess the Heusler phase [111], [112]. Heusler alloys are defined to be ternary ferromagnetic materials that crystallize in the Heusler phase, belonging to face-centered cubic (FCC) $L2_1$ ordered cubic phase (space group Fm3m (225)). Most commonly, Heusler phased materials retain an A_2BC nominal composition. It is often the case A and B are transition metals [113], [114], with exceptions of B belonging to rare earth metals [115]. Material C tends to be a non-metal or non-magnetic element. In addition to the Heusler structure, similar materials with nominal compositions of ABC can form half-Heusler structures. An example of the Ni_2MnGa Heusler structure is shown in Figure 3.6. The unit cell consists of four interpenetrating FCC sub-lattices with atomic positions shown in Table 3.1. The $\left(\frac{1}{2}\frac{1}{2}\frac{1}{2}\right)$ site is vacant for half-Heusler materials.

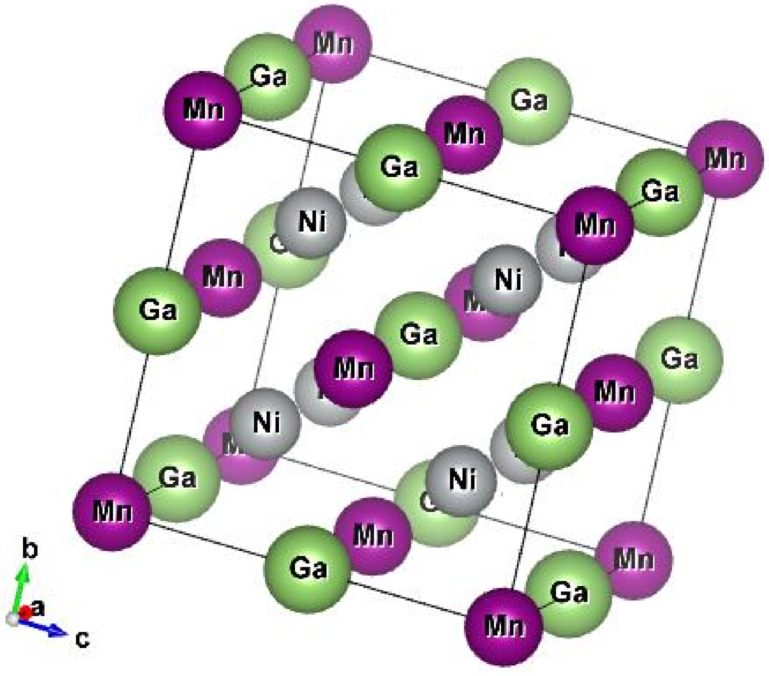

Figure 3.6: Ni_2MnGa Heusler crystal structure.

Despite the evident interest in Heusler related alloys, the properties and potential applications of Ni-Mn-Ga alloys due to the magnetic shape memory effect (MSME) are still of pronounced interest. Unfortunately, the exact atomic positions of Ni-Mn-Ga related alloys are not very well understood. Furthermore, the physical properties such as martensitic transformation temperatures along with magnitude of MSME for Ni-Mn-Ga alloys change based on the composition of each element. For example, slight changes in chemical composition, between $Ni_2Mn_{1.2}Ga_{0.8}$ and $Ni_{1.95}Mn_{1.19}Ga_{0.86}$, are reported to possess two different modulated martensitic phases [116], [117]. Based on this, there is much debate on the atomic positions and overall structure of near stoichiometric Ni_2MnGa phases.

Table 3.1: Atomic positions for A, B, and C for Heusler phased materials.

	A	B	C
Lattice Position	(000), $(\frac{1}{2}\frac{1}{2}\frac{1}{2})$	$(\frac{1}{4}\frac{1}{4}\frac{1}{4})$	$(\frac{3}{4}\frac{3}{4}\frac{3}{4})$

The majorities of the Heusler alloys are ferromagnetically ordered and saturate in relatively weak magnetic fields. In particular, if the magnetic moment is carried by manganese, such as A_2MnC, a value close to four times the Bohr magneton is typically reported [118]. A list of these magnetic Heusler phased materials is presented in Table 3.2, which demonstrates alloys containing 3d transition metals (V, Cr, Mn, Fe, Co, Ni) as the B site and 3d, 4d, and 5d elements as the A site [119].

Table 3.2: Nominal composition and magnetic order of full Heusler alloys (FEM: ferrimagnetic, FM: ferromagnetic, PM: paramagnetic, AFM: antiferromagnetic).

B	A	C	Magnetic Order
V	Mn	Al, Ga	FEM
	Fe	Al, Ga	FM
	Fe	Si	PM
	Co	Al, Ga, Sn	FM
Cr	Co	Al, Ga	FM
	Fe	Al, Ga	FM
Mn	Cu	Al, In, Sn	FM
	Cu	Sb	AFM
	Ni	Al	AFM
	Ni	Sb	FM
	Ni	Al, Ga, In, Sn, Sb	FM
	Co	Al, Si, Ga, Ge, Sn	FM
	Co	Sb	FEM
	Fe	Al, Si	FM
	Pb	Al	AFM
	Pb	In	AFM
	Pb	Ge, Sn, Sb	FM
	Pb	Sb	FM
	Pb	Te	AFM
	Rh	Al, Ga, In	FM
	Rh	Ge, Sn, Pb	FM
	Rh	Sb	FM
	Ru	Ga	FM
	Au	Zn, Cu	AFM
	Au	Al, Ga, In	AFM
	Au	Sb	FM
	Pt	Al, Ga	AFM
	Pt	Ga	FM
	Ir	Al	AFM
	Ir	Ga	AFM
Fe	Fe	Al, Si	FM
	Co	Al, Si, Ga	FM
Co	Fe	Ga	FM
Ni	Fe	Al, Ga	PM

The structure and phase behavior of near stoichiometric Ni_2MnGa alloys is heavily dependent on temperature and composition of corresponding elements [120],

[121]. During phase transformations, explicitly during the cooling stages, an atomic ordering increases as temperature decreases [122]; this relationship is displayed in Figure 3.7. The first solidus transformation for Ni-Mn-Ga constrained by these circumstances occurs from liquid to high temperature disordered A2 (BCC) phase; which is shown when $x \leq 15$ at%. Moreover, this phase transformation was not reported when Mn content ranges from $15 \leq x \leq 40$ at% [122]. In the A2 phase, atomic positions are arbitrary. In the case of $15 \leq x \leq 40$, a phase transformation from liquid towards B2' occurs within a range of 200 K, which forms a simple cubic structure. In comparison to the A2 phase, the B2' phase is more ordered (FCC and simple cubic (SC), respectively), where Ni atoms occupy the body center, and Ga along with Mn atoms arbitrarily share corner sites. The thermodynamic phase diagram for various compositions of Ni-Mn-Ga related alloys have been investigated [123], [124], that report solidus temperatures between 1750 K and 1060 K. Beyond this, the transformation from B2' to $L2_1$ occurs and the corresponding temperature is heavily dependent on composition; albeit this transformation behavior seems to be parabolically related. Upon further cooling, the $L2_1$ phase forms a martensitic phase. The reversible transformation from the parent, $L2_1$ phase, to the martensitic phase is the reversible martensitic transformation.

Martynov *et al* [125] were among the first to examine the crystal structure of Ni_2MnGa and were the first to observe modulations in the structure. They reported, during single crystal investigation, the presence of four extra spots between the reflections related to the tetragonal lattice. This data was interpreted as having fivefold superstructure (5M), involving five-consecutive unit cells. Since then, extra peaks between main reflections have been associated with superstructures involving 5, 7, 10, and 12 unit cells indicated by 5M, 7M, 10M, and 12M modulation. The structural modulations in martensite phases are associated with the instability of the parent cubic structure which produces shuffling of atomic layers along selected directions [125].

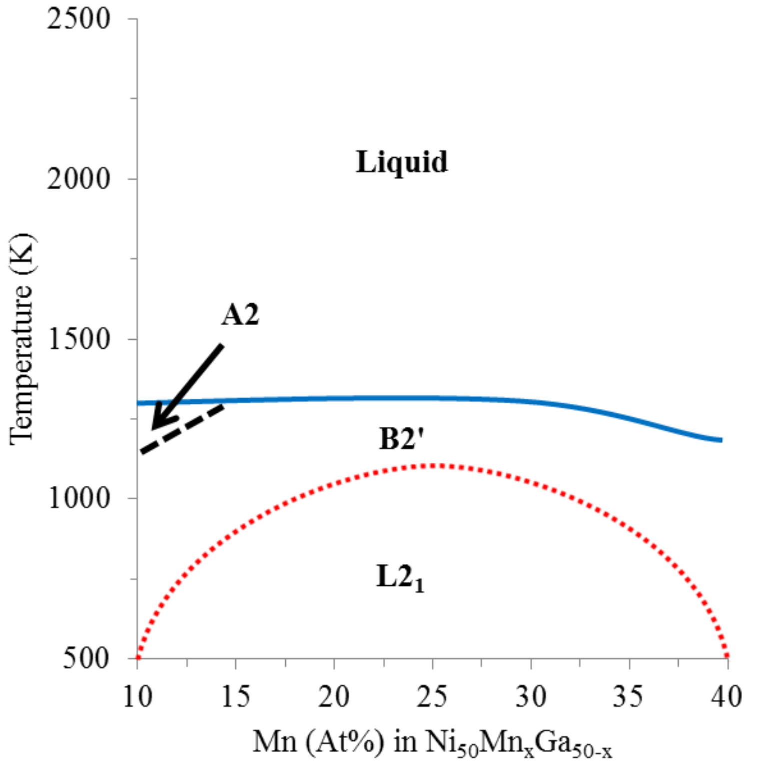

Figure 3.7: Experimental quasi-binary temperature-composition diagram for $Ni_{50}Mn_xGa_{50-x}$ in the range of $15 \leq x \leq 35$ [122]. The solid and dashed lines represent theoretical predictions for phase transformations. Dotted lines represent a fit to trend of experimental data.

The unit cell of 5M martensite was initially reported, based on the $L2_1$ lattice of high temperature phase, as body centered cubic with tetragonal distortion [125], [126]. This proposed unit cell was later dismissed, as a result of extended 5M martensite crystal structure investigation [127]–[129]. For instance, Righi *et al* [128] reported a more complex crystal structure of 5M martensite: the incommensurate 5M modulated martensite was reported as orthorhombic while the commensurate 5M martensite retained a monoclinic structure.

Since the initial investigation of the Ni-Mn-Ga structure, several martensitic phases have been reported in near stoichiometric Ni_2MnGa alloys. In Ni-Mn-Ga alloys, the $L2_1$ martensitic structure undergoes spontaneous uniform lattice distortion [129]. As a result, the martensitic structure can retain a tetragonal, orthorhombic, or monoclinic unit cell depending on the composition and temperature of the Ni-Mn-Ga alloy [130]. Furthermore, notable satellites in diffraction patterns are evidence of lattice modulations, varying with each unit cell. As mentioned, several modulations (non-modulated (NM), 5M, and 7M) have been observed in martensitic phases in Ni-Mn-Ga alloys. Most commonly, tetragonal unit cells preserve the non-modulated (NM) martensite [131]. The 5M modulated martensitic phase can hold an orthorhombic or monoclinic unit cell, depending on the periodicity of the modulations. For instance, commensurate modulations indicate the 5M martensitic phase has the monoclinic structure and incommensurate modulations of 5M martensite possess the orthorhombic configuration [127], [128]. If the Ni-Mn-Ga alloy possesses a 7M martensitic modulation, the unit cell assembles as a monoclinic unit cell [129].

These martensitic phases have also been classified by Chernenko *et al* [22] into three groups that are based on the martensitic transformation temperatures. The first set is comprised of the nearly stoichiometric Ni_2MnGa. These alloys are known to have low transformation temperatures compared to the Curie temperature (approximately 373 K). The second series of alloys include those of martensitic transformation temperatures around room temperature. These alloys show the large strains when a magnetic field is present. The third series are those alloys that have martensitic transformation temperatures above the Curie. These phases are more commonly referred to as five-layered modulation (5M), seven-layered modulation (7M) and non-modulation (NM), respectively [132]. The 7M monoclinic crystal structure desired for the giant MFIS occurs in slight manganese rich $Ni_2Mn_{1.05}Ga_{0.95}$ [22]. The 5M phase resembles those MFIS reported by Murray *et al* [133], and the NM tetragonal structure resembles field induced strains in the order of 0.02%, similar to those first reported in 1996 [4].

Examples of these modulations can be seen in Figure 3.8, which shows an illustration of the Ni-Mn-Ga microstructure with (a) 5M and (b) 7M modulations. Note the shifting of atoms via stacking sequences, for the modulated martensite; resulting is small angle changes in stacking directions.

In the case of non-modulated (NM) martensite for Ni-Mn-Ga, the structure is based on the austenite $L2_1$ unit cell, but with a tetragonal distortion along the c-direction. The work presented in this document reports only NM and 5M modulated martensite for Ni-Mn-Ga alloys.

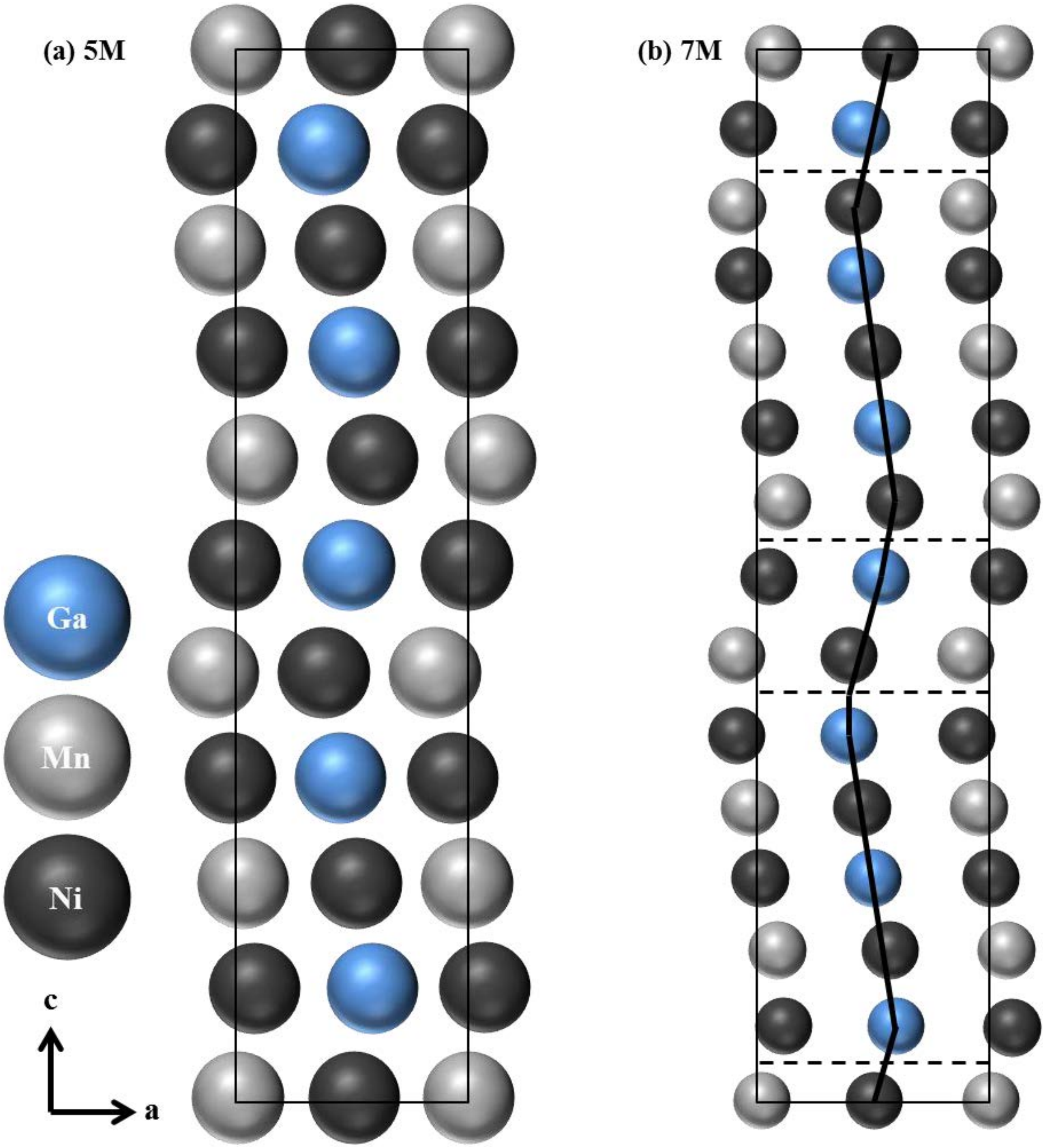

Figure 3.8: (a) View along the b-axis of the 5M commensurate modulated martensite and (b) view along the b-axis of the 7M modulated martensite.

3.5 Magnetic Field Induced Deformation

In section 2.3.4, it was established the NM, 5M, and 7M martensitic phases possess periodicities (i.e. modulations). These modulations are responsible for the formation of crystallographic twins in the martensitic phases of Ni-Mn-Ga alloys. The crystallographic twins along with the ferromagnetic properties (strong coupling between structure and magnetic order), results in magnetic field induced motion of the twin boundaries [10]. The coupling interaction between structure and magnetic order is expressed as the magnetic anisotropy constant, K_u [134]. The magnetic field applied to induce crystallographic reorientation is proportional to the mechanical stress, at low field values. At larger field values, such that the field is larger than the saturation field, the magnetic domains disassociate from the magnetic domains. Therefore, the limit of the maximum stress, σ_{max}, due to the applied magnetic field is controlled by K_u [135]. This relationship is expressed as:

$$\sigma_{\mathrm{max}} = \frac{k_{\mathrm{u}}}{\varepsilon_{\mathrm{max}}} \tag{3.2}$$

Here, ε_{max} is the maximum strain achievable by crystallographic twin reorientation, constrained by the lattice parameters. Since the maximum strain value achievable is dependent upon the lattice parameters, a detailed explanation will be pursued.

The movement of the twin variants in the martensitic phases has been extendedly investigated, resolved with various models and explanations [136], [137]. The nature of twin boundary motion occurs by means of motion of twinning disconnections. These disconnections are line defects in relation to Burgers vectors and step components at interface sites [138], [139]. Furthermore, for twin-twin interactions, step defects of the disconnections form disconnection walls [140]. In the particular case that twin disconnections in a stress field interacts with a strain field, given by the Burgers vector, the response of the disconnection to the stress field is governed by the Peach-Koehler equation [141], [142]. The Peach-Koehler equation describes the mechanical force exerted by a stress field on a dislocation, such as a disconnection. In the case of ferromagnetics, forces are generated on the disconnections due to the influence of the magnetic field. This applied force is restricted by the magnetic anisotropy constant. With that being said, a balance can be established between the magnetic and mechanical forces that yield the maximum magneto-shear-stress, $\tau_{M,\ max.}$ This relationship is given as:

$$\tau_{M,max} = \frac{K_u}{S_t} \tag{3.3}$$

where S_t is the twinning shear strain [143].

In section 2.3.4, it was also established Ni-Mn-Ga alloys in the martensitic phase can retain several crystallographic structures. It should be noted, when deliberating magneto-mechanics it is more convenient to assume the 5M martensite as a pseudo-tetragonal and 7M as a pseudo-orthorhombic unit cell. Moreover, these proposed unit cells are derived from a distorted $L2_1$, FCC unit cell. Furthermore, for these assumptions, and simplicity, the modulations are neglected. Therefore, the maximum strain, and in particular the magnetic field induced strain (MFIS), as well as the twinning shear strain can be expressed in terms of lattice parameters, a and c. The maximum achievable strains occur in the (101) and $[10\bar{1}]$ twinning system, expressed as [132]:

$$\varepsilon_{max} = 1 - \frac{c}{a} \tag{3.4}$$

Along with, maximum shear stress based on lattice parameters:

$$S_t = \frac{a}{c} - \frac{c}{a} \tag{3.5}$$

In addition to these simple models used to describe the maximum strains achievable based on lattice parameters, additional more sophisticated models have been reported [144], [145]. Nevertheless, the lattice parameters govern these strains thus, the crystal structure of the martensitic phase is vital for achieving large MFIS's. As a result, the martensitic phases are often described by their lattice parameters as (c/a) ratios. As directed by Equation 3.4, large strains are reachable when c/a ratio satisfies the following; $c/a<1$ and $a>b>c$. Since these models assume the 5M and NM martensite are pseudo-tetragonal and the 7M martensite is pseudo-orthorhombic, the above mentioned constraint of $a>b>c$ is only feasible in 7M martensite. Typical lattice parameters for all three martensitic phases have been reported in Table 3.3, along with the MFIS's measured and calculated [132]. The proposed model holds reasonably true for 5M and 7M martensitic phases. Furthermore, in best cases, giant strains of approximately 6% and 9.5% were obtainable in modulated martensite of Ni-Mn-Ga alloys.

Table 3.3: Table of reported variables for Ni-Mn-Ga alloys in three martensitic phases [132].

Martensite Type	5M (c/a<1)	NM (c/a>1)	7M (a>b>c)
Composition (at %, ±0.5%)	$Ni_{49.2}$ $Mn_{29.6}$ $Ga_{21.2}$	$Ni_{52.2}$ $Mn_{27.3}$ $Ga_{20.6}$	$Ni_{48.8}$ $Mn_{29.7}$ $Ga_{21.5}$
Lattice Parameters (nm)	a = 0.594 b = 0.594 c = 0.559	a = 0.546 b = 0.546 c = 0.658	a = 0.619 b = 0.580 c = 0.553
ε_{max} = (1-c/a) (%)	5.89	20.5	10.66
MFIS (%)	5.8	< 0.02	9.4

The models based on lattice parameters represent twinning via the motion of twinning disconnections. Subsequent disconnections react to stress fields by means of Burgers vector, and so dislocation theory applies for these disconnection-to-disconnection interactions; along with disconnection-to-interface interactions [146]. Grain structure effects in the case of polycrystalline materials can be understood in a similar way when compared to grain-size hardening. Twin disconnections create pile-ups at grain boundaries, ultimately causing stress on the disconnection source. Accordingly, twinning stresses above the magnetic induced stress such that magnetic field induced stains are inhibited. The pile-up stresses lead to stress concentrations and under mechanical forces, the brittleness of the grain boundaries are relaxed by means of fracture [134].

The above-mentioned models are exceptional for describing single crystal MFIS's for Ni-Mn-Ga alloys. Albeit the model is not able to accurate describe MFIS's in polycrystalline samples. Polycrystalline samples have several grains with random orientations. The model based on lattice parameters can accurately predict the movement of a single unconstrained grain, but when grains near other grains, the twin motion is constrained, unless a texture is present. These constraints from neighboring grain boundaries inherently limit the overall MFIS. To the best of my knowledge, no model is available for predicting MFIS's in polycrystalline Ni-Mn-Ga alloys.

3.6 Recent Research of Ni-Mn-Ga Alloys

The interest in Ni-Mn-Ga is still prevalent in present time due to the giant magnetically induced strain properties in the presence of relatively low magnetic fields. Many researchers are investigating doping agents into the Ni-Mn-Ga mother alloy in attempts to study the effects with respect to martensitic transformation temperatures, MFIS's, and mechanical properties [147]–[149]. Other attempts are being made at understanding the optical and magneto-optical properties during the martensitic transformation [150]. Engineering aspects of the mother alloy are also still being studied, in which [151] examines the fatigue life and fracture mechanics in single crystals due to rotating magnetic fields. Thus, the principles of the proposed research could eventually obtain similar interest to above-mentioned studies.

3.7 Applications of Ni-Mn-Ga alloys

This section will briefly mention applications of Ni-Mn-Ga alloys including actuators, sensors, micro-fluidics, and magneto-calorics. This section will not cover a literature review of all the reports and possible uses for Ni-Mn-Ga alloys, but rather to mention key prospects based on literature.

3.7.1 Actuators

Ni-Mn-Ga alloys have very promising potential for actuator applications due to extremely large MFIS values. As mentioned previously, these MFIS values can reach approximately 10% in best cases. Based on this, over the years, Ni-Mn-Ga alloys have been examined for actuator purposes. Moreover, just recently, a motionless drive system was built from Ni-Mn-Ga for localized magnetic shape memory actuation for the creation of motionless micro-pumps [152]. These pumps can produce fluid movement from magnetic fields comparable to Nb-Fe-B systems.

3.7.2 Sensors

Sensing often occurs during the reverse of an actuation, inherently coupling the actuation-sensing systems. Recently, Ni-Mn-Ga single crystals have been investigated to examine deformation-induced change of magnetic permeability for a strain measurement technique [153]. In this study, the single crystal Ni-Mn-Ga sensor was tested statically and dynamically in compressive conditions with cycling frequencies between 25 Hz and 100 Hz. The sensor under a biased magnetic field varied from 2000 Oe to 8000 Oe. These cyclic displacements produced a varying strain between 0.5 % and 4.5 %.

3.7.3 Micro-Fluidics

In several instances, Ni-Mn-Ga alloys single crystals have been designed behave as micro-pumping systems. These micro-pumps are utilized to transport small amounts of liquid (pL - μL), in short periods of time (18 - 48 seconds) at high pressures (35 - 45kPa) [154]. These micro-pumps are single component, non-contact mechanism that actuate via the magnetic shape memory effect (MSME). The Ni-Mn-Ga micro-pumps have additional value as the flow rate can be reversed and simultaneously operates the valve and pump, unlike other micro-pumping technologies [155]. In addition, this design can incorporate viscous liquids and even gaseous materials.

3.7.4 Magnetic Refrigeration

Magneto-caloric materials operate via a magneto-thermodynamic phenomenon in which a transfer of temperature for a specific material is caused by introducing the magneto-caloric to a direction-varying magnetic field. Magneto-caloric effects are enhanced when the following conditions are met: the material possesses a small heat capacity, large change in magnetization versus temperature at constant magnetic field and ability to withstand a large applied magnetic field. Ni-Mn-Ga, along with Ni-Mn related alloys show promising potential for magnetic refrigeration [156]. In addition to this, several reports show replacing Ga with In and/or Sn cause a super-elastic and inverse magneto-caloric effect [157], [158]. Most important is the fact Ni-Mn-Ga and related Ni-Mn alloys have promising potential beyond the giant MFIS's achievable through the MSME.

4. Experimental Methods

4.1 Powder Synthesis

The additive manufactured Ni-Mn-Ga specimens prepared in this research were 3D printed from micrometer sized pre-alloyed Ni-Mn-Ga powders. The powders serve as the feed stock/source material in the binder jetting technique. Crucial for the process, the repeatability of certain properties such as chemical composition, which determines most of the functional properties of the FSMA, is therefore essential. Thus, the steps necessary to produce Ni-Mn-Ga powder will be elaborated upon. This section will cover two methods that have been used to produce Ni-Mn-Ga powder; the first being spark erosion and the other is ball milling.

4.1.1 Spark Erosion

Spark erosion involves creating electrical (spark) discharges between electrodes and chunks of material immersed in a dielectric cryogenic liquid [159]. The application of the electrical charge is generated by means of heavy currents between electrodes. The charge is distributed amongst the electrodes and chunks of material (typically 3 – 5 mm) through the dielectric. The goal during spark erosion is to apply the large current between chunks of material by means of vibrating the containment apparatus, subsequently creating 5 μs to 100 μs long electrical discharges [160]. The electrical discharges create arcing between granules via conduction from electrodes. Instantaneous spark discharges produced at the break a-part contact points generate superheated localized volumes at the material surface. As the result of spark collapse, molten droplets of various sizes are ejected from the boiling volumes, and then quenched *in situ* in the dielectric liquid. Depending on the process parameters particle size can vary from nanometers to tenths of micrometers. A quite large variety of pre-alloyed powders have been produced by spark erosion process: Fe-Si-B, Si-Ge, Al-Ni-Co, Co-Fe, U-Mo, Fe-Ga, Ni-Mn-Ga, Ti-Ni-Zr-Cu, Bi-Sb-Te, Ni-Al, Ti-Ni-Hf, Zr-Cu-Al-Ni-Ti, etc. [16], [19], [20], [160]–[165]. Ni-Mn-Ga powders used in this work were spark-eroded using two different dielectric liquids: liquid argon (LAr) and liquid nitrogen (LN_2).

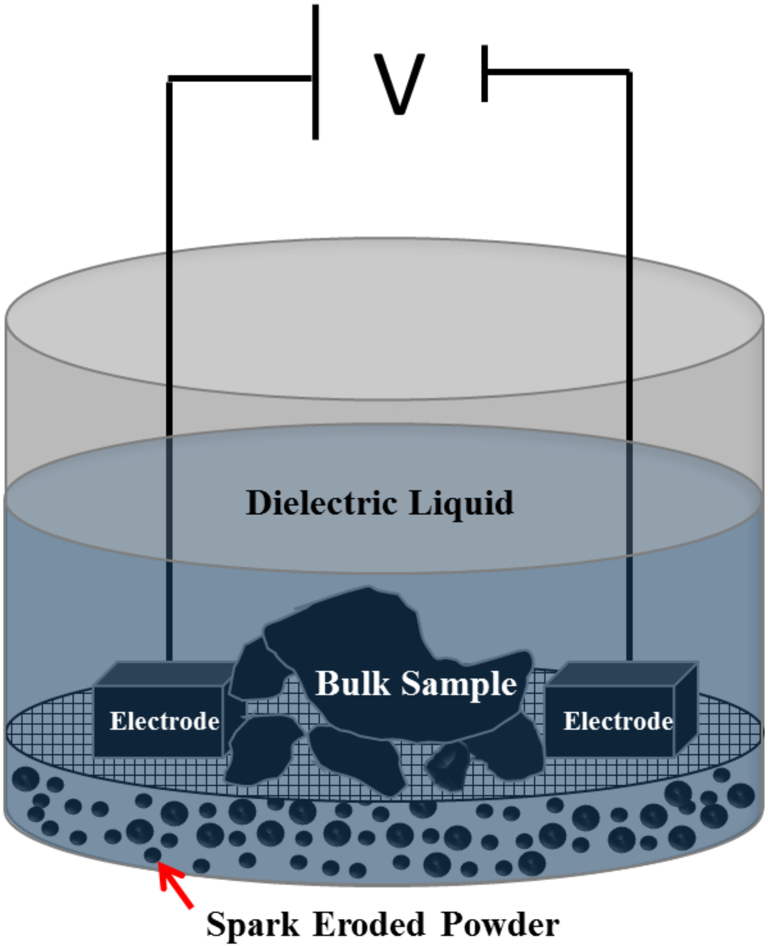

Figure 4.1: Illustration displaying the principal scheme of the spark erosion process.

A sieve (metallic screen) separates the larger granules from the newly formed metallic powders. Following the quenching of molten material, the powders sink to the bottom, passing through the sieve permitting an easy material retrieval. After the sparking process the powders are kept contained in the apparatus, submersed in the dielectric until all liquid is evaporated followed by passivation by means of hexane to prevent pyrophoric combustion of ultra-fine (nanometer) particles. The entire process is sketched by illustration in Figure 4.1. The Ni-Mn-Ga powders utilized in this research were produced at the University of California, San Diego (UCSD) in the Center for Memory and Recording Research under the supervision of Dr. Ami E. Berkowitz.

4.1.2 Ball Milling

The synthesis of ball milled (BM) Ni-Mn-Ga powder begins with the creation of the mother alloy. High purity elements of Ni (99.99 at %), Mn (99.95 at %), and Ga (99.99 at %) (Alfa Aesar) were arc melted to produce $Ni_{49.73}Mn_{29.03}Ga_{21.24}$ (at %) alloys. The high purity elements were placed in an Edmund Bühler GmbH MAM1 arc melting furnace, Figure 4.2 (a). Electrical breakdown of gases produce continuous electrical discharges, known as an arc. The source, an electrical current, is passed through a nonconductive medium, which in this particular case is ultra-high-purity (UHP) argon gas. The arc relies on thermionic emissions of electrons from the tungsten electrode, creating extremely high temperatures when interacting with the end point. The temperature of the arc depends on the voltage applied and typically creates visible light.

The melting of the Ni-Mn-Ga alloy is conducted under a positive argon pressure (0.05 – 0.07 Bar). The melting platform (copper) is water cooled during the entirety of the experiment. The arcing chamber is displayed in Figure 4.2 (b). In order to ensure homogeneity in the arc melted alloys, the blends were flipped and re-melted several times. In addition to this, the alloys were crushed and re-melted, respectively.

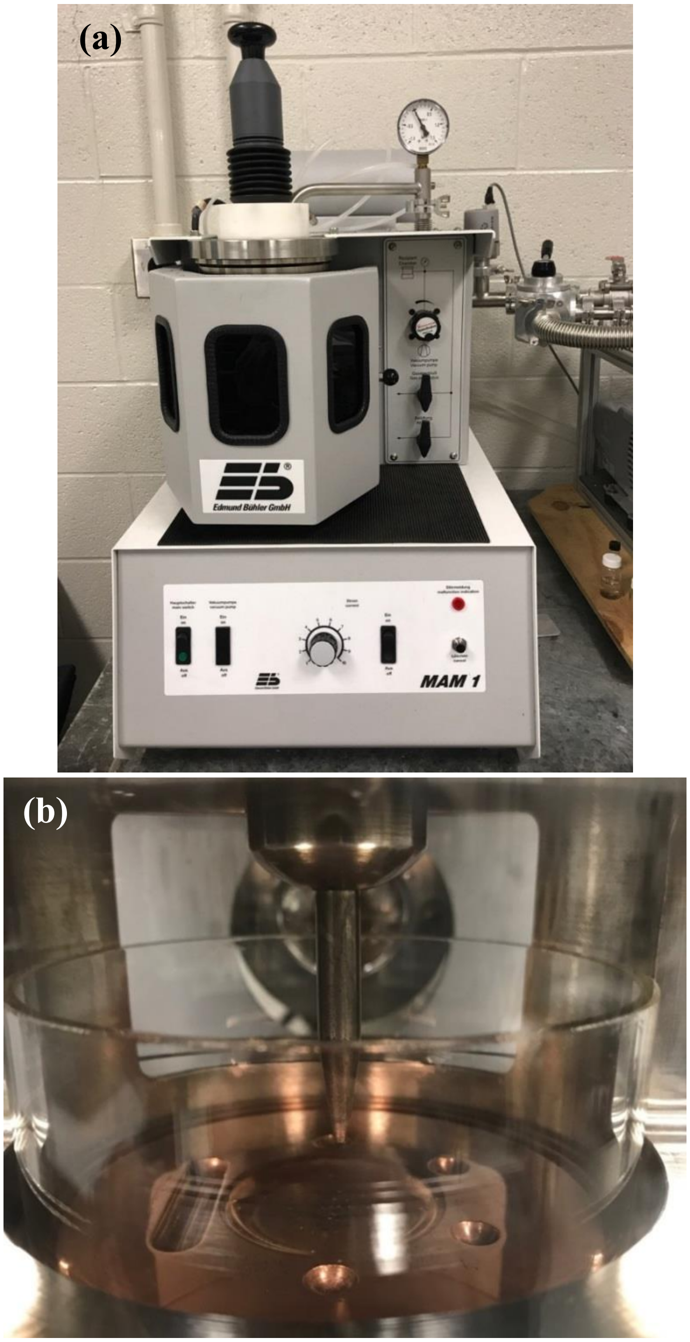

Figure 4.2: (a) Edmund Bühler GmbH MAM1 arc melting furnace; (b) Chamber of the arc melting furnace.

The newly formed alloys are then cut in half using a low concentration diamond wafer blade, sealed in quartz tube under UHP argon atmosphere to undergo a homogenization heat treatment at 1273 K for 24 h. The purpose of the heat treatment is to diffuse any localized atomic segregations as well as reveal the martensitic phase, observable due to millimeter sized twin variants. An ingot after homogenization is displayed in Figure 4.3.

Figure 4.3: Arc melted Ni-Mn-Ga alloy after being cut & heat treated at 1273 K for 24 h.

Amalgamated halved ingots are then placed in a zirconia crucible with two zirconia milling balls. The alloy and zirconia containing vessel is placed in a SPEX Sample Prep Mixer/Mill 8000M, Figure 4.4, and milled for one hour. The high strain interactions cause by the ingots and zirconia balls during the milling are the basis for ingots to fracture, breaking into smaller pieces. These interactions are repeated creating Ni-Mn-Ga powder. Once the milling is concluded, the material is sieved to a size less than 100 µm. After sieving, larger granules are place back in the ball mill and the process is repeated. Powders < 100 µm are collected for the binder jetting AM process. It is worth noting Ni-Mn-Ga powders have been produced from ball milling where the morphology, chemical composition, structure, and magnetic properties have been studied [166]–[168].

Figure 4.4: Ball milling apparatus used to create pre-alloyed Ni-Mn-Ga powders (BM).

4.2 Powder Characterization

The techniques described in this section are methods for Ni-Mn-Ga powder characterization. The methodologies described here are tailored to ensure the successful 3D printing of the ferromagnetic powders. Therefore, particle size distribution, morphology, chemical analysis, and structure were investigated. In addition, methods of powder characterization provide a closed loop feedback system for the powder production procedures.

4.2.1 Particle Size Distribution Analysis

Initially, several attempts were made to print Ni-Mn-Ga powders produced by spark-erosion in liquid nitrogen and liquid argon dielectrics. Unfortunately, no compact part was obtained. Several reasons for this were related to particles morphology and packing factor – binder saturation relationship. In the case of particles obtained by spark-erosion in LAr, an attempt to increase the packing rate was performed to optimize the additive manufacturing process. Spherical particles were mechanically separated from irregular shaped material. Ni-Mn-Ga powders made in LAr were thoroughly crushed using a mortar and pestle until a smooth consistency was obtained. This material was then sieved into classifications of size. Crushed Ni-Mn-Ga LAr sieved size classifications include 0-20 µm, 25-45µm, 45-53µm, and 53-75µm. To quantify the increase in packing rate, SEM images of each size distribution were taken using a JEOL IT-300 and used for image processing. The image processing was done using ImageJ software to quantify the number of spherical particles in each image. Scanning electron micrographs were calibrated utilizing scale bars and converted to binary using ImageJ. The binary images are then watershed to separate agglomerated particles and analyzed using 0.50 to 1.0 circularity; circularity ranges from 0 (infinitely elongated polygon) to 1 (perfect circle). Equation 4.1 displays the relationship between circularity and particle size parameters. These micrographs were processed to compute spherical particle count and corresponding histogram of size distribution. Ni-Mn-Ga LN_2 powders were not crushed to preserve structure due to the hollow morphology.

$$Circularity = 4\pi * \frac{Area}{Perimeter^2} \tag{4.1}$$

An additional analytical method to investigate particle size was also used. Particle size distribution results for all three Ni-Mn-Ga powders were obtained using a Cilas 1190 laser particle size analyzer, Figure 4.5. This instrument incorporates three lasers to ensure a high level of accuracy, allowing for a resolution between 0.04 – 2500 µm. The Cilas 1190 allows for dry or wet measurements, although for safety precautions the wet analysis method was employed. Once submersed, powders are agitated in a water solution and read via the tri-laser (patented design) for diffraction analysis. The amount of powder added to the water varied from test to test, although an obscurity value between 10 and 14 % was maintained. A range of 10 – 15 % obscurity is recommended by the manufacturer. Each powder (LN_2, LAr, and BM) was measured several times for numerical analysis.

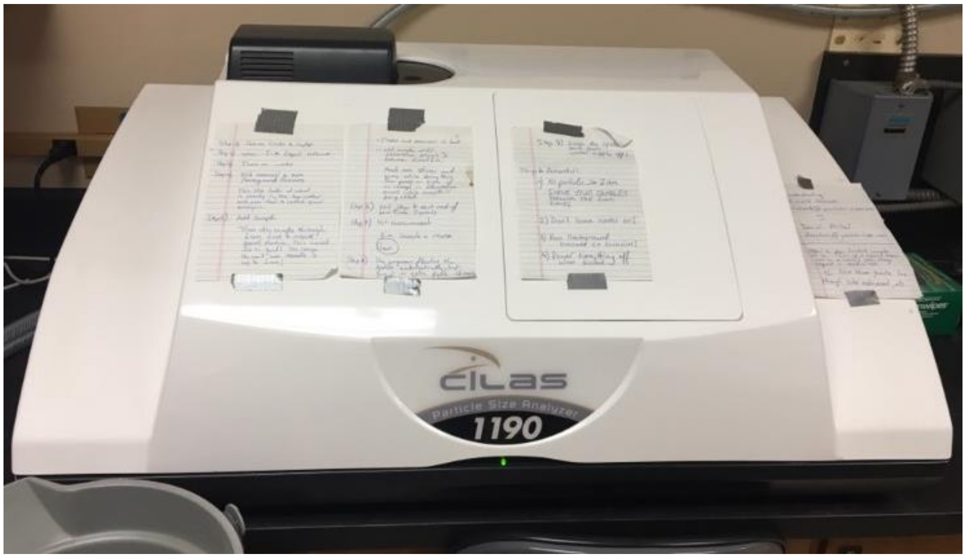

Figure 4.5: Cilas 1190 laser particle size analyzer.

The laser diffraction analysis process does not depend on volumetric flow rate. The basis for the analysis comes from the Fraunhofer diffraction theory, which states the intensity of light scattered by a particle is directly proportional to the particle size [169].

Moreover, the angle of the laser(s) and particle size share an inversely proportional relationship where the diffracted angle increases as particle size decreases [170]. Fraunhofer diffraction is constrained by;

$$\frac{W^2}{L\lambda} \ll 1 \tag{4.2}$$

where W is the aperture size, λ is the wavelength of the laser and L is the distance from the aperture [171]. The results of the particle size distribution analysis assisted in determining the layer thickness parameter for the binder jetting 3D printing process.

4.2.2 Morphology and chemical analysis via SEM and EDS

Particle morphology and chemical analysis for the three Ni-Mn-Ga powders were investigated using electron microscopy and energy dispersive spectroscopy techniques. In particular, two scanning electron microscopes (SEM) were used to investigate particle morphology; ^{1}JEOL JSM-7600F (Figure 4.6 (a)) and ^{2}JEOL IT-300 (Figure 4.6 (b)). In addition to imaging, an EDAX Octane silicon drift detector X-ray energy dispersive spectrometer (EDS) was used to collect characteristic x-rays for chemical analysis. Before chemical analysis the EDS spectrometer was calibrated with a homogeneous $Ni_{50.90}Mn_{29.23}Ga_{19.86}$ (at %) single crystal reference sample.

Scanning electron microscopy relies on the production and interaction of electrons with a conductive sample. Electrons are generated via an electron gun source. There are a variety of electron guns, albeit this research uses two particular sources; field emission (Schottky) and tungsten filaments for the JSM-7600F and IT-300, respectively. Electron sources are fixed at the top of the electron beam column. Electrons are excited at the gun and "peeled off" then guided down the electromagnetic column. Later, the electrons interact with the intended sample producing multiple signals that can be collected to obtain specific information. One of the most important aspects to understanding the general usage of a scanning electron microscope is to understand the electromagnetic column.

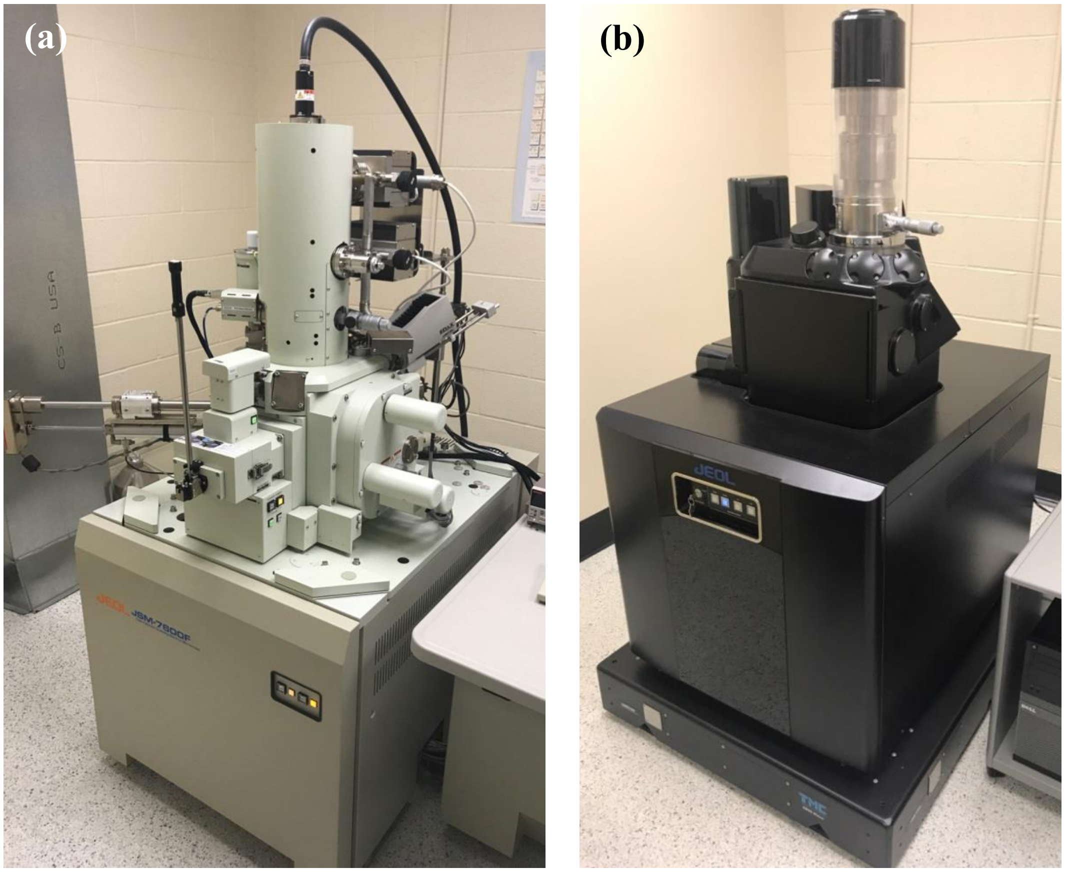

Figure 4.6: (a) JEOL JSM-7600F SEM; (b) JEOL IT-300 variable pressure SEM.

These accelerated electrons typically possess 0.1 to 30 keV [172], therefore the electrons carry significant amounts of kinetic energy. The relationship between the kinetic energy (KE) and the momentum of an electron is given by [173]:

$$KE = \frac{P^2}{2m} \tag{4.3}$$

where p is the momentum and m is the mass of an electron. Once the momentum is determined, the de Broglie wavelength of an electron can be obtained by [173]:

$$\lambda = \frac{h}{p} \tag{4.4}$$

here λ is the wavelength of the electron, h is Plank's constant and p is the aforementioned momentum. If we assume the kinetic energy of an electron is given as 30keV, the calculated de Broglie wavelength will be approximately 0.007 nm. This compared to the visible light in the electromagnetic spectrum (~390 to 700 nm) is considerably less. The typical maximum resolution obtainable in a scanning electron microscope is in the order of 1 – 3 nm [172].

Additional ion and electron beam microscopy was conducted on 3D printed LAr parts. A JEOL JIB-4500 multi beam system with Ga ion source was used for the focused ion beam (FIB) imaging and manipulation. With this system, a two-particle interface was cross-sectioned to prepare a lamella. This lamella was then thinned and polished using the FIB, in order to manufacture a sample for transmission electron microscopy (TEM). An Omniprobe OMP-AUTOPROBE 200.1 nano-manipulator was used for the manipulation of the lamella. The JEOL JIB-4500 is also equipped with gas injection systems (GIS), allowing for the deposition of carbon and tungsten. The Ni-Mn-Ga lamella (approximately 100 nm thick) was then investigated via TEM using a JEOL 2100 scanning/transmission electron microscope. The JEOL 2100 possesses both bright and dark field STEM imaging capabilities. In addition to this, the JEOL 2100 is equipped with energy dispersive X-ray detector for chemical analysis. The JEOL JIB-4500 and JEOL 2100 are housed in the electron microscopy facility at Youngstown State University.

In order to determine the martensite crystal structure (5M, 7M, NM), TEM is the adequate investigation tool. Transmission electron microscopy (TEM) specimens of a particular LAr sample was prepared using the lift out method [174]–[176] via focused ion beam (FIB) techniques, with a JEOL JIB-4500 multi-beam system. A sintered LAr sample was mounted and polished. The surface of the mounted sample was mechanically polished until a two-particle sintered interface was encountered, Figure 4.7 (a). Using the FIB, two portions (top and bottom) of a target area were milled, producing a lamella of Ni-Mn-Ga, Figure 4.7 (b). The lamella is then cut free using the ion beam and attached to a TEM grid, Figure 4.7 (c). Once attached, the lamella is approximately 1-3 μm in thickness, however to be electron transparent, the lamella should be <100 nm. Utilizing the same ion source, the lamella was thinned via ion polishing to an approximate thickness of 100 nm. Figure 4.7 (d) shows the FIB polished lamella. Several features, perhaps twins and/or grain boundaries can be observed due to ion channeling contrast.

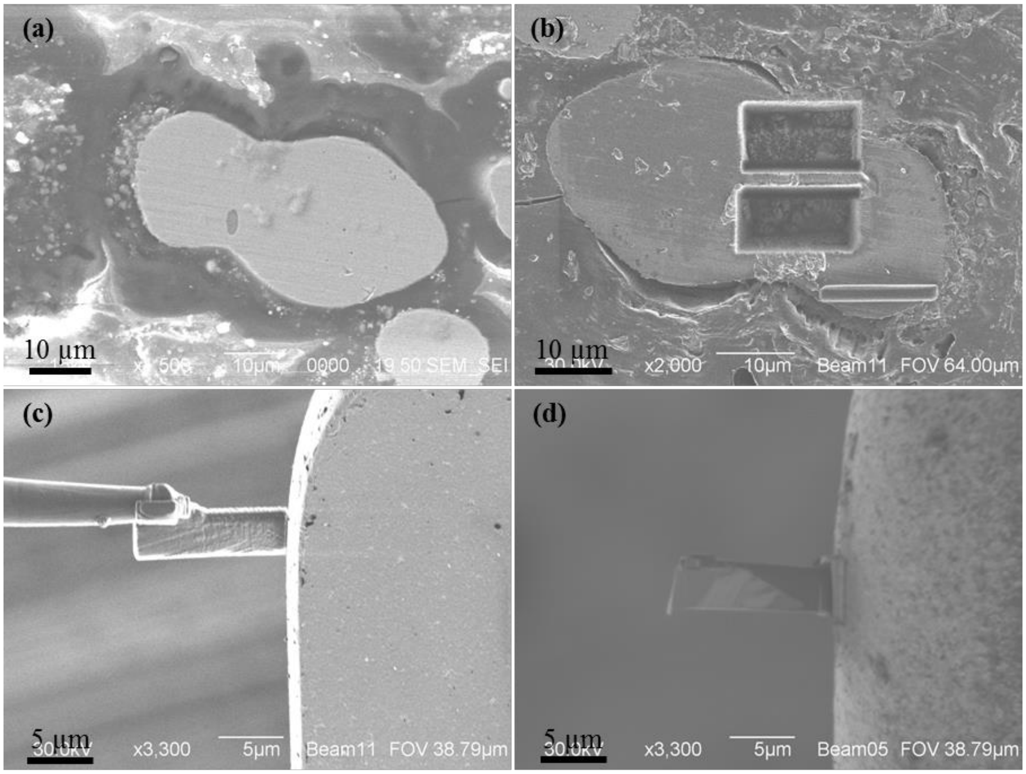

Figure 4.7: (a) Secondary electron image showing the cross-section of two sintered particles in a 3D printed part obtained from spark eroded LAr powders. The interface of the two sintered particles is indicated by arrows. (b) Ion milled volumes atop and below the FIB lamella from which the TEM sample will be prepared. (c) Manipulation of the FIB lamella being attached to a TEM grid. (d) Ion milled electron transparent TEM sample.

4.2.3 X-Ray Diffraction

Microstructural analysis of the powder samples was conducted using a Bruker Prospector CCD diffractometer with copper micro-source X-ray tube, Figure 4.8. The prospector is typically used for single crystal diffraction albeit is quite diverse for material analysis. In particular, capillary, powder, and bulk samples can be analyzed.

Furthermore, the X-ray beam is one of high resolution, concentrated towards a 0.1mm^2 circular area. In most cases, diffraction patterns collected were at room temperature between one minute and two hours spanning a range of 10 – 110°. It is worth noting, a few experiments have been conducted below room temperature.

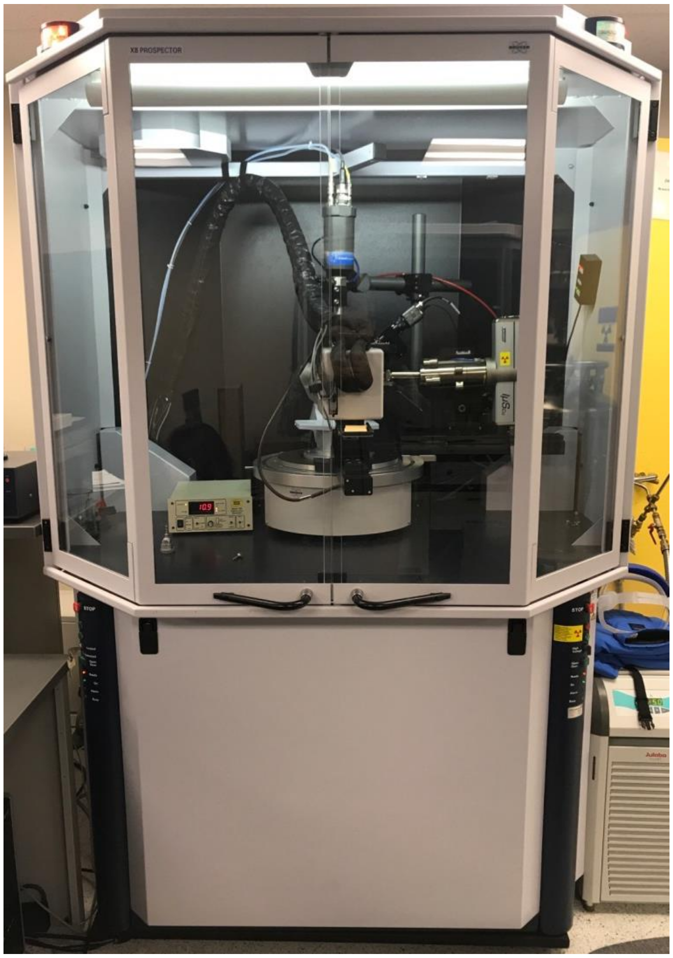

Figure 4.8: Bruker Prospector CCD diffractometer.

Information obtained via X-ray diffraction assists in providing information regarding atomic positions, space group, and molecular structure of the material tested. During experiments, incident X-ray beam interacts with the crystalline structure of the sample and diffracts, depending on the orientation of the sample and the beam. The diffraction scattering conditions (Bragg diffraction, [177]) have been established as:

$$n\lambda = 2d \sin\theta \tag{4.5}$$

where n is an integer, λ is the wavelength of the x-ray beam, d is the d-spacing between crystallographic planes, and θ is the angle of diffraction. Based on this, the knowns are the wavelength of the X-ray beam and the angle, collected via the instrument, thus enabling the determination of the corresponding d-spacing. X-ray diffraction provides a better understanding of the crystal structure, including atomic position, chemical bonds, and any disorder [178]. Each crystalline material possesses a unique diffraction pattern thus allowing for the identification of any/all phases present in a specimen. These patterns were determined via software, Diffract EVA (Bruker AXS, Madison, WI). This software compares the collected diffraction pattern to the International Center for Diffraction data (ICDD).

Ni-Mn-Ga, as discussed previously, is known to possess three crystal structures for martensitic phases of near stoichiometric Ni_2MnGa alloys. The collection of these diffraction patterns allowed for the determination of each specific phase present.

4.3 3D Printing Parameter Selection and Part Formulation

This section discusses the methodologies for predicting the binder jetting printing parameters including binder-to-particle testing, as well as the design of the components. After these investigations, the printing parameters and designed components were used to successfully 3D print Ni-Mn-Ga alloys.

4.3.1 Binder testing

The parameter selection for the binder jetting additive manufacturing process is determined by a few key variables. The first to be discussed, binder saturation (%) value refers to the volume of binder deposited on the powder surfaces per printing layer. Voids are inherently created in the AM process, due to the prealloyed powder morphology and size distribution. The number of voids in the as-printed samples can be quantified by the packing density. Powder as well as air occupies a known volume, where the packing density refers to the volume of powder present.

Therefore, the volume of binder applied must be sufficient to fill the air space unoccupied by powder. To determine this, “table top” binder-to-particle testing was conducted on each Ni-Mn-Ga powder. Thus, 5 mm x 5 mm squares of sticky conductive carbon tape were cut as standards for the binder testing. One side of the sticky conductive tape was fixed to an aluminum stub used for SEM analysis. The stub with sticky conductive tape is then pressed onto a bed of Ni-Mn-Ga powder, resulting in a “layer” of powder adhered to the tape. Various amount of binder are then deposited, ranging from 0.5 to 5 µL using a SCILOGEX micro-pipet. The binder is then air dried and examined by means of SEM to correlate the amount of binder and interaction between particles such as surface exchanges.

4.3.2 Design of Components

Components designed for the binder jetting process were created in SolidWorks, computer aided design (CAD) software. Several mesoscale components were created for additive manufacturing ranging from simple shapes (parallelepiped, cubes) to more complex geometries such as lattice structures, tresses, and gyrocubes. These designs are saved as standard triangle language (.STL) files. The STL files describe unstructured triangulated surfaces by unit normal and vertices of triangles using 3D Cartesian coordinate systems [179]. The STL files are subsequently used for the additive manufacturing, Figure 4.9 (a, b).

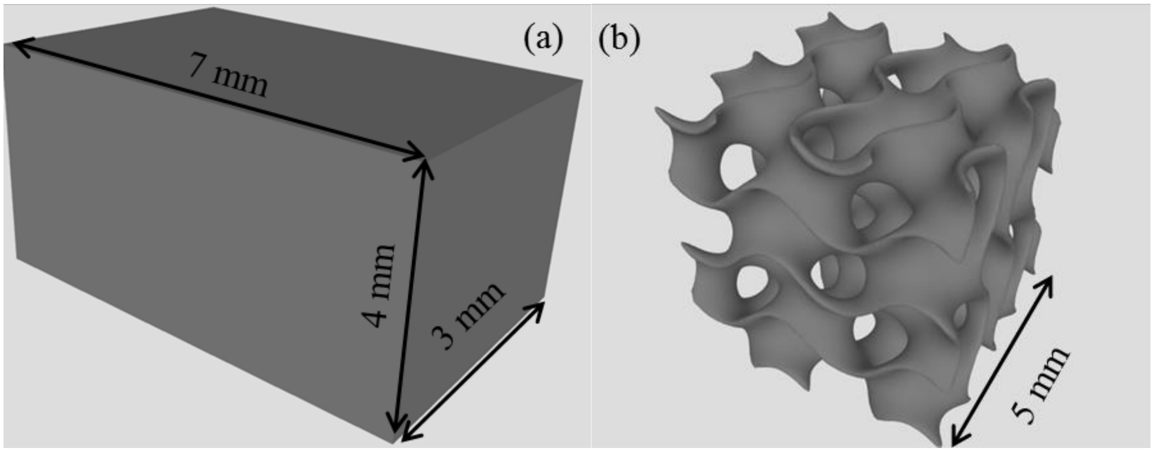

Figure 4.9: CAD files of (a) parallelepiped and (b) gyrocube designs used in the additive manufacturing of Ni-Mn-Ga alloys.

After designing the components to be 3D printed, these files are uploaded to the X1-Lab, by ExOne. The X1-Lab is a binder jetting 3D printer, commonly used for meso-scale additive manufacturing. An image of the X1-Labs 3D printing system is shown in Figure 4.10.

An ExOne proprietary binder (BS004) optimized for metallic powders was used in the experiment. To ensure the Ni-Mn-Ga powders demonstrated suitable adhesion with the binder, a test similar to the bench top method was employed, explained in later chapters. Major printing parameters for binder jetting additive manufacturing process include layer thickness and binder saturation. For successful printing, the minimum value of layer thickness should be larger than the maximum particle size. Binder saturation depends on the packing density of the particulate materials, which is a function of particle morphology and the size distribution. Layer thickness and binder saturation parameters used in this experiment and determined by trial and error. The layer thickness parameter used to successfully 3D print Ni-Mn-Ga powders varied between 53 µm and 90 µm. Binder saturation parameter also varied between 110 % and 250 %, depending on powder morphology. Nevertheless, each parameter has been investigated and reported in later sections.

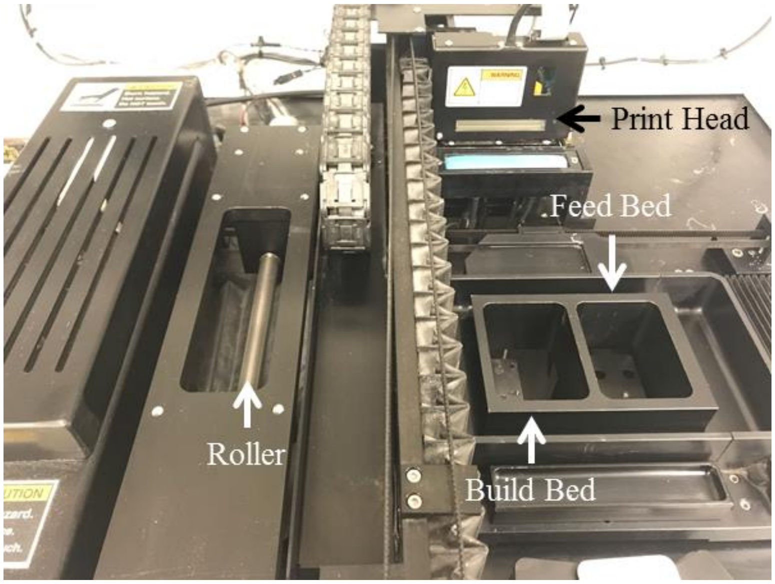

Figure 4.10: The X1-Lab 3D printing system highlighting the build and feed beds, roller, and print head.

4.4 Post Processing

As previously mentioned, the 3D printing process was conducted using the X1-Lab (ExOne). The parts manufactured require post processing for further progression.

Further processing includes independent steps of curing and sintering. This section covers the procedures to complete the above-mentioned curing and sintering procedures.

4.4.1 Curing

The curing of the as-printed parts was conducted in an ExOne digital materializing oven. Parts are heated to 463 K for 4 h, which thermally sets the binder, strengthening the parts to the point of physical manipulation. The oven is then left to cool to room temperature. The now cured parts are removed from the powder bed and brushed to remove residual loose powders. The loose powders are recollected for additional printing sessions.

4.4.2 Sintering

In order to further increase part strength and complete the binder jetting process, particles need to be sintered. Sintering of the 3D printed Ni-Mn-Ga components was investigated in this research. Various sintering methods were studied such as, vacuum and inert atmospheric sintering, with and without the presence of oxygen getters. The temperatures of sintering for Ni-Mn-Ga range between 1273 K and 1373 K between 5 and 50 h. The above-mentioned sintering temperatures are well above 923 K, where the water-based binder is “burnt off” with minimal carbon residue. The sintering process was performed in a Thermolyne 21100 tube furnace for vacuum conditions and a Thermolyne 48000 furnace for inert atmospheric sintering. Optimal sintering conditions for 3D printed Ni-Mn-Ga was found to occur when the samples were sealed in quartz tube under ultra-high purity argon gas with the presence of an oxygen getter, Figure 4.11. Quartz tubes were sealed using an oxygen-acetylene torch.

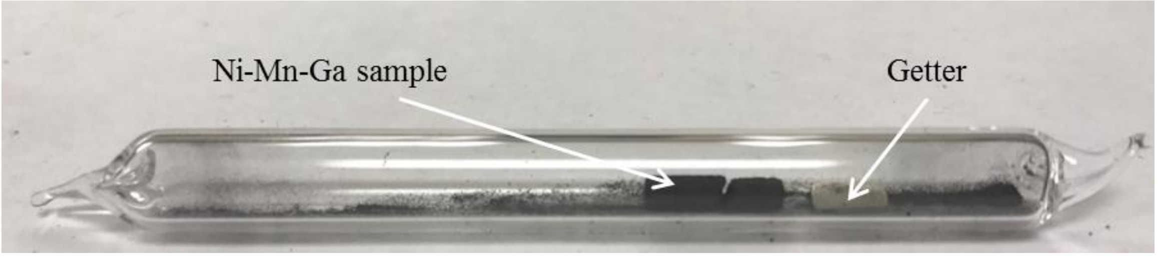

Figure 4.11: Ni-Mn-Ga 3D printed part sealed in quartz with an oxygen getter. This picture displays the sample before sintering.

4.5 Characterization of Printed Parts

This section covers the characterization methods for sintered Ni-Mn-Ga alloys produced from BM, LAr, and LN_2 powders. The methods of characterization for the sintered Ni-Mn-Ga alloys include XRD, microstructure (morphology, composition) using light and electron microscopy, density, phase transformation behavior using differential scanning calorimetry (DSC), mechanical properties (nano-indentation, Instron compression testing), magnetic properties, and magnetic field induced strain values. The XRD and SEM techniques used in this research have been presented above. The other experimental techniques are presented below.

4.5.1 Optical-Microscopy

The use of optical microscopy to investigate the microstructure begins with the preparation of the sample. Sintered Ni-Mn-Ga alloys (BM, LAr, LN_2) were embedded in fast-set cold mount epoxy (Allied High Tech Products, INC). Afterwards, mounted samples were ground and polished using silicon carbide abrasive grinding paper (Struers, INC) in a sequence of 180, 320, 500, 800, 1000, 2400, 4000 grit. After polishing, samples were set in a vibration polishing system (Vibromet 2) suspended in colloidal silica (0.06 µm) and ran at 55 % intensity for two hours. The vibrating polish creates a near-stress free surface on the Ni-Mn-Ga samples as well as reveals twin variants in the martensitic phase. Typical martensitic phase morphology, as observed using light microscopy is shown in Figure 4.12.

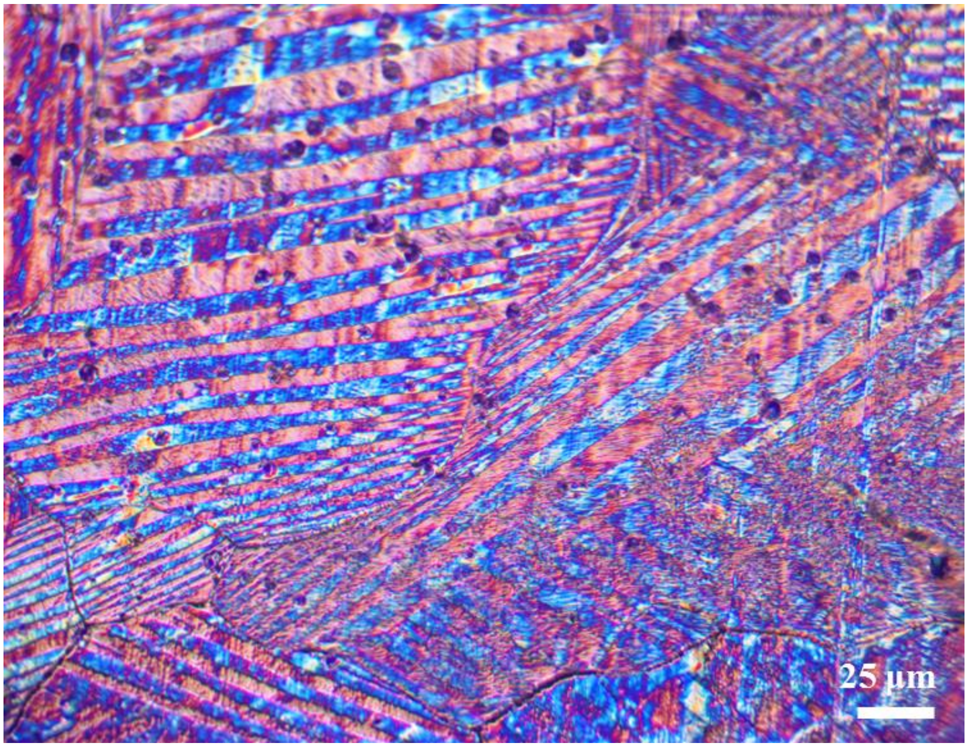

Figure 4.12: Differential interference contrast (DIC) image of a typical Ni_2MnGa martensitic microstructure.

The polished samples were then investigated using a LECO 300 metallograph optical microscope equipped with differential interference contrast (DIC) imaging capabilities. DIC imaging separates polarized light into two orthogonal coherent parts that are spatially displaced at the plane of the sample. The result produces an image of polarized light, with 90 ° difference between planes. The result from imaging Ni-Mn-Ga in a martensitic phase produces a red and blue image sequential with the twin variants present in the microstructure as seen in Figure 4.12.

Density measurements were taken from 3D printed samples of BM, LAr and LN_2, before and after sintering. To do so, mass and volume measurements were taken in a statistical manor to ensure reported results are accurate. The obtained density from these measurements (g/cm^3), were compared to a calculated theoretical density based on the chemical composition obtained during this work.

4.5.2 Thermal Analysis via DSC

Differential scanning calorimetry (DSC) is a thermo-analytical method for acquiring specific amounts of heat necessary to increase the temperature of a sample and reference simultaneously. DSC has been profoundly used in characterizing the thermal behaviors of polymers, liquid crystals, drugs as well as safety screens and oxidation studies. The objective of DSC is to measure the exchange of energy (in the form of heat) amongst two samples, specifically changes in enthalpy during physical transitions associated with the generation or consumption of heat [180].

DSC experiments in this research were conducted via a Perkin Elmer Diamond DSC equipped with cooling apparatus. Achievable temperatures range from 243 K to 973 K (-30 – 700 °C). Ni-Mn-Ga samples were fragmented after sintering to pieces no larger than 500 mg. The fragmented pieces were placed in aluminum DSC crucibles (Perkin Elmer) and thermally cycled between 253 K and 432 K (-20 – 150 °C) at a rate of 10

°/minute. The resulting thermal curves were investigated for martensitic transformation temperatures and associated enthalpy energies.

4.5.3 Mechanical Behavior Investigation

Mechanical behaviors of additively manufactured sintered Ni-Mn-Ga components were examined using two methods. (i) nano-indentation and (ii) quasi-static mechanical properties via compression by means of Instron.

(i) Nano-indentation testing involves a hard tip (typically diamond) with known mechanical properties being pressed into a material with unknown properties. A load is placed on the indenter tip and increased as it penetrates the sample until a desired maximum load is reached and the residual area is measured. Indentation hardness testing is a common method of determining mechanical properties of materials such as Young's modulus, yield strength and material hardness [181], [182]. An M1 mechanical tester (Nanoeva) equipped with a Berkovich tip was used to find the elastic modulus and hardness for each sintered Ni-Mn-Ga part (BM, LAr, LN_2). For nano-indentation sample preparation refer to section 4.5.2.1 for details on mounting, grinding and polishing. Indentation testing of AM Ni-Mn-Ga involved loads ranging from 10 – 200 mN that have been applied to the sintered Ni-Mn-Ga sample surfaces. These loads are statically held for one minute and removed. These investigations provide the results in the form of load versus depth, subsequently inspected to determine mechanical properties.

(ii) Compression of meso-scale AM Ni-Mn-Ga parts were tested using an Instron model 5500R attached to a 4206-model base. The Instron model 5500R held a 150kN load cell, programmed to quasi-statically load at a rate of 0.5 %/minute. Sample geometry varied although typically cubic Ni-Mn-Ga samples were printed with 5 x 5 x 5 mm dimensions (Length x Width x Height), following the ASTM C1424 standard. During mechanical testing, Bluehill 3 software recorded load versus displacement data representative of the mechanical responses from AM Ni-Mn-Ga samples. Afterwards, the load is converted to stress (σ) values based on the following:

$$\sigma = \frac{F}{A} \tag{4.6}$$

here, F is the load applied (recorded via Bluehill 3 software) and A is the cross sectional area of the 3DP Ni-Mn-Ga. The displacements recorded by Bluehill 3 software were converted to strain (ε) values calculated via:

$$\varepsilon = \frac{\Delta l}{l} \tag{4.7}$$

where Δl represents the change in length and l is the original length of the sample before compression. The Young's modulus of the 3DP samples were also determined by the slope of the stress-strain relationship in the elastic region of deformation. This calculation follows:

$$E = \frac{\sigma}{\varepsilon} \tag{4.8}$$

Ni-Mn-Ga samples in this research have been mechanically compressed in the martensitic and austenite phases.

4.5.4 Magnetic Properties

Ferromagnetic properties of AM Ni-Mn-Ga alloys (LN_2, LAr, and BM) have been investigated by means of vibrating sample magnetometer (VSM). Two series of experiments were conducted in this research using two different VSM models with diverse testing conditions. The first tests involved cross sectioning Ni-Mn-Ga samples in order to prepare 1 mm thick, 3 mm diameter disks for measurement using a Lakeshore model 4710 housed at Case Western Reserve University. These disks were secured to a quartz rod with Teflon tape. In the first series of experiments, $LN_{2,}$ LAr, BM and bulk disk samples underwent a hysteresis loop experiencing a field magnitude of ±17000 Oersted (Oe) at room temperature. The resulting field versus magnetization relationship revealed saturation and coercivity values for the 3D printed Ni-Mn-Ga.

The second series of magnetic experiments were conducted on a DMS Model 10 VSM, Figure 4.13. This system is housed in the Magnetic Materials Laboratory at Boise State University (BSU). The DMS Model 10 system has heating and cooling capabilities achievable temperatures include 173 K to 473 K (-100 – 200 °C), well in the range of the martensitic transformation temperatures. Utilizing the heating and cooling abilities, BM Ni-Mn-Ga samples underwent thermo-magnetic measurements. BM samples were fixed to a quartz rod with Teflon tape and attached to the VSM, subsequently experiencing low and high magnetic fields while temperatures were thermally cycled (heating and cooling). Low field measurements include 500 – 1000 Oe and high fields include 10000 – 20000

Oe. A thermocouple is attached to the quartz rod via super glue, contacting the sample to retrieve accurate temperature measurements. The result of the thermo-magnetic analysis presents magnetization behavior of BM samples versus temperature. Furthermore, the martensitic phase transformations are exploited in these measurements, which will be deliberated in the results and discussion chapter. In addition to the thermo-magnetic investigations BM samples underwent hysteresis loops of ±20000 Oe. Notably temperature-magnetization experiments served as a dual purpose for martensitic reorientation; e.g. thermo-magnetic training of twin variants.

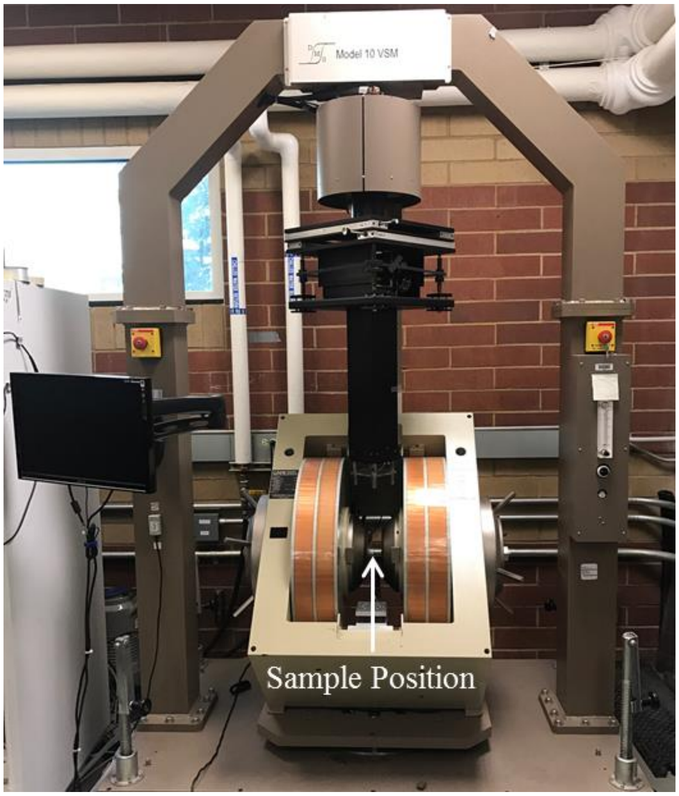

Figure 4.13: DMS Model 10 Vibrating Sample Magnetometer.

4.5.5 Magnetic Field Induced Strain (MFIS)

The necessity to determine the magnitude of the magnetic shape memory effect (MSME) in Ni-Mn-Ga parts created using AM techniques is critical for determining part functionality. The term functional refers to the materials reversible (martensitic) response (strain) to a magnetic field. For this, Ni-Mn-Ga samples of LN_2 and BM were designed and 3DP with 3 x 4 x 7 mm geometries (Width, Height, and Length) and sintered using pre-determined parameters, section 4.2.2.

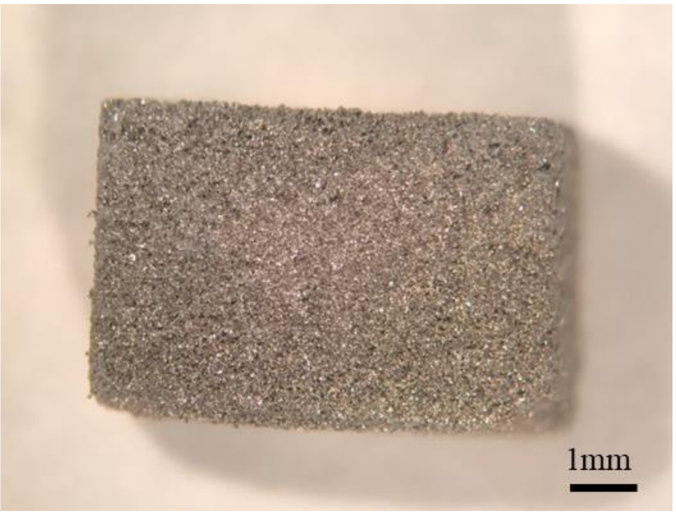

Figure 4.14: Porous BM Ni-Mn-Ga sample designed for MFIS measurements.

A picture of a 3 x 4 x 7 mm BM sample can be seen in Figure 4.14. These samples were designed to fit a custom made apparatus used to measure the magnitude of the MSME/or magnetic field induced strain (MFIS).

The apparatus shown in Figure 4.15 (a) is inserted in a 0.97 T Hallbach cylinder which can be rotated amongst the sample several thousand times. The rotation of the magnetic field causes a reorientation of the martensite in the Ni-Mn-Ga samples, and ultimately produces a reversible MFIS, where maxima elongation occur every 180 °

(opposite field direction). It is important to note; this system is referred to as the “IBAG” after the company that built the rotating mechanism. The IBAG system, Figure 4.15 (b), is also housed in the Magnetic Materials Laboratory at Boise State University (BSU).

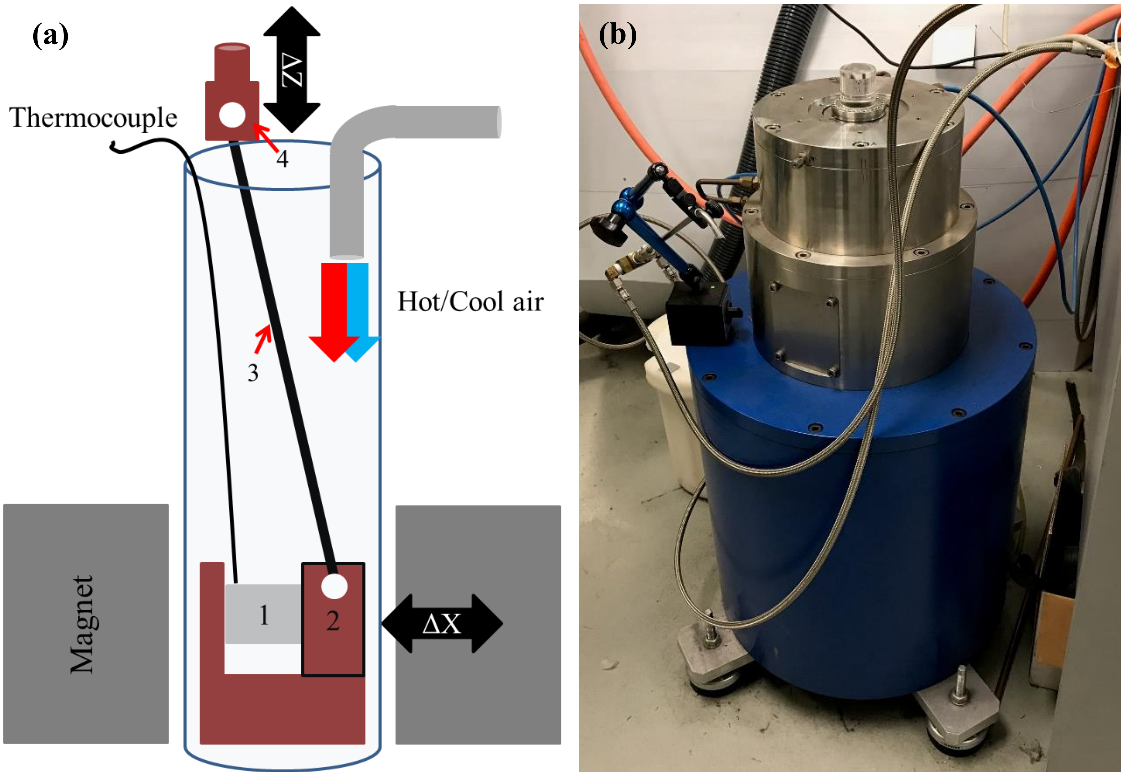

Figure 4.15: (a) Sample holder for the MFIS measurement system. Here, (1) represents the Ni-Mn-Ga sample, (2) the sliding head attached to the sample, (3) a ceramic rod to translate movement in the x direction into the z direction, and (4) top of the apparatus attached to an optical encoder. (b) Image of the IBAG system.

The shortest edge of the sample was placed parallel to the magnetic field rotational axis, which was perpendicular to the field direction. One end of the sample was glued to a fixed sample holder (Figure 4.15 (a)) made of Vespel®, and the other end was glued to the sliding head. The horizontal displacement due to the magnetic shape-memory effect induced by the rotational magnetic field was transformed into a vertical displacement by a ceramic push rod connected at one end to the sliding head and at the other end to a Heidenhain (Traunreut, Germany) linear encoder with a resolution of approximately 10 nm. The Heidenhain extensometer and sample holder inserted in the rotating magnetic field is attached to the device shown in Figure 4.16. Since the response of the sample to the magnetic field produces a shift in the X direction, a geometrical relationship is needed to translate the displacement into the Z direction. This relationship is given below in Equation 4.9. This relationship is referred to the geometrical factor (GF) since it is dependent upon the sample length.

$$GF = \frac{\sqrt{{L_c}^2 - (C + L_z)^2}}{C + L_z} \tag{4.9}$$

where L_z is the sample length, L_c is the length of the ceramic rod, and C is the constant related to the mounting apparatus.

The Heidenhain is an analog device that measures the shift in the Z direction in terms of encoder counts. The Heidenhain measures these encoder counts using sinusoidal waves with a specific periodicity (2 μm). The area under those curves are interpolated and depending on the interpolation factor (AM samples used in this research use an IF 400) are then translated to a digital signal, given as raw data.

The transfer from the extensometer to data points are recorded by Lab View software and reported in text files after each data collection period. The text files report these data points as encoder counts. The equation for calculating the MSME in terms of strain percentage is shown below:

$$\varepsilon = \frac{(encoder\ count) * GF}{4 * IF(400) * L_z(\mu m)} * 100 \tag{4.10}$$

In Equation 4.10, ε represents the MFIS as a strain percentage, GF is the geometrical factor, IF is the interpolation factor, and Lz is the original sample length. The encoder counts change based upon the strain magnitude of the sample, which is directly related to the angle of the rotating magnetic field. For example, one should expect maxima MSME values every 180˚ of field rotation.

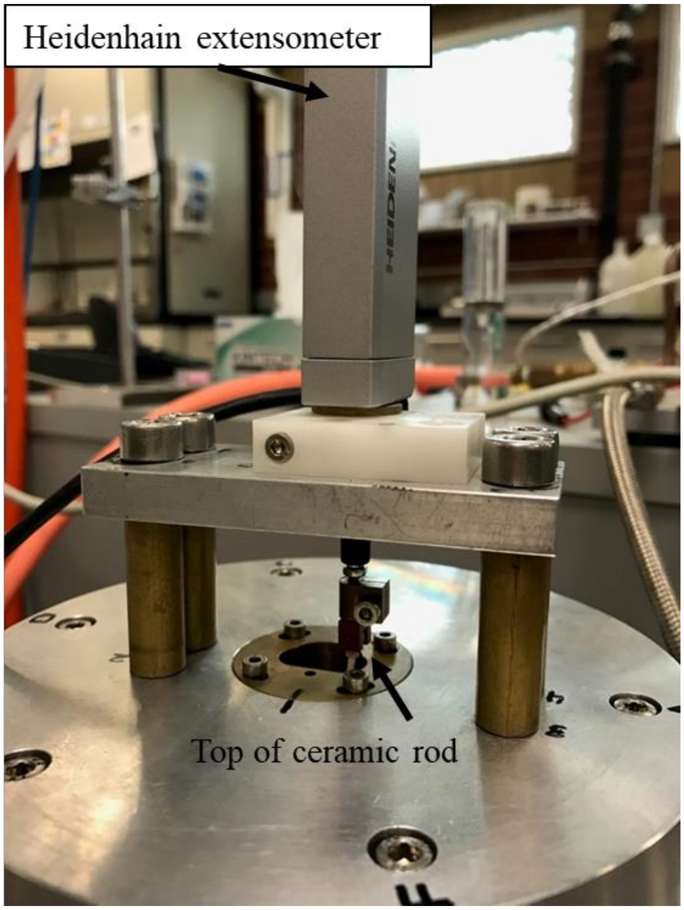

Figure 4.16: Heidenhain extensometer attached to the sample mount.

IBAG data collected in this research involved recording AM Ni-Mn-Ga sample responses over five magnetic field rotations at a speed of 30 rpm, collecting 1000 data points per rotation. To aid in data analysis, VBA code (excel macro) was written to semi-automate this procedure. The macro allows the operator to import the raw text file from the IBAG computer. Once opened, the macro will process the conversion from increments to magnetic field angle, calculate the GF (after the sample length is input) and convert encoder counts into strain. Afterwards, a plot of angle (x-axis) vs the MFIS (y-axis) is displayed.

Moreover, samples were magneto-mechanical trained by increasing magnetic field rotation from 100 rpm for the first thousand rotations to 1000 rpm for the next ten thousand rotations. Later, the samples were thermo-magneto-mechanically trained by thermally cycling the sample several times from 293 K to 323 K using either hot or cold air under a rotating field of 30 rpm. MSME measurements were recorded in ten and five °C increments. A thermocouple was placed on the surface of the sample to accurately record temperatures within a degree Celsius.

VBA CODE:

```
Sub test()
Dim OpenFileName As String
Dim wb As Workbook
'Select and Open workbook
OpenFileName = Application.GetOpenFilename("clients saved spreadsheet,*.txt")
If OpenFileName = "False" Then Exit Sub
Set wb = Workbooks.Open(OpenFileName)
```

```
'Get data EXAMPLE
ThisWorkbook.Sheets(1).Range("B5:C7").Value = wb.Sheets(1).Range("B5:C7").Value


Range("E13").Select
ActiveCell.FormulaR1C1 = "Angle"
Range("E14").Select
ActiveCell.FormulaR1C1 = _
        "=IF(RC[-1]<=1543,((RC[-1]/1600)*373), IF(RC[-1]>=1544, ((RC[-1]-1543)/1600)*360))"
Range("E14").Select
Selection.AutoFill Destination:=Range("E14:E5013")
Range("E14:E5013").Select
Dim myValue As Variant
myValue = InputBox("Enter Sample Length (um)")
Range("H1").Value = myValue
Range("H2").Select
ActiveCell.FormulaR1C1 = _
    "=(SQRT((87500^2)-(6136+R[-1]C[0])^2)/(6136+R[-1]C[0]))*-1"
Range("F13").Select
ActiveCell.FormulaR1C1 = "Strain"
Range("F14").Select
ActiveCell.FormulaR1C1 = _
    "=((R[0]C[-3])*(R2C8))/(4*400*(R1C8))*100"
Range("F14").Select
Selection.AutoFill Destination:=Range("F14:F5013")
Dim xaxis As Range
Dim yaxis As Range
Dim fullRange As Range
Dim topcell As Range
```

```
Set xaxis = Range("$E14", Range("$E$5013").End(xlDown))
Set yaxis = Range("$K14", Range("$K$5013").End(xlDown))



Set fullRange = Union(xaxis, yaxis)
fullRange.Select
ActiveSheet.Shapes.AddChart.Select
ActiveChart.ChartType = xlXYScatter
ActiveChart.SetSourceData Source:=fullRange
   Range("G14").Select
   ActiveCell.FormulaR1C1 = "=MIN(RC[-1]:R[4999]C[-1])"
   Range("H14").Select
   ActiveCell.FormulaR1C1 = "=IF(R14C7<=0,(ABS(R14C7)), IF(R14C7>=0, (-R14C7)))"
   Range("I14").Select
   ActiveCell.FormulaR1C1 = "=RC[-3]+R14C8"
   Range("I14").Select
   Selection.AutoFill Destination:=Range("I14:I5013")
   Range("I14:I5013").Select
   Range("J14").Select
   ActiveCell.FormulaR1C1 = "=SLOPE(RC[-1]:R[36]C[-1],RC[-5]:R[36]C[-5])"
   Range("K14").Select
   ActiveCell.FormulaR1C1 = "=RC[-2]-(R14C10*RC[-6])"
   Range("K14").Select
   Selection.AutoFill Destination:=Range("K14:K5013")
   Range("K14:K5013").Select
   ActiveSheet.ChartObjects("Chart 1").Activate
   ActiveChart.SeriesCollection(1).Select
End Sub
```

5. Characterization of Ni-Mn-Ga Powders

The results presented in this chapter will focus on powder characterization of ferromagnetic Ni-Mn-Ga shape memory alloy powders. Investigated here are three different Ni-Mn-Ga powders synthesized using two different methods. One method is spark erosion, while the other method is ball milling. All three powders possess different packing densities, morphologies, and compositions. The varieties of parameters inherently affect the additive manufacturing parameters.

5.1 Morphology

Figure 5.1 (a) – (c) shows the morphology of liquid argon (LAr) and liquid nitrogen (LN_2) spark eroded, and ball milled powders, respectively. Secondary electron images recorded from the spark eroded material show that the powder consists of a combination of spherical and irregular-shaped particles. Electron micrographs of the cross-sectioned particles prepared in LN_2 and LAr are presented in Figure 5.1 (d) and (e), respectively. The cross-sections have been prepared by embedding the particulate material into fast-curing epoxy, followed by mechanical grinding and polishing. From cross-section images, it can be observed that the spherical particles prepared in LN_2 are mostly hollow, while the ones prepared in LAr are solid. This morphology has been reported before in Ni-Mn-Ga, Fe-Ga, Co-Ga, Ni and Ti particles prepared in cryogenic liquids [19], [20], [163], [164]. Monastyrsky reported that spherical particles, which represent approximately 70% to 90% of the powder volume depending on the alloy, are formed due to rapid quenching of the molten droplets into dielectric liquid [160]. Berkowitz *et al.* suggested two mechanisms for Ni-Mn-Ga hollow particle formation:

bagging and cryogen solubility [19]. In the bagging mechanism a molten platelet can close on itself to produce a bubble that may contain smaller particles and vaporized cryogen. That might be the case of several hollow particles indicated with arrows on Figure 5.1 (a). In the case of cryogen solubility mechanism, vaporized cryogen might be soluble at high temperatures in a molten droplet, but much less soluble at lower temperatures. This leads to trapped gas within the particle after solidification. Typical morphologies formed as the result of cryogen solubility mechanism are non-spherical particles containing large multiple pores, as indicated by arrows in Figure 5.1 (d).

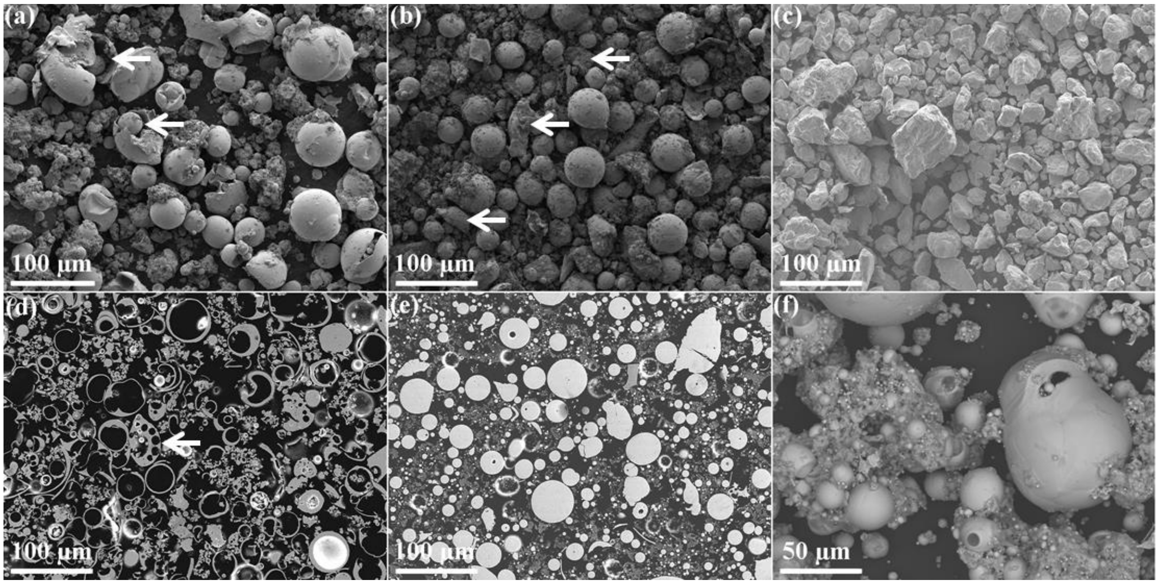

Figure 5.1: Electron micrographs of Ni-Mn-Ga particulate materials used in this study. (a), (b) Particles produced by spark erosion in liquid nitrogen (LN_2) and liquid argon (LAr), respectively. (c) Typical morphology of ball milled particles. (d), (e) Polished cross-sections of epoxy-embedded hollow and solid particles produced by spark erosion in LN_2 and LAr, respectively. (f) Foam-like structure accompanying spherical spark eroded particles. See the text for the explanation on the features indicated by arrows.

Two irregular-shaped particle fractions are also observed in LN_2 and LAr powders. The large irregular-shaped particles, indicated with arrows in Figure 5.1 (b), might form as the result of mechanical separation of small pieces from the Ni-Mn-Ga chucks, due to the electro-mechanical impacts during spark erosion. This hypothesis is supported by the fact that Ni-Mn-Ga alloys are very brittle and fracture easily under mechanical impact. A second, larger fraction of irregular-shaped volumes has a foam-like structure. A higher magnification image of such a structure is displayed in Figure 5.1 (f). Irregular-shaped particles with foam-like structures accompanying spherical particles produced by spark erosion have been observed and reported before [20], [160], [164]. The structures are made of agglomerations of sub-micron and nanometer scale particles and are attached to the micrometer-size spherical particles. Figure 5.2 (a) captures the above-mentioned scenario as a BSE micrograph, for which sub-micron and nanometer sized particles are fixed to the surfaces of micrometer sized Ni-Mn-Ga particle after spark erosion. Furthermore, Figure 5.2 (b) shows the presence of nanometer sized particles held together at the surface by a cloud-like matrix material. The contrast mechanism of BSE imaging displays materials with higher atomic number ratios as a brighter contrast. Therefore, the cloud like matrix responsible for creating the surface agglomerations is of lower atomic ratio when compared to the micrometer and sub-micrometer particles.

The sub-micron size particles are formed due to the explosion of molten droplets, while the nanoscale particles are formed as the result of condensation of evaporated constituents [160]. Usually, the chemical compositions of these agglomerates are different than the chemical composition of the micrometer and sub-micrometer size spherical particles that are identical to that of the starting material. The contrast of the

BSE micrograph in Figure 5.2 (a) suggests different chemical composition on nanoparticles compared with the larger particles.

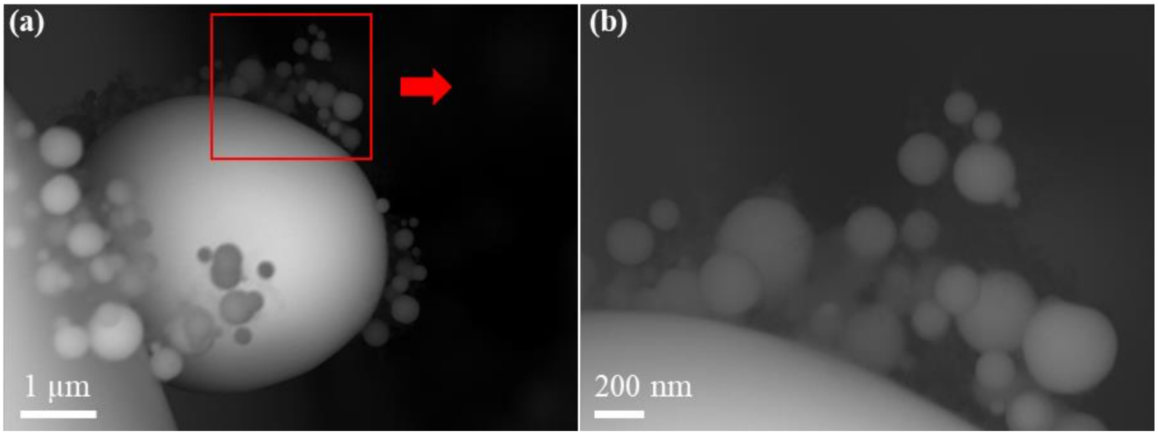

Figure 5.2: (a) BSE micrograph of LN_2 spark eroded micrometer and sub-micrometer particulate material; (b) High resolution BSE micrograph, recorded from the material shown in (a), displaying surface agglomerates containing nanometer size particles.

The electron micrograph in Figure 5.1 (c) shows the morphology of ball milled powders after sieving. Due to the nature of the ball milling process, anisotropic shaped powders with spread size distribution have been obtained [183]. BSE imaging techniques have also been used to investigate BM Ni-Mn-Ga powders, Figure 5.3. As observed, a uniform contrast is presented which is representative of a homogenous material.

Also observed in Figure 5.3 is the presence of martensitic plates found at the surface of fractured particles, superseded by the red lines. Based on this finding, the martensitic phase observed in bulk alloys is preserved over the ball milling process. The presence of martensitic plates on the ball milled powders point to a particular fracture behavior during ball milling. The proposed postulate involves granules of Ni-Mn-Ga which fracture due to crack formation and propagation in a perpendicular direction with respect to the martensitic plates. Crack propagation, as indicated by the arrow in Figure 5.3 show a directional cracking, subsequently causing failures and creating smaller granules of Ni-Mn-Ga. Additionally, the existence of martensite after milling implies collisions between granules during ball milling are insufficient to cause a stress induced phase transformation. Induced stress on the martensitic phase in shape memory alloys can cause a phase change, which is not observed in Figure 5.3 for Ni-Mn-Ga particulate material.

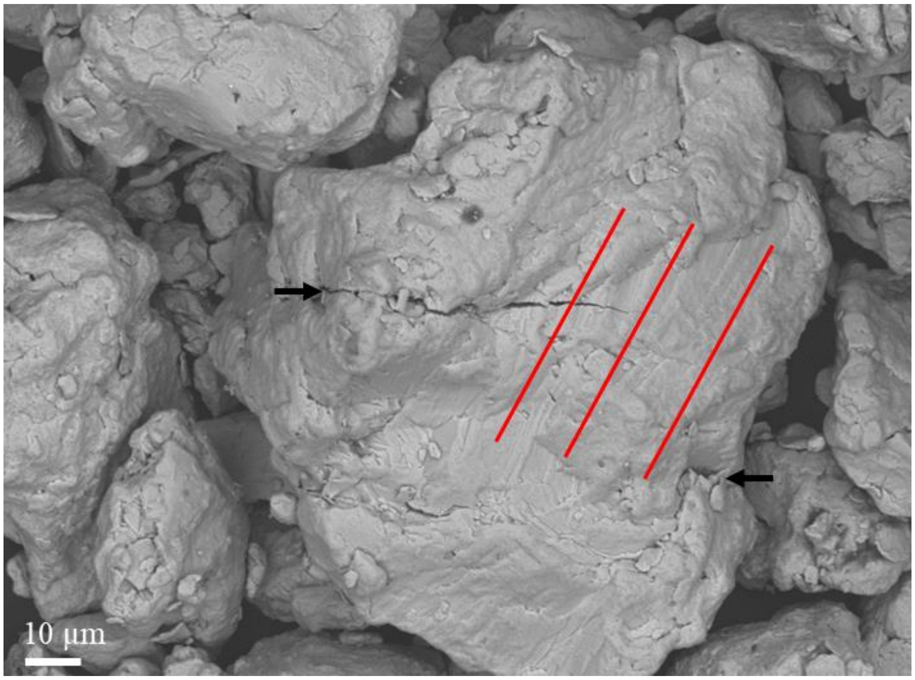

Figure 5.3: BSE micrograph of BM powder after sieving. Refer to text for explanation.

Tian *et al* [166]–[168], [184] investigated size distribution and chemical composition of ball milled and annealed Ni-Mn-Ga powders. Their produced arc melted Ni-Mn-Ga alloys, having the chemical composition nearly identical to the material used in this research. After vacuum annealing at 1123 K (850 ° Celsius) for 10 h, the ingots were milled for 4 h via stainless steel media. The Ni-Mn-Ga powder morphology reported by Tian's team refers to "irregular equiaxial particles with sizes ranging from 5 – 50 µm" [184]. In addition to the irregular equiaxial particles obtained after milling, they also report a flakey morphology powder with less than ten micrometers in thickness and up to 50 µm in diameter [167]. Aside from the flakey Ni-Mn-Ga powders, the morphology and size of milled Ni-Mn-Ga powders reported by Tian *et al* are substantially similar to the powders obtained in this research, as seen in Figure 5.1 (c) and Figure 5.3.

5.2 Size Distribution Analysis

Due to the difference in chemical composition between spherical and foam-like particles (discussed later), mechanical separation of two fractions was attempted for the spark eroded powders. The Ni-Mn-Ga powders made in LAr were thoroughly crushed using a mortar and pestle until a smooth consistency was obtained. Figure 5.4 (a) and (b) compares the morphological differences between Ni-Mn-Ga LAr raw powder material and crushed material, respectively. Observed in Figure 5.4 (a), is the presence of irregular shaped material, as previously discussed, which can be detrimental to the binder jetting process. Figure 5.4 (b) displays the morphology of the LAr Ni-Mn-Ga powders after crushing. Because of the crushing process, spherical morphology particles are separated from the irregular-shaped material. The crushing process removes irregular shaped material from the surface of LAr powder and pulverizes the remaining of the irregular shaped material.

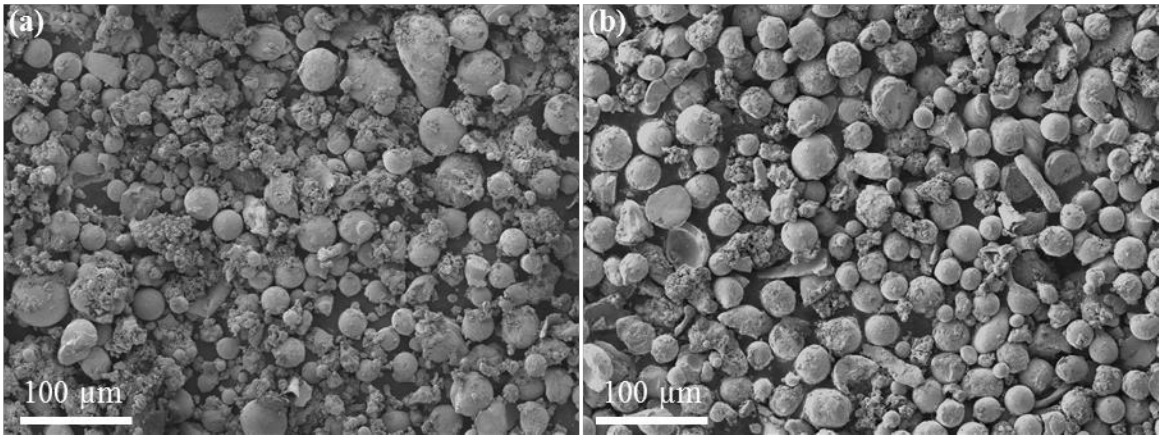

Figure 5.4: SE micrographs of LAr Ni-Mn-Ga powders as (a) raw material and (b) crushed.

There are occasions during the crushing of LAr powders, where compressive forces via mortar and pestle cause particle fracture. An example of a fractured particle is seen in Figure 5.5. Comparable to the fractures cause by ball milling in the BM powders (Figure 5.3), crack propagation is clearly observed and responsible for particle splitting. This was considered notable since broken particles could affect particle size distribution analysis.

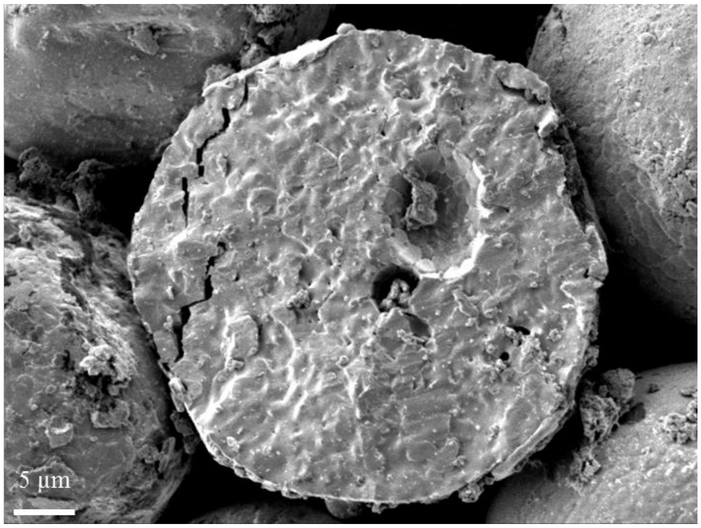

Figure 5.5: Fractured surface of LAr Ni-Mn-Ga particle.

After crushing the LAr material it was then sieved and classified in four group sizes: 0 - 20 µm, 20 - 45µm, 45 - 53µm, and 53 - 75µm. Micrographs showing the typical morphology of the particles in the four groups are presented in Figure 5.6. The irregular-shaped foam-like material seems to be predominating in the two groups corresponding to sieved powders smaller than 20 µm and larger than 53 µm.

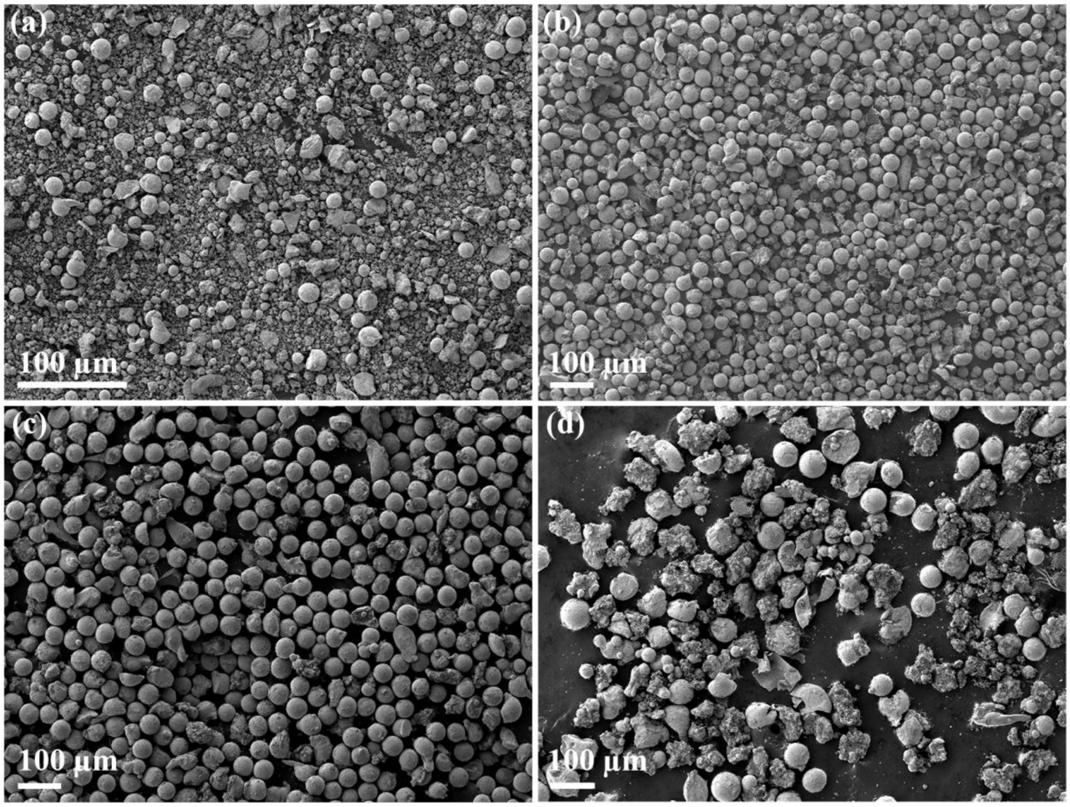

Figure 5.6: Secondary electron (SE) micrographs of LAr particles after sieving and classification in four group sizes: (a) 0 - 20 µm, (b) 20 - 45µm, (c) 45 - 53µm, and (d) 53 - 75µm. The combined 20 – 53 µm sized LAr particles had been used for 3D binder jetting printing.

In order to quantify the increase in spherical particle count after crushing, SEM images of each size distribution were taken and used for image processing, Figure 5.6.

The image processing was done using ImageJ software to quantify the number of spherical particles in each image. Using image processing it was determined that the spherical particle yield increased with more than 40% for the particles in group size 20 - 45µm and 45 - 53µm. The results of the spherical particle count from image processing for each size classification are presented in Table 5.1.

Table 5.1: Spherical particle count and increase of spherical particle yield following mechanical processing and sieving.

	Spherical particle count	Increase in spherical particle yield from raw material
Raw material	240	100%
10-20µm	139	-
20-45µm	413	141.8%
20-53µm	479	149.9%

Histograms of as sparked, 20-45µm and 20-53µm were generated to acquire a statistical representation for size distributions of Ni-Mn-Ga powders. Histograms shown in Figure 5.7 were only generated for Ni-Mn-Ga LAr powders relevant to the additive manufacturing process. It can be observed that particles in the 20-45µm (b) class size have a more uniform distribution than the as-sparked (a) and 20-53 µm (c) particles. The 20 – 53 µm sized LAr particles have been combined and used for binder jetting printing in this work. A similar approached was attempted in the case of LN_2 particles. However, due to the powders hollow morphology and material brittleness, the spherical particles collapsed during mechanical separation. As a result, as-sparked LN_2 powders were used in the printing process.

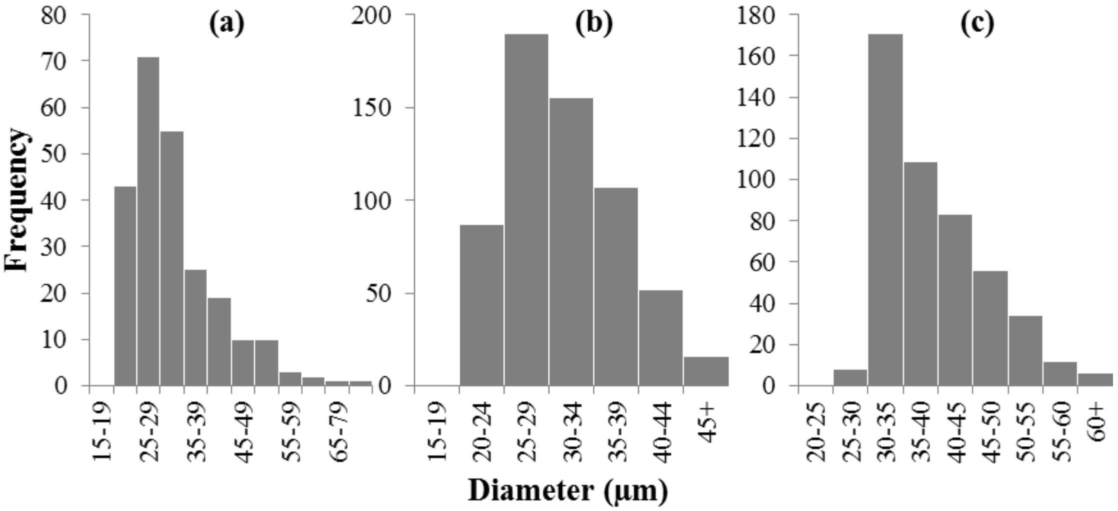

Figure 5.7: Histograms of size distribution of Ni-Mn-Ga LAr powders obtained by image processing: (a) as-sparked; (b) mechanically separated and sieved to 20-45µm; and (c) mechanically separated and sieved to 20-53µm.

Additionally, the particle size distributions for LN_2, LAr, and BM powders, determined by laser diffraction using a Cilas 1190 instrument, are shown in Figure 5.8. All three powders show unimodal distribution with almost identical mean particle size for LN_2 and LAr powders, 35.00 µm and 32.86 µm, respectively. The mean particle size for ball mill powders was 43.75 µm. All powders were sieved to ensure the maximum particle size would be less than 100 µm. While the layer thickness parameter for printing Ni-Mn-Ga powders varied, sieving ensured the maximum layer thickness did not exceed 110 µm. For LN_2 and BM powders it can be observed that 100 % particle sizes are below 100 µm, while for LAr powder, the maximum particle size is below 60 µm. As mentioned previously, LAr powders were sieved and combined into a size classification of 20 – 53 µm.

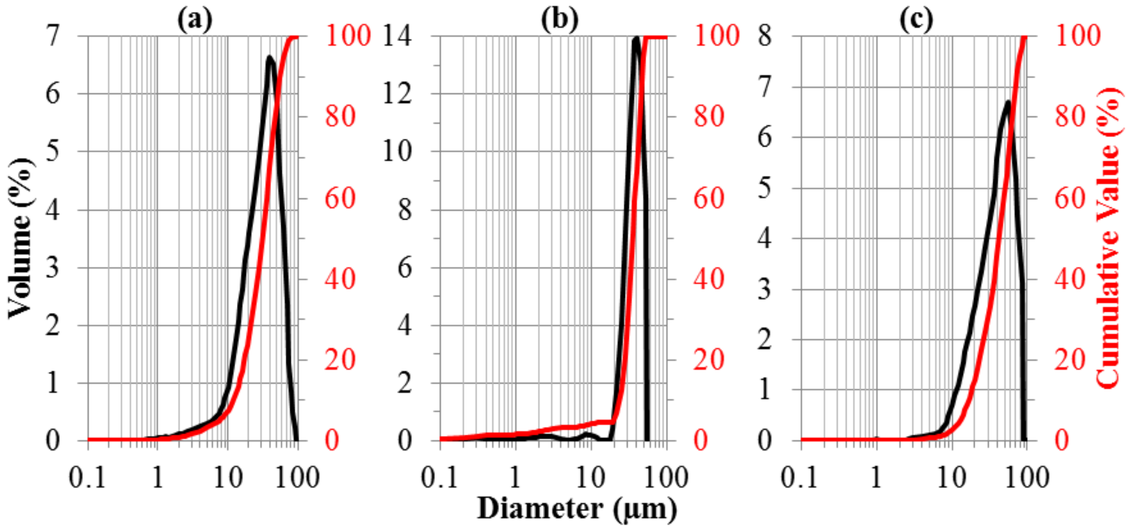

Figure 5.8: Particle size distributions, as determined by laser diffraction, of Ni-Mn-Ga powders produced by: (a) spark erosion in liquid nitrogen, (b) spark erosion in liquid argon, and (c) ball milling.

The size distribution for particles sparked in LN_2 dielectric show: 90 % of particles are 61.4 µm or less, 50 % are 32.0 µm or less, and 10 % are 12.1 µm or less. The size distribution for powders sparked in LAr dielectric is as follows: 90 % of particles are 48.25 µm or less, 50 % are 35.8 µm or less, 10 % are 22.38 µm or less. Ball milled powders showed 90 % of particles being 88.7 µm or less, 50 % 45.4 µm or less and 10 % 14.4 µm or less. The three Ni-Mn-Ga powders were sieved to control size distribution. In the cases of LN_2 and BM material, powders were sieved to a size of less than 100 µm. In the case of LAr powders, due to mechanical separation the size distribution is predominately between 20 – 60 µm.

5.3 Chemical Composition

For Ni-Mn-Ga alloys the transformation temperatures corresponding to reversible martensitic transition, responsible for the shape memory effect, are very sensitive to element concentration [121], [185], [186]. Also, homogeneous chemical composition of the powder is a critical parameter in ensuring uniform quality and reproducibility of the 3D printed parts. The chemical composition of two fractions of spark eroded powders, namely spherical particles and companion foam-like structures, and ball milled powders were determined by quantitative EDS analysis in SEM. For accurate chemical analysis, samples were flat-polished, as shown in Figure 5.1 (d) and (e), and a homogeneous $Ni_{50.90}Mn_{29.23}Ga_{19.86}$ (at %) single crystal was used as a reference standard for calibration. For each powder, X-ray spectra was collected from at least 30 different positions with 100 second acquisition time for each spectrum, and then processed with EDAX TEAM^{TM} software for quantitative analysis. Table 5.2 shows the quantitative concentrations for the powders including statistical standard error values. The ball milled powder seems to be very homogeneous.

Table 5.2: The average element concertation of spherical and foam-like fractions of spark eroded powders and ball milled powders, including standard deviation based on 30 measurements for each powder.

Powders	Ni (at %)	Mn (at %)	Ga (at %)	O (at %)
Spherical LAr	53.32 ± 1.93	28.51 ± 2.09	18.17 ± 1.99	-
Spherical LN_2	52.31 ± 4.46	28.16 ± 2.39	19.48 ± 4.57	-
Foam-like LAr	13.26 ± 3.97	19.63 ± 5.08	14.98 ± 1.16	52.11 ± 8.00
Foam-like LN_2	23.87 ± 18.04	15.2 ± 3.32	14.47 ± 0.70	46.45 ± 20.66
BM	52.22 ± 2.00	30.07 ± 0.96	17.04 ± 1.69	-

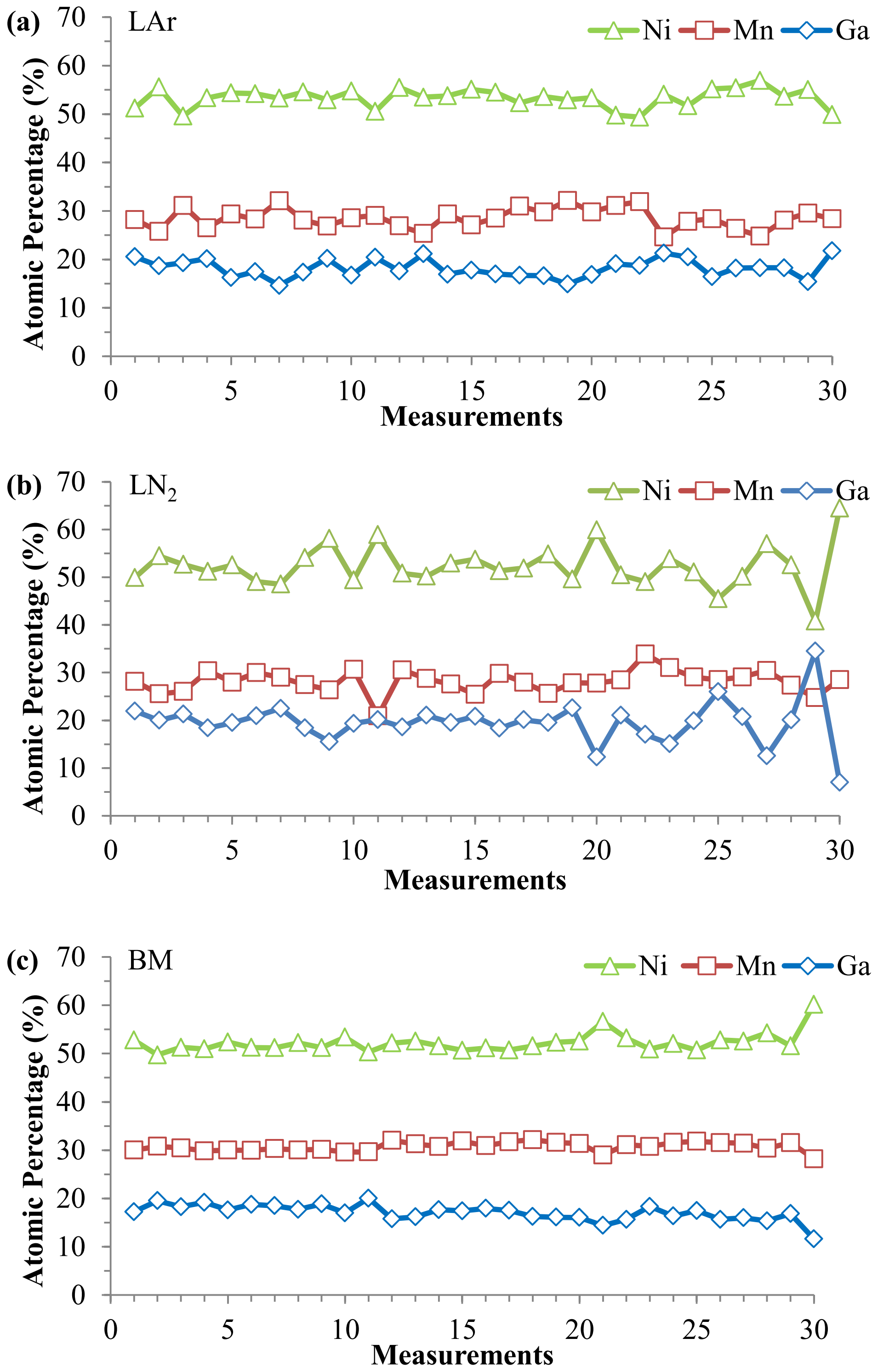

Figure 5.9: Graphs displaying results of chemical analysis measurements for (a) LAr, (b) LN$_2$ and (c) BM powders.

The results of EDS quantitative chemical analysis are also displayed graphically in Figure 5.9 (a) – (c). As seen in Figure 5.9 (a), (b) the spark eroded powders (LAr and LN_2) show large relative differences between measurements. For example, manganese and gallium content for LN_2 powders varied between 20.9 – 33.9 at % Mn and 7.02 – 34.47 at % Ga. These differences in chemical composition could be a derivative of the spark erosion process, caused via segregation during solidification mechanisms [160].

The maximum standard deviation (Table 5.2) is very close to the analytical precision and accuracy of the EDS method (±1 – 2 %, [172]). This is confirmed by the backscatter electron micrograph in Figure 5.10 (a) which shows uniform elemental compositional contrast for the ball milled powders. In the case of spark eroded powders the chemical composition of foam-like fraction is very different than that of spherical particles. The high oxygen content in the foam-like particles might be related to the formation of the component metals oxides, such as MnO [20].

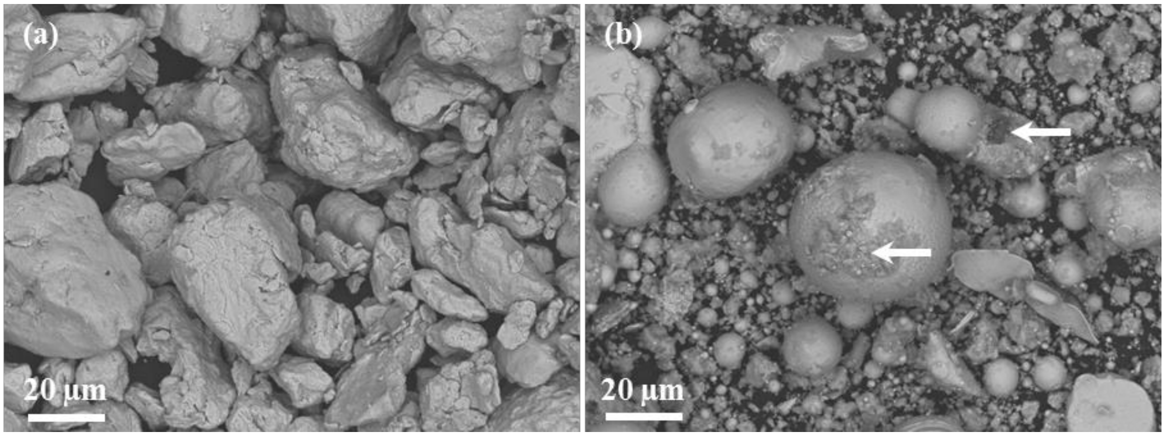

Figure 5.10: Backscattered electron (BSE) micrographs indicating: (a) compositionally homogeneous ball milled powders and (b) some chemical inhomogeneity in liquid argon powders. The arrow indicates darker contrast foam-like material suggesting lower atomic number elements than in the solid particle.

On the other hand, the oxygen content in spherical LAr and LN_2, and BM powders is negligible, relative to the oxygen content in the foam-like particles. For spark eroded powders the difference in chemical composition might be related to the different formation mechanism of the two particulate fractions, as discussed above and addressed/referred in literature [160], [164]. The difference in chemical composition between the foam-like material and spherical particles is visible in the backscatter electron micrograph of LAr powders shown in Figure 5.10 (b). The foam-like material, indicated by arrows, has darker contrast than the spherical particles suggesting lower atomic number elements than in the solid particle. Bright nanoscale dots observed throughout the field of view of the image in Figure 5.10 (b) can be attributed to elemental Ni-Mn-Ga nanoparticles, reported to form in spark eroded Ni-based powders [160].

5.4 Crystallographic Structure and Thermal Properties

The XRD measurements for heat treated Ni-Mn-Ga ingots and ball milled powders were carried out in the range of 25°- 85° and compared to the 5M Ni_2MnGa phase [128], Figure 5.11. The X-ray patterns collected from the 5M Ni_2MnGa polycrystalline sample have been indexed by $Ni_2Mn_{1.15}Ga_{0.85}$, a Mn-rich Ni_2-Mn-Ga phase. The existence of 26.5° (015), 42.7° (200), and 43.7° (202) peaks indicate the presence of a martensitic phase having a commensurate 5M crystallographic modulation. This observation is in line with previous reports on 5M modulated martensite observed in Ni-Mn-Ga Mn-rich alloys [128]. On the other hand, the 5M modulation was not observed in the heat treated ingot (used to produce BM powder), despite the fact that X-ray pattern shows characteristic peaks that closely match a slight Mn-rich Ni_2-Mn-Ga phase. This indicates an atomic ordering transition beginning with the Ni-Mn-Ga ingot material during homogenization. The pattern collected from ball milled powders could not be indexed due to the high density of lattice defects induced by high strain rate deformation. However, the XRD pattern from the BM powders does reveal the presence of a few characteristic peaks. Explicitly, the 44.5° (125), 42.7° (200), 80.0° (1215) and 82.8° (240) planes are observable. These planes display characteristics of quasi-amorphous and/or distorted lattice structures. Semi-amorphous peaks tend to have wide peak areas, which are recognizable in Figure 5.11. In addition, the high strain rate deformation caused by ball milling is responsible for lattice defects, ultimately severely altering the microstructure of the ball milled powders.

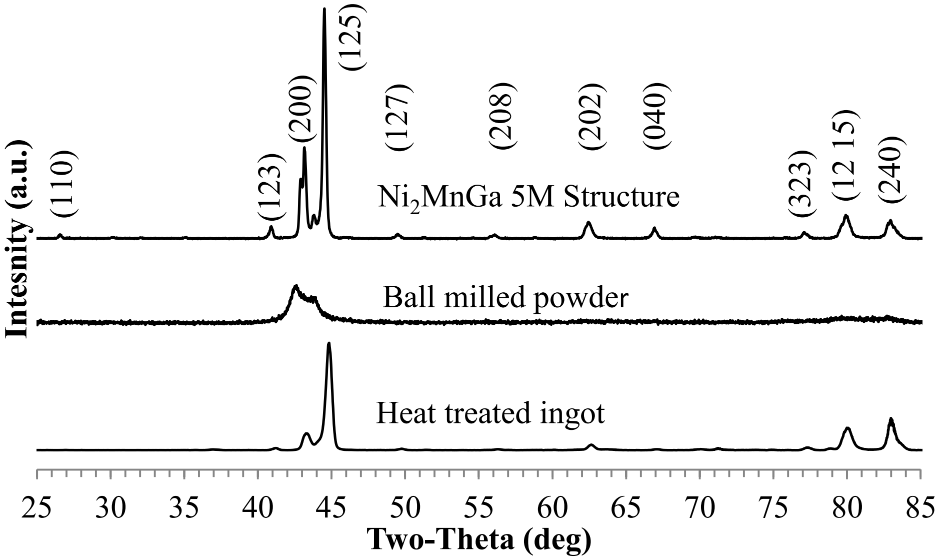

Figure 5.11: XRD patterns for heat treated ingot (bottom), ball milled powders (middle) and a typical 5M modulated martensitic structure in equiatomic Ni_2MnGa alloy (top).

Above-mentioned atomic transitions are apparent in the initial Ni-Mn-Ga ingot heat treated for homogenization, ball milled powders, and a typical 5M modulated martensitic structure in a Ni_2MnGa alloy, Figure 5.11. These atomic transitions have been investigated by Tian *et al* [184] by inspecting ball milled Ni-Mn-Ga powders after annealing at various temperatures. During this investigation, they examined the crystal structure and thermal behaviors by means of XRD and DSC, respectively. They report ball milled powders to possess a disordered face centered cubic (FCC) tetragonal structure. Recall the 5M modulated martensite in Ni-Mn-Ga is often presumed to be tetragonal basis, Section 2.3.4. However, Tian's team observed a noticeable change in the structure of ball milled powders when annealed between 553 – 723 K (280 °C – 450 °C). They suggest a structural transition from the disordered face centered cubic tetragonal to disordered body centered cubic (BCC) structure occurring around 633 K (360 °Celsius). Furthermore, two exothermic peaks were observed during heating in DSC curves with peak positions at 578 K and 683 K (305 °C and 410 °C) [184].

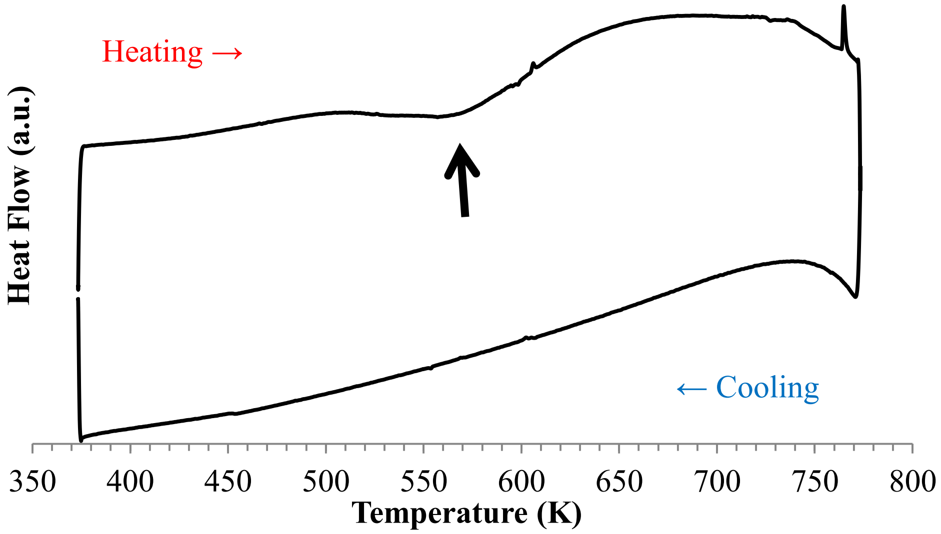

Figure 5.12: DSC curve of BM powders after ball milling. Endothermic reactions are displayed up.

BM powders produced in this research underwent a similar DSC investigation, for which as-milled powders experienced heating and cooling from 373 – 773 K (100 °C – 500 °C) at a rate of 10°/min, Figure 5.12. One exothermic peak is observed from the DSC curves of as-milled powders with a peak position at approximately 559 K (286 °C), indicated via the arrow in Figure 5.12. The peak position is in line with the above mentioned reported temperatures of between 578 K and 683 K (305 °C and 410 °C). Moreover, these exothermic peaks are well below the oxidation temperatures for Ni-Mn-Ga alloys (>600 °C) [187].

The structural investigation of spark eroded Ni-Mn-Ga powders (LN_2 & LAr) in the as-sparked state will be described in subsequent chapters that also describe the as-sintered microstructure. Furthermore, the thermic properties of as-sparked Ni-Mn-Ga powders display no distinguishable exothermic or endothermic transformations.

6. Binder Jetting 3D Printing of Ni-Mn-Ga Powders

This chapter presents the results of parameter investigation and selection for Ni-Mn-Ga powders, as well as the binder jetting 3D printing of those powders. The parameters of 3D binder jetting printing can be classified into three categories: powder-related parameters, binder-related parameters, and 3D printer-related parameters. Extensive information on the definition and effect of each parameter on the printed structure integrity and resolution had been reported by Lu & Reynolds [100]. In this work, one powder-related parameter (layer thickness) and one binder-related variable (binder saturation) have been optimized for the 3D printing of Ni-Mn-Ga powders, while the other parameters have been pre-determined based on the literature recommendation and previous experience with 3D binder jetting printing of different metal powders.

6.1 Printing Parameter Selection

6.1.1 Powder-Related Printing Parameters

The printing layer thickness was determined based on the maximum size of LN_2, LAr, and BM powders. In order to preserve the integrity of the printed part during the printing process and achieve the required dimensional tolerance, the printing layer thickness must be larger than the maximum particle size. Another powder-related parameter is the efficiency for which the powder comes together, better known as packing density. The packing density is defined as the percentage of powder filling a known volume, while the remaining space unoccupied by powder is typically occupied by atmosphere. The packing density of the powders determines the density of the green part and is given as a density value (g/cm^3) and subsequently compared to the theoretical density to achieve a percentage of packing (%). The packing density for the Ni-Mn-Ga powders was calculated by measuring the mass of the powder filling a known volume. An illustrated example of packing density is shown in Figure 6.1. The red arrow indicates powder that occupies space in the known volume on the other hand the blue arrow indicates space occupied by atmosphere.

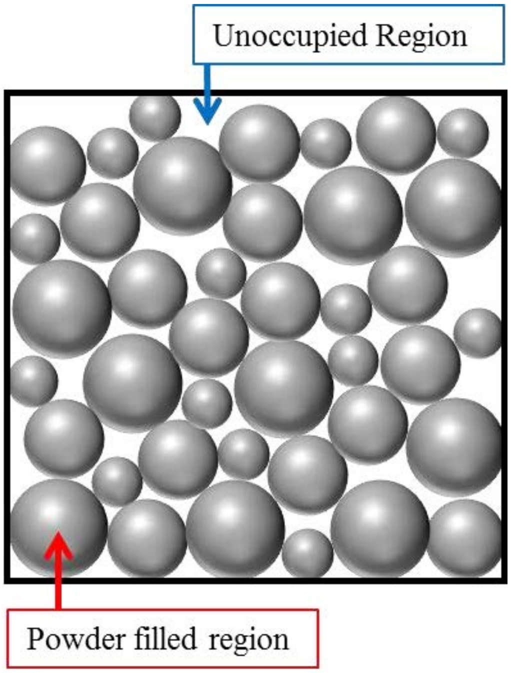

Figure 6.1: Illustration of packing density where the red arrow displays the space occupied from powders while the blue arrow is an example of unoccupied space.

The packing density for the Ni-Mn-Ga BM, LN_2 and LAr powders calculated using this method was determined to be 3.66 g/cm^3, 1.164 g/cm^3 and 2.987 g/cm^3, respectively. Atomic compositions of the Ni-Mn-Ga powders, as presented in Table 5.2 were used to determine the theoretical density using Equation 6.1, [188].

$$\rho_T = \frac{C_1A_1 + C_2A_2 + C_3A_3}{\frac{C_1A_1}{\rho_1} + \frac{C_2A_2}{\rho_2} + \frac{C_3A_3}{\rho_3}} \tag{6.1}$$

where ρ_T is the theoretical density, C_n is the composition of the element (at %), A_n is the atomic mass and ρ is the theoretical density of element n.

Using Equation 6.1 and chemical compositions shown in Table 5.2, the theoretical densities have been calculated as 7.663 g/cm^3, 7.709 g/cm^3, and 7.602 g/cm^3 for LN_2, LAr and BM powders respectively. The packing percentages were then determined to be 48.12 %, 38.74 %, and 15.18 %, respectively. The above-mentioned results for each powder are presented in Table 6.1. In addition, the maximum particle size and the values of layer thickness parameters for the three powders used in the experiment are presented in Table 6.1.

Table 6.1: Powder characteristics and optimized 3D binder jetting printing parameters used in printing of spark eroded and ball milled Ni-Mn-Ga powders.

Powders	Max. Particle Size	Layer Thickness	Packing Density	Relative Density	Packing Rate	Binder Saturation (X1-Lab input value)
Ni-Mn-Ga LN_2	90 µm	100 µm	1.164 g/cm^3	7.663 g/cm^3	15 %	250 %
Ni-Mn-Ga LAr	53 µm	80 µm	2.987 g/cm^3	7.709 g/cm^3	38 %	150 %
Ni-Mn-Ga BM	90 µm	110 µm	3.66 g/cm^3	7.602 g/cm^3	48 %	110 %

6.1.2 Binder-Related Printing Parameters

6.1.2.1 As-Sparked Powder: LN_2

Binder saturation is another major parameter in the printing process. The binder saturation parameter is critical for printed part quality. Binder saturation is defined as the percentage of the air space volume between powder particles that is occupied by a binder volume [75]. Optimal binder saturation creates strong bonds between particles and ensures the integrity of pre- and post-cured printed parts. Binder saturation level affects both the breaking strength, as well as the dimensional tolerance of the green printed part. Insufficient binder reduces the mechanical strength of the green part, which can affect the integrity of the part when removed from the printer or manipulated in between the printer and curing oven. On the other hand, too high saturation produces lateral binder spreading which translated into poor dimensional tolerance of the printed part [189]. The binder saturation depends on the powder packing density, or packing rate. A water-based binder (BS004), provided by ExOne, was used in the experiment. In order to find the optimum binder saturation for Ni-Mn-Ga powders, a method similar to the bench top test was used [15], [190]. Cured samples impregnated with various amounts of binder were investigated using SEM techniques, Figure 6.2 (a) and (b). The purpose of this investigation was twofold. First, to understand the amount of binder required to saturate the Ni-Mn-Ga powder, to assist in determining the printing parameters. Second, to examine the binder wetting of the particle's surface.

Figure 6.2 (a) is a hybrid micrograph obtained by combing the SE and BSE signals in the JEOL IT-300 SEM. The micrograph shows LN_2 particles impregnated with

2 μL of binder. The contrast generated by BSE electrons clearly shows binder distribution amongst the particles, due to the large difference in atomic number between the chemical elements of the binder and those of the metal powders. It seems this amount of binder is not enough to completely wet the particles, as indicated by the white arrow in Figure 6.2 (a). A possible explanation might be provided by taking into the account the LN_2 particle's morphology. Most of the LN_2 particles are hollow, and the binder fills the voids of the particles as indicated by the black arrow in Figure 6.2 (b). Moreover, the foam-like materials observed among the spherical particles seems to absorb a large amount of binder. This is suggested by the appearance of the foam-like particles marked with black arrows in Figure 6.2 (a). Therefore, in the case of LN_2 particles the binder volume must be increased above 4 μL, to achieve binder saturation. Ultimately, the lower packing density is responsible for the necessary increase in binder, in order to saturate LN_2 particulate material. The distinct morphology of hollow shell-like LN_2 powders inherently decreases the packing density.

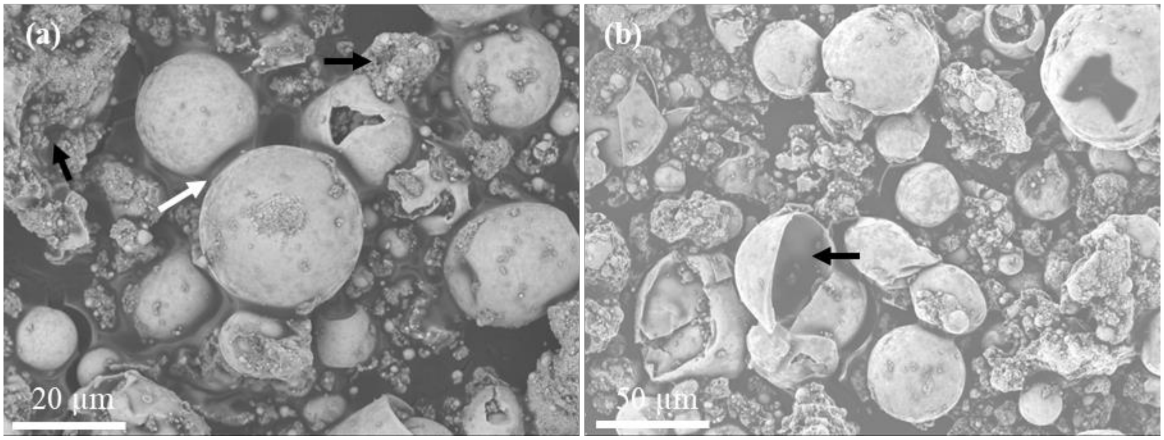

Figure 6.2: (a) SE-BSE image of LN_2 Ni-Mn-Ga powders impregnated with 2 μL of binder; (b) An additional SE-BSE image of LN_2 powders indicating binder occupying voids inside of LN_2 powders.

6.1.2.2 As-Sparked Powder: LAr

Figure 6.3 (a) displays Ni-Mn-Ga LAr powders post-mechanical separation. Figure 6.3 (b) shows mechanically separated LAr powders impregnated with 2µL of binder. Figure 6.3 (c) shows mechanically separated LAr powders saturated with 4µL of binder. Binder volume and bonding of particle to binder was examined. For the binder to be permissible in the binder jetting AM process, powders should exhibit suitable adhesion behavior. The binder should coat the surface of each particulate and fill any void space in between particles. Using micropipettes, binder amounts of 0.5 µL to 4 µL were impregnated onto Ni-Mn-Ga powders. In order to maintain a standardized analysis, 5 mm x 5 mm areas of conductive double sided carbon tape were sectioned and stuck to SEM analysis stubs. The stubs were then pressed into beds of Ni-Mn-Ga powders to create a powder bed of uniform thickness. The investigation revealed an optimum binder volume of 2µL for LAr powders; while 4µL was over saturated. A binder saturation of 2µL provided suitable adhesion between layers of particles while covering particulate surfaces.

During the binder saturation investigation, a comparison between Ni-Mn-Ga LAr and 420 stainless steel gas atomized powders, produced by ProMetal was deployed. Since a significant amount of research has already been conducted on the 420 stainless steel powders, it was considered an appropriate reference. The stainless steel powders showed equivalent morphology and size distributions to that of Ni-Mn-Ga LAr. Moreover, ProMetal reports the packing rate of their stainless steel powders to be between 50-60 %. The packing rate for stainless steel was measured and calculated to be approximately 52.8 %. Using the same method, Ni-Mn-Ga displayed a packing rate of approximately 38 %.

Based on this measurement, conditions for 3DP Ni-Mn-Ga LAr will need an increase in binder saturation compared to the well-established 70 % binder saturation needed to effectively print 420 stainless steel components. It must be mentioned that this 70 % binder saturation is the input number required by the X1-Lab machine.

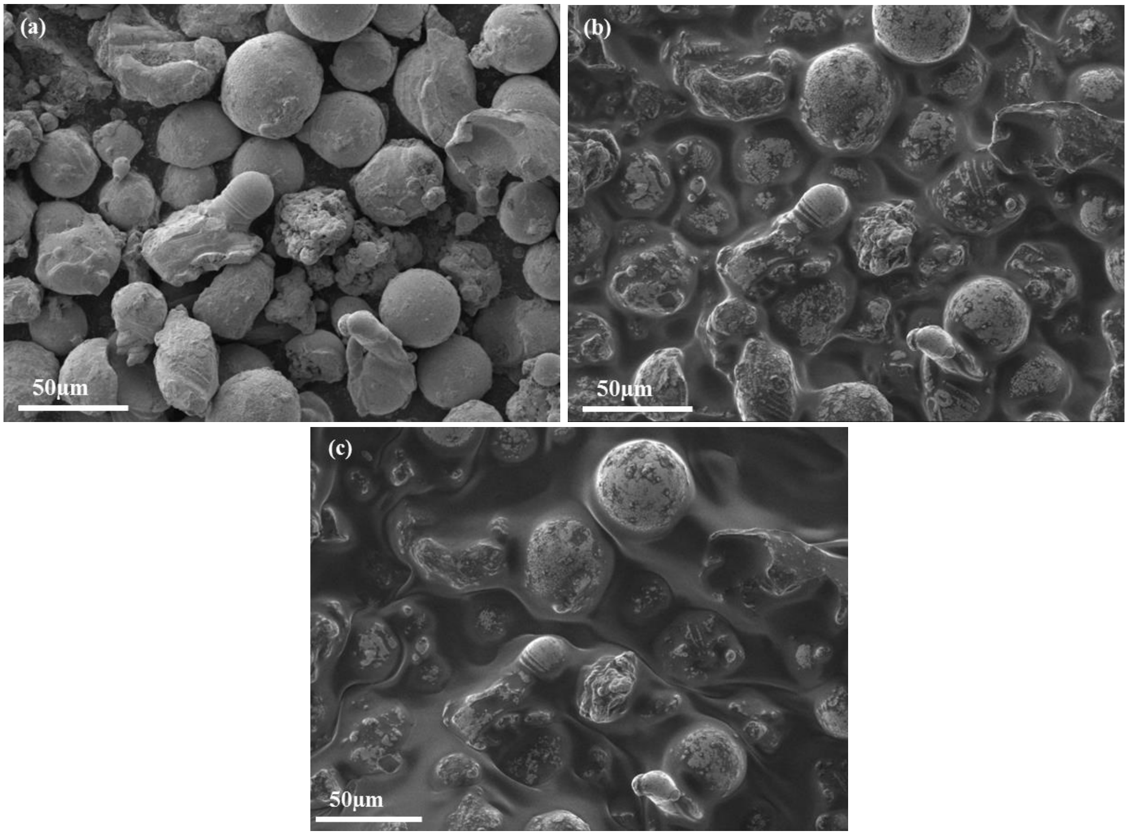

Figure 6.3: SE images of Ni-Mn-Ga LAr powders: (a) as-sparked; (b) impregnated with 2 μL of binder; (c) impregnated with 4 μL of binder.

6.1.2.3 Ball Milled Powder

Binder saturation testing was performed on the powders prepared by ball milling using the same process for as-sparked powders. Various amounts of binder were impregnated onto the surface layer of the anisotropic shaped powders. A particular example, as seen in Figure 6.4, shows a secondary electron image of ball milled powders saturated with 2 μL of binder. In order to obtain the same binder saturation information as previous mentioned for as-sparked powders, the comparison between BM and LAr is considered. LAr and BM powders possess similar packing densities, 38 % and 48 % respectively. Since the BM and LAr powders possess similar packing densities, the two inherently require similar amounts of binder to achieve saturation. This comparison is pointed out via Figure 6.3 (b) (LAr) and Figure 6.4 (BM), where 2 μL of binder is deposited on each powder, respectively. Since the packing density of the ball milled powder is the highest for all three powders (48 %), it required the least amount of binder to saturate. Moreover, the 2 μL impregnated on BM powders achieves the saturation requirements mentioned above. The surfaces of the anisotropic BM powders are covered as well as adhered to surrounding particulate material. Also noticeable is a slight over saturation, evident in the form of clumping of powder material. This over saturation from the impregnated binder is due to a higher packing density of approximately 10 %, when compared to LAr powders.

Based on the printing parameter selection investigation, the printing parameters used to produce a green part made of ball milled powders are: a layer thickness of 110μm, binder saturation of 110%, and speed of layer deposition of 0.5mm/s, Table 6.1. The measured values for packing density and packing rate for the three powders, along with the binder saturation values identified by trial and error and used in the printing process, are presented in Table 6.1. As expected, the binder saturation increases with the decrease in packing rate, i.e. from 110 % for BM powders (49 % packing rate) to 250 % for LN_2 powders (15 % packing rate).

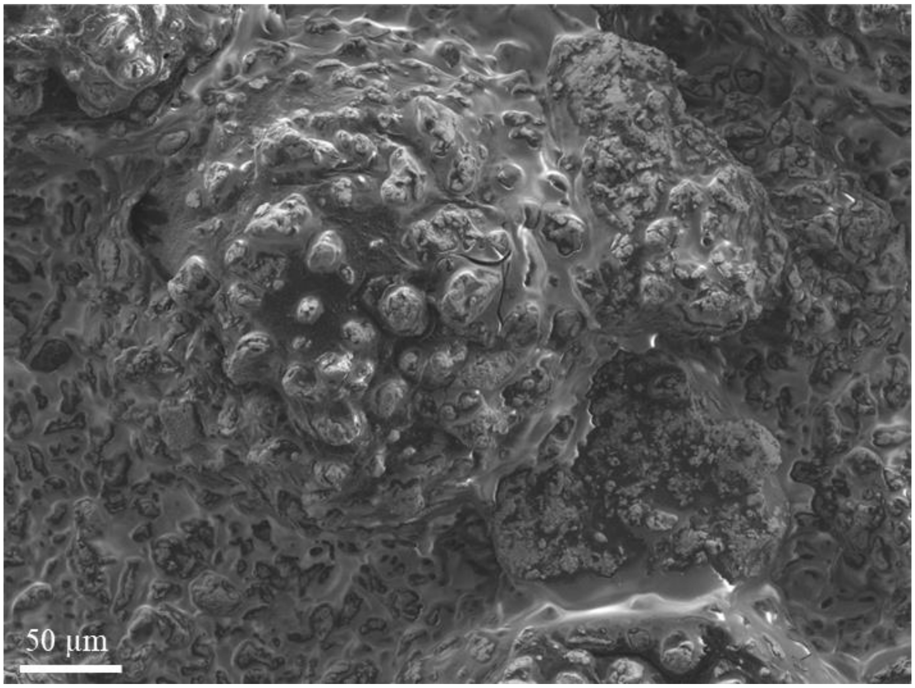

Figure 6.4: SE micrograph of BM Ni-Mn-Ga powder impregnated with 2 µL of binder.

6.2 3D Binder Jetting Printing of Complex-Shaped Parts from Ni-Mn-Ga Powders

Thus far, full considerations of particle morphology, packing factor, size distribution and binder saturation relationships have been documented in attempts to establish printing parameters. These printing parameters have been experimentally determined and are shown in Table 6.1. The next step of the additive manufacturing process is the binder jetting 3D printing of the powder material. The binder jetting process begins with the design of components to be manufactured. A more detailed description of the design and files used can be found in Section 4.3.3. Nevertheless, SolidWorks, CAD software, was utilized to design components. Among these CAD files developed in Solid Works, geometries include rectangular parallelepipeds, cubes, rods, washers, springs, lattice structures and gyro-spheres. An example of a lattice structure CAD design can be observed in Figure 6.5 (a).

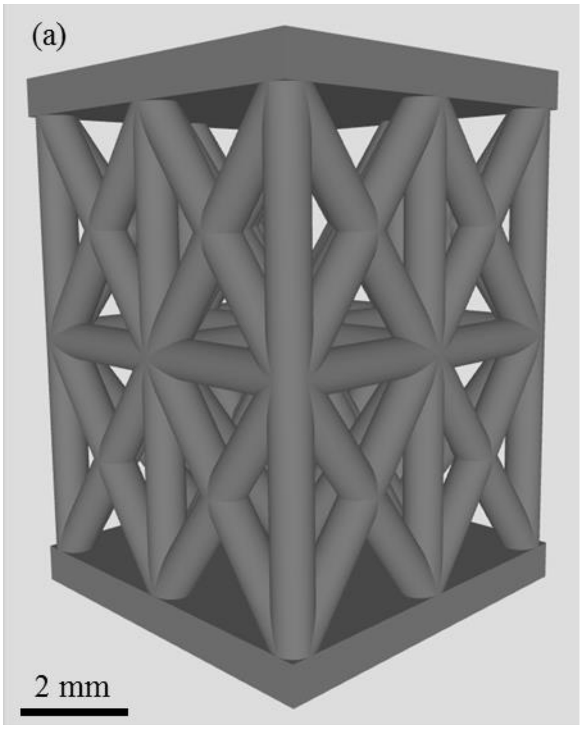

Figure 6.5: (a) CAD design for 3D printing of a lattice structure; (b) An image of the 3D printed Ni-Mn-Ga lattice structure in the as-cured state.

After the design aspects, there is some significance in preparation before printing. The ExOne X1-Lab must be thoroughly cleaned to remove any possible contaminants from previous builds as well as system operations check. This is essential for successful prints. Residual powder from previous builds could be incorporated during printing and subsequently effect the physical properties of 3D printed components, such as chemical composition. Furthermore, operation system components in the X1-Lab must be fully functioning before the printing process. In particular, the printing head, which deposits binder onto the powder bed, must be clean and depositing binder through each orifice.

The print head in the X1-Lab has close to 140 square cavities where binder is "sprayed" through. Testing the operation of each orifice must be verified before each print; otherwise part integrity could be compromised due to insufficient binder. An example of the X1-Lab moments before print initialization can be seen in Figure 6.6 (a) and (b).

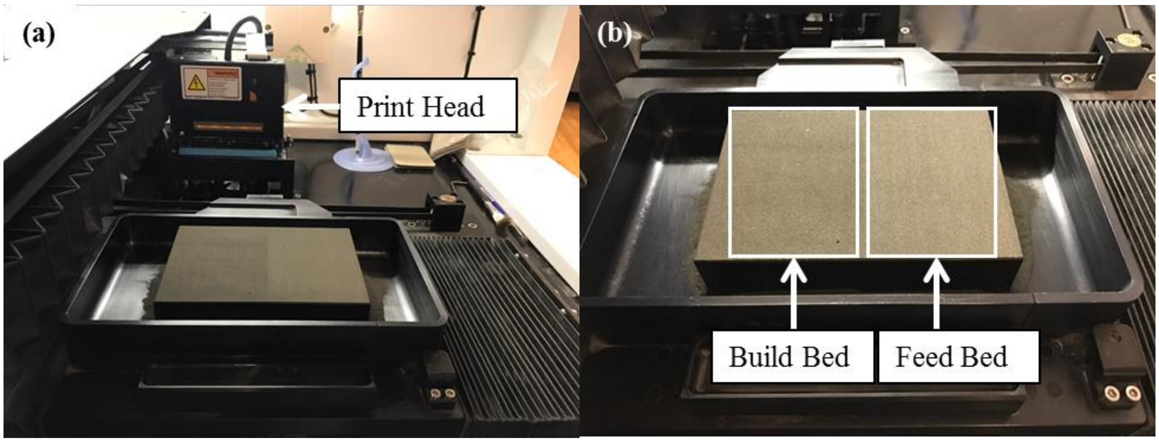

Figure 6.6: Images of the X1-Lab binder jetting printer: (a) stand by position of the print head; (b) displaying the build and feed bed.

After 3D printing, the printing bed containing the pre-cured printed parts were removed from the printer and heated to 463 K (190 °C) for 4 h in a curing oven (in air). Curing the binder increases the strength of the green Ni-Mn-Ga parts for handling purposes. After four hours the binder is completely cured, and the parts are removed from the print bed.

Figure 6.5 (b) presents a post-cured lattice structure manufactured by 3D printing from Ni-Mn-Ga BM powders. As previously mentioned, due to the brittleness it is very difficult to manufacture net shape structures from Ni-Mn-Ga alloys using conventional machining and forming operations. To the best of my knowledge, there is no detailed report on manufacturing structures with complex geometries from Ni-Mn-Ga alloys while maintaining a porous microstructure. Furthermore, a few articles pertaining to the additive manufacturing of Ni-Mn-Ga materials have been reported [183], [191], [192].

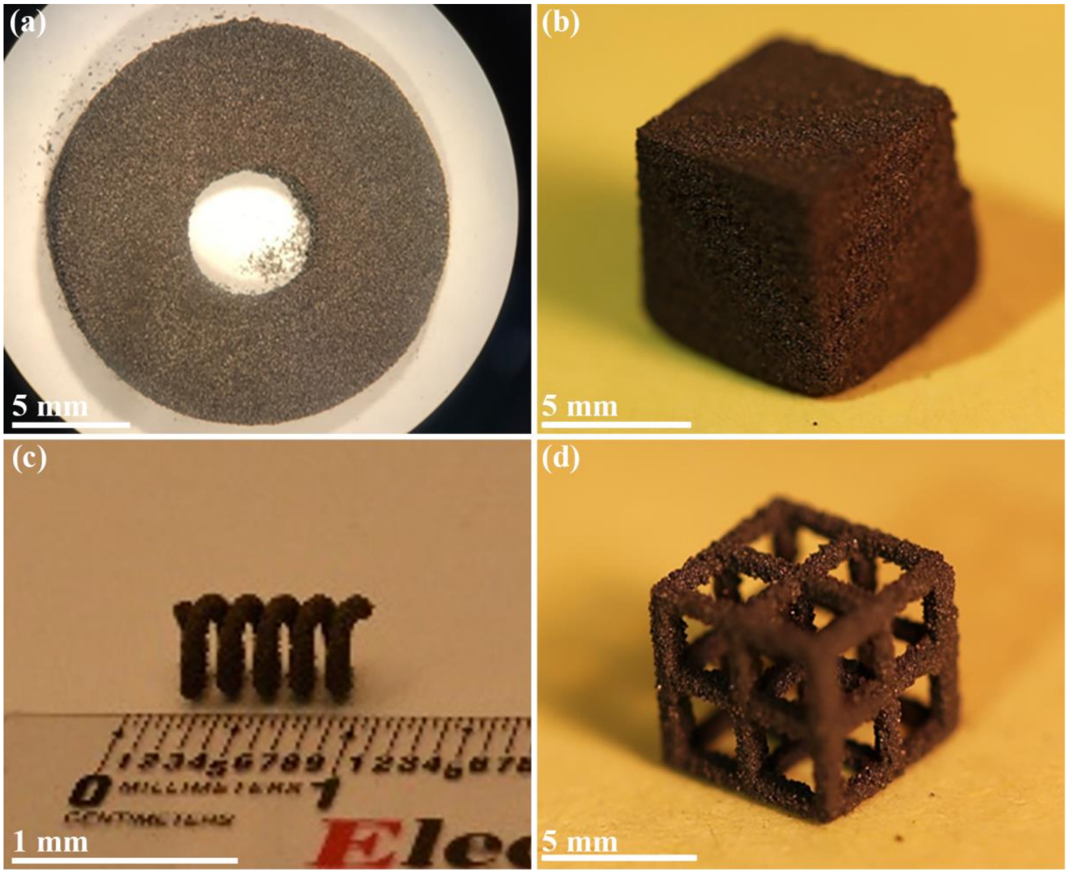

Figure 6.7: Post cured net shape parts 3D printed from: (a) Ni-Mn-Ga powders spark eroded in liquid nitrogen, (b) Ni-Mn-Ga powders spark eroded in liquid argon, (c) and (d) Ni-Mn-Ga powders obtained by ball milling.

In addition, to the lattice structure, more Ni-Mn-Ga structures in the post-cured state are presented in Figure 6.7 (a) to (d). Figure 6.7, (a) shows a 3D printed washer made from LN_2 spark eroded powders, while Figure 6.7 (b) to (d) show simple and complex geometries made from BM powders. These geometries range from simple cubes Figure 6.7 (a), to more convoluted components such as a cuboid Figure 6.7 (d). As previously stated, Ni-Mn-Ga possesses very brittle mechanical properties, therefore traditional machining and/or forming processes for this material are challenging. Thus, the advantages to manufacture complex shapes via 3D printing, such as a spring Figure 6.7 (c) from Ni-Mn-Ga powders, are apparent. Furthermore, the introduction of porosity due to the binder jetting process cannot be replicated by means of forming or traditional molding from molten materials.

7. Sintering of Additive Manufactured Ni-Mn-Ga Parts

Post processing of the additive manufactured parts encompasses the final steps before the 3D printed parts are finished. A critical post-printing step is sintering. Maintaining stoichiometry during any processing of SMA's is necessary in order to preserve functionality [193]–[195]. Moreover, sintering of SMA's, requires sensitive conditions for reducing oxidation that could occur at elevated temperatures [187]. This chapter encompasses the initial sintering attempts towards 3D printed Ni-Mn-Ga, effects on physical properties due to changes in temperature and time of sintering, and numerical modeling of diffusion behavior between Ni-Mn-Ga particulates.

7.1 Initial Attempts and Challenges of Sintering

First attempts of sintering were conducted on 3D printed parts composed of LAr spark eroded powders under high vacuum. Samples in the as-cured state were placed in quartz tube, evacuated to 10^{-5}-10^{-6} Torr later sealed using an oxygen acetylene torch. Evacuation was held while samples experienced temperatures of up to 1373 K (1100 °C). Investigation of the part after the heat treatment by means of SEM revealed nano-structures in the shape of wires and rods on the surface of each particulate with no evidence of sintering, Figure 7.1 (a). Figure 7.1 (b) shows high magnification backscatter electron examination of the nano-wires. Figure 7.1 (c) shows an EDS spectrum from the base of the nano-structure. Figure 7.1 (d) shows an EDS spectrum taken from the tip of the nano-structure. The results from EDS analysis of Figure 7.1 (c) and (d) imply the base of the nano-structure is an oxide phase of manganese and the metallic tip, in area D, is comprised of a Ni-based alloy in the form of a nano-particle. In order to verify these findings, XRD patterns were taken from the sample in attempts to determine the exact phase of the nano-structures. XRD (Bruker AXS X8 Prospector) patterns reveal the presence of two distinct phases: manganosite (MnO) and a highly Mn deficient phase of Ni-Mn-Ga, Figure 7.2. Based on the findings from EDS, it is possible that the Ni based metallic tip of the nano-oxide rod could be acting as a catalyst, promoting the growth of the nano-structures.

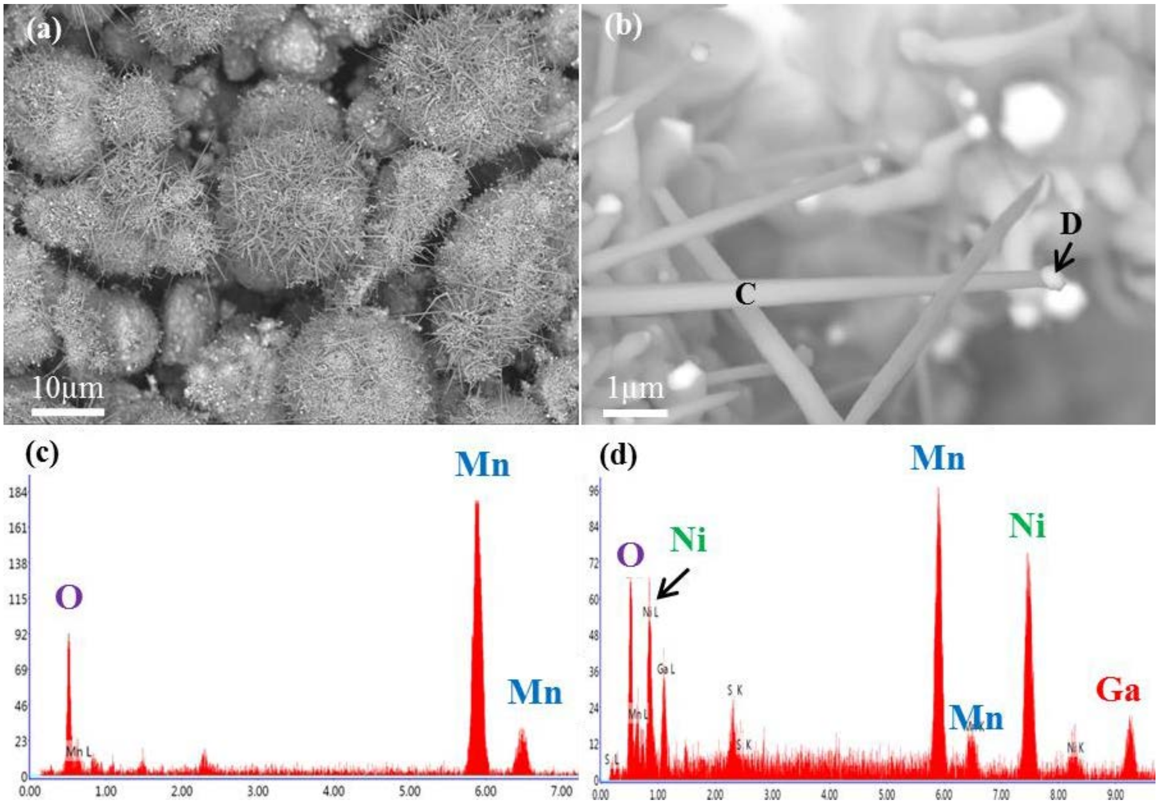

Figure 7.1: (a) BSE image of LAr spark eroded Ni-Mn-Ga powders with surface nanostructures; (b) BSE image of nanostructures; (c) EDS spectrum from the base of the nano-structure (region C); (d) EDS spectrum collected from the tip of the nano-structure (region D).

The XRD patterns indicate specific details about diffusion mechanisms for vacuum sintering conditions. The diffraction patterns point to a transformation within the Ni-Mn-Ga material during sintering. It appears Mn, in the Ni-Mn-Ga system, diffuses outward towards the surface, in order to oxidize. This oxidation behavior implies the existence of oxygen as a partial pressure in the evacuated quartz during the sintering process. The oxidation of Mn is most evident because it is thermodynamically favored over Ni and Ga [196], [197]. Moreover, certain phases in manganese-oxygen systems are favored thermodynamically, such as Mn_3O_4 and MnO_2. Therefore, the existence of MnO points towards oxygen being the limiting factor in this reaction. The fact that sintering was conducted in a high vacuum, agrees with this hypothesis, most likely due to oxygens' existence as a partial pressure. However, the oxidation states in Ni-Mn-Ga alloys drastically effect the shape memory effect as well as martensitic transformation temperatures [198]. In particular, oxidation of Ni-Mn-Ga systems can inhibit shape memory effect, lower magnetic saturation values, and prevent kinetics between the intermetallics [199]–[201].

The oxidation behavior in Ni-Mn-Ga was empirically hypothesized above, stating that Mn diffuses outward from the material allowing it to oxidize. In order to support this hypothesis, a piece of bulk Ni-Mn-Ga ingot was heated to 1273 K (1000 °C) in atmospheric conditions for 24 h. The ingot was then cooled to room temperature, polished using methodologies discussed in section 4.5.2.2, and analyzed via SEM. When the ingot was recovered from the furnace, it was apparent a heavy oxidized layer was present and coated the entire surface of the ingot. This layer was extremely brittle, and easy to remove from the base material. After removal, both the oxide layer and the polished ingot were examined via SEM and EDS. A SE micrograph of the oxide layer can be seen in Figure 7.3 (c) while the polished ingot is displayed in Figure 7.3 (d).

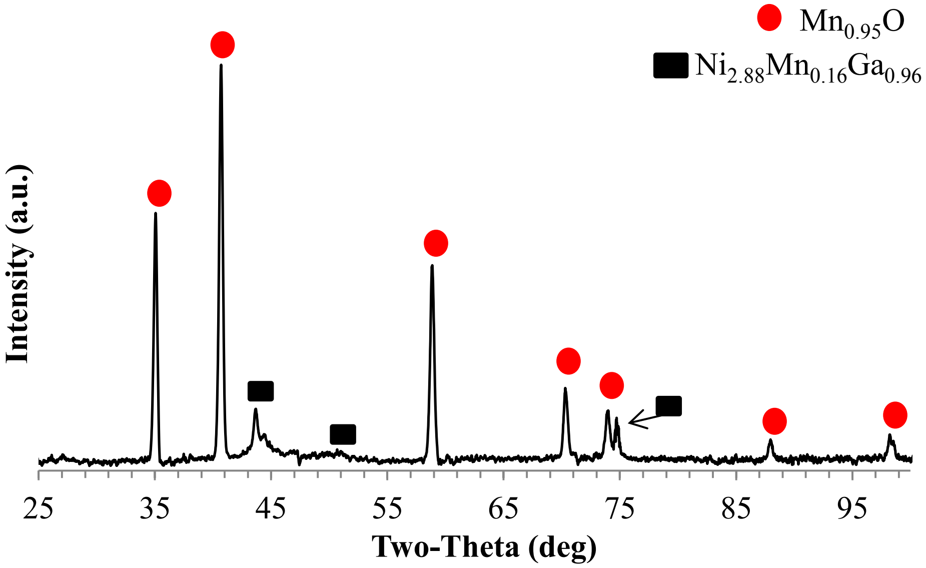

Figure 7.2: XRD pattern of 3D printed LAr spark eroded Ni-Mn-Ga powders after sintering in vacuum.

A schematic illustration is shown to depict the oxide layer and Ni-Mn-Ga ingot after oxidation, Figure 7.3 (a) and (b). It can be easily observed the oxide layer has an approximate thickness of 100 µm, Figure 7.3 (c). Moreover, the morphology of the top and bottom of this layer vary considerably. The change in morphology could however be related to the change of chemical composition. To confirm this, EDS line scan covering the 100 µm thick layer was captured, Figure 7.3 (e). The line scan reveals the presence of manganese-oxide, in an unknown phase. Similar oxidation studies on Ni-Mn-Ga alloys point towards the Mn-O phase possessing one of Mn_3O_4 or MnO_2 [187], [202]. Furthermore, throughout the scan oxygen content appears to fluctuate. This behavior is observed until the latter portion of the scan, where a steady decrease in oxygen and slight increase in Ga is detected.

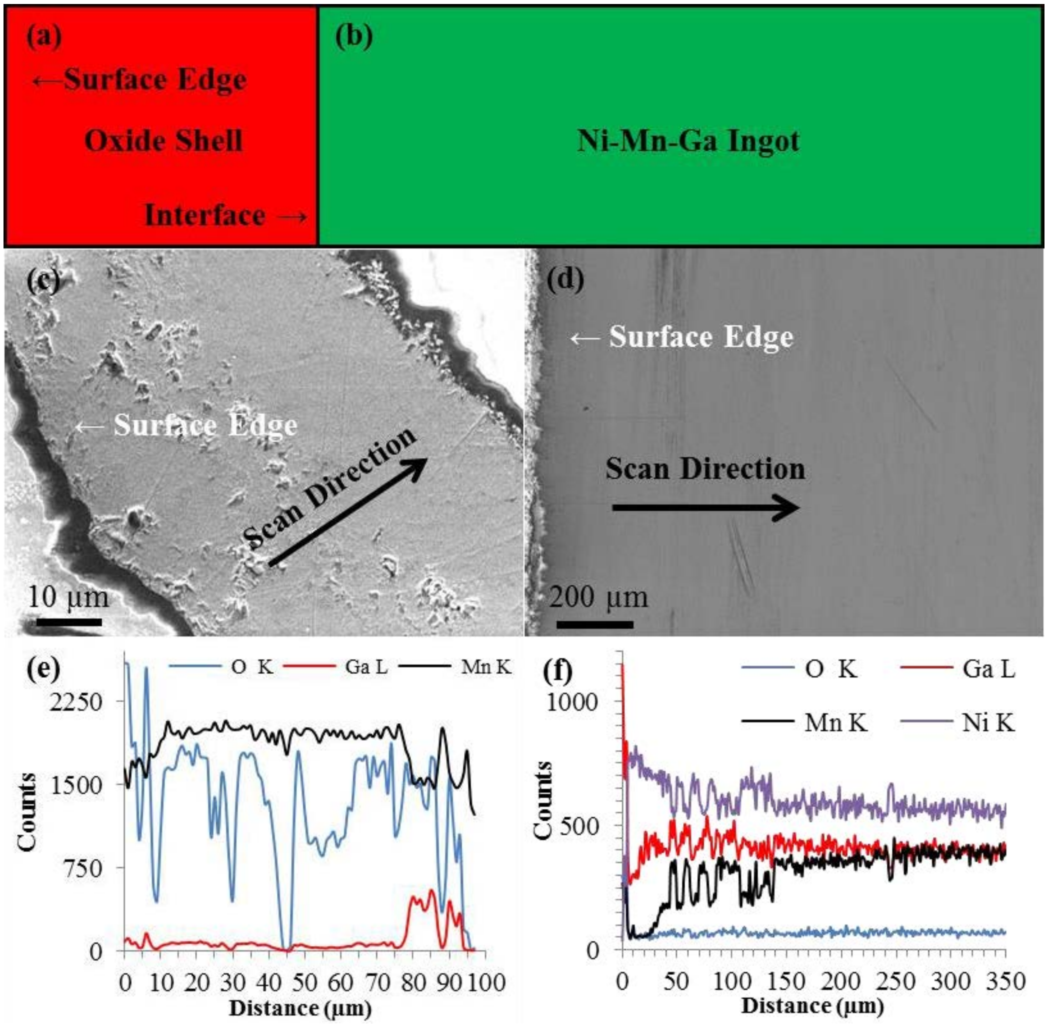

Figure 7.3: Schematic representation of (a) the oxide layer and (b) Ni-Mn-Ga ingot after oxidation. (c) SE micrograph from the cross-sectioned oxide layer; (d) Se micrograph of the cross-sectioned Ni-Mn-Ga ingot core after controlled oxidation; (e), (f) EDS line scans from the cross-sectioned oxide layer and ingot recorded along the scan direction shown in (c) and (d), respectively.

An additional EDS line scan was taken from the polished ingot. The line scan results, which begin at the surface edge, are displayed in Figure 7.3 (d). The line scan represents the composition of approximately 350 µm of material. The first 10 µm of the scan indicate large deviations in composition of the ingot. Initially, large counts of manganese and oxygen were detected, followed by a sudden increase in gallium content with consequent decreases in manganese and oxygen. This behavior continues until approximately 25 µm into the ingot. At the depth of 25 µm the oxygen content reduces to negligible amounts. Moreover, between 25 – 75 µm the counts of manganese gradually increase to a stable amount, around 100 µm. This behavior suggests manganese content between 25 – 75 µm is deficient. Notably, this is in agreement with the aforementioned hypothesis in regard to manganese diffusion mechanisms. Moreover, deviations occur between 0 – 75 µm; which in most cases, is the approximate size of most Ni-Mn-Ga particles used for printing, Figure 5.8. Thus, if the printed Ni-Mn-Ga components experience any partial pressure of oxygen during sintering, the entire part would be compromised.

In addition, Ni and Ga content remain constant for depths > 25 µm. Unexpectedly Ga showed increased counts from the beginning of the scan to approximately 25 µm. This could point towards Ga having increased mobility during high temperatures in Ni-Mn-Ga materials. In fact, the illusiveness of Ga in the Ni-Mn-Ga modulated structures have been discussed in particular reports [203]–[205]. In fact, the atomic position of Ga in Ni-Mn-Ga is still being investigated.

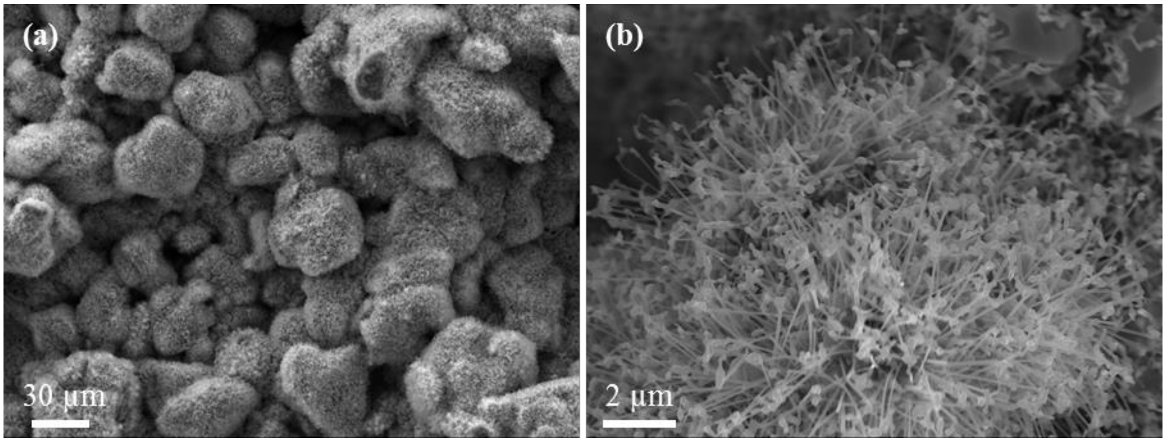

Figure 7.4: (a) SE image of ball milled Ni-Mn-Ga powders covered with TiO nano-structures; (b) High magnification SEM image of the nano-wires formed on the powders during sintering.

Nevertheless, attempts to amend the formation of the nano-structures while maintaining stoichiometry is the focus and goal of sintering Ni-Mn-Ga 3D printed components. Moreover, attempts to amend the oxidation of manganese during sintering of 3D printed parts came with using a titanium getter. Titanium is well known for the oxidation states present in temperatures ranging 673 K - 1173 K (400 °C – 900 °C) at atmospheric pressure [206]. Oxygen diffusion into titanium occurs at lower temperatures when compared to manganese oxides; at low oxygen partial pressures [207], [208]. The presence of titanium as a getter showed inconsistent results. Instances when titanium was present during sintering resulted in successful diffusion between particles as well as similar nano-structure rod-like growth on particulate surfaces. Figure 7.4 (a) shows a secondary electron image of ball milled powders sintered with a titanium getter. The nano-structures can be seen more clearly in Figure 7.4 (b). EDS confirmed the nano-structures belonged to a phase of TiO. Similar to the MnO nano-structures, the TiO nano-structures shown in Figure 7.4 possess a nano-particle at the top of each structure. In a similar fashion, the top and bottoms of the nano-structures were analyzed via EDS. The results show similar characteristics of oxide nano-structures stemming from particulate material and at the top of each, a Ni-based nano-particle.

The formation of Ti-based nano-structures when sintering in the presence of a titanium getter supports the hypothesis of the presence of oxygen as partial pressures in the evacuated quartz. In order to reduce oxygen presence in the evacuated quartz, argon was back filled after evacuation. The evacuation and back filling process was repeated several times for each sintering instance. The evacuation, purging and sealing of the samples in quartz was done using a custom built experimental set up, Figure 7.5. This set up allows for two sized quartz tubes to be prepared for sintering, with inner diameters of 6 and 12 mm. This process begins with the loading of the Ni-Mn-Ga sample into a quartz tube, with one end sealed. The tube is then placed into a vacuum hose, which is then evacuated using a roughing pump (~10^{-2}-10^{-3} Torr). The vacuum is left to run for approximately 15 minutes, then backfilled with ultra-high purity (UHP) argon gas for 5 minutes and repeated several times. Afterwards the tube is left with approximately atmospheric pressure of argon and sealed via oxygen acetylene torch. The tube containing Ni-Mn-Ga samples is next placed in the furnace to be sintered. Sintering temperature for Ni-Mn-Ga powders vary depending on physical properties, such as morphology and chemical composition. Ni-Mn-Ga powders have been found to have an optimum sintering temperature between 1273 K (1000 °C) and 1373 K (1100 °C).

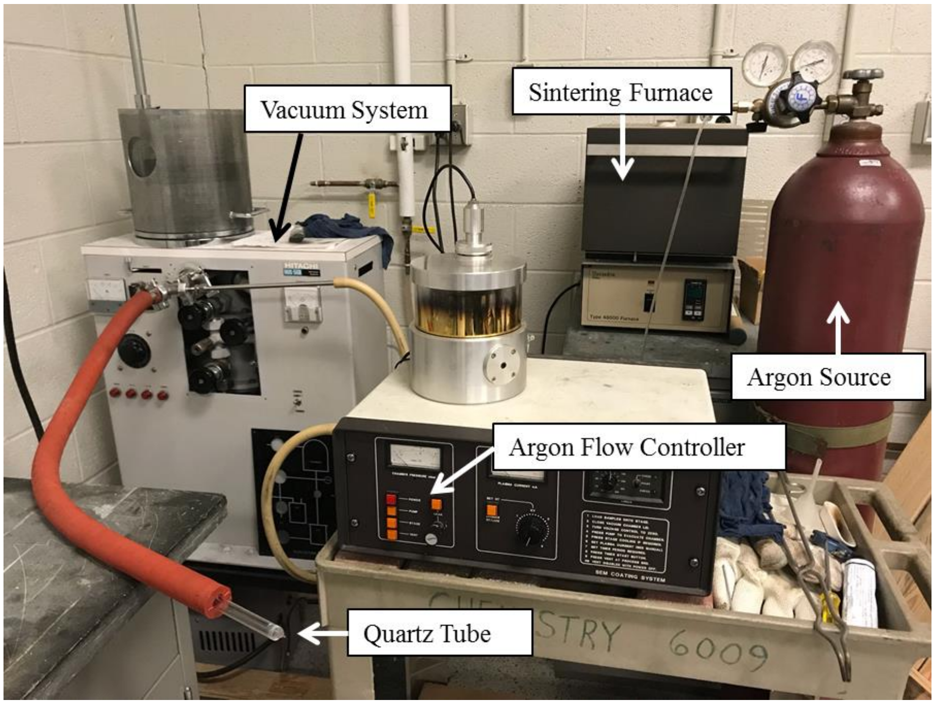

Figure 7.5: Custom built experimental set up for sintering of 3D printed Ni-Mn-Ga samples.

The usage of high purity argon purging method, substantially reduced oxygen from the sintering atmosphere, and produces well sintered, compact parts. Figure 7.6 (a) shows a sintered rod of ball milled particles using the above mentioned sintering conditions. Arrows indicate the existence of individual layers after sintering, a typical morphology observed in the binder jetted parts. Figure 7.6 (b) and (c) show sintered LN_2 and LAr powders using the same sintering conditions. Arrows in (b) and (c) indicate sintering necks. Figure 7.6 (d) show the sintered microstructure of BM parts.

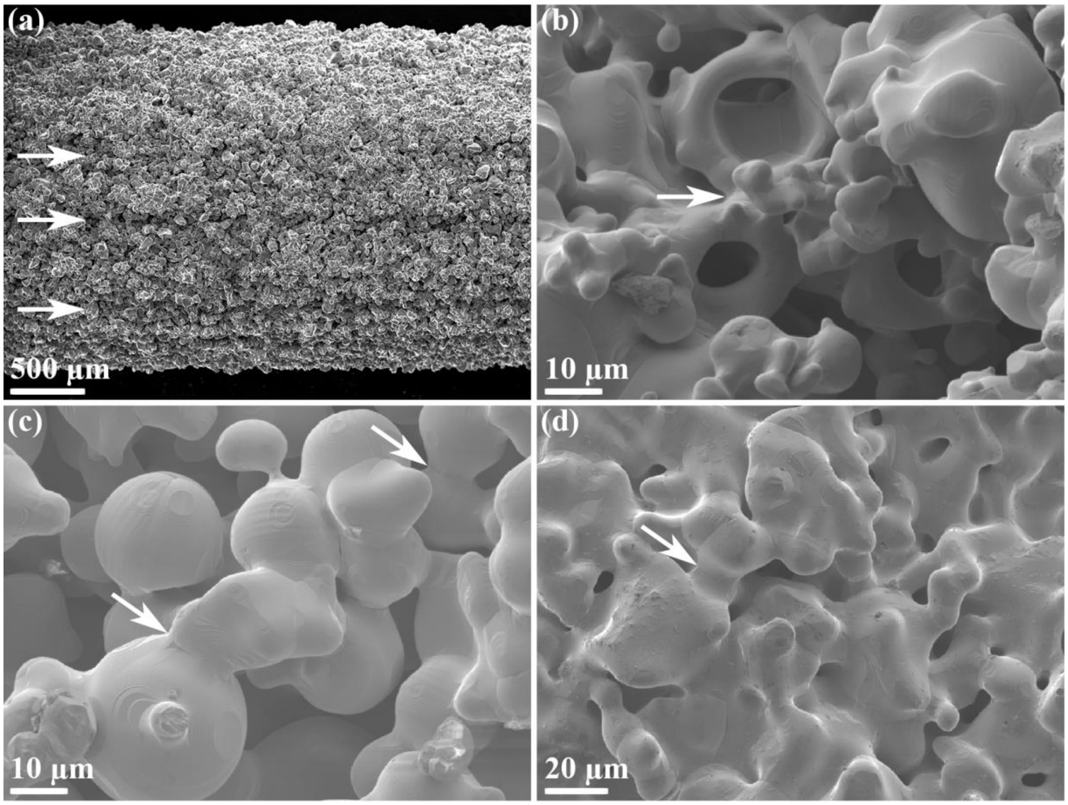

Figure 7.6: Secondary electron images of sintered Ni-Mn-Ga parts made from (a) ball milled powders, (b) LAr powders, (c) LN_2 Powders and (d) BM powders.

Figure 7.7 (a) shows the BSE micrograph from the surface of the sintered part obtained from LN_2 powders. The body of sintered spherical particles shows homogeneous composition, while the foam-like shell made of agglomerated sub-micron and nanoscale particles shows inhomogeneous composition, as indicated by the BSE contrast. In order to assess the differences in chemical composition, EDS spectra were recorded from area C and B in Figure 7.7 (a). It was revealed, that the foam-like material possesses more manganese, in substitute of Ga, after sintering, Figure 7.7 (b). The chemical composition of area C retains the expected near stoichiometric Ni_2MnGa composition. There are no recordings of segregation observed via BSE investigation for

LAr and BM material. Recall, the irregular shaped material was pulverized during mechanical separation in the case of LAr powder.

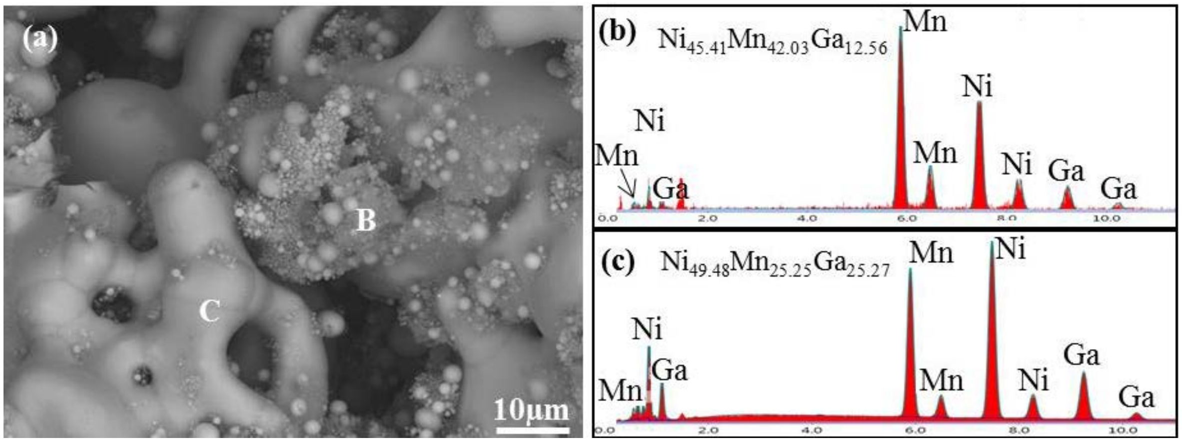

Figure 7.7: (a) Backscatter electron (BSE) micrograph of sintered LN_2; (b), (c) EDS spectra from areas B and C in (a), indicating different compositions.

The sintered microstructure is clearly distinguishable, since particles are necked together in such a way, forming localized agglomerates. Another notable feature of the microstructure is the porosity in the case of 3D printed and sintered Ni-Mn-Ga samples. This porosity is also observed in Figure 7.8 (a) to (d) where several sintered parts are presented.

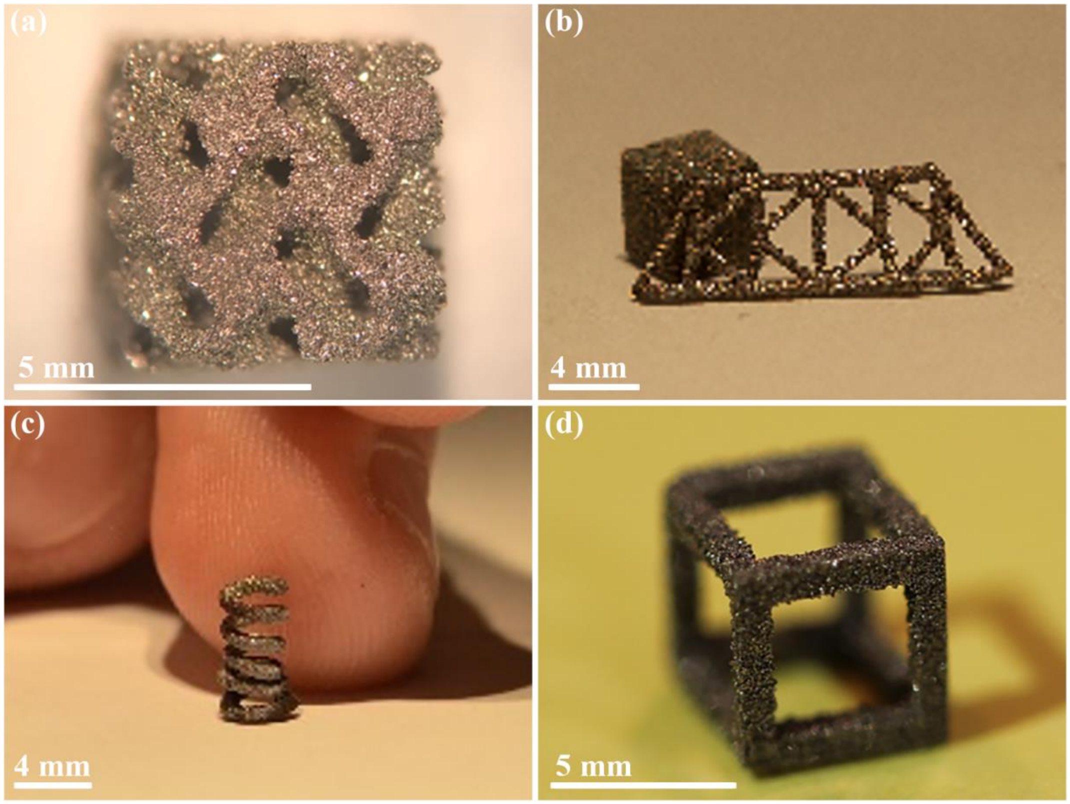

Figure 7.8: Sintered net shape parts made by binder jetting from ball milled Ni-Mn-Ga powders.

7.2 Investigation of Sintered Microstructures

7.2.1 X-Ray Diffraction

In the present work, through AM and post processing, fused metallic parts with pre-determined geometries have been produced from Ni-Mn-Ga powders. The question is: did the sintered material transform reversibly from a high temperature phase to a low temperature one (martensitic transformation)? As mentioned above the reversible martensitic transformation is a necessary condition for the existence of SME. Therefore, it is necessary to assess both the existence of martensite in the sintered part, as well as its reversible martensitic behavior. As reported in literature [145], [209], [210] the Ni_2MnGa Heusler structure shows martensitic transformation behavior. In order to assess the existence of Ni_2MnGa Heusler phase in sintered parts, XRD investigation was performed (Bruker AXS X8 Prospector). XRD measurements were carried out between $2\theta = 20° - 90°$. Figure 7.9 (a) shows the XRD patterns of as-sparked LN_2 powders and after sintering. Diffraction patterns collected for as sparked LN_2 powders are comparable to a Ni_2MnGa phase with amorphous/nano-crystalline features due to the broad nature of the peaks, specifically at 85° [20], [21]. In addition, an undesired phase such as $Ni_{13}Ga_9$ is also presents the in as-sparked powders. The existence of this phase is most likely due to incomplete mixing within the solid solution during fast quenching of spark-eroded material. These constituent phases are thought to diffuse into the matrix material upon sintering. Thus, after sintering the LN_2 parts show diffraction patterns that match a Ni_2MnGa orthorhombic Heusler phase with incommensurate 5M modulation. The martensitic transformation temperature (T_{Mf}) for this particular LN_2 occurs at 270 K (-3 °C). For this, sintered LN_2 parts were cooled to 200 K to ensure the martensitic phase was present during investigation. Moreover, it can readily be observed the emergence of multiple peaks due to recrystallization. This transition most likely occurs as the result of atomic ordering during sintering. Atomic ordering allows the formation of the martensitic phases by ultimately reducing internal stresses imposed on the lattice caused by rapid quenching during the spark erosion process.

Diffraction patterns collected from as-sparked LAr powders show the possible existence of two phases: $Ni_{2.25}Mn_{0.75}Ga$ and β-manganese, Figure 7.9 (b). XRD patterns also imply the LAr as sparked powders possess amorphous/nano-crystallinity, due to the existence of broad peaks. Moreover, the phases identified indicate one Ni-Mn-Ga phase deficient in manganese. Upon the sintering of LAr parts, the diffraction pattern closely resembles a $Ni_{2.12}Mn_{0.84}Ga$ phase, concluding some of the β-manganese diffused into the matrix material during the sintering process. This near stoichiometric Ni_2MnGa phase is known for possessing a tetragonal crystal structure, and subsequently a non-modulated (NM) martensite. These XRD patterns were taken after mechanical separation process, described in section 5.2. Furthermore, the irregular shaped material removed during the mechanical separation contained more manganese, inherently removing considerable amounts of manganese from the LAr powder system. This statement is in agreement with the above-mentioned phases indexed for LAr material before and after sintering, being manganese deficient, compared to the Ni_2MnGa Heusler phase.

Figure 7.9 (c) shows XRD patterns from ball milled powders and sintered parts. Powders produced by ball milling show patterns with characteristic peaks of a slightly rich Mn phase of the Heusler alloy, $Ni_2Mn_{1.15}Ga_{0.85}$. The sintered part also shows a slight Mn rich phase, $Ni_2Mn_{1.05}Ga_{0.95}$. Furthermore, the XRD patterns were additionally examined to determine the martensite types. The martensite types were determined based on the c/a ratios, where c and a are the lattice parameters with respect to the crystal structure. The lattice parameters have been obtained as a result of X-ray diffraction. The sintered parts comprised of LN_2 powders have $c/a<1$, which shows possible existence of 5M martensite type. A $c/a>1$ found in parts made of LAr powders indicates a NM martensite. Parts made of ball milled powders retain dimensions of $c/a<1$, that indicates a 5M martensite type. It is well known that 5M and NM martensitic phases demonstrate reversible martensitic transformations and SME's [129], [209].

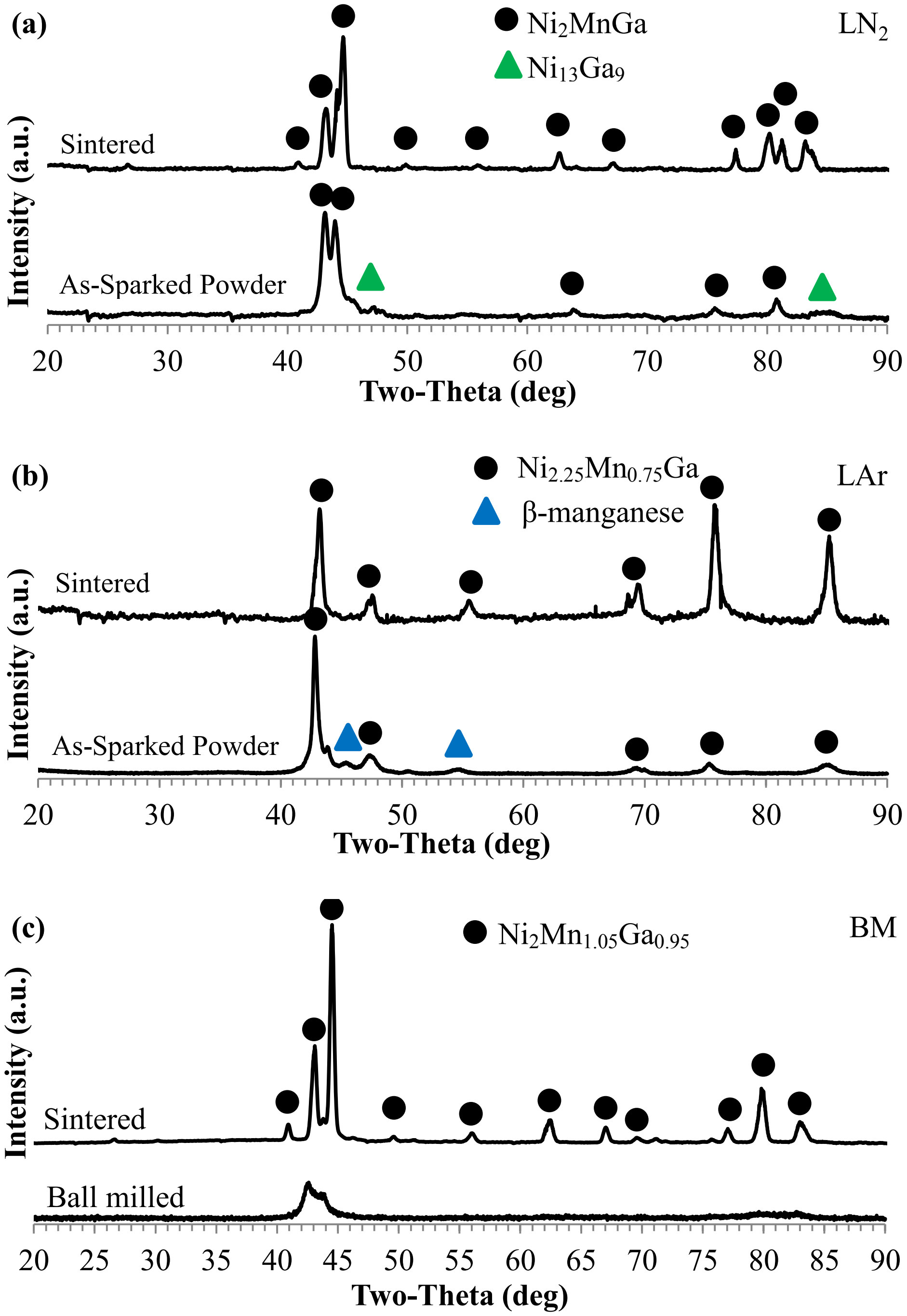

Figure 7.9: X-ray diffraction patterns from powders (bottom) and corresponding 3D printed and sintered part (top) for materials prepared from (a) spark-eroded LN_2; (b) spark-eroded LAr, and (c) ball milled powders.

Concluding the investigation of the powder and sintered microstructures for Ni-Mn-Ga material, it is shown all three types of powders/sintered parts possess a phase known for producing reversible martensitic transformations.

7.2.2 Microstructure Investigation via Electron Microscopy

The martensitic phase has a specific morphology, composed of twin variants which are visible using many imaging techniques. An example of the martensitic morphology is shown in Figure 4.12. Therefore, the existence of martensite can be also proved by microscopy investigations. The microstructural examination of sintered parts made of LAr powders was done using focus ion beam and scanning electron microscopy technique. The top of two sintered particles were ion milled in the JEOL JIB-4500 FIB/SEM multi-beam system in order to cross-section the sample and investigate martensite morphology at the two particle interface. Figure 7.10 (a) and (b) shows the low magnification and high magnification image of sintered dual particle interface, respectively. Martensitic twins appear visible due to ion channeling contrast. In the case of sintered LAr Ni-Mn-Ga particles, twin martensitic morphology is observed, as well as individual grains, as indicated by the arrow in Figure 7.10 (a). The existence of additional grain boundaries indicates the sintered material is polycrystalline.

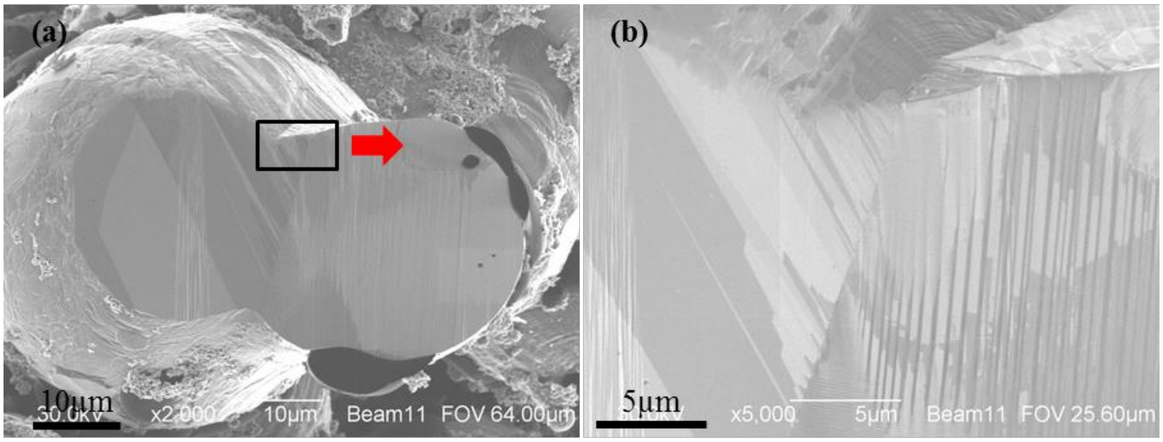

Figure 7.10: Secondary ion images of: (a) low magnification sintered cross sectioned LAr particles; (b) high magnification of the area marked in (a).

To further investigate the existence of martensite in the sintered parts, TEM investigation of the sintered material was performed. Figure 7.11 (a) and (b) shows dark field (DF) transmission electron microscopy (TEM) images of the Ni-Mn-Ga lamella obtained by FIB. Typical martensite morphology, containing twins can be observed, which concludes the existence of martensite. Upon further investigation, using selected area electron diffraction patterns (SADP), Figure 7.11 (d), indicates a non-modulated (NM) martensite. The observed NM martensite agrees with the data obtained from XRD. However, near stoichiometric Ni_2MnGa Heusler structures are known for possessing commensurate and incommensurate modulations in martensitic phases [128].

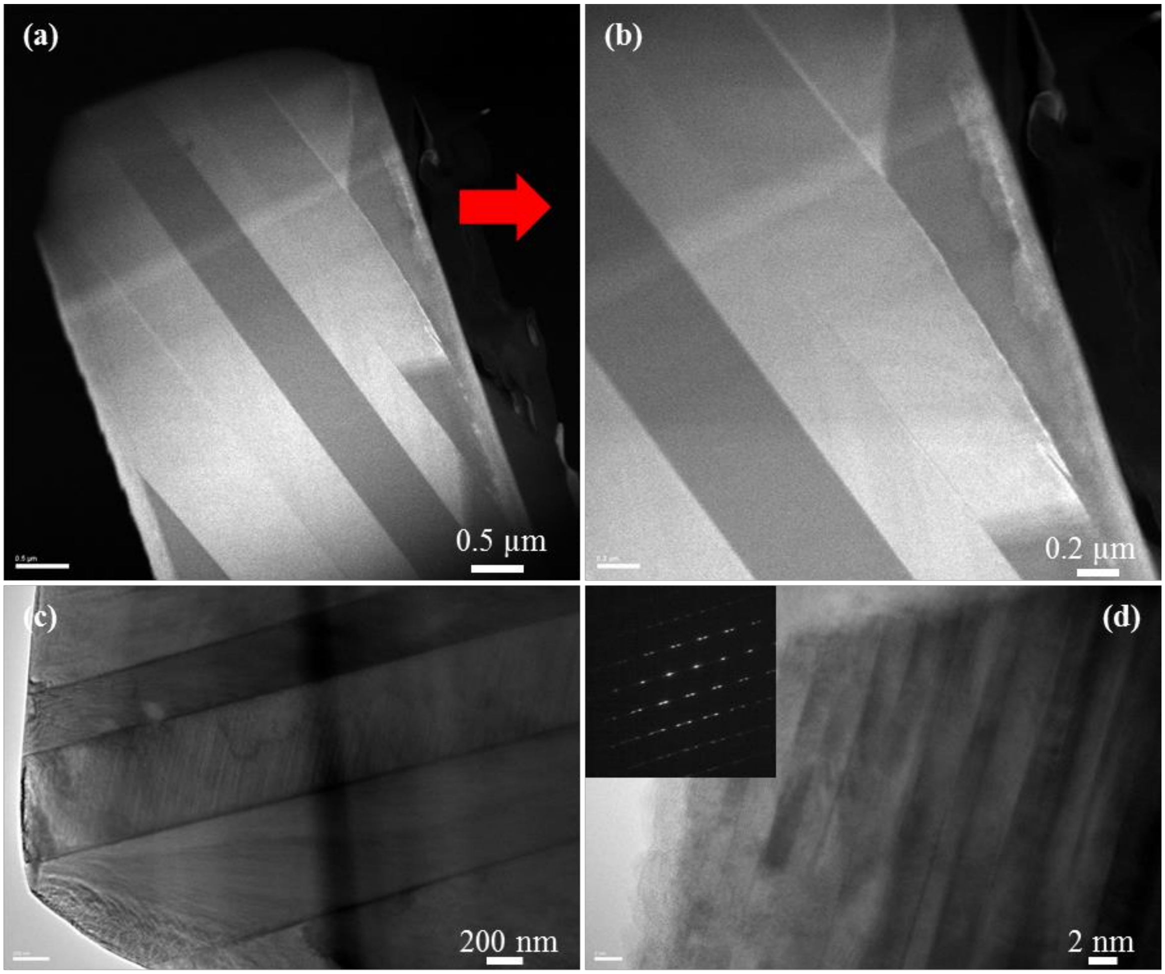

Figure 7.11: (a) DF-STEM image of sintered LAr Ni-Mn-Ga; (b) A close up of (a) displaying twin boundaries; (c) BF-TEM micrograph of twin variants; (d) High magnification TEM micrograph from one of the twins in (c) with corresponding SADP.

Additional exploration of the LAr Ni-Mn-Ga lamella revealed the existence of phase segregation. Figure 7.12 (a) which shows a DF-TEM micrograph of the sintered material microstructure and indicated by the red circle, which is the segregation observed in the microstructure. EDS was used to determine the chemical composition of the individual grain; that was revealed to possess primarily manganese Figure 7.12 (b). This observation supports the claims of atomic micro-segregation, especially in the case of manganese. This is important for future discussion of sintered LAr properties. Similar TEM investigation was attempted with a sintered part from LN_2 particles. However, it was exceptionally difficult to process the TEM lamella due to the hollow morphology. Microstructural TEM investigation on parts produced from ball milled powders were not attempted or investigated, only SEM/EDS investigation was done for this material.

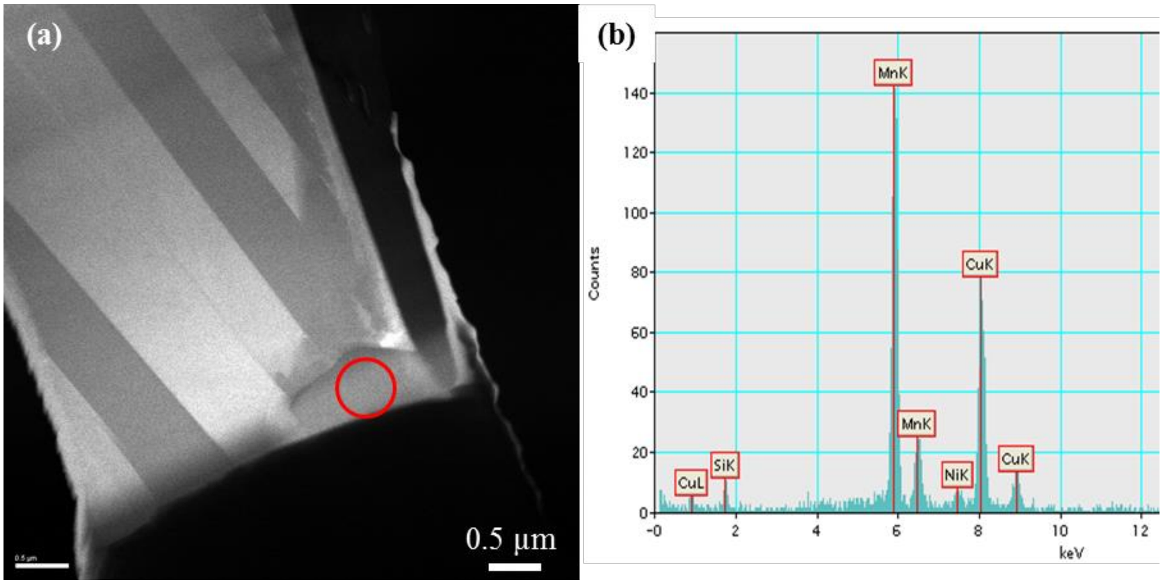

Figure 7.12: (a) DF-TEM images of sintered LAr Ni-Mn-Ga indicating (red circle) an inhomogeneity in the microstructure; (b) EDS spectrum from the material segregation.

7.2.3 Thermal Analysis

Based on XRD and EM investigations we can conclude that martensite is present in sintered parts. In order to prove the reversible behavior of martensitic transformation in 3D printed parts, DSC experiments were performed using a Perkin Elmer Diamond DSC. DSC curves of sintered LN_2, LAr, and ball milled Ni-Mn-Ga 3D printed parts are shown in Figure 7.13. Endothermic reactions are displayed up while exothermic reactions are down. Each sample was thermally cycled in the DSC several times to verify the martensitic transformation was reversible. The transformation temperatures measured for the sintered 3DP LN_2 parts reveal the austenitic start temperature (T_{As}) to be approximately 282 K and the austenitic finish temperature (T_{Af}) 290 K. The martensitic start temperature (T_{Ms}) is 279 K while the martensitic finish (T_{Mf}) is 268 K. The Curie point was determined to occur at 380 K. In the case of sintered LAr 3DP part temperatures are T_{As} = 355 K, T_{Af} = 376 K, TM_s = 363 K, T_{Mf} = 341 K, while for the parts made of ball milled (BM) powders the transformation temperatures are T_{As} = 318 K, T_{Af} = 338 K, T_{Ms} = 307 K, and T_{Mf} = 289 K, respectively. Paramagnetic transformation temperature for ball milled parts occurs at 390 K. The Curie temperature was not observed in the case of sintered parts made of LAr powders due to an austenite transformation temperature near the Curie point. The broad behavior of the peaks in the martensitic-austenite transformations of sintered LAr powders can be ascribed by micro-segregation [128]. The strong change in transformation temperatures between parts made of LN_2 and LAr powders can be explained as compositional effects with respect to martensitic-austenite transformation temperatures [121], [211]. As reported by Wu & Yang [121], changes in Mn content do not disturb transformation temperatures significantly; albeit changes in Ni and Ga have strong influences on transformation temperatures.

Here, the reversible martensitic transformation in sintered 3D printed Ni-Mn-Ga components is confirmed, Figure 7.13. However, the thermo-physical properties tend to vary from sample to sample. Moreover, the DSC can provide more information about phase transformations. These variations and thermal properties will be elaborated upon in subsequent sections.

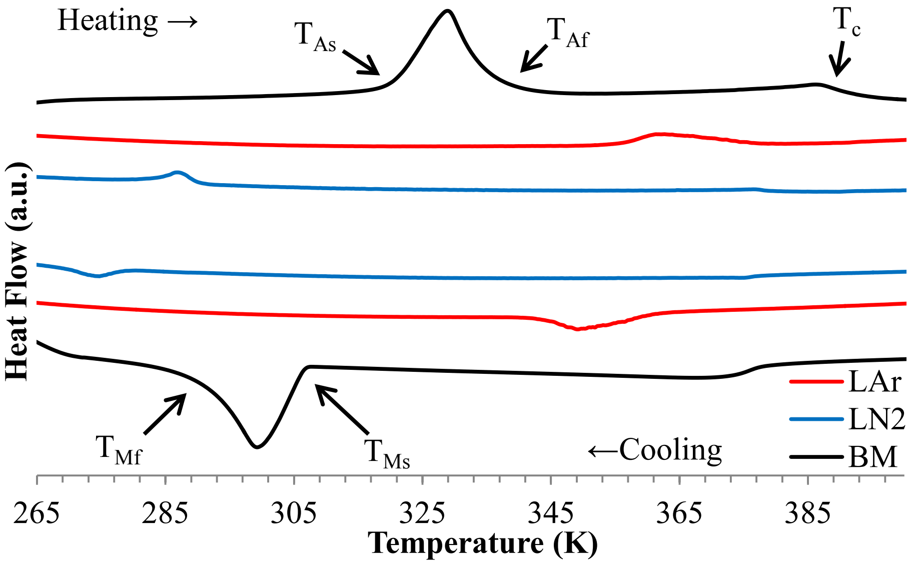

Figure 7.13: DSC curves of sintered Ni-Mn-Ga parts made from LAr (red) LN_2 (blue), and BM (black) powders. T_{As} and T_{Af} are the austenitic start and finish temperatures; T_{Ms} and T_{Mf}, are the martensitic start and finish temperatures; T_c is the Curie temperature.

7.3 Isothermal Sintering Effects on Additive Manufactured Ni-Mn-Ga Shape Memory Alloys: A Microstructure and Thermal Analysis

This subchapter examines the effects on the microstructure, chemical composition, and thermo-physical properties as an outcome of isothermal sintering conditions for 3D printed parts comprised of BM powders. Insufficient quantities of spark eroded powders prohibited these studies for LAr and LN_2 material. In this study, high purity elements of Ni (99.9 at %), Mn (99.9 at %), and Ga (99.9 at %) (Alfa Aesar) were arc melted to produce $Ni_{49.73}Mn_{29.03}Ga_{21.24}$ alloys. These alloys were crushed and re-melted several times then homogenized at 1273 K for 24 h. The homogenized ingots were then ball milled for 1 h using zirconia balls. The result of the ball milling produces micro-meter sized pre-alloyed Ni-Mn-Ga powders, which were used in the binder jetting additive manufacturing (AM) process. The printing parameters used were 110 μm layer thickness, 110 % binder saturation, and 1.5 mm/s speed of layer deposition. Cylindrical components of approximately 3 mm in diameter and 50 mm in length were printed and cured at 463 K for 4 h. The entire manufacturing process is illustrated in Figure 7.14.

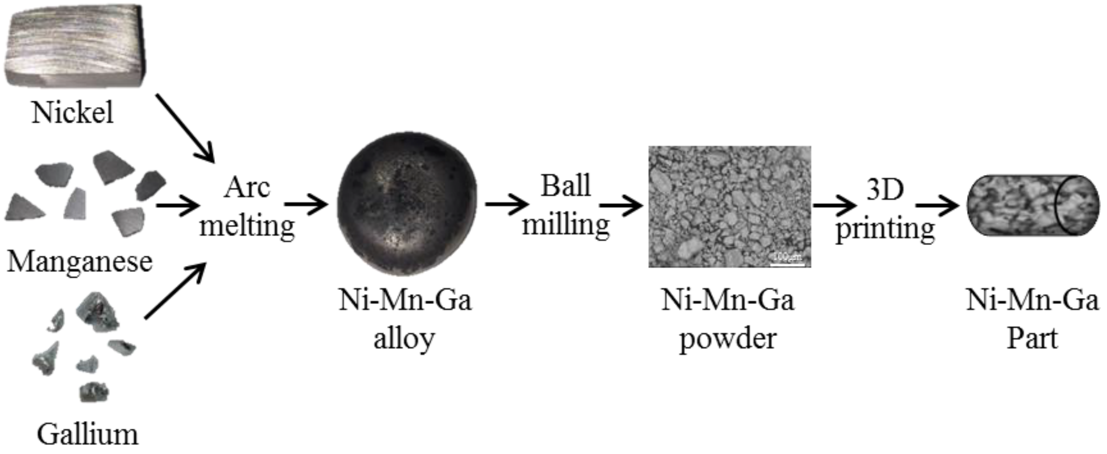

Figure 7.14: Flow chart displaying the manufacturing process of porous AM Ni-Mn-Ga parts.

The cured components were sectioned into five cylindrical shaped pieces with approximate lengths of 10 mm. These sectioned cylinders were encapsulated in quartz tube which had been evacuated and purged with high purity argon several times. These samples were then sintered at 1353 K for 10, 20, 30, 40, and 50 h. Post sintering, sample densities were calculated using mass and volume measurements, using techniques described previously in chapter 4. Afterwards, samples were cut and embedded in cold mount epoxy and mechanically polished concluded by vibration polishing with colloidal silica (0.06 μm) for two hours. The polished samples were then carbon coated for microstructural and chemical analysis using a JEOL JSM-7600F FESEM, equipped with EDAX Octane EDS silicon drift detector. Crystallographic phase identification was done using a Bruker Prospector CCD diffractometer with copper micro-source X-ray tube at room temperature. Thermal analysis was done using a Perkin Elmer Diamond (DSC) at a rate of 10° K/min.

7.3.1 Microstructure Analysis

The volume and density of the AM Ni-Mn-Ga parts were characterized before and after sintering. Figure 7.15 (a) displays the average measured volumes for AM Ni-Mn-Ga cylindrical samples as a function of sintering time. Average volumes are based on five measurements recorded from each sample. Figure 7.15 (a) exhibits an apparent decrease in volume after the heat treatment, indicating a densification during the sintering process. The decrease in volume is a result from solid state sintering, which causes consolidation of metallic particles. This consolidation subsequently decreases part volume while inherently increasing part density. The part densities were quantified by measuring the mass and dividing the volume. These densities were then divided by the calculated density of each sample based on atomic composition, Equation 6.1, to obtain a density percentage. These density percentages are shown in Figure 7.15 (b). The average green part density was shown to be approximately 3.48 g/cm^3 (~45.9 %). Post sintering, the density was shown to increase with time. This sintering behavior has been studied previously [75], [212], in which similar results were reported. The calculated densities for Ni-Mn-Ga parts sintered between 10 h and 50 h are listed in Table 7.1.

Table 7.1: Density measurements from 3D printed parts from BM powders sintered for 10 h, 20 h, 30 h, 40 h, and 50 h.

Sintering Time	10 h	20 h	30 h	40 h	50 h
Density (g/cm^{3})	5.67	5.90	6.11	6.24	6.35
Percentage Density (%)	74.6	77.6	80.4	82.2	83.6

It has been shown that the MFIS in polycrystalline Ni-Mn-Ga can be increased by introducing porosity to the microstructure [9], [105], [134]. The increase in MFIS in porous polycrystalline Ni-Mn-Ga is due to grain free surfaces that allow twinning dislocations for all variants at low twinning stress [213]. While these studies do not the correlation between porosity and MFIS; this report shows the ability to control porosity based on sintering time. In addition to controlling part porosity, earlier work shows the ability to produce complex geometries with a porous microstructure from pre-alloyed Ni-Mn-Ga powders with the use of AM [183]. Through this, MFIS in 3D printed Ni-Mn-Ga can be investigated as a combination of part porosity and part complexity.

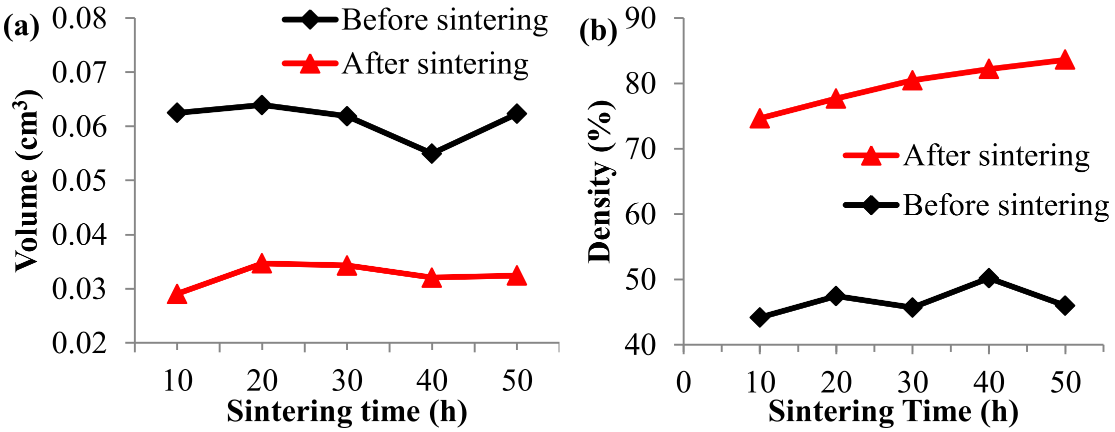

Figure 7.15: (a) Ni-Mn-Ga cylindrical sample volumes before and after sintering; (b) Relative density percentages for respective samples before and after sintering.

The changes in the length and radii of the cylindrical samples have also been investigated and the results are presented in Figure 7.16 (a) and (b), respectively. The linear dimensions of green parts decrease after sintering. Notably, changes in sample length tend to remain fairly constant, while the radii steadily decrease with increasing sintering time.

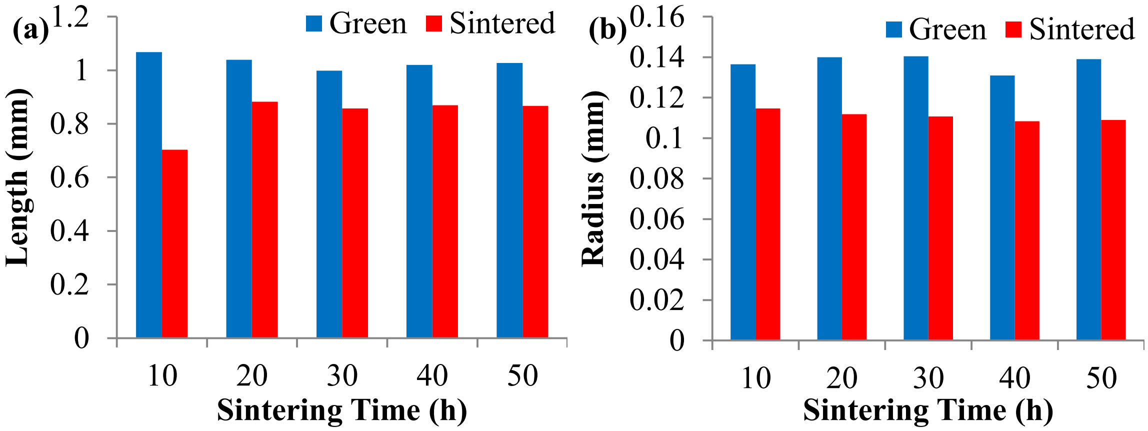

Figure 7.16: The relationship between (a) length and (b) radius for 3D printed Ni-Mn-Ga cylinders in the green and sintered state.

Figure 7.17 (a) to (e) shows SE micrographs of carbon coated polished cross-sectioned Ni-Mn-Ga samples sintered for 10, 20, 30, 40, and 50 h, respectively. As presented, all sintered AM Ni-Mn-Ga samples possess voids. These voids are created in the AM process, due to the prealloyed powder morphology and size distribution. The number of voids in the as printed samples can be classified by the packing density. Powder as well as air occupies a known volume, where the packing density refers to the volume of powder present. A reduction of voids occurs during the sintering process where the primary driving force for diffusion is the differential of chemical potential between particulates. As diffusion occurs, prealloyed powders agglomerate, successively reducing void size. In isothermal conditions, microstructural voids continue to decrease in size over time. This phenomenon is displayed in Figure 7.17 (a) to (e) by the reduction of both number of voids and volume of voids intersecting the cross-section area. For the samples presented in Figure 7.17 (a) to (e) the density increases from approximately 74% to 83% corresponding to the density measurements shown in Table 7.1. It is worth noting, Bai & Williams [75] examined the binder jetting of copper powders investigating part density, sintering time and mechanical strength. Likewise, as sintering time increased, so did part density, as well as ultimate tensile strength. This indicates the strength of AM Ni-Mn-Ga parts could also increase with respect to sintering time, although these properties have not been investigated in this study.

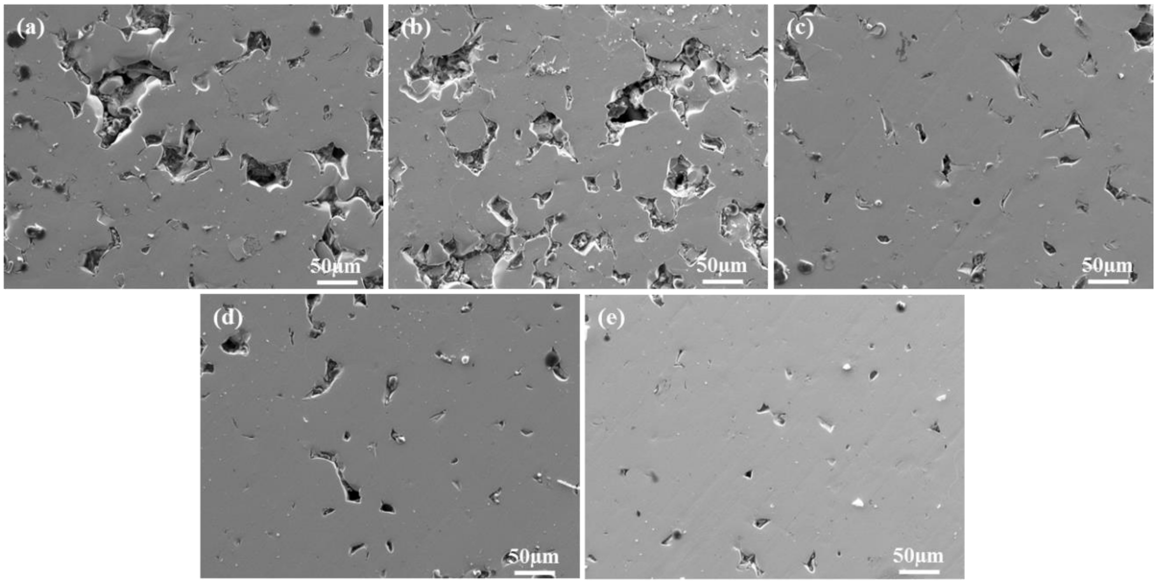

Figure 7.17: SE micrographs of polished cross-sectioned AM Ni-Mn-Ga samples sintered for (a) 10 h, (b) 20 h, (c) 30 h, (d) 40 h, and (e) 50 h.

In order to verify the chemical composition of AM Ni-Mn-Ga samples, quantitative EDS analysis was performed using previously described methods. X-ray spectra were collected for one hundred second intervals from ten randomly selected areas. The average composition and standard deviations from these collections are shown in Table 7.2. The quantitative EDS analysis of the prealloyed Ni-Mn-Ga powder indicates there is a slight Ni rich composition ($Ni_{51.51}Mn_{30.07}Ga_{18.43}$) compared to the starting material ($Ni_{49.73}Mn_{29.03}Ga_{21.24}$). It should be noted, a loss of Ga is observed, and that is substituted by Ni, while Mn remains at a reasonable content. After the printing and sintering processes, the chemical analysis shows reasonable values of approximately $Ni_{50}Mn_{30}Ga_{20}$ in all five AM Ni-Mn-Ga samples, while slight variations are acknowledged.

Table 7.2: Summary of chemical compositions for Ni-Mn-Ga powder and AM cylindrical samples.

	Ni (at %)	Mn (at %)	Ga (at %)
Powders	51.51±1.08	30.07±0.34	18.43±0.96
10 h	49.80±0.43	30.26±0.40	19.93±0.78
20 h	49.45±0.30	30.10±0.30	20.44±0.51
30 h	48.27±0.33	30.26±0.18	21.45±0.48
40 h	49.50±0.28	30.29±0.24	20.15±0.47
50 h	49.82±0.32	30.29±0.33	19.87±0.51

When the sintered parts are compared to the powder used to manufacture the samples, a loss of Ni is observed. It is possible during the sintering process; Ni diffuses throughout the material, inherently creating a more homogenous chemical composition. While this has not been proven, it is postulated based on the results from Table 7.2. On the other hand, Mn is observed to hold equally constant throughout the entire AM process. This behavior contradicts the oxidation behavior of Ni-Mn-Ga related alloys, as Mn is very reactive with oxygen at low partial pressures [187], and previously discussed.

As a result of this, a drop in Mn content is often observed in Ni-Mn-Ga alloys after heat treating processes. Also, Ga concentration fluctuation is expected, due to high vapor pressure, as reported by many authors working on the synthesis of Ni-Mn-Ga alloys [214], [215]. Albeit, by means of the sintering process developed in this work, is demonstrates the ability to sinter Ni-Mn-Ga without heavily altering chemical composition.

7.3.2 Phase Analysis via XRD

Figure 7.18 shows the room temperature XRD patterns collected from Ni-Mn-Ga samples, produced by 3D binder jetting printing of BM powders, sintered for time intervals from 10 h to 50 h. For all five samples, the XRD patterns collected at room temperature were indexed considering the martensitic phase, which was confirmed by DSC analysis. Characteristic peaks at 40.8˚, 42.7˚, 43.0˚, and 44.5˚, along with others, indicate the presence of 5M martensitic phases [116]. Additionally, small shifts in peak position were observed between AM samples, indicating lattice parameter variations. In order to address these lattice deviations, the cell of the 5M martensite was adjusted based on peak position for each AM Ni-Mn-Ga sample. These adjusted lattice parameters are displayed in Table 7.3. Crystal volumes and c/a ratios are also shown in Table 7.3. The crystallographic parameters reported in Table 2 are very similar with the ones reported by Righi *et al* [128] indicating that all five AM samples are 5M martensite with either orthorhombic or monoclinic structures.

The unit cell of 5M martensite was initially reported, based on the $L2_1$ lattice of high temperature phase, as body centered cubic with tetragonal distortion, by Richard *et* *al* [126]. This proposed unit cell was later dismissed, as a result of extended 5 M martensite crystal structure investigation [127]–[129]. For instance, Righi *et al* [128] reported a more complex crystal structure of 5 M martensite: the incommensurate 5M modulated martensite is orthorhombic while the commensurate 5M martensite is monoclinic. One method of determining if the 5M martensitic phase is commensurate or incommensurate based on XRD patterns, is to investigate the (202) peak at 62.5˚ [128]. If the 5M martensitic phase is commensurate, the (202) peak will split into two peaks: ($\bar{2}02$) at approximately 62˚, and (202) at approximately 62.5˚. Based on the enlarged XRD spectrum, shown as an insert in Figure 7.18, it can be concluded samples 10 h, 20 h, and 40 h possess a commensurate 5M martensite and samples 30 h and 50 h possess incommensurate martensite at room temperature, respectively. Figure 7.18 inset displays the XRD patterns between 61.5 ° – 63.5 °.

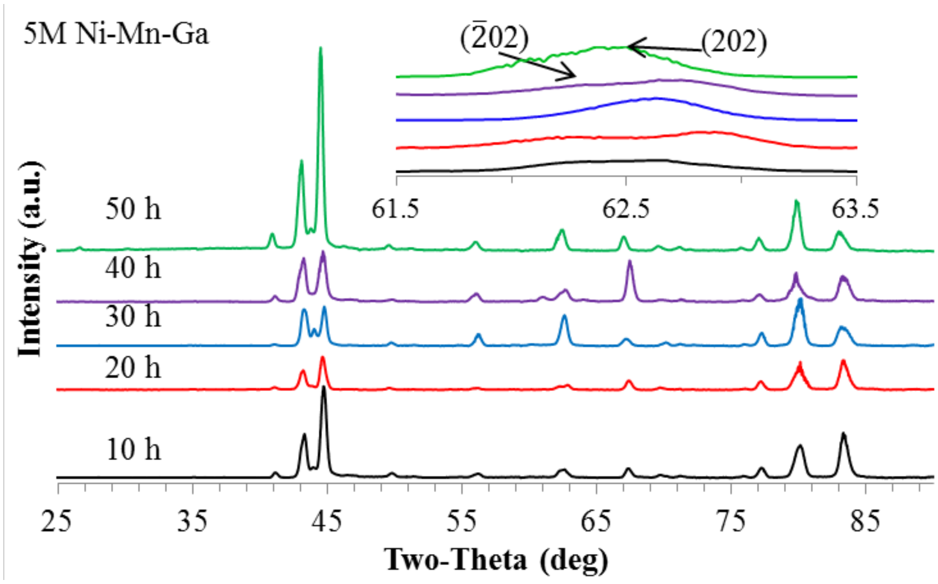

Figure 7.18: XRD patterns collected from AM Ni-Mn-Ga samples sintered for 10, 20, 30, 40, and 50 h.

For Ni-Mn-Ga martensitic systems the magnetic field induced strain (MFIS) values can be theoretically obtained and approximated based on the crystal structure [10], [11], [133], [216]. These reports have concluded for tetragonal, orthorhombic and monoclinic structure in Ni-Mn-Ga martensite the MFIS is approximated by the c/a ratio. In a one-dimensional system, the MFIS can be approximated as ε_{max}= (1-c/a). Additional factors play a role in determining these values. It is critical to possess a c/a<1 or a<b<c lattice parameter relationship [217], [218]. Notably, the lattice parameters reported in Table 7.3 show all five Ni-Mn-Ga samples retain a c/a<1. Generally, the martensite type can be associated with the lattice parameter relationships such that: a NM holds a/c>1, 5M possesses c/a<1 and 7M retains a<b<c [10].

Table 7.3: Lattice parameters, c/a ratios, and crystal unit cell volumes of the 5M martensitic phase in 3D printed and sintered Ni-Mn-Ga parts.

	a (Å)	b (Å)	c (Å)	c/a	volume $Å^3$
10 h	4.23998	5.55884	4.20057	0.99071	99.00479
20 h	4.22662	5.55661	4.19453	0.99241	98.51138
30 h	4.21917	5.52701	4.17125	0.98864	97.27102
40 h	4.21088	5.55005	4.17476	0.99142	97.56662
50 h	4.22282	5.5828	4.20386	0.99551	99.10667

7.3.3 Thermal Analysis using DSC

For the sake of evaluating reversible martensitic transformation temperatures, each Ni-Mn-Ga sample was thermally cycled several times using DSC techniques. Figure 7.19 displays the last thermal cycle of each sample from 275 K (3 °C) to 400 K (127 °C). As a result of these cycles, endothermic (heating) and exothermic (cooling) peaks were observed. Endothermic reactions correspond to the phase transformation from martensite to austenite, where the tangential slopes represent the austenitic start (T_{As}) and finish (T_{Af}) temperatures. The exothermic peaks during cooling represent the energy in the form of enthalpy from the austenite to martensite transformation, where similarly, the tangential slopes signify the martensitic start (T_{Ms}) and finish (T_{Mf}) temperatures. Transformation temperatures are listed in Table 7.4. The Curie temperatures (T_c) range from 377 K (sample sintered for 10 h) to 379 K (sample sintered for 50 h). The transformation temperatures listed in Table 7.4 show that the printed Ni-Mn-Ga materials undergo T_{As} temperatures slightly above room temperature, ranging from 303 K to 322 K. Consequently, the T_{Ms} temperatures range from 311 K to 316 K. These transformation temperatures are very close to the values obtained by other authors in near stoichiometric Ni_2MnGa alloys [219]–[221].

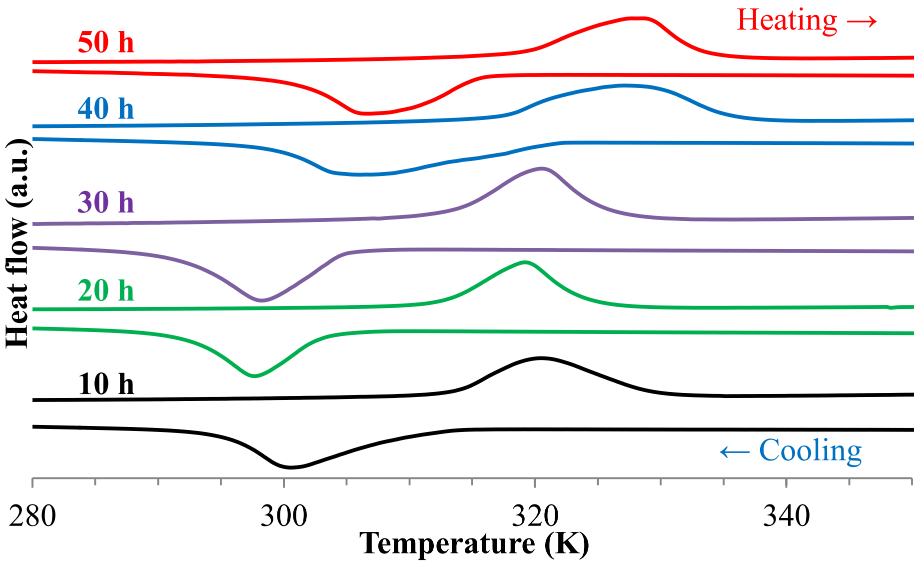

Figure 7.19: DSC curves of AM BM Ni-Mn-Ga samples sintered for 10, 20, 30, 40, and 50 h.

In addition to the martensitic transformation temperatures mentioned previously, the peak transformations are also listed in Table 7.4. The austenite peak transformation is displayed as T_{Ap} and the martensitic peak transformation is displayed as T_{Mp}.

Table 7.4: Summary of the reversible martensitic transformation temperatures for AM BM Ni-Mn-Ga.

	T_{As} (K)	T_{Ap} (K)	T_{Af} (K)	T_{Ms} (K)	T_{Mp} (K)	T_{Mf} (K)
10 h	310.9	320.2	294.6	312.9	300.0	328.5
20 h	303.6	320.4	287.5	311.5	297.3	323.8
30 h	305.4	320.2	292.1	311.6	298.4	326.7
40 h	322.4	326.7	297.0	315.2	306.4	335.5
50 h	315.0	328.0	299.6	316.5	306.7	333.4

In order to assess the effects of sintering time on the thermodynamic properties during heating and cooling instances, a thermal analysis based on enthalpy (ΔH) measurements was conducted. Endothermic and exothermic reactions were integrated using DSC curves, to obtain the energy consumed or emitted (enthalpies), respectively. Enthalpies were determined by following:

$$\Delta H = \int_{T1}^{T2} C_p dT \tag{7.1}$$

where T_2 and T_1 are the temperature limits of the reaction, C_p is the specific heat of the material, which is a function of temperature and material specific.

Changes in enthalpy during heating and cooling transformations supported in calculating changes in entropy (ΔS) and Gibb's free energies (ΔG) using [222]:

$$\Delta S = \frac{\Delta H}{T_o} \tag{7.2}$$

and

$$T_o = \frac{(M_s + A_f)}{2} \tag{7.3}$$

where M_s is the martensitic start temperature and A_f is the austenite finish temperature.

The Gibb’s energy was determined via:

$$\Delta G = \frac{\Delta H \cdot \Delta T}{T_o} \tag{7.4}$$

for which;

$$\Delta T = T_o - M_p \tag{7.5}$$

The calculated values ΔG and ΔS are displayed in Table 7.5. Enthalpy values have been calculated in the range from 2.6 J/g to 3.6 J/g. The enthalpies measured from AM Ni-Mn-Ga samples are comparable to polycrystalline Ni-Mn-Ga alloys where transformation energies are reported in the range of 0.3 J/g to 8 J/g [121], [223]. Wu & Yang [121], showed that slight changes in composition can have significant effects on martensitic transformation temperatures; it was reported that a change in Ni of 0.16 at% effects the M_s by approximately 40 K. In the same study, it was shown that M_s and ΔH have a linear relationship indicating Ni-Mn-Ga alloys undergo a thermoelastic martensitic transformation. It has been reported elsewhere that changes in enthalpy are related to atomic disordering, as well as annealing conditions such as temperatures and time [168], [183], [184], [223]–[225]. Based on these reports, and the data presented in Figure 7.19 and Table 7.4, there is a strong indication that no significant change with respect to chemical compositions is observed between all five AM Ni-Mn-Ga samples after various sintering times. Furthermore, no atomic disordering was observed based on DSC analysis, which agrees with aforementioned XRD analysis. Although it should be noted, AM Ni-Mn-Ga sample sintered for 40 h was reported to have the highest enthalpy amongst all five samples, for endothermic and exothermic reactions. This regression in enthalpy for AM Ni-Mn-Ga 40 h sample has adverse effects while determining thermodynamic properties, such as ΔG. Moreover, this study does not investigate the effects of enthalpy based on different annealing temperatures; albeit it is shown there is no prominent change in enthalpy as a function of sintering time.

Table 7.5: Summary of thermal properties from AM BM Ni-Mn-Ga samples sintered for 10, 20, 30, 40, & 50 h.

	$\Delta H_{heating}$ (J/g)	$\Delta H_{Cooling}$ (J/g)	$\Delta S_{Heating}$ (J/g °C)	$\Delta S_{Cooling}$ (J/g °C)	$\Delta G_{Heating}$ (J/g)	$\Delta G_{Cooling}$ (J/g)
10 h	3.48	-3.07	0.074	-0.065	1.46	-1.29
20 h	3.19	-2.92	0.078	-0.072	1.29	-1.18
30 h	2.68	-2.92	0.063	-0.069	1.10	-1.20
40 h	3.51	-3.63	0.062	-0.065	1.41	-1.46
50 h	2.95	-3.16	0.0577	-0.062	1.01	-1.08

In attempt to correlate the effects of sintering time with the thermal properties of the AM Ni-Mn-Ga samples, the peak transformation temperatures (T_{As}, T_{Mp}) along with electron concentration (e/a) ratios were examined. The electron concentration was calculated using [223]:

$$\frac{e}{a} = \frac{10 \cdot Ni(at\,\%) + 7 \cdot Mn\,(at\,\%) + 3 \cdot Ga\,(at\,\%)}{Ni\,(at\,\%) + Mn(at\,\%) + Ga\,(at\,\%)} \tag{7.6}$$

Figure 7.20 shows the peak transformation temperatures (TA_p, TM_p) for samples sintered for 10 h to 50 h along with the corresponding e/a ratio It can be observed, the peak transformation decreases from 10 h to 20 h, and the e/a ratio follows suite. The respective variables follow this trend between all five samples.

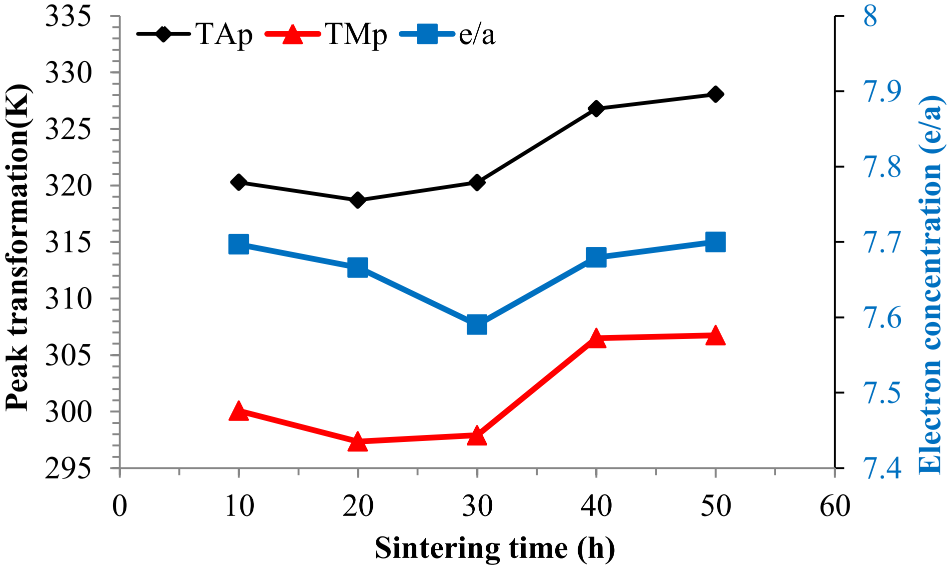

Figure 7.20: Evolution of peak temperature and electron concentrations (e/a) in AM Ni-Mn-Ga samples as a function of sintering temperature.

It is important to reiterate there is a relationship between transformation temperatures and chemical composition. Explicitly, there are two mechanisms responsible for shifts in thermal properties in Ni-Mn-Ga alloys. The size factor (unit cell), and electron concentration (e/a) ratio (chemical composition) are two dynamics that have significant impacts on the transformation temperatures in Ni-Mn-Ga alloys [120]. When Ga atoms are replaced by Ni atoms a shrinkage in the unit cell occurs with a subsequent increase in electron concentration [226]. This occurs because the Ni atoms have smaller atomic radii and larger electron valence. It has been shown as the cell volume decreases and electron concentration increases, the A_s temperature increases [120], [121], [226]. The fact that there is a distinct relationship between the e/a ratio and peak transformations of these samples provides supporting evidence for the collection of accurate chemical composition in each AM Ni-Mn-Ga sample. Moreover, the physical relationship between the e/a ratio (unit cell volume) and the peak transformation temperatures has been successfully recorded.

Figure 7.21 (a) displays the entropy (ΔS) for heating and cooling transformations for Ni-Mn-Ga samples sintered for 10, 20, 30, 40, and 50 h. The values observed portray the overall trend of the entropy, and appear to decrease as a function of sintering time. The entropy for the first transformation (10 h) during heating begins at 0.074 J/g °C and finishes (50 h) at 0.0577 J/g °C. Likewise, the entropy during cooling transformations begins at -0.065 J/g °C and finishes at -0.062 J/g °C, respectively. As entropy is most commonly associated with the disorder in a system, it can be inferred that the disorder in Ni-Mn-Ga martensitic transformations decrease with increasing sintering time. Furthermore, entropy can also be related to the efficiency at which thermal energy is converted into mechanical energy. Therefore, it is shown in Figure 7.21 (a) the efficiency of thermal-to-mechanical energy conversion can be optimized by controlling sintering conditions, such as time and/or temperature.

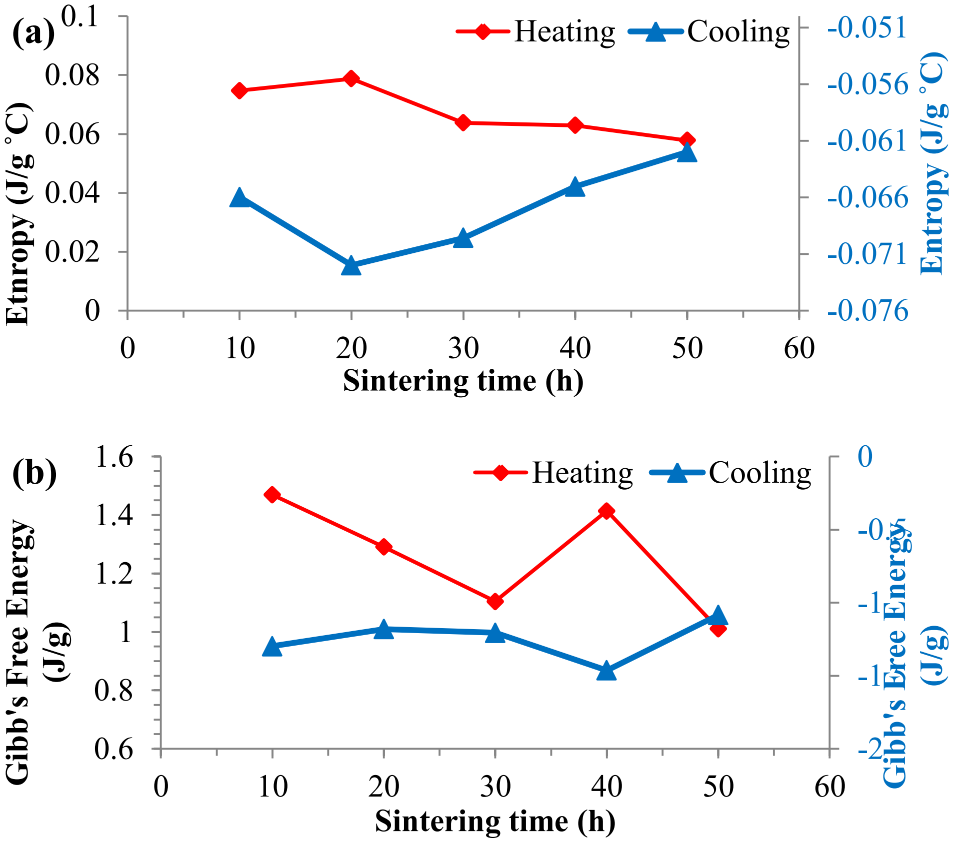

Figure 7.21: Evolution in (a) enthalpy and (b) Gibb's energy of printed Ni-Mn-Ga as a function of sintering time. Black lines represent the endothermic reactions (heating) and red are exothermic reactions (cooling).

The subsequent Gibb's energy of each heating and cooling transformation, respectively, has been calculated and the progression is shown in Figure 7.21 (b). Similar to the entropies in (Figure 7.21 (a)) the behavior of the Gibb's energy decreases as a function of increasing sintering time. Specifically, during heating the Gibb's energy for sample 10 h is 1.46 J/g while 50 h sample was computed to 1.01 J/g. The effect on the martensitic transformation as Gibb's energy decreases causes a more favorable reaction. During cooling transformations, the values for 10 and 50 h samples are -1.29 J/g and -1.08 J/g, respectively. The Gibb's energy in sample 40 h does not follow the respective trend, however can be explain by the enthalpies. While computing the Gibb's energy, two factors heavily affect the calculation of the respective value; the enthalpy and transformation temperatures. As previously mentioned, the enthalpy recorded for sample 40 h was shown to possess the largest value for both heating and cooling transformations. Moreover, the reversible martensitic transformation is broad, therefore spreading the transformation temperatures. Consequently, the Gibb's energy appears to deviate from the trend of samples 10, 20, 30, and 50 h. However, both entropy and Gibb's energy for all five samples are substantially similar to the values reported by Kök & Aydogdu [225] where the thermal properties of Ni-Mn-Ga alloys annealed at temperatures ranging between 1073 K – 1273 K (800 °C – 1000 °C) were studied.

7.4 Influence of Sintering Temperature on Microstructural and Thermal Properties of 3D Printed Parts Produced from Ball Milled Ni-Mn-Ga Powders

This subchapter presents the influences on the density and thermal properties of 3D printed Ni-Mn-Ga because of sintering at various temperatures ranging from 1273 K to 1373 K (1000 °C – 1100 °C). Section 7.3 explored the microstructure, thermal properties and phases present in printed parts because of varying sintering temperatures at constant sintering time. Since no significant change was observed in the case of XRD, this section will focus primarily on the variations in density and thermic properties. It is essential to keep in mind; porosity is one of the most important parameters when examining the MFIS. Moreover, since in the previous subchapter it was clarified that the microstructure of sintered material consists of 5M martensite, with variations between incommensurate and commensurate modulations, this aspect won't be discussed here.

7.4.1 Microstructural Effects

This investigation begins with sintering six printed BM Ni-Mn-Ga samples for 5 hours at 1273 K (1000 °C), 1293 K (1020 °C), 1313 K (1040 °C), 1333 K (1060 °C), 1353 K (1080 °C) and 1373 K (1100 °C). Bar shaped BM Ni-Mn-Ga samples were encapsulated into a single quartz tube, back filled with UHP argon gas several times and after sintering, sectioned into six pieces. Each piece was weighed, and cross-sectional dimensions were measured several times. Afterwards, each sample's density was determined. The results in terms of density percentages are shown in Figure 7.22. Moreover, the densities are presented in Table 7.6.

Table 7.6: Density measurements from 3D printed parts from BM powders sintered at 1273 K, 1293 K, 1313 K, 1353 K, and 1373 K.

	1273(K)	1293(K)	1313(K)	1333(K)	1353(K)	1373(K)
Density (g/cm^3)	3.523	3.765	3.983	4.148	4.517	4.600
Percentage Density (%)	46.4	49.5	52.3	54.5	59.4	60.5

Notably and even more so than the above mentioned study in Section 7.3, is the ability to lower the relative density of 3D printed BM Ni-Mn-Ga samples. In particular, relative densities range as low as 46.4 %, and as high as 60.5 %. Moreover, the green part relative density has been established as approximately ~45.9 %. Based on these results, sintering at a temperature of 1273 K (1000 °C) for 5 h shows an insignificant increase in density of 0.5 % when compared to the green state. It is essential for the reader to retain the importance of porosity on the MFIS of Ni-Mn-Ga. Recall, the large MFIS observed in porous polycrystalline Ni-Mn-Ga was approximately 62 % [9]. The work reported here shows the ability to readily control porosity percentage by volume in the sintered sample in between 53.6 % and 39.5 %, based on sintering temperature.

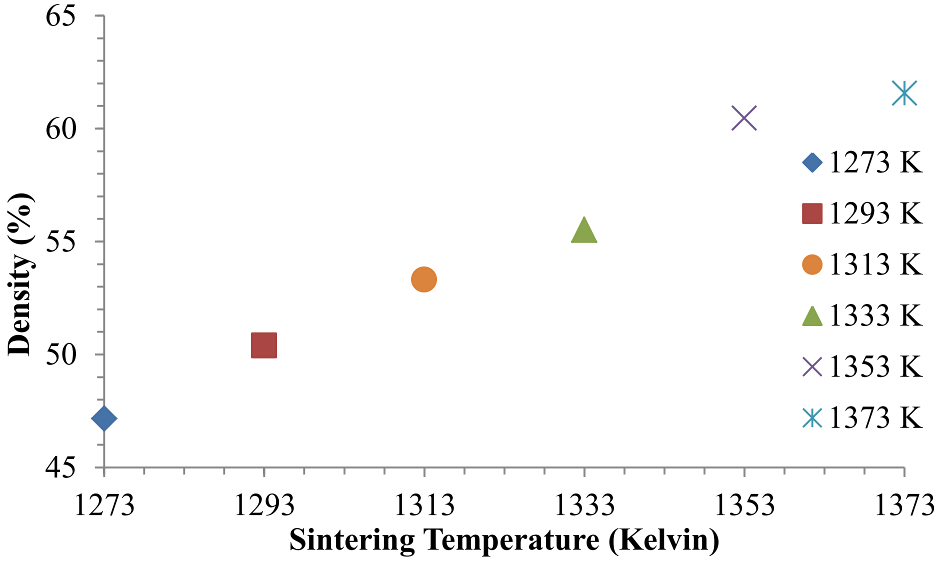

Figure 7.22: Graphical display of density as a function of sintering temperature for BM Ni-Mn-Ga parts.

In addition, the reversible martensitic transformations were investigated by means of DSC. The resulting heat flow curves are displayed in Figure 7.23. Based on these curves, the transformation temperatures vary considerably. In particular, the austenite start (T_{As}) temperature fluctuates between 304 K – 315 K (31.36 °C – 42.29 °C), a difference of approximately 11 K (11 °C). A list of all the transformation temperatures is provided in Table 7.7. The Curie temperatures range between approximately 371 K and 374 K (98 °C and 101 °C).

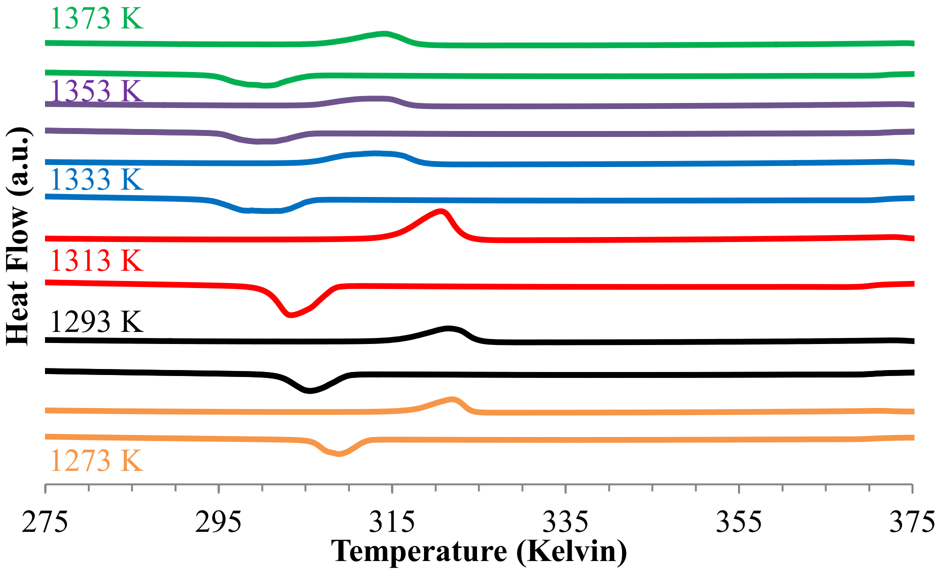

Figure 7.23: DSC curves for BM Ni-Mn-Ga samples sintered from 1273 K to 1373 K (1000 °C – 1100 °C) for 5 h.

The transformation temperatures are slightly above room temperature, as comparable to the above-mentioned isothermal sintering studies. Due to this, and the fact that no change in crystal structure occurred previously, it is being assumed the XRD patterns do not vary between samples. Therefore, it is assumed these samples possess 5M martensite.

Table 7.7: Summary of BM Ni-Mn-Ga reversible transformation temperatures for samples sintered from 1273 K to 1373 K (1000 °C – 1100 °C) for 5 h.

Sample	T_{As} (K)	T_{Af} (K)	T_{Ap} (K)	T_{Ms} (K)	T_{Mf} (K)	T_{Mp} (K)
1273 K	315	325	321	312	304	308
1293 K	314	326	321	310	300	305
1313 K	311	325	320	309	298	303
1333 K	304	319	312	306	293	300
1353 K	305	318	310	306	294	299
1373 K	306	318	314	305	293	300

The thermal properties as a result of these transformations such as; enthalpy, entropy, and Gibb's energy underwent a similar analysis to that explained in Section 7.3.3. These calculated values are displayed in Table 7.8. Based on the reported values, there is no clear trend for any of the thermal properties. However, it can be stated that entropy and Gibb's energies in the case of samples sintered for 1273 K (1000 °C) and 1293 K (1020 °C) are the lowest of the six samples. As previously mentioned, lower entropy values allow for more efficient energy conversions and respective Gibb's energies allow for favorable reactions. These two properties coupled with the lowest porosity reported in this work could potentially produce sample that display optimal MFIS values.

Table 7.8: Summary of thermic properties for BM Ni-Mn-Ga parts sintered for 5 h between 1000 – 1100 °C.

	$\Delta H_{heating}$ (J/g)	$\Delta H_{cooling}$ (J/g)	$\Delta S_{heating}$ (J/g °C)	$\Delta S_{cooling}$ (J/g °C)	$\Delta G_{heating}$ (J/g)	$\Delta G_{cooling}$ (J/g)
1000°C	3.219	-3.882	0.069419	-0.083728	0.722	-0.872
1020°C	3.501	-3.383	0.076888	-0.074294	0.991	-0.958
1040°C	4.116	-4.272	0.092736	-0.096269	1.301	-1.351
1060°C	3.778	-3.857	0.093901	-0.095881	1.176	-1.201
1080°C	3.449	-3.859	0.088008	-0.098451	1.115	-1.248
1100°C	3.572	-3.629	0.090756	-0.092188	1.090	-1.108

7.4.2 The Basis for an Original Approach of Calculating the Volumetric Changes in Ni-Mn-Ga Alloys Throughout Stages of Sintering

This section examines an original approach for calculating the volumetric changes along with the kinetics between Ni, Mn, and Ga as it diffuses into Ni-Mn-Ga alloys. The investigation is based on the kinetic behavior from particle to particle as a function of temperature. The goal of this study is to experimentally model the volume change and diffusion coefficient for Ni, Mn, and Ga using imaging processing and numerical calculations. Moreover, this model can be applied to any material which has equally sized spherical particles that experience a sintering process. For information regarding principals of sintering refer to section 2.1.5.

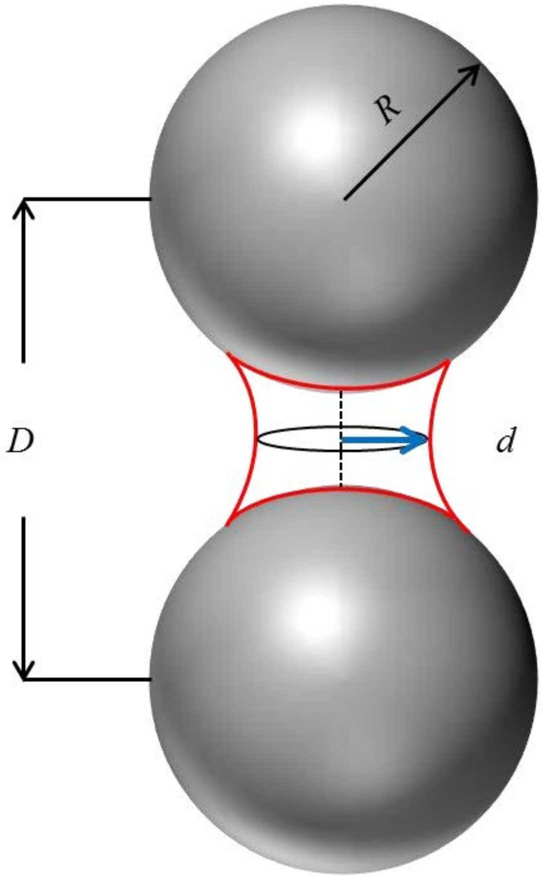

Figure 7.24: Schematic of a sintering instance for two equally sized spherical particles. *R* represents the radii, *D* is the distance between the two particle centers, *d* is the diameter of the diffusion area, and red contour indicated the volume of material sintered.

This study begins with the conceptual formulation and understanding, as a numeric approach of kinetics. For this, we refer to Figure 7.24, which displays a schematic of a specific sintering instance. For this numeric approach to be valid, a few assumptions are necessary. It is assumed that each particle is spherical, and they are the exact same size, and the volumes of these particles do not change during sintering. Moreover, the diffused volumetric area after sintering must be a paraboloid, indicated by the red contour in Figure 7.24. In addition to these, we consider R as the radius of each particle, D as the distance between the two particles, d as the diameter of the diffused area while red signifies the diffused volumetric area.

The numerical approach starts with Equation 2.1 which describes the rate of material transport from material source to material sink [79]. Equation 2.1 can be expressed in a more simplistic form:

$$\frac{dv}{dt} = JAV_m \tag{7.7}$$

where J is the flux density of material transport, A is the diffused area, V_m is the molar volume and dv/dt is the change in material volume diffused over time.

The molar volume (V_m) for crystalline solids is described as [227]:

$$V_M = \frac{N_A * V_{cell}}{Z} \tag{7.8}$$

here, N_A is Avogadro’s number, V_{cell} is the volume of the crystal unit cell, and Z is the integer number of formula units.

V_{cell} and Z both can be obtained from the joint committee on powder diffraction standards associateship (JCPD, International Center for Diffraction Data); which is experimentally obtained after annotation of X-ray diffraction patterns. In this particular case, Z = 2, V_{cell} = 98.53 Å^3 and Avogadro's number is 6.022x10^{23} atoms/mol. Thus a molar volume of approximately 296.68 mol/cm^3 was obtained. Furthermore, the diffusional area (*A*) is a function of diameter, *d*, described previously, Figure 7.24.

The next variable for investigation is the volumetric change of material, *dv*. For this, the volume, *V* of a paraboloid as one in Figure 7.24, can be expressed as:

$$V = \pi\left(\frac{d}{2}\right)^2 \int_{(D-2R)/2}^{(D-2R)/2} \left[1 + \frac{y^2}{(D-2R)^2}\right] dy \qquad (7.9)$$

Post-integration, this expression takes on a more simplistic form:

$$V = \pi\left(\frac{d}{2}\right)^2 \left[\frac{13}{12}(D-2R)\right] \qquad (7.10)$$

Equation 7.10 allows for the determination of the volumetric material transfer during sintering of equally sized particles over a period, *dt*. After determining the volumetric change, *V*, diffusion flux, *J*, can be solved for using Equation 7.7. Moreover, the expression for diffusion flux, for changes in pressure can be extrapolated:

$$J = -\frac{D(P_2 - P_1)}{R'T} \qquad (7.11)$$

where *D* is the diffusion coefficient, *ΔP* measures the difference in pressure, *R'* is the universal gas constant, and *T* is absolute temperature.

Since sintering of Ni-Mn-Ga occurs in a pressure controlled environment, changes in pressure are negligible. Thus, determining the diffusion coefficient becomes apparent. The universal gas constant value used was R' = 82.057 cm^3atm/kmol.

To this point, the model used to volumetric change and derive flux as well as diffusion coefficients from sintered particle instances is somewhat simplistic; however, lacks the experimental verification. Therefore, an experimental design for sintering was created using spherical LAr powders. The LAr powders were chosen for this experiment due to several reasons. First, they have a controlled powder size distribution, ranging from 20 – 60 μm thus, inherently increasing the chances for equal sized particles to be sintered. Second, the morphology of individual LAr particles is a solid sphere. These two factors somewhat fulfill the above-mentioned assumptions of spherical and identical sized particles. 3D printed LAr components were sintered for 5 h, with varying temperatures of 1273 K (1000 °C), 1293 K (1020 °C), and 1313 K (1040 °C) and then examined via SEM. The goal was to capture particle sintering instances, similar to that in Figure 7.24. This investigation does not account for LAr parts sintered above 1313 K (1040 °C). Sintering above 1313 K (1040 °C) would result in excessive amounts of material transfer due to high temperatures, subsequently effecting particle morphology and size. For this, the constructed model would be invalid.

The results of the microstructure investigation by means of SEM are presented in Figure 7.25 (a) to (c). These SE micrographs show LAr particles sintered at 1273 K (1000 °C), 1293 K (1020 °C), and 1313 K (1040 °C), respectively. The primary focus for these images is towards the size of diffusional areas between particles. In particular, the *D*, *R*, and *d* values were measured from the micrographs. Throughout

Figure 7.25 (a) to (c), the sintering necks increase as a function of sintering temperature. It can be inferred, based on well-known kinetic and diffusion principals, [228]–[230], as temperatures increase so does transport rate of material. In fact, this phenomenon is observed experimentally in Figure 7.25, (a) to (c).

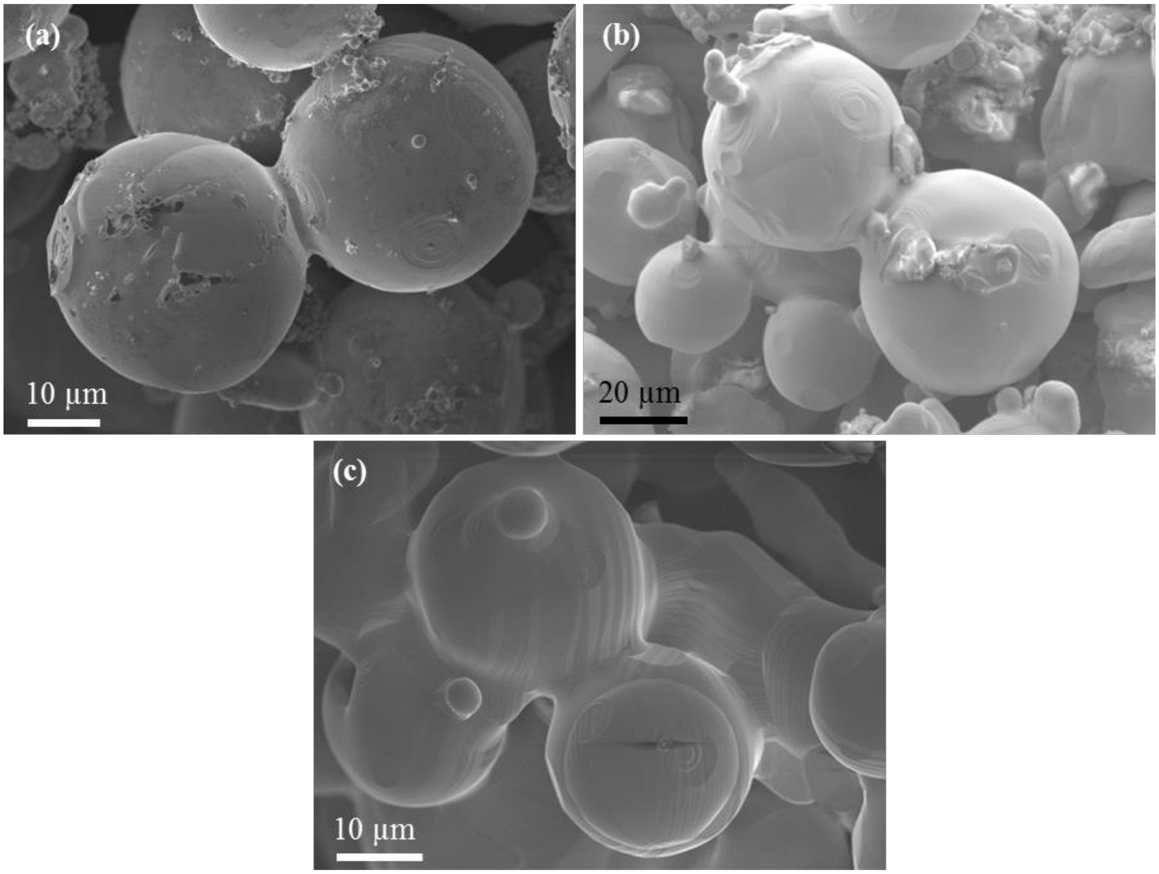

Figure 7.25: SE micrographs of LAr Ni-Mn-Ga parts sintered at (a) 1273 K (1000 ◦C), (b) 1293 K (1020 °C), and (c) 1313 K (1040 °C) for 5 h. The *D*, *R* and *d* parameters were determined by direct measurement from these images, using ImageJ software.

In order to apply the above derived model and obtain a statistical representation for diffusion, a series of approximately 30 images were taken from each sintering temperature. Only images of equally sized sintered particles were captured. These images underwent size calibration and processing using ImageJ, image processing software. ImageJ was used to determine the parameters necessary for calculating the volume of diffused material and subsequently lead to calculating flux density and diffusion coefficient at each individual temperature.

Average values based on 30 measurements for calculated volumetric material transfer, flux and diffusion coefficient are shown in Table 7.9. Diffusion coefficients calculated for Ni-Mn-Ga alloy system are compared to established values of iron based materials. In particular, calculated coefficients are compared to manganese diffusion into iron at 1273 K (1000 °C), which was reported to yield a diffusion coefficient of 3.64×10^{-11} m^2/s [231]. Manganese diffusion into iron was considered a good candidate for comparison due to similar atomic radii. In addition, it should be noted the calculated diffusion coefficients are comparable to vanadium diffusion rates into nickel at 630 °C. It has been reported, the diffusion coefficient of vanadium diffusion into nickel is 5.00×10^{-14} m^2/sec [232]. The calculated diffusion coefficients for Ni, Mn, and Ga into Ni-Mn-Ga LAr particles varies from $2.12 \times 10^{-12} - 1.01 \times 10^{-11}$ m^2/sec from 1273 K (1000 °C) to 1313 K (1040 °C). These calculated diffusion coefficients are in line with others reported for different materials and temperatures, as mentioned above.

The diffusion coefficient for Ni, Mn, and Ga into Ni-Mn-Ga alloys has not been reported previously, to the best of my knowledge. Furthermore, to properly conduct these kinetic studies, a series of experiments would need to determine individual transfer rates between elements; i.e. nickel into manganese, gallium into nickel, etc. Nevertheless, utilizing analytical characterization, and image analysis, the above derived model was proven to be successful for describing the kinetics as a metallic alloy system. Moreover, the model could be further validated. This would include more extensive kinetic studies.

Table 7.9: Summary of kinetic properties of Ni-Mn-Ga LAr particles as a function of temperature.

	LAr Sintered at 1000 °C	LAr Sintered at 1020 °C	LAr Sintered at 1040 °C	Manganese into Iron at 1000 °C
Volume of Material Transported (μm^3)	322.35	609.86	1256.21	-
Calculated Flux ($mol/\mu m^2*sec$)	$6.09x10^{-18}$	$1.36x10^{-17}$	$1.34x10^{-17}$	-
Calculated Diffusion Coefficient (m^2/sec)	$2.12x10^{-12}$	$9.83x10^{-12}$	$1.01x10^{-11}$	$3.64x10^{-11}$

8. Mechanical and Magnetic Properties of AM Ni-Mn-Ga

This chapter investigates the mechanical and magnetic properties of sintered parts produced by binder jetting from Ni-Mn-Ga. Bulk Ni-Mn-Ga alloy produced by ark melting was used as reference material. The mechanical properties of these materials have been examined using two methods: nano-indentation and compression testing. The magnetic properties of these materials were determined using vibrating sample magnetometer (VSM) techniques. Therefore, this chapter will be split into two subchapters: mechanical properties and magnetic properties.

The magnetic and mechanical properties of single crystal, bulk, and thin films have been well studied by several researchers [217], [233]–[238]. The magnetic and mechanical properties of foams and composites have also been investigated [9], [239]–[242]. However, there are no reports on these properties in the case of 3D printed Ni-Mn-Ga materials made from pre-alloyed powders. Moreover, there are very few reports on magnetic and mechanical properties of Ni-Mn-Ga powders [168], [243]. Most of the reports are on magnetic and mechanical properties of composites made using of Ni-Mn-Ga powders. Furthermore, none of these reports are on the mechanical and magnetic properties of sintered Ni-Mn-Ga powders. To the best of my knowledge, there is no information on magnetic and micro-mechanical properties of additively manufactured Ni-Mn-Ga parts. One paper reports on the magnetic properties of Ni-Mn-Ga powders produced by means of spark erosion in various dielectrics [244]. Regarding the mechanical properties of Ni-Mn-Ga spark eroded powders, they were only studied as composites [245]. Therefore, in order to develop 3D parts from these powders the magnetic and micro-mechanical properties must be investigated and determined. The purpose of this chapter is to report on the magnetic and micro-mechanical properties for porous Ni-Mn-Ga parts produced using binder jetting AM.

8.1 Mechanical Properties

8.1.1 Nano-Indentation

In order to verify the samples produced for nano-indentation possessed the properties necessary for the shape memory effect, they were characterized using aforementioned methods. Therefore, differential interference contrast imaging (DIC) techniques were employed to present the micro-structure of polished cross-sectioned AM Ni-Mn-Ga parts, Figure 8.1 (a). DIC images correspond to a sintered Ni-Mn-Ga part made from BM powders and clearly expose the existence of martensitic morphology and a porous microstructure.

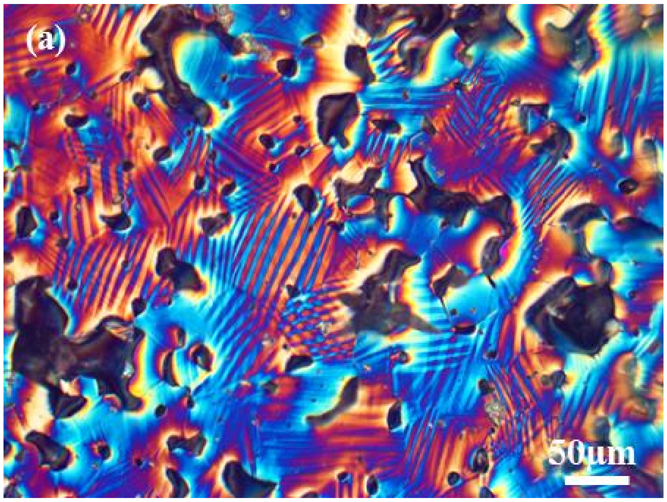

Figure 8.1: (a) DIC image of sintered BM Ni-Mn-Ga microstructure.

It should be noted, as a result of sintering, it is possible to produce stoichiometric deviations in the Ni-Mn-Ga powders [20]. Thus, the chemical composition from sample to sample could vary slightly. Therefore, chemical compositions of Ni-Mn-Ga parts investigated in the nano-indentation study were investigated after sintering using previously described methods. The average atomic compositions for the sintered materials are shown in Table 8.1.

Table 8.1: Summary of chemical compositions for AM Ni-Mn-Ga parts consisting of sintered BM, LAr, and LN2 powders.

	Ni (at %)	Mn (at %)	Ga (%)
BM	50.9±1.6	30.7±0.8	18.4±2.3
LAr	50.8±1.5	28.8±0.1	20.4±1.8
LN_2	48.6±5.3	27.3±2.6	24.1±8.0

Micromechanical testing was conducted on each sintered Ni-Mn-Ga sample using a M1 mechanical tester (Nanoeva) equipped with a Berkovich tip. Load was applied to each polished surface with loads ranging between 10 mN to 200 mN. Load was applied quasi-statically until the respective maximum load was reached. The load was then held static for one minute and subsequently removed. The microstructure of BM parts before and after the indentation process is shown in Figure 8.2 (a) and (b), respectively.

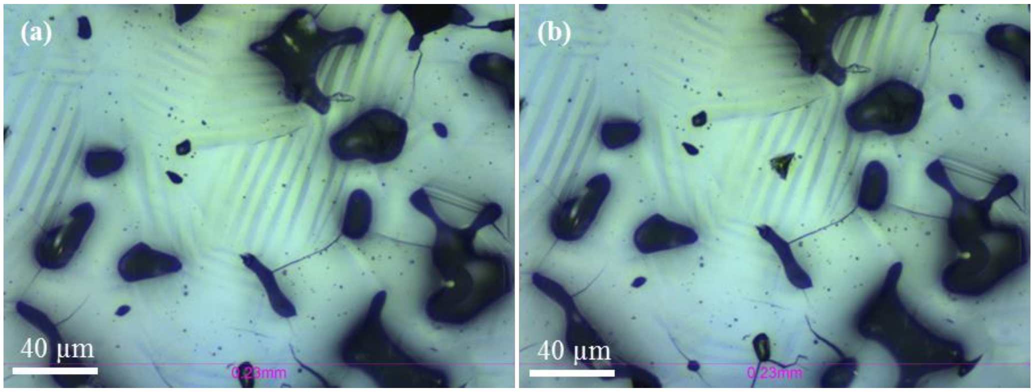

Figure 8.2: Polished microstructure of BM part microstructure (a) before and (b) after nano-indentation. The indent is clearly seen in (b).

The results of these measurements are shown in Figure 8.3. The Young's modulus, E, can be derived by measuring the slope of initial unloading moment;

$$E = \frac{dP}{dD} \tag{8.1}$$

where E is the Young's modulus, dP is the change in load, and dD is the change in depth.

Similarly, the hardness can be calculated by;

$$H = \frac{P_{max}}{A} \tag{8.2}$$

where H is the hardness, P_{max} represents the maximum load applied, and A is the residual area after indentation. The indent is clearly seen in Figure 8.2 (b).

The Young's modulus and hardness values obtained from these measurements are discussed later. The modulus and hardness along with standard deviations are based on ten measurements from randomly selected areas of the microstructure.

The BM part seems to behave pseudo-elastically during loading and unloading. Recall, pseudo-elasticity occurs when the shape memory alloy is deformed in the austenitic phase. This performance is based on observations during micromechanical testing, Figure 8.3. The sample was loaded to 200 mN, afterwards the static load was held for one minute. Upon unloading, deformation caused by the static force was fully recovered, as seen in Figure 8.3, inset (indicated by the arrow). Figure 8.3, inset, shows loading curves as black while unloading as green. In addition, unrecovered deformations were calculated by measuring the difference between initial and final depths caused from the mechanical testing; while minimal loads were present, Table 8.3.

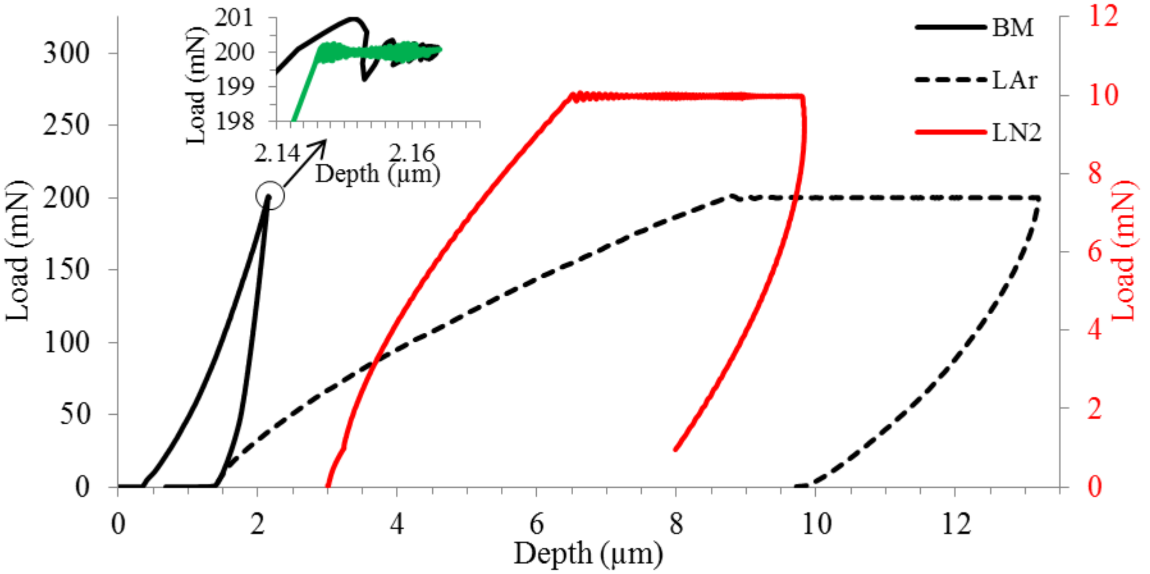

Figure 8.3: Results of the micro-mechanical testing for Ni-Mn-Ga parts obtained from BM powders (black, solid), LAr powders (black, dotted) and LN_2 powders (red, secondary axis). The insert shows the enlarged plot of the BM parts curve where black represents loading and green represents unloading.

In order to verify the distinct mechanical response of the BM part, the sample was thermally cycled via DSC from 273 K to 413 K (0°C – 140°C) to determine the transformation temperatures, Figure 8.4. DSC samples have been cycled several times, but only the last thermal cycle is presented in Figure 8.4. No change in transformation temperatures was observed. The reversible martensitic transformation temperatures (A_s, A_f, M_s, M_f) are shown in Table 8.2. Furthermore, the ambient temperature in which these samples were tested was approximately 299 K (26 °C). The martensitic finish temperature for BM parts was shown to occur at approximately 296 K (23.6 °C). Based on this, the BM part possesses a mixture of phases at room temperature: austenite and martensite, Figure 8.4. Nevertheless, based on the results from the micromechanical testing, the BM part shows a relatively large elastic modulus, compared to the as-sparked material. Furthermore, the BM part allows much of the deformation cause from the static force to be recovered due to the aforementioned pseudoelasticity. The mechanical properties for 3D printed BM parts based on 10 measurements can be found in Table 8.3.

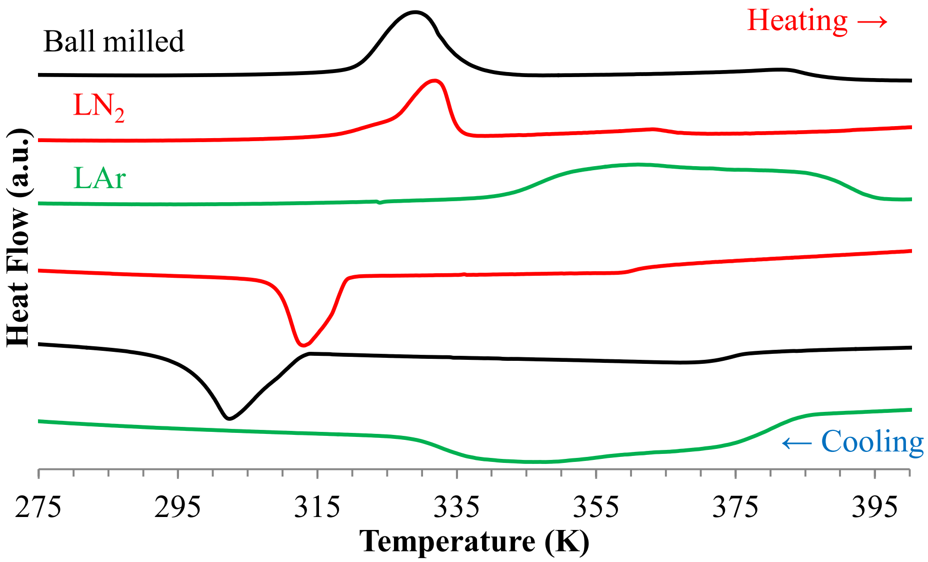

Figure 8.4: DSC curves from sintered Ni-Mn-Ga parts 3D printed from; BM (black), LN_2 (red), and LAr (green) powders. All three samples are in the martensitic state are room temperature.

The as-sparked 3D printed material, (LAr and LN_2) display different mechanical responses. It can be seen in Figure 8.3 the loading and static force applied caused relatively large amounts of deformation to the as-sparked LAr and LN_2 3D printed part microstructures in the tested zones. It should be noted, the LAr part underwent the same micromechanical testing as the BM part however, LN_2 parts experienced a maximum load of 10 mN, with a static force applied for one minute then unloaded. The reason for this is that most of the LN_2 particles are hollow with wall thicknesses of approximately 1 μm, Figure 5.1 (d). As a result, their mechanical properties are very poor when compared to BM and LAr particles. A load of 200 mN caused the LN_2 particles to fracture, puncturing the hollow shells. Due to this, the indentation load was reduced to 10 mN, after trial and error, to obtain appropriate surface mechanical characteristics.

Table 8.2: Summary of reversible martensitic transformation temperatures.

	A_s (C)	A_f (C)	M_s (C)	M_f (C)
BM	47.2	62.9	39.4	23.6
LAr	70.5	120.9	113.2	56.6
LN_2	48.1	63	47.7	35.1

The results from micromechanical tests of LAr and LN_2 3D printed parts show relatively low values for modulus and hardness. The mechanical properties for LAr and LN_2 3D printed parts are summarized in Table 8.3. These poor mechanical properties can be attributed to the martensitic phase which was present during the investigation, confirmed by DSC, Figure 8.4. The transformation temperatures for the LAr and LN_2 parts are summarized in Table 8.2. Moreover, the martensitic phase of Ni-Mn-Ga alloys is known to be extremely brittle. On the other hand, the micromechanical properties acquired in this study are similar to those reported for bulk and thin film Ni-Mn-Ga [217], [221], [234], [236].

As observed in Figure 8.3, the unrecovered deformation due to the static load is on the order of micrometers in the case of LAr and LN_2 3D printed parts. An explanation for this is; as load is applied to the martensitic phase, present in LAr and LN_2 parts, the load causes stress-induced reorientation of martensite. This can be clearly observed in Figure 8.3, as the static load applied causes constant deformation. Upon unloading, the deformation is maintained. This is an example of the one way shape memory effect.

Table 8.3: Summary of the mechanical properties based on micromechanical testing.

	BM	LAr	LN_2
Young's modulus (GPa)	57.34±5.36	4.08±1.09	0.64±0.11
Hardness (GPa)	3.60±0.46	0.38±0.19	0.07±0.03
Unrecovered deformation (μm)	0.891±0.27	7.343±2.31	4.718±0.66

8.1.2 Compression Testing

Compression tests by means of Instron were ran on separate Ni-Mn-Ga BM 3D printed and bulk samples in both martensite and austenite phases. The objective of the compression trials was envisioned to provide information on mechanical behavior of 3D printed Ni-Mn-Ga for potential engineering applications. On the other hand, while testing bulk Ni-Mn-Ga, the mechanical properties of 3D printed material could be compared on a density basis. In order to accomplish this, Ni-Mn-Ga samples were mounted on an Instron model 5500R and heated/cooled using hot air via heat gun. During heating and cooling experiments, a thermocouple was placed on the surface of the sample to monitor the temperature within a tenth degree Celsius. As previously mentioned, throughout the thermal analysis from BM Ni-Mn-Ga materials the transformation temperatures are between 303 K (30 °C) and 323 K (50 °C). Therefore, to ensure a complete phase transformation during compression testing, BM Ni-Mn-Ga samples were heated to above 100 °C. Samples were compressed with a 150 kN load cell at a strain rate of 0.05 %/min, following ASTM E9-89a standard. The cross-sectional area of the samples, considered an isotropic material, ranged between 4 x 4 mm and 6 x 6 mm. However, all graphs reported here display results as stress-strain relationships.

This study begins with compressive tests on 3D printed and bulk Ni-Mn-Ga at ambient temperatures. An example of 3D printed BM sample's mechanical response is displayed in Figure 8.5. AM Ni-Mn-Ga BM samples were compressed to failure revealing ultimate strength of approximately 270 MPa ± 25 MPa, based on 3 measurements. Moreover, 3D printed Ni-Mn-Ga material shows the typical compression behavior of porous SMA's in the martensitic phase which causes stress induced martensitic reorientation, and later failure [246], [247]. Regarding the strain values at failure for printed parts, they are characteristic for brittle Ni-Mn-Ga experiencing similar compressions [248], [249].

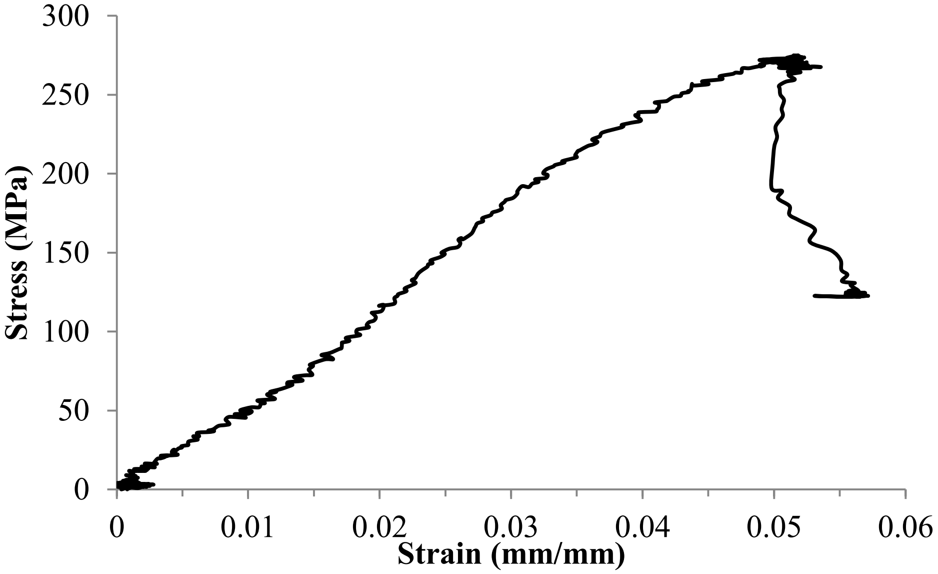

Figure 8.5: Example of the typical stress-strain behavior of porous 3D printed BM Ni-Mn-Ga obtained from BM powders.

Figure 8.6 shows the compressing stress-strain curve of bulk Ni-Mn-Ga. The ultimate strength of the bulk Ni-Mn-Ga is approximately 1475 MPa ± 93 MPa, based on 3 measurements. This comparison between 3D printed and bulk Ni-Mn-Ga showed increased yield strength of five times over in the case of bulk material. The increase in ultimate strength between the two counterparts is because, unlike AM samples, bulk Ni-Mn-Ga is fully dense. It is well known, material strength increases with density [101]. However, it should be acknowledged, the specific strength of Ni-Mn-Ga, as a function of density, can be increased through different designs. It has been shown, through the use of lattice structures, the specific strength of Ni-Mn-Ga increase by 32.4 % when compared to fully dense Ni-Mn-Ga [250].

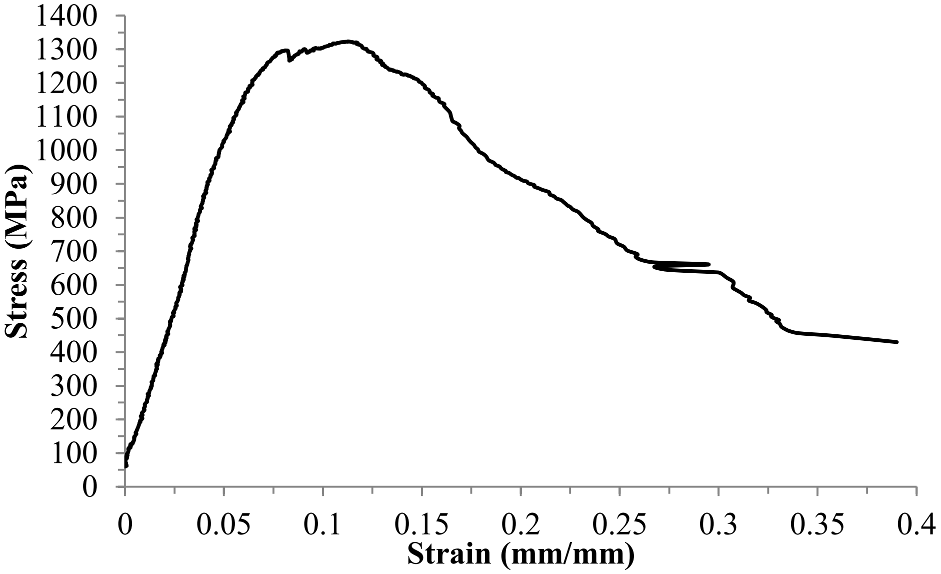

Figure 8.6: Example of the typical stress-strain behavior of bulk Ni-Mn-Ga.

Responses from compression tests on porous metallic samples display unique strain reactions at specific stress values. Traditional fully dense materials, such as metallic compounds, tend to have very predictable mechanical behaviors. In most cases, the stress-strain behavior is linear in elastic zones and then deviates during plastic deformation. However, porous metallic structures, especially foam-like SMA’s, possess a stress-strain behavior that is very unpredictable. It is often the case in which the stress distribution is non-uniform. As a result, the structure strains heterogeneously throughout the body. The investigation of porous strain behavior was simulated using finite element analysis (FEA) using a two-dimensional model [251]. The product of this investigation portrayed several stress concentrators on the two-dimension microstructure. Ultimately, these stress concentrators lead to the failure of the simulated structure. These concentrators are envisioned to exist in three-dimensions, and inherently cause failure in the AM porous structure. Future work will involve FEA of 3D bodies obtained from micro-computer tomography of AM Ni-Mn-Ga samples.

Mechanical properties for AM and bulk Ni-Mn-Ga were examined above austenite transformation temperatures. Bulk Ni-Mn-Ga samples were heated to approximately 373 K (100 °C) and compressed under strain controlled conditions. Compression cycles began by straining and then removing load to examine the mechanical response. Bulk samples were cycled 4 times, straining for 2 %, 4 %, 8 %, and 15 %. The results from cycling bulk Ni-Mn-Ga are shown in Figure 8.7. The stress-strain response from 2% straining is displayed on the secondary axis for clarity. Most notable is the shape memory effect observed during loading and unloading over the four test cycles. This is observed by the mechanical hysteresis response. A characteristic of the stress-strain reaction for shape memory alloys is a near full recovery of deformation [252].

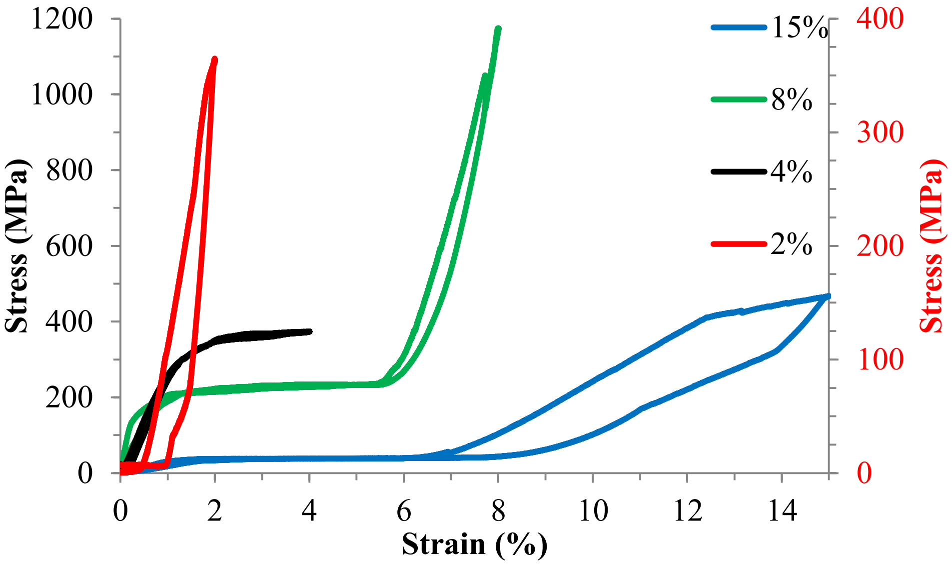

Figure 8.7: Compression stress-strain relationship for bulk Ni-Mn-Ga at high temperature (373 K) strained between 2 % and – 15 %. The 2 % strain compression is displayed on the secondary axis for clarity.

The pseudo-elastic effect follows a particular mechanical response to compression, as described in section 2.2.3. The pseudo-elastic effect is clearly observed in Figure 8.7. Most notable for the compression of bulk Ni-Mn-Ga is the plateau region of stress induced martensite. Upon compressing the alloy to 4 %, 8 %, and 15 %, the plateau for stress induced martensite is apparent. Moreover, the stress required to induce martensite appears to decrease over compression cycles. In fact, this phenomenon has been reported previously. Studies involving the compression of single crystal Ni-Mn-Ga with different chemical compositions revealed two variables affecting the twinning stress: the orientation of the crystal during compression and the number of compression cycles the crystal experienced [253]. The reduction of twinning stress is accredited to crystallographic reversibility and absence of slip during transformations [254]. The bulk

Ni-Mn-Ga tested in this research revealed initial twinning stress was approximately 400 MPa, observed during the 4 % strain compression. Subsequent compressive cycles revealed the twinning stress reduces to approximately 200 MPa and 40 MPa, for 8 % and 15 %, respectively. In addition, plastic deformation was observed during compression to 8 % strain; where cracking at grain boundaries was noticed. The sample was further compressed to 15 %, where defects from previous compressive cycles are observed due to a much lower twinning stress and uncharacteristic behavior.

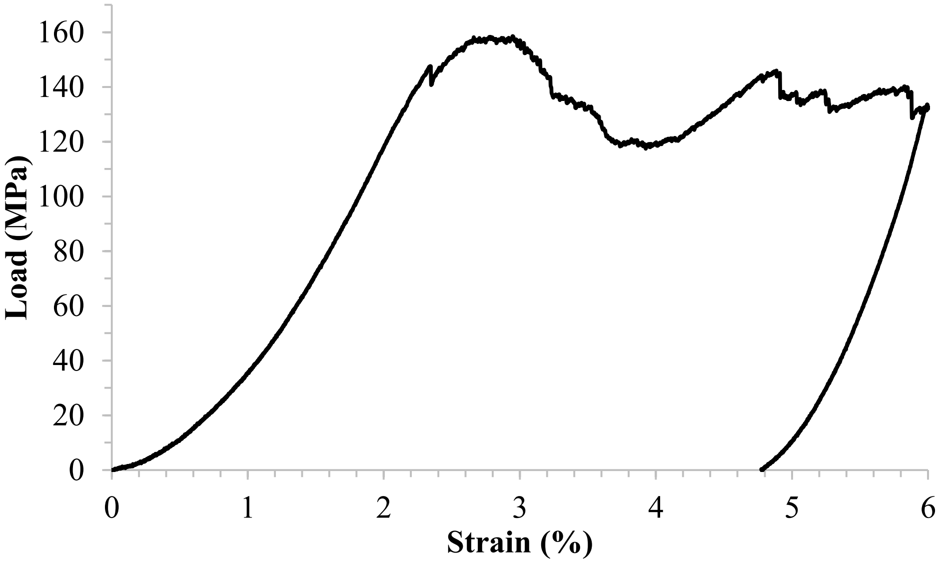

Figure 8.8: Compressive stress-strain behavior of a 3D printed part obtained from BM Ni-Mn-Ga powders. The sample was subjected to a compressive strain of 6 %.

Next, AM Ni-Mn-Ga samples made from BM powders were compressed at 373 K (100 °C), where the austenite phase is present. Due to the unpredictable mechanical behavior of the porous AM Ni-Mn-Ga, the compression test was strain controlled to 6 %. The mechanical response shown in Figure 8.8 is characteristic of metallic part subjected to compressive load [255], [256]. As observed, the sample undergoes a typical elastic mechanical response until approximately 150 MPa, for which failures in the microstructure begin occurring. These failures support the findings mentioned previously reported regarding the FEA modeling of compressive behavior of two-dimensional models. It is thought, stress concentrators cause failures in struts of the material due to irregular cross-sections. Moreover, the initial twinning stress of 200 MPa for bulk Ni-Mn-Ga was not reached in this case. Instead, failures occurred before stress induced martensite was observed which could be an indicator for overall strength of AM Ni-Mn-Ga material. In addition to this, the recovery for the AM Ni-Mn-Ga is substantially less when compared to the bulk counterparts. Specifically, approximately 4.8 % of the sample was plastically deformed and inherently unrecovered after compression. However, the shape memory effect has been previously reported in porous Ni-Ti materials, by using similar compressive testing methods [101], [257]. The failures from the AM Ni-Mn-Ga during high temperature compressions begin around 150MPa, most likely due to the aforementioned stress concentrators.

8.2 Magnetic Properties

This sub chapter focuses on the characterization of the magnetic properties for 3D printed and bulk Ni-Mn-Ga samples. The magnetic properties have been characterized by analyzing VSM data collected from magnetic hysteresis loops at constant temperatures, as well as low and high field magnetization measurements as a function of temperature. The results of these measurements are reported and discussed here.

Room temperature magnetic properties of AM Ni-Mn-Ga samples were measured by VSM. Aforementioned 3 mm diameter disks were mounted on a quartz rod to experience a hysteresis loop with a maximum and minimum field of ± 10 kOe. Figure 8.9 presents the results of the hysteresis loops for bulk and AM Ni-Mn-Ga samples. Magnetization loops were examined to conclude the magnetic properties (saturation magnetization and coercivity); these values are summarized in Table 8.4.

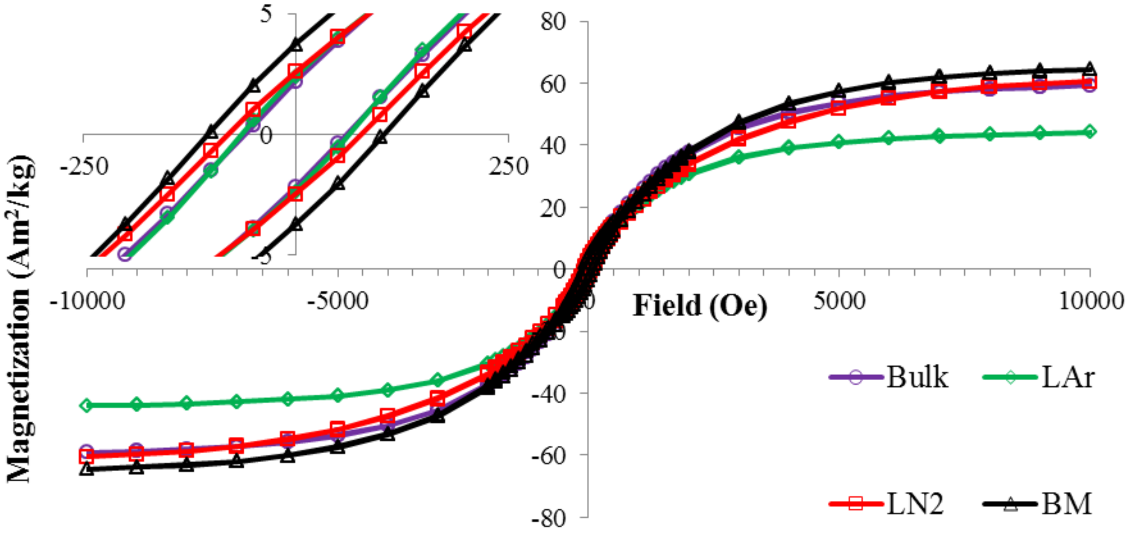

Figure 8.9: Magnetization curves for bulk (purple), LAr (green), LN$_2$ (red), and BM (black) Ni-Mn-Ga samples.

Based on these findings, the Ni-Mn-Ga samples display ferromagnetic behaviors at room temperature and furthermore soft magnetic properties based on coercivities. The saturation values were normalized based on the mass of the samples analyzed. The magnetic saturations obtained in AM Ni-Mn-Ga parts are comparable to those of bulk alloys reported elsewhere [235], [236], [258], [259]. The LAr part indicated the lowest magnetic saturation value of samples analyzed. The magnetic properties in Ni-Mn-Ga are significantly dependent on the structural ordering of the microstructure [260]; due to this phenomenon, X-ray diffraction (XRD) studies were conducted on each sample. The diffraction patterns show similar phases for BM and LN_2 parts by indexing characteristic peaks of near stoichiometric Ni_2MnGa; albeit the patterns collected for LAr show a very disordered structure with multiple Ni-Mn-Ga related phases present at room temperature. Furthermore, the reversible martensitic transformation temperature intervals in the LAr part is very broad, Figure 8.4. This wide DSC transformation behavior is often associated with atomic disordering in the form of micro-segregation, which is in agreement with the afroementioned XRD patterns collected for the LAr sample.

Table 8.4: Magnetic properties of 3D printed parts obtained from spark eroded and ball milled powders. The mass of the samples used in VSM testing is also indicated.

	Mass (g)	Saturation Magnetization (Am^2/kg)	Coercivity (Oe)
Bulk	0.024737	60.91	60
BM	0.042560	66.19	100
LAr	0.015261	45.57	64
LN_2	0.007652	62.65	78

In addition to the hysteresis loops, the magnetization of 3D printed Ni-Mn-Ga samples was studied at constant applied magnetic fields as a function of temperature. To achieve this, 3D printed BM Ni-Mn-Ga samples were mounted to a DMS Model 10 VSM with Teflon tape. A thermocouple fixed to the sample measured changes in temperature accurate to a tenth degree Kelvin. It should be acknowledged; the Curie temperatures measured using VSM and DSC show temperature discrepancies.

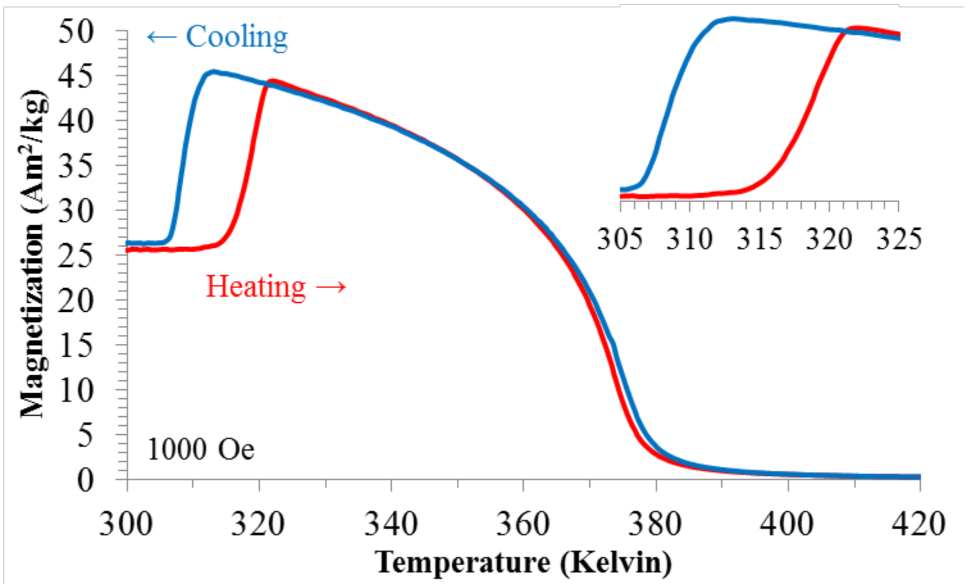

Figure 8.10: Low field (1000 Oe) magnetization measurements for 3D printed BM Ni-Mn-Ga as a function of temperature.

The sample underwent heating and cooling from room temperature to 413 K (140 °C) at a rate of approximately 10°/min. Figure 8.10 displays the magnetization results as a function of temperature for a constant field of 1000 Oe. Most notable are the sharp changes in magnetization ranging between approximately 308 K and 323 K (35 °C – 50 °C). These changes in magnetization correspond to the martensitic transformations. For heating, the transformation to austenite occurs between T_{As} = 314 K (41.33 °C) and T_{Af} = 321 K (48.32 °C). On the other hand, the martensitic transformation begins at T_{Ms} = 311 K (38.55 °C) and ends at T_Mf = 306 K (33.24 °C). Furthermore, the Curie temperature can be determined from the sharp decrease in magnetization as temperature increases. This phenomenon occurs at approximately T_c = 376 K (103 °C) due to the magnet susceptibility's inversely proportional relationship to temperature.

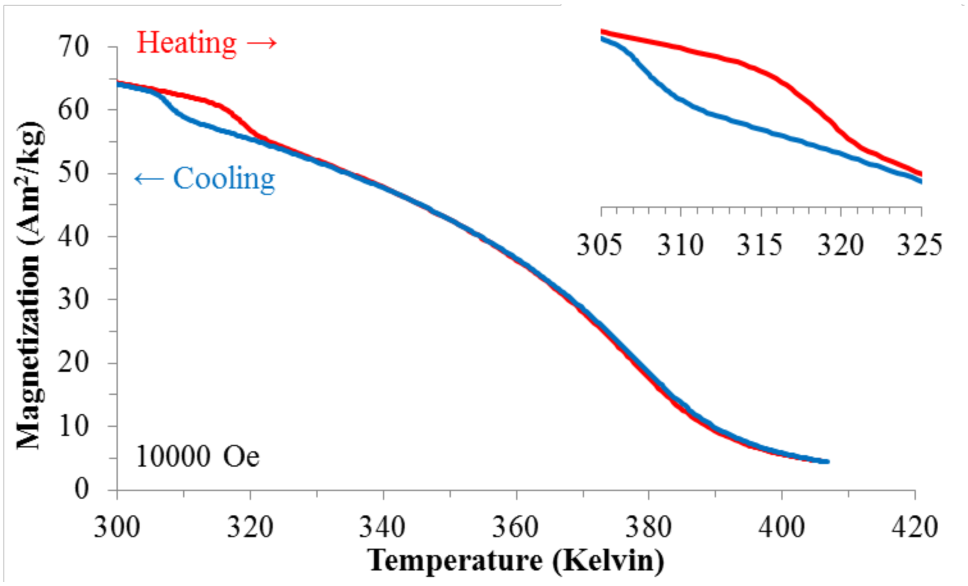

Figure 8.11: High field (10000 Oe) magnetization measurements for 3D printed BM Ni-Mn-Ga as a function of temperature.

Afterwards, the field was increased to 10000 Oe, while the sample experienced the same heating and cooling cycle during magnetization experiments. It is clearly observed that the higher external field inherently increases the magnetization at ambient temperatures. Moreover, the transformation temperatures were examined as previously mentioned. Transformation temperatures for the high temperature phase begin at T_{As} = 314 K (41.42 °C) and end at T_{Af} = 321 K (48.06 °C); while martensitic phase transformations temperatures are T_{Ms} = 311 K (38.01 °C) and T_{Mf} = 305 K (32.9 °C), respectively. The Curie temperature in the case of the high field magnetization experiment was determined to occur at approximately 403 K (130 °C).

The temperatures reported from low and high field magnetization measurements were compared to the transformation temperatures from DSC measurements. A summary of all three measurements can be found in Table 8.5. Neither method of analysis (VSM or DSC) shows significant differences between transformation temperatures.

Table 8.5: Summary of transformation temperatures for a particular 3D printed BM Ni-Mn-Ga sample. Transformation temperatures were determined using two methods: DSC and VSM.

	T_{As} (K)	T_{Af} (K)	T_{Ms} (K)	T_{Mf} (K)
0.1 T VSM	314.33	321.32	311.55	306.24
1 T VSM	314.42	321.06	311.01	305.90
DSC	314.83	325.12	313.83	303.17

9. Magnetic Shape Memory Effect in AM Ni-Mn-Ga Parts

The magnetomechanical experiments were conducted in a 0.97 T (Hallbach cylinder) rotating magnetic field. Samples of BM and LN_2 3D printed Ni-Mn-Ga parts with approximate dimensions of 5.55 mm length, 2.83 mm width, and 3.71 mm height were mounted using super glue to a custom device made of Vespel® and placed in the rotating magnetic field. A ceramic rod attached to the mount, interprets one dimensional deformation from the sample into a vertical translation; which is recorded using a linear extensometer (Heidenhain, Traunreut, Germany) with a resolution of approximately 10 nm. During investigations, the sample experienced five magnetic field rotations in order to record the magnetic shape memory effect (MSME). Subsequently, the 3D printed samples experienced approximately ten field rotations during initial tests. Afterwards, the samples sustained dynamic magnetomechanical training by imposing ten thousand field rotations to the parts causing several thousand actuations at a speed of 100 rpm for the first thousand rotations and 1000 rpm for the latter. Next, samples were thermo-magneto-mechanically trained by thermally cycling the samples several times between 253 K and 323 K (-20 °C and 50 °C) using hot/cool air under a rotating field of 30 rpm. MSME measurements were recorded in ten and five degree Kelvin increments. A thermocouple was placed on the surface of the sample to accurately record temperatures within a degree. For clarity, throughout this chapter individual samples will be identified via names as subchapters, as for example: Sample A, Sample B and Sample C. The results from the most representative samples will be reported for the parts printed from BM and LN_2 powders. The same magneto-mechanical experiments have been used to characterize magnetic field induced strains (MFIS) in other Ni-Mn-Ga alloys [12], [105], [261].

9.1 BM - Sample A

Initial magnetomechanical measurements were conducted on Sample A, BM 3D printed Ni-Mn-Ga sample in the “as sintered” condition; connoting twin variants have not undergone a reversible martensitic transformation prior to these investigations. Figure 9.1 (a) displays the result of the first MSME measurement. As observed in Figure 9.1 (a), the magnetic shape memory effect behaves in a wave-like motion, where maxima and minima occur every 180 °, due to the reverse of the magnetic field direction. The initial MSME measurement shows the magnetic shape memory effect in the 3D printed part produced a maximum deformation of approximately 0.0025 %.

A Ni-Mn-Ga single crystal of similar composition to the foam investigated in this study has been reported to produce reversible magnetic induced strains of about 6% [104]. Magnetic shape memory effects of this magnitude can completely conceal other phenomenon, such as magnetostriction; which is often discounted in Ni-Mn-Ga alloys due to much larger magnetic field induced strains (MFIS). Moreover, measuring the magnetostriction in Ni-Mn-Ga alloys requires the sample to be well constrained; to prevent any movement of twin variants during strong field (>1T) investigations. This results in demanding sample preparation with destructive analysis techniques. Albeit, magnetostriction of a single crystal Ni-Mn-Ga ($Ni_{49.1}Mn_{29.1}Ga_{21.2}$) with five-layered (5M) martensite has been investigated [262]. The magnetostriction value reported by Heczko [262] was 50 ppm (0.005%), which is substantially similar to the values observed in this initial magnetic shape memory effect measurements. This observation implies that two possible phenomena are occurring during MSME measurements. First, the shape memory effect initially observed is primarily due to the magnetostriction occurring in the 3D printed Ni-Mn-Ga part. Second, the effect might be due to the randomly distributed twin variants with multidirectional orientations, which would result in a near net zero magnetic shape memory effect due imposed constraints during martensitic transformations from neighboring twins. To elucidate between these two postulated circumstances, additional magneto-mechanical experiments were conducted.

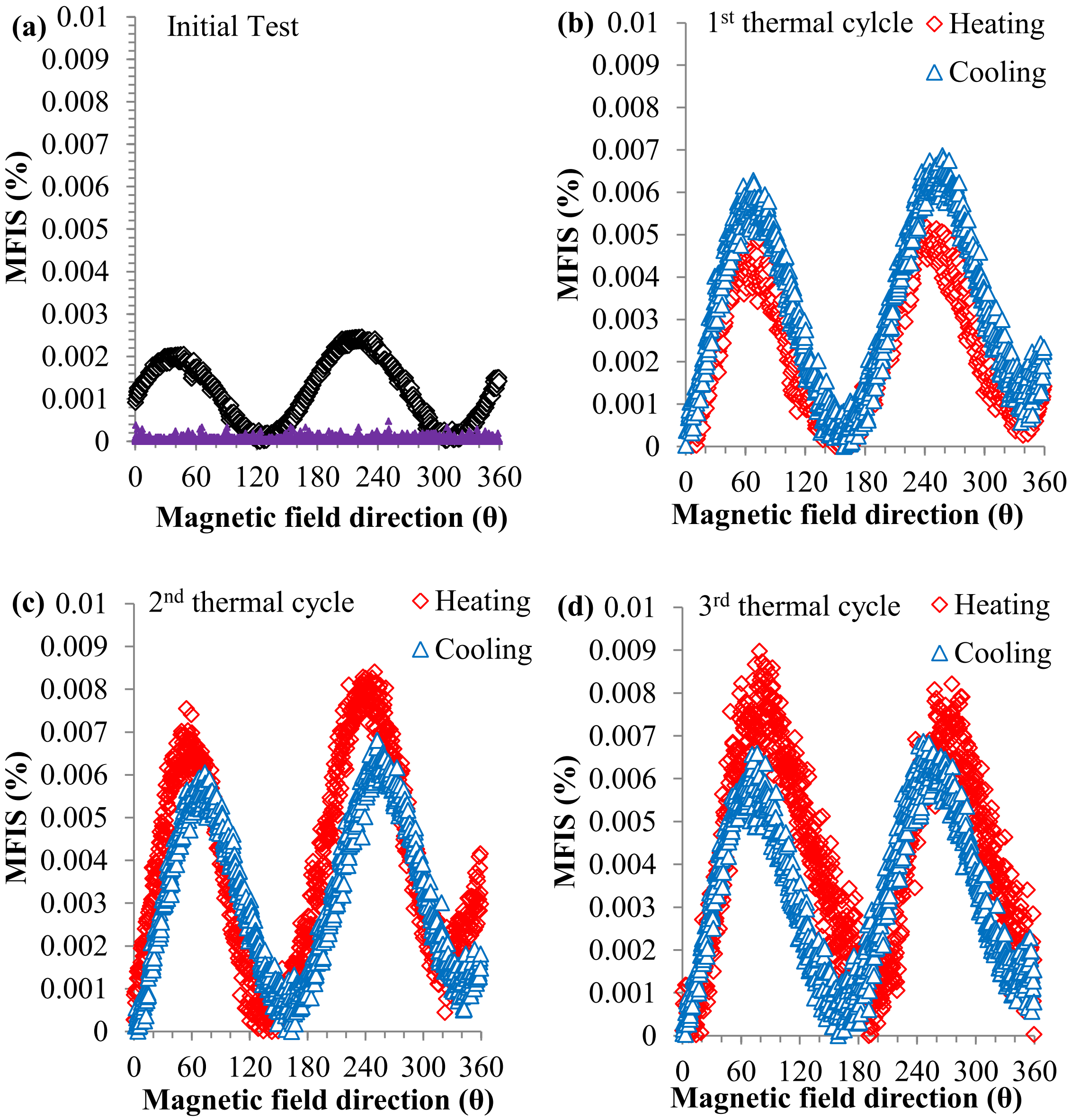

Figure 9.1: MFIS as function of magnetic field direction for a sintered sample A: (a) the initial measurement, and (b) first, (c) second, and (d) third heating/cooling cycle. The

MFIS was about 0.002 % during the initial measurement, followed by an order of magnitude increase to about 0.01 % after the third thermal cycle. In (a) purple indicates the response from calibration.

After the initial magnetic shape memory effect measurements, the revolving magnetic field was rotated at a speed of 100 rpm until the 3D printed Ni-Mn-Ga foam sample experienced 1,000 total revolutions. After that, the revolution speed was increased to 1,000 rpm until 10,000 revolutions were endured. After approximately 10,000 revolutions, the magnitude of the magnetic shape memory effect was tested. The result of this measurement was a magnetic shape memory response of approximately 0.001 %, which is even lower than the initial measurement of 0.0025 %. Next, the sample began thermo-magneto-mechanical training by heating and cooling from 293K to 323 K (20 °C to 50 °C) three consecutive times. The magnetic field was rotating at a constant speed of 30 rpm during thermal cycling. MSME measurements were recorded at 313 K (40 °C), where martensitic phase is known to be present, Figure 9.1 (b) – (d). It should be noted, the MFIS measurement system was calibrated using a ceramic reference sample. The reason for the calibration was to ensure the low MFIS responses observed were indeed, magnetic responses due to twin reorientation. The results from the calibration are shown in Figure 9.1 (a), indicated by the purple color. The level of noise is approximately an order of magnitude lower than the initial MFIS recorded.

The MSME for the 3D printed Ni-Mn-Ga sample is shown to increase initially upon the first thermal cycle. Heating the sample to 313 K (40 °C) for the first time resulted in the MSME increasing to a maximum value of approximately 0.005 %, which is double the initial measurement from the foam in the as sintered state, and exactly the magnetostriction value reported by Heczko [262]. After the sample reached a temperature of 323 K (50 °C), it was cooled to 213 K (40 °C) where another magnetomechanical measurement was taken. The 3D printed foam produced a MSME of approximately 0.0065 %, which is a slight increase from the initial heating measurement, Figure 9.1 (b). The 3D printed part was then cooled to 293 K (20 °C), and heated again, beginning the second heating sequence. Measurements were recorded at 40 °C during heating and cooling for the second time, respectively. The results of the MSME measurements from the second heating and cooling sequence are presented in Figure 9.1 (c). The 3D printed foam produced a 0.007 % response during the heating and 0.006 % during cooling. The result from the third heating and cooling cycle is displayed in Figure 9.1 (d). The MSME measurement from the third thermal cycle displays the 3D printed foam produced a MSME of approximately 0.009 % during the heating phase and 0.0068 % thru cooling.

At this point, the 3D printed Ni-Mn-Ga foam has produced a maximum MSME response in the order of 0.009 %, which is almost twice as large as the magnetostriction value reported earlier. This supplies supporting evidence against the possibility of the 3D printed part MSME belonging solely to magnetostriction, as postulated during the initial test. Furthermore, the peak intensities from initial measurements occur when the magnetic field direction is approximately 28 ° and 208 °, Figure 9.1 (a). After the dynamic-magneto-mechanical training, and during the first thermal cycle, it can be observed the peak of the MSME response shifts to when the magnetic field direction is approximately 58 ° and 238 °, Figure 9.1 (b). The peak position shifts even more over the analysis, in fact the third thermal cycle indicates the peak MSME occurs when the field direction is 75 ° and 255 °. These shifts could indicate the thermo-magneto-mechanical training causes twin variants in the 3D printed foam to reorient towards the preferred crystallographic martensitic direction (90 °).

The modulated martensitic phases possess an easy axis of magnetization, which is the c-axis in the Heusler coordinate system [263]. Therefore, a maximum magnetostress occurs when an external field is oriented 90 ° with respect to the c-axis. Based on the shifts where the maximum MSME occurs with respect to the magnetic field position, twin variants appear to be actively reorienting in such a way that the c-axis is perpendicular to the magnetic field. This reorientation of twin variants causes an increase in MFIS, as observed throughout this experiment, Figure 9.1 (a) – (d). Moreover, similar MSME behavior has been reported in less dense (54.8 % porous) part created by replication casting molten Ni-Mn-Ga in bimodal sodium aluminate preforms [105]. In addition, the MFIS response from the 3D printed Ni-Mn-Ga foam is comparable to Fe-Ga alloys (Galfenol), which have been shown to produce a magnetostriction value of 0.03 % [264]. Based on this, 3D printing Ni-Mn-Ga foams provides a viable method to manufacture mesoscale functional magnetic shape memory alloys.

9.2 BM –Sample B

Sample B is another 3D printed BM Ni-Mn-Ga part that underwent MSME measurements. Like Sample A, initial MFIS measurements were conducted on Sample B. The result from the initial measurement is shown in Figure 9.2 (a). The initial MFIS measurement produced a 0.001 % strain. Afterwards, the sample underwent the same thermo-magneto-mechanical training as described in Section 9.1. Afterwards, Sample B was thermally cycled while experiencing 30 magnetic rpm. Sample B experienced a series of 4 heating and cooling thermal cycles between 293K and 333 K (20 °C and 60 °C). Over these thermal cycles, the MFIS of sample B was recorded every 5 K to 10 K (5 °C – 10 °C). It was discovered that at 323 K (50 °C) during the 3rd heating cycle, Sample B produced the highest MFIS for all materials and samples tested in this research. The result of this measurement is shown in Figure 9.2 (b) for which sample B produced a MFIS of 0.01 %. Based on this result, sample B produced an order of magnitude increase of MFIS. This increase in MFIS is most likely due to the thermo-magneto-mechanical training, as previously discussed.

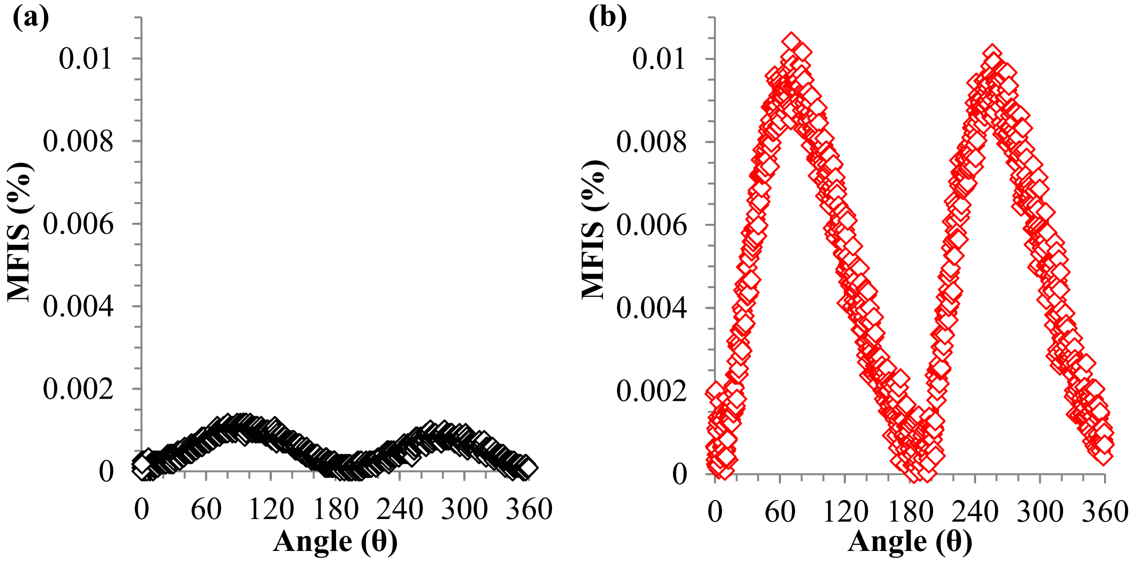

Figure 9.2: The MSME measurements from sample B at (a) the initial measurement and (b) at 323 K (50 °C) during the 3rd heating cycle. The MFIS obtained in this case is about 0.01 %.

In attempts to further understand the evolution of sample B's MFIS, the magnitude of the MSME measurements were plotted as a function temperature from heating and cooling. The result of this investigation is displayed in Figure 9.3. Perceiving the magnitude of the MFIS over the four thermal cycles, the steady increase in MFIS is obvious. With each subsequent heating and cooling cycle, the MFIS follows a particular trend of larger MFIS's during heating and lower responses during cooling. The lower MFIS during cooling is from dynamic crystallographic twin microstructure changes as a response to the revolving magnetic field. As briefly mentioned in section 9.1, twins with unfavorable orientation tend to reorient such that the c-axis is conforming towards the direction of the magnetic field. Over the course of several thousand cycles, most of the twin variants have crystallographic characteristics that have experienced the above-mentioned scenario. Nevertheless, the significance of this study portrays the ability to significantly increase the MFIS of porous BM Ni-Mn-Ga samples. Particularly shown for samples A and B, for which almost an order of magnitude increase in MFIS was achieved after thermo-magneto-mechanical training.

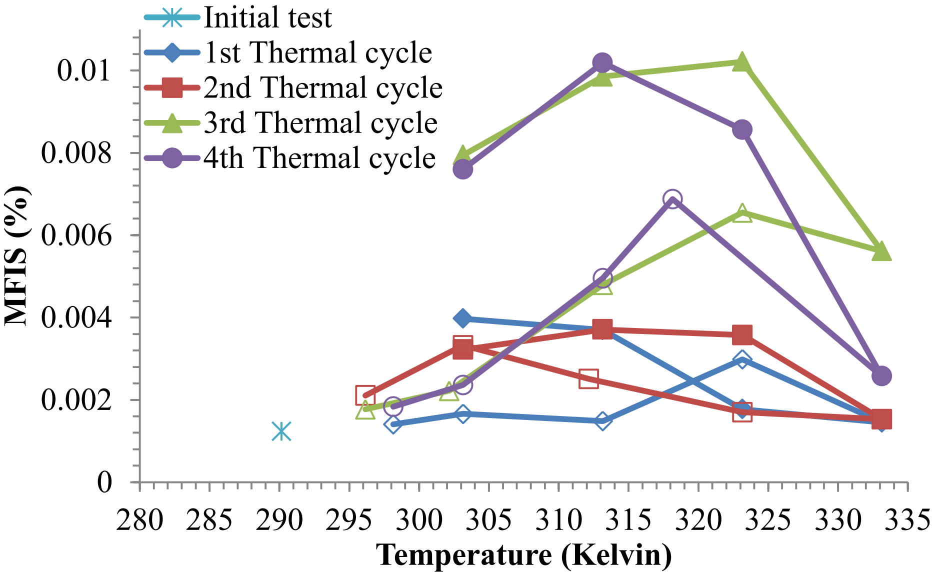

Figure 9.3: Sample B's MFIS evolution over four thermal cycles. Shapes of solid fill markers indicate heating while hollow markers represent cooling.

From the evaluation of Equation 4.8, the MFIS measured in Sample C, and the modulus of BM material found in Table 8.3; the stress applied by the BM sample was determined. Through the MFIS value of 0.01 %, the stress applied by the sample due to the magnetic field was calculated to be approximately 5.734 kN. This calculated value is similar to other Ni-Mn-Ga alloys reported elsewhere [265], [266].

9.3 LN_2 – Sample C

LN_2 parts were 3D printed and sintered with the intent to conducted MSME measurements. As previously mentioned, due to the hollow morphology of LN_2 powders, along with sintering at 1333 K (1060 °C) a very porous microstructure is obtained. Specifically, the porosities in the LN_2 3D printed parts are approximately 72 % of part volume. As mentioned previously, the 8.7 % MFIS was obtained in Ni-Mn-Ga porous metallic foam with 62 % porosity. Thus, based on previous reports [12], [134] claiming porosity increases MSME responses, the Ni-Mn-Ga part of 3D printed LN_2 should be comparable to the 8.7 % MFIS from the metallic foam [9]. In order to characterize the MFIS's the LN_2 parts underwent the exact thermo-magneto-mechanical training as previously described, ultimately experiencing several thousand field rotations along with thermal cycling. The LN_2 sintered parts possess reversible transformation temperatures below room temperature. Due to this, the thermal cycling was done between 253 K (-20 °C) and 293 K (20 °C). Sample C was thermally cycled between 253 K (-20 °C) and 293 K (20 °C) three times, recording temperatures between 5 and 10 °K intervals. Figure 9.4 (a) and (b) display results from MFIS measurements of sample C during (a) the first cooling cycle at 282 K (9 °C) and (b) the third cooling cycle at 265 K (-8 °C).

The MFIS results presented in Figure 9.4 (a) and (b) do not follow the trend of increased MFIS's over thermal cycling. During the initial test, Figure 9.4 (a), MFIS values as low as 0.002 % were reported from the extremely porous sample. After two subsequent heating and cooling cycles, the MFIS was again analyzed. The MFIS during the third cooling cycle at 263 K (-8 °C) had a magnitude of approximately 0.002 %, Figure 9.4 (b). The sample was cooled by flowing air through the apparatus which had been cooled using liquid nitrogen. What is most notable about the MFIS response in the case of LN_2 part is the fact of no increase in MSME was observed over the thermo-magneto-mechanical training. Furthermore, the overall MFIS value is remarkably low for possessing a remarkably high porosity.

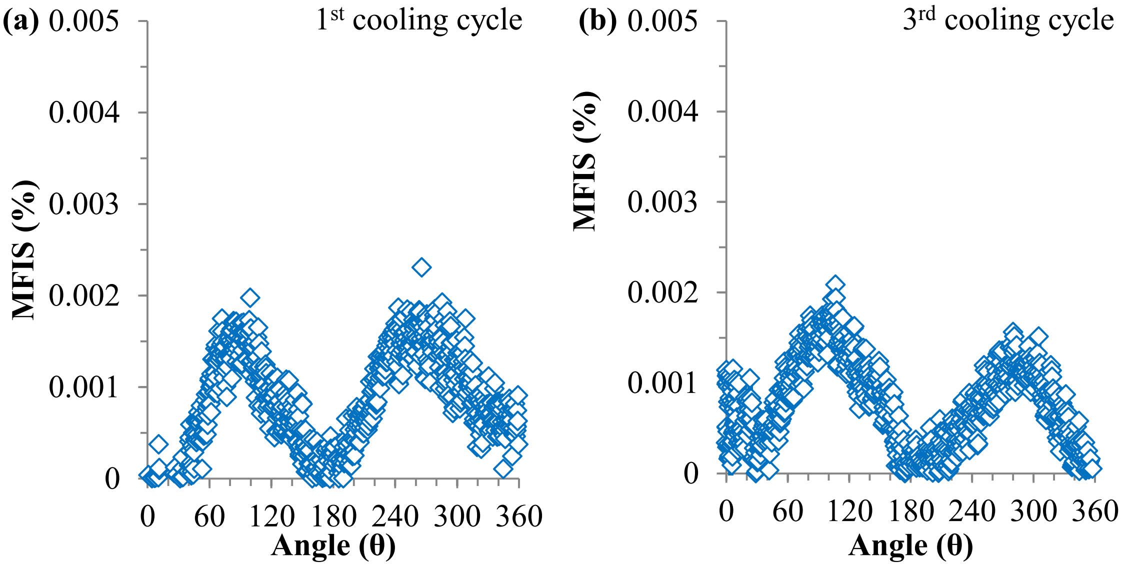

Figure 9.4: MFIS results from sintered LN_2 Ni-Mn-Ga parts during (a) the first cooling cycle at 282 K (9 °C) and (b) the third cooling cycle at 265 K (-8 °C).

The low MFIS value could be explained by difficulties encountered during sintering of the LN_2 parts due to the irregular shaped material; which is a direct result of the spark erosion process for Ni-Mn-Ga material. For example, the presence irregular shaped material could prohibit sintering between particulate materials. In addition to this, the irregular shaped material has been shown to possess chemical inhomogeneity. Therefore, it is possible for the LN_2 to possess undesirable properties after sintering, such as unexpected transformation temperatures. Furthermore, operating the IBAG at low temperatures proved to be detrimental for the super glue used to hold the sample in place. The sample broke free from the mounting apparatus as a result of the forces created from the rotating magnet and the ferromagnetic interaction, along with embrittled super glue. Due to this, it became difficult to measure the MFIS of LN_2 samples. Nevertheless, LN_2 sample C has shown the ability to produce some magnitude of MSME response, which is this case is a maximum of 0.002 %.

10. Conclusion

This research has displayed the ability to produce complex near net shaped components from Ni-Mn-Ga powders through additive manufacturing. The additive manufacturing technique used to manufacture these parts is binder jetting. Post printing, Ni-Mn-Ga parts have been sintered and characterized. Based on the work carried out in this research it can be concluded:

- Three different Ni-Mn-Ga powders have been synthesized and characterized for usage in binder jetting 3D printing.
- Through this research, Ni-Mn-Ga powders have been utilized to produce complex geometries from LN_2, LAr, and BM powders.
- Due to various powder morphologies and combined with sintering conditions, this work provides the flexibility to control the density of additive manufactured Ni-Mn-Ga parts between 26.5 % and 83.6 %.
- Additive manufactured Ni-Mn-Ga parts show reversible martensitic transformations, which is a necessary condition for the shape memory effect. Crystallography investigations confirm the presence of modulated martensitic phases in 3D printed Ni-Mn-Ga parts from all three powders.
- The magnetic and mechanical properties of the parts have been characterized. These parts displayed a maximum magnetic field induced strains in the order of 0.01%, which indicates successful 4D printing of Ni-Mn-Ga.

References

[1] I. Vronsky, "History of Gold | Gold Eagle," *http://www.gold-eagle.com/article/history-gold*, 01-Jan-1997. [Online]. Available: http://www.gold-eagle.com/article/history-gold. [Accessed: 18-Oct-2017].

[2] E. Photos, "The question of meteoritic versus smelted nickel-rich iron: Archaeological evidence and experimental results," *World Archaeol.*, vol. 20, no. 3, pp. 403–421, Feb. 1989.

[3] D. C. Lagoudas, *Shape Memory Alloys: Modeling and Engineering Applications*. Springer, 2008.

[4] K. Ullakko, J. K. Huang, C. Kantner, R. C. O'Handley, and V. V. Kokorin, "Large magnetic-field-induced strains in Ni2MnGa single crystals," *Appl. Phys. Lett.*, vol. 69, no. 13, pp. 1966–1968, Sep. 1996.

[5] R. C. O'Handley, S. J. Murray, M. Marioni, H. Nembach, and S. M. Allen, "Phenomenology of giant magnetic-field-induced strain in ferromagnetic shape-memory materials (invited)," *J. Appl. Phys.*, vol. 87, no. 9, pp. 4712–4717, Apr. 2000.

[6] S. Roth, U. Gaitzsch, M. Pötschke, and L. Schultz, "Magneto-Mechanical Behaviour of Textured Polycrystals of NiMnGa Ferromagnetic Shape Memory Alloys," *Adv. Mater. Res.*, vol. 52, pp. 29–34, 2008.

[7] U. Gaitzsch, J. Romberg, M. Pötschke, S. Roth, and P. Müllner, "Stable magnetic-field-induced strain above 1% in polycrystalline Ni–Mn–Ga," *Scr. Mater.*, vol. 65, no. 8, pp. 679–682, Oct. 2011.

[8] "2010 Index IEEE Transactions on Ultrasonics, Ferroelectrics and Frequency Control Vol. 57," *IEEE Trans. Ultrason. Ferroelectr. Freq. Control*, vol. 57, no. 12, pp. 2851–2904, Dec. 2010.

[9] M. Chmielus, X. X. Zhang, C. Witherspoon, D. C. Dunand, and P. Müllner, "Giant magnetic-field-induced strains in polycrystalline Ni–Mn–Ga foams," *Nat. Mater.*, vol. 8, no. 11, pp. 863–866, Nov. 2009.

[10] A. Sozinov, A. A. Likhachev, N. Lanska, and K. Ullakko, "Giant magnetic-field-induced strain in NiMnGa seven-layered martensitic phase," *Appl. Phys. Lett.*, vol. 80, no. 10, pp. 1746–1748, Mar. 2002.

[11] P. Müllner, V. A. Chernenko, and G. Kostorz, "Large cyclic magnetic-field-induced deformation in orthorhombic (14M) Ni–Mn–Ga martensite," *J. Appl. Phys.*, vol. 95, no. 3, pp. 1531–1536, Jan. 2004.

[12] P. Müllner, X. X. Zhang, Y. Boonyongmaneerat, C. Witherspoon, M. Chmielus, and D. C. Dunand, "Recent Developments in Ni-Mn-Ga Foam Research," *Mater. Sci. Forum*, vol. 635, pp. 119–124, 2010.

[13] W. Frazier, "Metal Additive Manufacturing: A Review," *J. Mater. Eng. Perform.*, vol. 23, no. 6, pp. 1917–1928, Jun. 2014.

[14] H. Seitz, W. Rieder, S. Irsen, B. Leukers, and C. Tille, "Three-dimensional printing of porous ceramic scaffolds for bone tissue engineering," *J. Biomed. Mater. Res. B Appl. Biomater.*, vol. 74B, no. 2, pp. 782–788, Aug. 2005.

[15] B. R. Utela, D. Storti, R. L. Anderson, and M. Ganter, "Development process for custom three-dimensional printing (3DP) material systems," *J. Manuf. Sci. Eng. Trans. ASME*, vol. 132, no. 1, pp. 110081–110089, Feb. 2010.

[16] A. E. Berkowitz and J. L. Walter, “Spark erosion: A method for producing rapidly quenched fine powders,” *J. Mater. Res.*, vol. 2, no. 2, pp. 277–288, Apr. 1987.

[17] A. E. Berkowitz and J. L. Walter, “Amorphous particles produced by spark erosion,” *Mater. Sci. Eng.*, vol. 55, no. 2, pp. 275–287, Sep. 1982.

[18] A. E. Berkowitz, J. L. Walter, and K. F. Wall, “Magnetic Properties of Amorphous Particles Produced by Spark Erosion,” *Phys. Rev. Lett.*, vol. 46, no. 22, pp. 1484–1487, Jun. 1981.

[19] A. E. Berkowitz *et al.*, “Hollow metallic microspheres produced by spark erosion,” *Appl. Phys. Lett.*, vol. 85, no. 6, pp. 940–942, Aug. 2004.

[20] V. C. Solomon, J.-I. Hong, Y. Tang, A. E. Berkowitz, and D. J. Smith, “Electron microscopy investigation of spark-eroded Ni–Mn–Ga ferromagnetic shape-memory alloy particles,” *Scr. Mater.*, vol. 56, no. 7, pp. 593–596, Apr. 2007.

[21] V. C. Solomon, D. J. Smith, Y. Tang, and A. E. Berkowitz, “Microstructural characterization of Ni-Mn-Ga ferromagnetic shape memory alloy powders,” *J. Appl. Phys.*, vol. 95, no. 11, pp. 6954–6956, Jun. 2004.

[22] V. A. Chernenko and S. Besseghini, “Ferromagnetic shape memory alloys: Scientific and applied aspects,” *Sens. Actuators Phys.*, vol. 142, no. 2, pp. 542–548, Apr. 2008.

[23] S. Shiva, I. A. Palani, S. K. Mishra, C. P. Paul, and L. M. Kukreja, “Investigations on the influence of composition in the development of Ni–Ti shape memory alloy using laser based additive manufacturing,” *Opt. Laser Technol.*, vol. 69, pp. 44–51, Jun. 2015.

[24] B. V. Krishna, S. Bose, and A. Bandyopadhyay, “Laser Processing of Net-Shape NiTi Shape Memory Alloy,” *Metall. Mater. Trans. A*, vol. 38, no. 5, pp. 1096–1103, Apr. 2007.

[25] K. V. Wong and A. Hernandez, “A Review of Additive Manufacturing,” *ISRN Mech. Eng.*, pp. 1–10, Jan. 2012.

[26] M. B. Mawale, A. M. Kuthe, and S. W. Dahake, “Additive layered manufacturing: State-of-the-art applications in product innovation,” *Concurr. Eng.*, vol. 24, no. 1, pp. 94–102, Mar. 2016.

[27] J. J. Beaman, J. W. Barlow, D. L. Bourell, R. H. Crawford, H. L. Marcus, and K. P. McAlea, *Solid Freeform Fabrication: A New Direction in Manufacturing: with Research and Applications in Thermal Laser Processing*. Springer Science & Business Media, 2013.

[28] W. R. Morrow, H. Qi, I. Kim, J. Mazumder, and S. J. Skerlos, “Environmental aspects of laser-based and conventional tool and die manufacturing,” *J. Clean. Prod.*, vol. 15, no. 10, pp. 932–943, Jan. 2007.

[29] Y. Luo, Z. Ji, M. C. Leu, and R. Caudill, “Environmental performance analysis of solid freedom fabrication processes,” in *Proceedings of the 1999 IEEE International Symposium on Electronics and the Environment (Cat. No.99CH36357)*, 1999, pp. 1–6.

[30] B. Utela, D. Storti, R. Anderson, and M. Ganter, “A review of process development steps for new material systems in three dimensional printing (3DP),” *J. Manuf. Process.*, vol. 10, no. 2, pp. 96–104, Jul. 2008.

[31] C. X. F. Lam, X. M. Mo, S. H. Teoh, and D. W. Hutmacher, "Scaffold development using 3D printing with a starch-based polymer," *Mater. Sci. Eng. C*, vol. 20, no. 1, pp. 49–56, May 2002.

[32] J. Suwanprateeb, "Improvement in mechanical properties of three-dimensional printing parts made from natural polymers reinforced by acrylate resin for biomedical applications: a double infiltration approach," *Polym. Int.*, vol. 55, no. 1, pp. 57–62, Jan. 2006.

[33] L. Li and Q. Jiang, "Editorial on the original article entitled '3D printing of composite calcium phosphate and collagen scaffolds for bone regeneration' published in the Biomaterials on February 14, 2014," *Ann. Transl. Med.*, vol. 3, no. Suppl 1, May 2015.

[34] D. Godlinski and S. Morvan, "Steel Parts with Tailored Material Gradients by 3D-Printing Using Nano-Particulate Ink," *Mater. Sci. Forum*, vol. 492–493, pp. 679–684, 2005.

[35] J. Moon, A. C. Caballero, L. Hozer, Y.-M. Chiang, and M. J. Cima, "Fabrication of functionally graded reaction infiltrated SiC–Si composite by three-dimensional printing (3DP^{TM}) process," *Mater. Sci. Eng. A*, vol. 298, no. 1, pp. 110–119, Jan. 2001.

[36] E. M. Sachs, C. Hadjiloucas, S. Allen, and H. J. Yoo, "Metal and ceramic containing parts produced from powder using binders derived from salt," US6508980 B1, 21-Jan-2003.

[37] Z. C. Cordero, D. H. Siddel, W. H. Peter, and A. M. Elliott, "Strengthening of ferrous binder jet 3D printed components through bronze infiltration," *Addit. Manuf.*, vol. 15, no. Supplement C, pp. 87–92, May 2017.

[38] S. Ford and M. Despeisse, "Additive manufacturing and sustainability: an exploratory study of the advantages and challenges," *J. Clean. Prod.*, vol. 137, no. Supplement C, pp. 1573–1587, Nov. 2016.

[39] J. Liu and M. Rynerson, "Method for article fabrication using carbohydrate binder," US6585930 B2, 01-Jul-2003.

[40] H. J. Jee and E. Sachs, "A visual simulation technique for 3D printing," *Adv. Eng. Softw.*, vol. 31, no. 2, pp. 97–106, Feb. 2000.

[41] J. F. Bredt, T. C. Anderson, and D. B. Russell, "Three dimensional printing material system and method," US6610429 B2, 26-Aug-2003.

[42] D. Brodkin, C. Panzera, and P. Panzera, "Dental restorations formed by solid free-form fabrication methods," US6994549 B2, 7-2006.

[43] A. M. Lorenz, E. M. Sachs, and S. M. Allen, "Techniques for infiltration of a powder metal skeleton by a similar alloy with melting point depressed," US6719948 B2, 13-Apr-2004.

[44] J. Liu and M. L. Ryneson, "Blended powder solid-supersolidus liquid phase sintering," US7070734 B2, 04-Jul-2006.

[45] F. K. Feenstra, "Method for making a dental element," US6955776 B1, 18-Oct-2005.

[46] D. R. White, A. W. Urquhart, M. K. Aghajanian, and D. K. Creber, "Metal matrix composites," US4828008 A, 09-May-1989.

[47] T. B. Sercombe and G. B. Schaffer, "Infiltrated aluminum preforms," US6823928 B2, 30-Nov-2004.

[48] T. Davidson *et al.*, “Three-dimensional printer,” US7037382 B2, 02-May-2006.
[49] A. Lorenz, E. Sachs, and S. Allen, “Freeze-off limits in transient liquid-phase infiltration,” *Metall. Mater. Trans. A*, vol. 35, no. 2, pp. 641–653, Feb. 2004.
[50] E. M. Sachs *et al.*, “Jetting layers of powder and the formation of fine powder beds thereby,” US6596224 B1, 22-Jul-2003.
[51] M. Cima *et al.*, “Three-dimensional printing techniques,” US5387380 A, 07-Feb-1995.
[52] L. G. Cima and M. J. Cima, “Preparation of medical devices by solid free-form fabrication methods,” US5490962 A, 13-Feb-1996.
[53] J. F. Bredt, T. C. Anderson, and D. B. Russell, “Three dimensional printing materials system,” US6416850 B1, 09-Jul-2002.
[54] M. Lanzetta and E. Sachs, “Improved surface finish in 3D printing using bimodal powder distribution,” *Rapid Prototyp. J.*, vol. 9, no. 3, pp. 157–166, Aug. 2003.
[55] J. F. Bredt and T. Anderson, “Method of three dimensional printing,” US5902441 A, 11-May-1999.
[56] J. T. Snow, W. Plante, and R. S. Zeller, “High-efficiency metal membrane getter element and process for making,” US5456740 A, 10-Oct-1995.
[57] A. Conte and F. Mazza, “Getter system for purifying the confinement volume in process chambers,” US6299746 B1, 09-Oct-2001.
[58] J. V. deceased, M. Tuniuns, and K. Rydinge, “Method of preventing clogging of nozzles,” US5781214 A, 14-Jul-1998.
[59] M. W. Keyes and D. A. B. Jr, “Print head shutter,” US6726306 B2, 27-Apr-2004.
[60] J. F. Bredt, “Binder composition for use in three dimensional printing,” US5660621 A, 26-Aug-1997.
[61] A. Pfister, R. Landers, A. Laib, U. Hübner, R. Schmelzeisen, and R. Mülhaupt, “Biofunctional rapid prototyping for tissue-engineering applications: 3D bioplotting versus 3D printing,” *J. Polym. Sci. Part Polym. Chem.*, vol. 42, no. 3, pp. 624–638, Feb. 2004.
[62] H.-R. Wang, M. J. Cima, B. D. Kernan, and E. M. Sachs, “Alumina-doped silica gradient-index (GRIN) lenses by slurry-based three-dimensional printing (S-3DP^{TM}),” *J. Non-Cryst. Solids*, vol. 349, pp. 360–367, Dec. 2004.
[63] C. Oriakhi and T. M. Lambright, “Calcium aluminate cement compositions for solid freeform fabrication,” US7258736 B2, 21-Aug-2007.
[64] E. M. Sachs, J. S. Haggerty, M. J. Cima, and P. A. Williams, “Three-dimensional printing techniques,” US5204055 A, 20-Apr-1993.
[65] P. Greil, “Polymer Derived Engineering Ceramics,” *Adv. Eng. Mater.*, vol. 2, no. 6, pp. 339–348, Jun. 2000.
[66] J. Moon, J. E. Grau, V. Knezevic, M. J. Cima, and E. M. Sachs, “Ink-Jet Printing of Binders for Ceramic Components,” *J. Am. Ceram. Soc.*, vol. 85, no. 4, pp. 755–762, Apr. 2002.
[67] J. Suwanprateeb and R. Chumnanklang, “Three-dimensional printing of porous polyethylene structure using water-based binders,” *J. Biomed. Mater. Res. B Appl. Biomater.*, vol. 78B, no. 1, pp. 138–145, Jul. 2006.
[68] J. Shen, “Material system for use in three dimensional printing,” US7049363 B2, 23-May-2006.

[69] J. F. Bredt, S. Clark, and G. Gilchrist, “Three dimensional printing material system and method,” US7087109 B2, 08-Aug-2006.

[70] D. C. Monkhouse, S. Kumar, C. W. Rowe, and J. Yoo, “Rapid prototyping and manufacturing process,” US6547994 B1, 15-Apr-2003.

[71] M. Yasrebi, R. Van Ginhoven, W. W. Kemp, B. J. Schmidt, and D. H. Sturgis, “Hydroxylated Carboxylic Acid Monomers as Stabilizing Agents for Yttria–Alumina Aqueous Suspensions,” *J. Am. Ceram. Soc.*, vol. 88, no. 3, pp. 536–539, Mar. 2005.

[72] W. S. Koegler and L. G. Griffith, “Osteoblast response to PLGA tissue engineering scaffolds with PEO modified surface chemistries and demonstration of patterned cell response,” *Biomaterials*, vol. 25, no. 14, pp. 2819–2830, Jun. 2004.

[73] D. K. Bynum, “Automated manufacturing system using thin sections,” US5088047 A, 11-Feb-1992.

[74] B. Khoshnevis, “Selective inhibition of bonding of power particles for layered fabrication of 3-D objects,” US6589471 B1, 08-Jul-2003.

[75] Yun Bai and Christopher B Williams, “An exploration of binder jetting of copper,” *Rapid Prototyp. J.*, vol. 21, no. 2, pp. 177–185, Mar. 2015.

[76] H. J. V. Tyrrell, “The origin and present status of Fick’s diffusion law,” *J. Chem. Educ.*, vol. 41, no. 7, p. 397, Jul. 1964.

[77] H. E. White and R. M. Shremp, “Beryllium Oxide: I*,” *J. Am. Ceram. Soc.*, vol. 22, no. 1–12, pp. 185–189, Dec. 1939.

[78] R. K. Bordia, S.-J. L. Kang, and E. A. Olevsky, “Current understanding and future research directions at the onset of the next century of sintering science and technology,” *J. Am. Ceram. Soc.*, vol. 100, no. 6, pp. 2314–2352, Jun. 2017.

[79] S.-J. L. Kang, *Sintering: Densification, Grain Growth and Microstructure*. Butterworth-Heinemann, 2004.

[80] M. N. Rahaman, *Sintering of Ceramics*. CRC Press, 2007.

[81] A. K. Varshneya, *Fundamentals of Inorganic Glasses*. Elsevier, 2013.

[82] J. G. R. Rockland, “The determination of the mechanism of sintering,” *Acta Metall.*, vol. 15, no. 2, pp. 277–286, Feb. 1967.

[83] X. Guo, M. M. Smedskjaer, and J. C. Mauro, “Linking Equilibrium and Nonequilibrium Dynamics in Glass-Forming Systems,” *J. Phys. Chem. B*, vol. 120, no. 12, pp. 3226–3231, Mar. 2016.

[84] R. Brückner and Y. Yue, “Non-Newtonian flow behaviour of glass melts as a consequence of viscoelasticity and anisotropic flow,” *J. Non-Cryst. Solids*, vol. 175, no. 2, pp. 118–128, Oct. 1994.

[85] R. L. Coble, “Sintering Crystalline Solids. I. Intermediate and Final State Diffusion Models,” *J. Appl. Phys.*, vol. 32, no. 5, pp. 787–792, May 1961.

[86] D. L. Johnson, “A General Model for the Intermediate Stage of Sintering,” *J. Am. Ceram. Soc.*, vol. 53, no. 10, pp. 574–577, Oct. 1970.

[87] J. Zhao and M. P. Harmer, “Sintering kinetics for a model final-stage microstructure: A study of AI2O3,” *Philos. Mag. Lett.*, vol. 63, no. 1, pp. 7–14, Jan. 1991.

[88] S.-J. L. Kang and Y.-I. Jung, “Sintering kinetics at final stage sintering: model calculation and map construction,” *Acta Mater.*, vol. 52, no. 15, pp. 4573–4578, Sep. 2004.

[89] L. C. Chang and T. A. Read, “Plastic Deformation and Diffusionless Phase Changes in Metals the Bold- Cadmium Beta Phase,” Columbia University, NYO-755, Nov. 1950.
[90] W. J. Buehler, J. V. Gilfrich, and R. C. Wiley, “Effect of Low-Temperature Phase Changes on the Mechanical Properties of Alloys near Composition TiNi,” *J. Appl. Phys.*, vol. 34, no. 5, pp. 1475–1477, May 1963.
[91] K. N. Melton and O. Mercier, “The mechanical properties of NiTi-based shape memory alloys,” *Acta Metall.*, vol. 29, no. 2, pp. 393–398, Feb. 1981.
[92] F. E. Wang, W. J. Buehler, and S. J. Pickart, “Crystal Structure and a Unique ``Martensitic'' Transition of TiNi,” *J. Appl. Phys.*, vol. 36, no. 10, pp. 3232–3239, Oct. 1965.
[93] L. M. Schetky, “Shape-Memory Alloys,” in *Kirk-Othmer Encyclopedia of Chemical Technology*, John Wiley & Sons, Inc., 2000.
[94] C. M. Wayman and J. D. Harrison, “The origins of the shape memory effect,” *JOM*, vol. 41, no. 9, pp. 26–28, Sep. 1989.
[95] M. O. Gök, M. Z. Bilir, and B. H. Gürcüm, “Shape-Memory Applications in Textile Design,” *Procedia - Soc. Behav. Sci.*, vol. 195, no. Supplement C, pp. 2160–2169, Jul. 2015.
[96] K. Otsuka and C. M. Wayman, *Shape Memory Materials*. Cambridge University Press, 1999.
[97] H. E. Karaca, I. Karaman, B. Basaran, Y. I. Chumlyakov, and H. J. Maier, “Magnetic field and stress induced martensite reorientation in NiMnGa ferromagnetic shape memory alloy single crystals,” *Acta Mater.*, vol. 54, no. 1, pp. 233–245, Jan. 2006.
[98] S. Dash and N. Brown, “An investigation of the origin and growth of annealing twins,” *Acta Metall.*, vol. 11, no. 9, pp. 1067–1075, Sep. 1963.
[99] S. Mahajan, C. S. Pande, M. A. Imam, and B. B. Rath, “Formation of annealing twins in f.c.c. crystals,” *Acta Mater.*, vol. 45, no. 6, pp. 2633–2638, Jun. 1997.
[100] K. Lu and W. T. Reynolds, “3DP process for fine mesh structure printing,” *Powder Technol.*, vol. 187, no. 1, pp. 11–18, Oct. 2008.
[101] Y. Zhao, M. Taya, Y. Kang, and A. Kawasaki, “Compression behavior of porous NiTi shape memory alloy,” *Acta Mater.*, vol. 53, no. 2, pp. 337–343, Jan. 2005.
[102] A. E. Clark, J. P. Teter, and O. D. McMasters, “Magnetostriction ‘“jumps”’ in twinned Tb0.3Dy0.7Fe1.9,” *J. Appl. Phys.*, vol. 63, no. 8, pp. 3910–3912, Apr. 1988.
[103] S.-E. Park and T. R. Shrout, “Ultrahigh strain and piezoelectric behavior in relaxor based ferroelectric single crystals,” *J. Appl. Phys.*, vol. 82, no. 4, pp. 1804–1811, Aug. 1997.
[104] S. J. Murray, M. A. Marioni, A. M. Kukla, J. Robinson, R. C. O’Handley, and S. M. Allen, “Large field induced strain in single crystalline Ni–Mn–Ga ferromagnetic shape memory alloy,” *J. Appl. Phys.*, vol. 87, no. 9, pp. 5774–5776, May 2000.
[105] C. Witherspoon, P. Zheng, M. Chmielus, D. C. Dunand, and P. Müllner, “Effect of porosity on the magneto-mechanical behavior of polycrystalline magnetic shape-memory Ni–Mn–Ga foams,” *Acta Mater.*, vol. 92, pp. 64–71, Jun. 2015.

[106] W. H. Meiklejohn and C. P. Bean, “New Magnetic Anisotropy,” *Phys. Rev.*, vol. 102, no. 5, pp. 1413–1414, Jun. 1956.

[107] E. P. Wohlfarth, “Relations between Different Modes of Acquisition of the Remanent Magnetization of Ferromagnetic Particles,” *J. Appl. Phys.*, vol. 29, no. 3, pp. 595–596, Mar. 1958.

[108] P. Gaunt, G. Hadjipanayis, and D. Ng, “Remanence relationships and domain wall pinning in ferromagnets,” *J. Magn. Magn. Mater.*, vol. 54–57, no. Part 2, pp. 841–842, Feb. 1986.

[109] D. Bilardello and K. P. Kodama, “Measuring remanence anisotropy of hematite in red beds: Anisotropy of high-field isothermal remanence magnetization (hf-AIR),” *Geophys. J. Int.*, vol. 178, no. 3, pp. 1260–1272, Sep. 2009.

[110] Y. Takahashi, “On the Origin of the Curie-Weiss Law of the Magnetic Susceptibility in Itinerant Electron Ferromagnetism,” *J. Phys. Soc. Jpn.*, vol. 55, no. 10, pp. 3553–3573, 1986.

[111] F. Heusler, “Über Manganbronze und über die Synthese magnetisierbarer Legierungen aus unmagnetischen Metallen,” *Angew. Chem.*, vol. 17, no. 9, pp. 260–264, Feb. 1904.

[112] F. Heusler and E. Take, “The nature of the Heusler alloys,” *Trans. Faraday Soc.*, vol. 8, no. October, pp. 169–184, Jan. 1912.

[113] A. Gonzàlez-Comas *et al.*, “Premartensitic and martensitic phase transitions in ferromagnetic ${\mathrm{Ni}}_{2}\mathrm{MnGa}$,” *Phys. Rev. B*, vol. 60, no. 10, pp. 7085–7090, Sep. 1999.

[114] P. J. Webster, K. R. A. Ziebeck, S. L. Town, and M. S. Peak, “Magnetic order and phase transformation in Ni2MnGa,” *Philos. Mag. Part B*, vol. 49, no. 3, pp. 295–310, Mar. 1984.

[115] R. M. Galera, J. Pierre, E. Siaud, and A. P. Murani, “Magnetic and electrical properties of heusler alloys with rare earths: RInAg2,” *J. Common Met.*, vol. 97, no. Supplement C, pp. 151–161, Feb. 1984.

[116] L. Righi, F. Albertini, L. Pareti, A. Paoluzi, and G. Calestani, “Commensurate and incommensurate ‘5M’ modulated crystal structures in Ni–Mn–Ga martensitic phases,” *Acta Mater.*, vol. 55, no. 15, pp. 5237–5245, Sep. 2007.

[117] L. Righi *et al.*, “Crystal structure of 7M modulated Ni–Mn–Ga martensitic phase,” *Acta Mater.*, vol. 56, no. 16, pp. 4529–4535, Sep. 2008.

[118] H. P. J. Wijn, *Magnetic Properties of Metals: d-Elements, Alloys and Compounds*. Springer Science & Business Media, 2012.

[119] H. P. J. Wijn, Ed., *Alloys and Compounds of d-Elements with Main Group Elements. Part 2*, vol. 19c. Berlin/Heidelberg: Springer-Verlag, 1988.

[120] C. Jiang, G. Feng, S. Gong, and H. Xu, “Effect of Ni excess on phase transformation temperatures of NiMnGa alloys,” *Mater. Sci. Eng. A*, vol. 342, no. 1–2, pp. 231–235, Feb. 2003.

[121] S. K. Wu and S. T. Yang, “Effect of composition on transformation temperatures of Ni–Mn–Ga shape memory alloys,” *Mater. Lett.*, vol. 57, no. 26–27, pp. 4291–4296, Sep. 2003.

[122] R. W. Overholser, M. Wuttig, and D. A. Neumann, “Chemical ordering in Ni-Mn-Ga Heusler alloys,” *Scr. Mater.*, vol. 40, no. 10, pp. 1095–1102, Apr. 1999.

[123] D. L. Schlagel, Y. L. Wu, W. Zhang, and T. A. Lograsso, “Chemical segregation during bulk single crystal preparation of Ni–Mn–Ga ferromagnetic shape memory alloys,” *J. Alloys Compd.*, vol. 312, no. 1, pp. 77–85, 2000.
[124] C. Jiang, J. Liu, J. Wang, L. Xu, and H. Xu, “Solid–liquid interface morphology and crystal growth of NiMnGa magnetic shape memory alloys,” *Acta Mater.*, vol. 53, no. 4, pp. 1111–1120, Feb. 2005.
[125] V. V. Martynov and V. V. Kokorin, “The crystal structure of thermally- and stress-induced Martensites in Ni2MnGa single crystals,” *J. Phys. III*, vol. 2, no. 5, pp. 739–749, May 1992.
[126] M. Richard, J. Feuchtwanger, D. Schlagel, T. Lograsso, S. M. Allen, and R. C. O’Handley, “Crystal structure and transformation behavior of Ni–Mn–Ga martensites,” *Scr. Mater.*, vol. 54, no. 10, pp. 1797–1801, May 2006.
[127] L. Righi *et al.*, “Incommensurate modulated structure of the ferromagnetic shape-memory Ni2MnGa martensite,” *J. Solid State Chem.*, vol. 179, no. 11, pp. 3525–3533, Nov. 2006.
[128] L. Righi, F. Albertini, L. Pareti, A. Paoluzi, and G. Calestani, “Commensurate and incommensurate ‘5M’ modulated crystal structures in Ni–Mn–Ga martensitic phases,” *Acta Mater.*, vol. 55, no. 15, pp. 5237–5245, Sep. 2007.
[129] L. Righi *et al.*, “Crystal structure of 7M modulated Ni–Mn–Ga martensitic phase,” *Acta Mater.*, vol. 56, no. 16, pp. 4529–4535, Sep. 2008.
[130] J. Pons, V. A. Chernenko, R. Santamarta, and E. Cesari, “Crystal structure of martensitic phases in Ni–Mn–Ga shape memory alloys,” *Acta Mater.*, vol. 48, no. 12, pp. 3027–3038, Jul. 2000.
[131] J. F. Duan *et al.*, “Magnetic entropy changes of NiMnGa alloys both on the heating and cooling processes,” *J. Alloys Compd.*, vol. 441, no. 1, pp. 29–32, Aug. 2007.
[132] A. Sozinov, A. A. Likhachev, and K. Ullakko, “Crystal structures and magnetic anisotropy properties of Ni-Mn-Ga martensitic phases with giant magnetic-field-induced strain,” *IEEE Trans. Magn.*, vol. 38, no. 5, pp. 2814–2816, Sep. 2002.
[133] S. J. Murray, M. Marioni, S. M. Allen, R. C. O’Handley, and T. A. Lograsso, “6% magnetic-field-induced strain by twin-boundary motion in ferromagnetic Ni–Mn–Ga,” *Appl. Phys. Lett.*, vol. 77, no. 6, pp. 886–888, Aug. 2000.
[134] D. C. Dunand and P. Müllner, “Size Effects on Magnetic Actuation in Ni-Mn-Ga Shape-Memory Alloys,” *Adv. Mater.*, vol. 23, no. 2, pp. 216–232, Jan. 2011.
[135] R. C. O’Handley, “Model for strain and magnetization in magnetic shape-memory alloys,” *J. Appl. Phys.*, vol. 83, no. 6, pp. 3263–3270, Mar. 1998.
[136] D. Shilo, G. Ravichandran, and K. Bhattacharya, “Investigation of twin-wall structure at the nanometre scale using atomic force microscopy,” *Nat. Mater.*, vol. 3, no. 7, p. nmat1151, Jun. 2004.
[137] P. Müllner, V. A. Chernenko, and G. Kostorz, “A microscopic approach to the magnetic-field-induced deformation of martensite (magnetoplasticity),” *J. Magn. Magn. Mater.*, vol. 267, no. 3, pp. 325–334, Dec. 2003.
[138] J. P. Hirth and R. C. Pond, “Steps, dislocations and disconnections as interface defects relating to structure and phase transformations,” *Acta Mater.*, vol. 44, no. 12, pp. 4749–4763, Dec. 1996.
[139] R. C. Pond and S. Celotto, “Special interfaces: military transformations,” *Int. Mater. Rev.*, vol. 48, no. 4, pp. 225–245, Aug. 2003.

[140] A. E. Romanov and A. L. Kolesnikova, "Application of disclination concept to solid structures," *Prog. Mater. Sci.*, vol. 54, no. 6, pp. 740–769, Aug. 2009.

[141] J. Weertman, "The Peach–Koehler equation for the force on a dislocation modified for hydrostatic pressure," *Philos. Mag. J. Theor. Exp. Appl. Phys.*, vol. 11, no. 114, pp. 1217–1223, Jun. 1965.

[142] E. C. Aifantis, "The physics of plastic deformation," *Int. J. Plast.*, vol. 3, no. 3, pp. 211–247, Jan. 1987.

[143] P. Müllner, V. A. Chernenko, M. Wollgarten, and G. Kostorz, "Large cyclic deformation of a Ni-Mn-Ga shape memory alloy induced by magnetic fields," *J. Appl. Phys.*, vol. 92, no. 11, pp. 6708–6713, Nov. 2002.

[144] A. Likhachev and K. Ullakko, "The model development and experimental investigation of giant magneto-mechanical effects in Ni–Mn–Ga," *J. Magn. Magn. Mater.*, vol. 226–230, no. Part 2, pp. 1541–1543, May 2001.

[145] A. A. Likhachev and K. Ullakko, "Magnetic-field-controlled twin boundaries motion and giant magneto-mechanical effects in Ni–Mn–Ga shape memory alloy," *Phys. Lett. A*, vol. 275, no. 1, pp. 142–151, Oct. 2000.

[146] P. Müllner, "Between microscopic and mesoscopic descriptions of twin–twin interaction," *Z. Für Met.*, vol. 97, no. 3, pp. 205–216, Mar. 2006.

[147] P. Ari-Gur *et al.*, "Neutron Diffraction Study of the Martensitic Transformation and Chemical Order in Heusler Alloy Ni1.91Mn1.29Ga0.8," *Mater. Today Proc.*, vol. 2, no. Supplement 3, pp. S853–S857, Jan. 2015.

[148] D. Kasimov, J. Liu, Y. Gong, G. Xu, F. Xu, and G. Lu, "Realization of magnetostructural coupling in a high temperature region in Mn0.85Co0.3Ni0.85Si1-xGax system," *J. Alloys Compd.*, vol. 733, no. Supplement C, pp. 15–21, Feb. 2018.

[149] T. X. Wang and W. M. Huang, "Shape Memory Alloys for Monitoring Minor Over-Heating/Cooling Based on the Temperature Memory Effect via Differential Scanning Calorimetry: A Review of Recent Progress," *Shape Mem. Superelasticity*, pp. 1–8, Oct. 2017.

[150] L. Beran *et al.*, "Optical and magneto-optical studies of martensitic transformation in Ni-Mn-Ga magnetic shape memory alloys," *J. Appl. Phys.*, vol. 117, no. 17, p. 17A919, Apr. 2015.

[151] T. Lawrence, P. Lindquist, K. Ullakko, and P. Müllner, "Fatigue life and fracture mechanics of unconstrained Ni–Mn–Ga single crystals in a rotating magnetic field," *Mater. Sci. Eng. A*, vol. 654, no. Supplement C, pp. 221–227, Jan. 2016.

[152] A. Armstrong, K. Finn, A. Hobza, P. Lindquist, N. Rafla, and P. Müllner, "A motionless actuation system for magnetic shape memory devices," *Smart Mater. Struct.*, vol. 26, no. 10, p. 105013, 2017.

[153] A. Hobza, C. L. Patrick, K. Ullakko, N. Rafla, P. Lindquist, and P. Müllner, "Sensing strain with Ni-Mn-Ga," *Sens. Actuators Phys.*, vol. 269, no. Supplement C, pp. 137–144, Jan. 2018.

[154] K. Ullakko, L. Wendell, A. Smith, P. Müllner, and G. Hampikian, "A magnetic shape memory micropump: contact-free, and compatible with PCR and human DNA profiling," *Smart Mater. Struct.*, vol. 21, no. 11, p. 115020, 2012.

[155] A. R. Smith, A. Saren, J. Järvinen, and K. Ullakko, "Characterization of a high-resolution solid-state micropump that can be integrated into microfluidic systems," *Microfluid. Nanofluidics*, vol. 18, no. 5–6, pp. 1255–1263, May 2015.

[156] X. Zhou, W. Li, H. P. Kunkel, and G. Williams, "A criterion for enhancing the giant magnetocaloric effect: (Ni–Mn–Ga)—a promising new system for magnetic refrigeration," *J. Phys. Condens. Matter*, vol. 16, no. 6, p. L39, 2004.

[157] A. Planes *et al.*, "Inverse magnetocaloric effect in ferromagnetic Ni–Mn–Sn alloys," *Nat. Mater.*, vol. 4, no. 6, p. 450, Jun. 2005.

[158] T. Krenke *et al.*, "Magnetic superelasticity and inverse magnetocaloric effect in Ni-Mn-In," *Phys. Rev. B*, vol. 75, no. 10, p. 104414, Mar. 2007.

[159] J. Carrey, H. B. Radousky, and A. E. Berkowitz, "Spark-eroded particles: Influence of processing parameters," *J. Appl. Phys.*, vol. 95, no. 3, pp. 823–829, Feb. 2004.

[160] G. Monastyrsky, "Nanoparticles formation mechanisms through the spark erosion of alloys in cryogenic liquids," *Nanoscale Res. Lett.*, vol. 10, Dec. 2015.

[161] G. Calugaru, C. M.-L, and I. Hopulele, "Structure and magnetic properties of Al–Ni–Co fine particles produced by spark erosion," *Powder Metall.*, vol. 42, no. 4, pp. 367–368, Apr. 1999.

[162] E. D. Cabanillas, M. López, E. E. Pasqualini, and D. J. Cirilo Lombardo, "Production of uranium–molybdenum particles by spark-erosion," *J. Nucl. Mater.*, vol. 324, no. 1, pp. 1–5, Jan. 2004.

[163] J. I. Hong, V. C. Solomon, D. J. Smith, F. T. Parker, E. M. Summers, and A. E. Berkowitz, "One-step production of optimized Fe–Ga particles by spark erosion," *Appl. Phys. Lett.*, vol. 89, no. 14, p. 142506, Oct. 2006.

[164] G. E. Monastyrsky, P. A. Yakovenko, V. I. Kolomytsev, Y. N. Koval, A. A. Shcherba, and R. Portier, "Characterization of spark-eroded shape memory alloy powders obtained in cryogenic liquids," *Mater. Sci. Eng. A*, vol. 481–482, pp. 643–646, May 2008.

[165] P. K. Nguyen *et al.*, "Spark erosion: a high production rate method for producing $Bi_{0.5}Sb_{1.5}Te_3$ nanoparticles with enhanced thermoelectric performance," *Nanotechnology*, vol. 23, no. 41, p. 415604, Oct. 2012.

[166] B. Tian, F. Chen, Y. Liu, and Y. F. Zheng, "Effect of ball milling and post-annealing on magnetic properties of Ni49.8Mn28.5Ga21.7 alloy powders," *Intermetallics*, vol. 16, no. 11–12, pp. 1279–1284, Nov. 2008.

[167] B. Tian *et al.*, "Phase transition of Ni–Mn–Ga alloy powders prepared by vibration ball milling," *J. Alloys Compd.*, vol. 509, no. 13, pp. 4563–4568, Mar. 2011.

[168] B. Tian, F. Chen, Y. Tong, L. Li, and Y. Zheng, "Phase Transformation and Magnetic Property of Ni-Mn-Ga Powders Prepared by Dry Ball Milling," *J. Mater. Eng. Perform.*, vol. 21, no. 12, pp. 2530–2534, Dec. 2012.

[169] A. Mudroch, J. M. Azcue, and P. Mudroch, *Manual of Physico-Chemical Analysis of Aquatic Sediments*. CRC Press, 1996.

[170] I. N. McCave, R. J. Bryant, H. F. Cook, and C. A. Coughanowr, "Evaluation of a Laser-Diffraction-Size Analyzer for Use with Natural Sediments: RESEARCH METHOD PAPER," *J. Sediment. Res.*, vol. 56, no. 4, 1986.

[171] A. Lipson, S. G. Lipson, and H. Lipson, *Optical Physics*. Cambridge University Press, 2010.

[172] J. I. Goldstein, D. E. Newbury, J. R. Michael, N. W. M. Ritchie, J. H. J. Scott, and D. C. Joy, *Scanning Electron Microscopy and X-Ray Microanalysis*. Springer, 2017.

[173] R. A. Serway, C. J. Moses, and C. A. Moyer, *Modern Physics*. Cengage Learning, 2004.

[174] L. A. Giannuzzi, J. L. Drown, S. R. Brown, R. B. Irwin, and F. A. Stevie, "Applications of the FIB lift-out technique for TEM specimen preparation," *Microsc. Res. Tech.*, vol. 41, no. 4, pp. 285–290, May 1998.

[175] L. A. Giannuzzi, B. W. Kempshall, S. M. Schwarz, J. K. Lomness, B. I. Prenitzer, and F. A. Stevie, "FIB Lift-Out Specimen Preparation Techniques," in *Introduction to Focused Ion Beams*, Springer, Boston, MA, 2005, pp. 201–228.

[176] L. A. Giannuzzi, J. L. Drown, S. R. Brown, R. B. Irwin, and F. A. Stevie, "Focused Ion Beam Milling and Micromanipulation Lift-Out for Site Specific Cross-Section Tem Specimen Preparation," *MRS Online Proc. Libr. Arch.*, vol. 480, ed 1997.

[177] B. E. Warren, *X-ray Diffraction*. Courier Corporation, 1969.

[178] F. H. Chung, "Quantitative interpretation of X-ray diffraction patterns of mixtures. II. Adiabatic principle of X-ray diffraction analysis of mixtures," *J. Appl. Crystallogr.*, vol. 7, no. 6, pp. 526–531, Dec. 1974.

[179] T. Grimm, *User's Guide to Rapid Prototyping*. Society of Manufacturing Engineers, 2004.

[180] G. Höhne, W. F. Hemminger, and H.-J. Flammersheim, *Differential Scanning Calorimetry*. Springer Science & Business Media, 2013.

[181] L. Qian, M. Li, Z. Zhou, H. Yang, and X. Shi, "Comparison of nano-indentation hardness to microhardness," *Surf. Coat. Technol.*, vol. 195, no. 2, pp. 264–271, May 2005.

[182] J. Y. Rho, P. Zioupos, J. D. Currey, and G. M. Pharr, "Microstructural elasticity and regional heterogeneity in human femoral bone of various ages examined by nano-indentation," *J. Biomech.*, vol. 35, no. 2, pp. 189–198, Feb. 2002.

[183] M. P. Caputo and C. V. Solomon, "A facile method for producing porous parts with complex geometries from ferromagnetic Ni-Mn-Ga shape memory alloys," *Mater. Lett.*, vol. 200, pp. 87–89, Aug. 2017.

[184] B. Tian, F. Chen, Y. Liu, and Y. F. Zheng, "Structural transition and atomic ordering of Ni49.8Mn28.5Ga21.7 ferromagnetic shape memory alloy powders prepared by ball milling," *Mater. Lett.*, vol. 62, no. 17–18, pp. 2851–2854, Jun. 2008.

[185] A. N. Vasil'ev *et al.*, "Structural and magnetic phase transitions in shape-memory alloys `${\mathrm{Ni}}_{2+x}{\mathrm{Mn}}_{1\ensuremath{-}x}\mathrm{Ga}$`," *Phys. Rev. B*, vol. 59, no. 2, pp. 1113–1120, Jan. 1999.

[186] V. V. Khovailo, V. Novosad, T. Takagi, D. A. Filippov, R. Z. Levitin, and A. N. Vasil'ev, "Magnetic properties and magnetostructural phase transitions in `${\mathrm{Ni}}_{2+x}{\mathrm{Mn}}_{1\ensuremath{-}x}\mathrm{Ga}$` shape memory alloys," *Phys. Rev. B*, vol. 70, no. 17, p. 174413, Nov. 2004.

[187] M. Kök, G. Pirge, and Y. Aydoğdu, "Isothermal oxidation study on NiMnGa ferromagnetic shape memory alloy at 600–1000 °C," *Appl. Surf. Sci.*, vol. 268, pp. 136–140, Mar. 2013.

[188] W. D. C. Jr and D. G. Rethwisch, *Fundamentals of Materials Science and Engineering: An Integrated Approach*. John Wiley & Sons, 2012.

[189] K. M. Myers, “Structure-Property Relationship of Binder Jetted Fused Silica Preforms to Manufacture Ceramic-Metallic Interpenetrating Phase Composites,” Youngstown State University, 2016.

[190] E. Wheat, “Process Mapping and Optimization of Titanium Parts Made by Binder Jetting Additive Manufacturing,” Jan. 2018.

[191] A. Mostafaei *et al.*, “Microstructural evolution and magnetic properties of binder jet additive manufactured Ni-Mn-Ga magnetic shape memory alloy foam,” *Acta Mater.*, vol. 131, pp. 482–490, Jun. 2017.

[192] S. L. Taylor, R. N. Shah, and D. C. Dunand, “Ni-Mn-Ga micro-trusses via sintering of 3D-printed inks containing elemental powders,” *Acta Mater.*, vol. 143, pp. 20–29, Jan. 2018.

[193] G. S. Firstov, R. G. Vitchev, H. Kumar, B. Blanpain, and J. Van Humbeeck, “Surface oxidation of NiTi shape memory alloy,” *Biomaterials*, vol. 23, no. 24, pp. 4863–4871, Dec. 2002.

[194] B. Thierry, M. Tabrizian, C. Trepanier, O. Savadogo, and L. Yahia, “Effect of surface treatment and sterilization processes on the corrosion behavior of NiTi shape memory alloy,” *J. Biomed. Mater. Res.*, vol. 51, no. 4, pp. 685–693, Sep. 2000.

[195] M. Es-Souni, M. Es-Souni, and H. Fischer-Brandies, “On the properties of two binary NiTi shape memory alloys. Effects of surface finish on the corrosion behaviour and in vitro biocompatibility,” *Biomaterials*, vol. 23, no. 14, pp. 2887–2894, Jul. 2002.

[196] J. D. Hem, “Redox processes at surfaces of manganese oxide and their effects on aqueous metal ions,” *Chem. Geol.*, vol. 21, no. 3, pp. 199–218, Feb. 1978.

[197] S. Fritsch and A. Navrotsky, “Thermodynamic Properties of Manganese Oxides,” *J. Am. Ceram. Soc.*, vol. 79, no. 7, pp. 1761–1768, Jul. 1996.

[198] K. V. Peruman, R. Chokkalingam, and M. Mahendran, “Annealing effect on phase transformation in nano structured Ni–Mn–Ga ferromagnetic shape memory alloy,” *Phase Transit.*, vol. 83, no. 7, pp. 509–517, Jul. 2010.

[199] M. Brandner, M. Bram, J. Froitzheim, H. P. Buchkremer, and D. Stöver, “Electrically Conductive Diffusion barrier layers for Metal-Supported SOFC,” *Solid State Ion.*, vol. 179, no. 27, pp. 1501–1504, Sep. 2008.

[200] S. H. Jang, T. Kang, H. J. Kim, and K. Y. Kim, “Effect of the nano-oxide layer as a Mn diffusion barrier in specular spin valves,” *Appl. Phys. Lett.*, vol. 81, no. 1, pp. 105–107, Jun. 2002.

[201] V. K. Dixit, K. Neishi, N. Akao, and J. Koike, “Structural and Electronic Properties of a Mn Oxide Diffusion Barrier Layer Formed by Chemical Vapor Deposition,” *IEEE Trans. Device Mater. Reliab.*, vol. 11, no. 2, pp. 295–302, Jun. 2011.

[202] J. Buschbeck, R. Niemann, O. Heczko, M. Thomas, L. Schultz, and S. Fähler, “In situ studies of the martensitic transformation in epitaxial Ni–Mn–Ga films,” *Acta Mater.*, vol. 57, no. 8, pp. 2516–2526, May 2009.

[203] I. Glavatskyy, N. Glavatska, I. Urubkov, J.-U. Hoffman, and F. Bourdarot, “Crystal and magnetic structure temperature evolution in Ni–Mn–Ga magnetic

shape memory martensite," *Mater. Sci. Eng. A*, vol. 481–482, pp. 298–301, May 2008.

[204] Y. Zhang *et al.*, "Epitaxial Ni–Mn–Ga films derived through high temperature in situ depositions," *Smart Mater. Struct.*, vol. 18, no. 2, p. 025019, 2009.

[205] Y. Zhang, R. A. Hughes, J. F. Britten, J. S. Preston, G. A. Botton, and M. Niewczas, "Self-activated reversibility in the magnetically induced reorientation of martensitic variants in ferromagnetic Ni-Mn-Ga films," *Phys. Rev. B*, vol. 81, no. 5, p. 054406, Feb. 2010.

[206] T. Kitashima and T. Kawamura, "Prediction of oxidation behavior of near-α titanium alloys," *Scr. Mater.*, vol. 124, pp. 56–58, Nov. 2016.

[207] P. Franke and R. Dieckmann, "Thermodynamics of iron manganese mixed oxides at high temperatures," *J. Phys. Chem. Solids*, vol. 51, no. 1, pp. 49–57, Jan. 1990.

[208] M. Keller and R. Dieckmann, "Defect Structure and Transport Properties of Manganese Oxides: (I) The Nonstoichiometry of Manganosite (Mn1-ΔO)," *Berichte Bunsenges. Für Phys. Chem.*, vol. 89, no. 8, pp. 883–893, Aug. 1985.

[209] V. A. Chernenko, C. Seguí, E. Cesari, J. Pons, and V. V. Kokorin, "Sequence of martensitic transformations in Ni-Mn-Ga alloys," *Phys. Rev. B*, vol. 57, no. 5, pp. 2659–2662, Feb. 1998.

[210] V. A. Chernenko, J. Pons, C. Seguí, and E. Cesari, "Premartensitic phenomena and other phase transformations in Ni–Mn–Ga alloys studied by dynamical mechanical analysis and electron diffraction," *Acta Mater.*, vol. 50, no. 1, pp. 53–60, Jan. 2002.

[211] M. Wuttig, C. Craciunescu, and J. Li, "Phase Transformations in Ferromagnetic NiMnGa Shape Memory Films," *Mater. Trans. JIM*, vol. 41, no. 8, pp. 933–937, 2000.

[212] Y. Li, F. Xu, X. Hu, B. Dong, Y. Luan, and Y. Xiao, "Discussion on Local Spark Sintering of a Ceramic-Metal System in an SR-CT Experiment during Microwave Processing," *Materials*, vol. 9, no. 3, p. 132, Feb. 2016.

[213] J. Banhart, "Manufacture, characterisation and application of cellular metals and metal foams," *Prog. Mater. Sci.*, vol. 46, no. 6, pp. 559–632, 2001.

[214] F. J. Castaño, B. Nelson-Cheeseman, R. C. O'Handley, C. A. Ross, C. Redondo, and F. Castaño, "Structure and thermomagnetic properties of polycrystalline Ni–Mn–Ga thin films," *J. Appl. Phys.*, vol. 93, no. 10, pp. 8492–8494, May 2003.

[215] P. Zheng, N. J. Kucza, C. L. Patrick, P. Müllner, and D. C. Dunand, "Mechanical and magnetic behavior of oligocrystalline Ni–Mn–Ga microwires," *J. Alloys Compd.*, vol. 624, pp. 226–233, Mar. 2015.

[216] A. Sozinov, A. A. Likhachev, and K. Ullakko, "Crystal structures and magnetic anisotropy properties of Ni-Mn-Ga martensitic phases with giant magnetic-field-induced strain," *IEEE Trans. Magn.*, vol. 38, no. 5, pp. 2814–2816, 2002.

[217] C. Seguí, V. A. Chernenko, J. Pons, E. Cesari, V. Khovailo, and T. Takagi, "Low temperature-induced intermartensitic phase transformations in Ni–Mn–Ga single crystal," *Acta Mater.*, vol. 53, no. 1, pp. 111–120, Jan. 2005.

[218] S. Wirth, A. Leithe-Jasper, A. N. Vasil'ev, and J. M. D. Coey, "Structural and magnetic properties of Ni2MnGa," *J. Magn. Magn. Mater.*, vol. 167, no. 1, pp. L7–L11, Mar. 1997.

[219] C. Jiang, Y. Muhammad, L. Deng, W. Wu, and H. Xu, “Composition dependence on the martensitic structures of the Mn-rich NiMnGa alloys,” *Acta Mater.*, vol. 52, no. 9, pp. 2779–2785, May 2004.

[220] V. Sánchez-Alarcos, J. I. Pérez-Landazábal, V. Recarte, J. A. Rodríguez-Velamazán, and V. A. Chernenko, “Effect of atomic order on the martensitic and magnetic transformations in Ni–Mn–Ga ferromagnetic shape memory alloys,” *J. Phys. Condens. Matter*, vol. 22, no. 16, p. 166001, 2010.

[221] O. Heczko, N. Lanska, O. Soderberg, and K. Ullakko, “Temperature variation of structure and magnetic properties of Ni–Mn–Ga magnetic shape memory alloys,” *J. Magn. Magn. Mater.*, vol. 242–245, Part 2, pp. 1446–1449, Apr. 2002.

[222] M. Sofronie, F. Tolea, V. Kuncser, and M. Valeanu, “Martensitic transformation and accompanying magnetic changes in Ni–Fe–Ga–Co alloys,” *J. Appl. Phys.*, vol. 107, no. 11, p. 113905, Jun. 2010.

[223] V. Sánchez-Alarcos, V. Recarte, J. I. Pérez-Landazábal, and G. J. Cuello, “Correlation between atomic order and the characteristics of the structural and magnetic transformations in Ni–Mn–Ga shape memory alloys,” *Acta Mater.*, vol. 55, no. 11, pp. 3883–3889, Jun. 2007.

[224] R. K. Singh, M. Shamsuddin, R. Gopalan, R. P. Mathur, and V. Chandrasekaran, “Magnetic and structural transformation in off-stoichiometric NiMnGa alloys,” *Mater. Sci. Eng. A*, vol. 476, no. 1–2, pp. 195–200, Mar. 2008.

[225] M. Kök and Y. Aydogdu, “Effect of heat treatment on the physical properties of Ni–Mn–Ga alloy,” *Thermochim. Acta*, vol. 548, pp. 51–55, Nov. 2012.

[226] Y. Ma, C. Jiang, Y. Li, H. Xu, C. Wang, and X. Liu, “Study of Ni50+xMn25Ga25−x (x = 2–11) as high-temperature shape-memory alloys,” *Acta Mater.*, vol. 55, no. 5, pp. 1533–1541, Mar. 2007.

[227] P. Ruelle, A. Farina-Cuendet, and U. W. Kesselring, “Changes of Molar Volume from Solid to Liquid and Solution: The Particular Case of C60,” *J. Am. Chem. Soc.*, vol. 118, no. 7, pp. 1777–1784, Jan. 1996.

[228] D. U. Tulyaganov, M. J. Ribeiro, and J. A. Labrincha, “Development of glass-ceramics by sintering and crystallization of fine powders of calcium-magnesium-aluminosilicate glass,” *Ceram. Int.*, vol. 28, no. 5, pp. 515–520, Jan. 2002.

[229] N. K. Tolochko *et al.*, “Selective laser sintering and cladding of single-component metal powders,” *Rapid Prototyp. J.*, vol. 10, no. 2, pp. 88–97, Apr. 2004.

[230] G. A. Shoales and R. M. German, “<Emphasis Type="Italic">In situ</Emphasis> strength evolution during the sintering of bronze powders,” *Metall. Mater. Trans. A*, vol. 29, no. 4, pp. 1257–1263, Apr. 1998.

[231] L. Král, B. Million, and J. Čermák, “Diffusion of Carbon and Manganese in Fe-C-Mn,” *Defect and Diffusion Forum*, 2007. [Online]. Available: https://www.scientific.net/DDF.263.153. [Accessed: 28-Mar-2018].

[232] S. P. Murarka, M. S. Anand, and R. P. Agarwala, “Diffusion of vanadium in aluminium and nickel,” *Acta Metall.*, vol. 16, no. 1, pp. 69–72, Jan. 1968.

[233] O. Heczko, N. Lanska, O. Soderberg, and K. Ullakko, “Temperature variation of structure and magnetic properties of Ni–Mn–Ga magnetic shape memory alloys,” *J. Magn. Magn. Mater.*, vol. 242–245, Part 2, pp. 1446–1449, Apr. 2002.

[234] I. Aaltio *et al.*, "Nanoscale surface properties of a Ni–Mn–Ga 10M magnetic shape memory alloy," *J. Alloys Compd.*, vol. 577, Supplement 1, pp. S367–S371, Nov. 2013.

[235] C. Liu *et al.*, "Microstructure and magnetic properties of Ni-rich Ni54Mn25.7Ga20.3 ferromagnetic shape memory alloy thin film," *J. Magn. Magn. Mater.*, vol. 320, no. 6, pp. 1078–1082, Mar. 2008.

[236] S. V. Kumar, R. K. Singh, M. M. Raja, A. Kumar, S. Bysakh, and M. Mahendran, "Microstructure and nanomechanical properties of Mn-rich Ni–Mn–Ga thin films," *Intermetallics*, vol. 71, pp. 57–64, Apr. 2016.

[237] C. Liu, Z. Y. Gao, X. An, H. B. Wang, L. X. Gao, and W. Cai, "Surface characteristics and nanoindentation study of Ni–Mn–Ga ferromagnetic shape memory sputtered thin films," *Appl. Surf. Sci.*, vol. 254, no. 9, pp. 2861–2865, Feb. 2008.

[238] Y. Xin, Y. Li, L. Chai, and H. Xu, "Shape memory characteristics of dual-phase Ni–Mn–Ga based high temperature shape memory alloys," *Scr. Mater.*, vol. 57, no. 7, pp. 599–601, Oct. 2007.

[239] N. Scheerbaum, D. Hinz, O. Gutfleisch, K.-H. Müller, and L. Schultz, "Textured polymer bonded composites with Ni–Mn–Ga magnetic shape memory particles," *Acta Mater.*, vol. 55, no. 8, pp. 2707–2713, May 2007.

[240] M. Mahendran, J. Feuchtwanger, R. Techapiesancharoenkij, D. Bono, and R. C. O'Handley, "Acoustic energy absorption in Ni–Mn–Ga/polymer composites," *J. Magn. Magn. Mater.*, vol. 323, no. 8, pp. 1098–1100, Apr. 2011.

[241] J. Feuchtwanger, K. Griffin, J. Huang, D. Bono, R. C. O'Handley, and S. M. Allen, "Mechanical energy absorption in Ni–Mn–Ga polymer composites," *J. Magn. Magn. Mater.*, vol. 272–276, Part 3, pp. 2038–2039, May 2004.

[242] M. Zeng, S. W. Or, and H. L. W. Chan, "Magnetic field-induced strain and magnetoelectric effects in sandwich composite of ferromagnetic shape memory Ni-Mn-Ga crystal and piezoelectric PVDF polymer," *IEEE Trans. Ultrason. Ferroelectr. Freq. Control*, vol. 57, no. 10, pp. 2147–2153, Oct. 2010.

[243] M. F. Qian, X. X. Zhang, L. S. Wei, L. Geng, and H. X. Peng, "Structural, Magnetic and Mechanical Properties of Oligocrystalline Ni-Mn-Ga Shape Memory Microwires," *Mater. Today Proc.*, vol. 2, pp. S577–S581, Jan. 2015.

[244] A. E. Perekos *et al.*, "Structure and magnetic properties of highly dispersed Ni-Mn-Ga powders prepared by spark-erosion," *J. Appl. Phys.*, vol. 112, no. 9, p. 093909, Nov. 2012.

[245] J. Feuchtwanger *et al.*, "Rearrangement of twin variants in ferromagnetic shape memory alloy–polyurethane composites studied by stroboscopic neutron diffraction," *J. Phys. Condens. Matter*, vol. 20, no. 10, p. 104247, 2008.

[246] C. Haberland, M. Elahinia, J. M. Walker, H. Meier, and J. Frenzel, "On the development of high quality NiTi shape memory and pseudoelastic parts by additive manufacturing," *Smart Mater. Struct.*, vol. 23, no. 10, p. 104002, 2014.

[247] J. Walker, M. T. Andani, C. Haberland, and M. Elahinia, "Additive Manufacturing of Nitinol Shape Memory Alloys to Overcome Challenges in Conventional Nitinol Fabrication," p. V02AT02A037, Nov. 2014.

[248] D. K. Sheity, A. R. Rosenfield, and W. H. Duckworth, “Fracture Toughness of Ceramics Measured by a Chevron-Notch Diametral-Compression Test,” *J. Am. Ceram. Soc.*, vol. 68, no. 12, pp. C–325, Dec. 1985.
[249] E. Hoek and Z. T. Bieniawski, “Brittle fracture propagation in rock under compression,” *Int. J. Fract. Mech.*, vol. 1, no. 3, pp. 137–155, Sep. 1965.
[250] R. S. Vannutelli, “Mechanical Behavior of 3D Printed Lattice-Structured Materials,” Youngstown State University, 2017.
[251] E. J. Myers, “Finite Element Modeling (FEM) of Porous Additively Manufactured Ferromagnetic Shape Memory Alloy Using Scanning Electron Micrograph (SEM) Based Geometries,” Youngstown State University, 2017.
[252] S. M. Saghaian, H. E. Karaca, M. Souri, A. S. Turabi, and R. D. Noebe, “Tensile shape memory behavior of Ni50.3Ti29.7Hf20 high temperature shape memory alloys,” *Mater. Des.*, vol. 101, pp. 340–345, Jul. 2016.
[253] A. Sozinov, A. A. Likhachev, N. Lanska, O. Söderberg, K. Ullakko, and V. K. Lindroos, “Stress- and magnetic-field-induced variant rearrangement in Ni–Mn–Ga single crystals with seven-layered martensitic structure,” *Mater. Sci. Eng. A*, vol. 378, no. 1, pp. 399–402, Jul. 2004.
[254] V. A. Chernenko, V. L’vov, J. Pons, and E. Cesari, “Superelasticity in high-temperature Ni–Mn–Ga alloys,” *J. Appl. Phys.*, vol. 93, no. 5, pp. 2394–2399, Mar. 2003.
[255] J. T. Beals and M. S. Thompson, “Density gradient effects on aluminium foam compression behaviour,” *J. Mater. Sci.*, vol. 32, no. 13, pp. 3595–3600, Jan. 1997.
[256] A. Paul and U. Ramamurty, “Strain rate sensitivity of a closed-cell aluminum foam,” *Mater. Sci. Eng. A*, vol. 281, no. 1, pp. 1–7, Apr. 2000.
[257] B.-Y. Li, L.-J. Rong, and Y.-Y. Li, “Stress–strain behavior of porous Ni–Ti shape memory intermetallics synthesized from powder sintering,” *Intermetallics*, vol. 8, no. 5, pp. 643–646, May 2000.
[258] O. Heczko and L. Straka, “Compositional dependence of structure, magnetization and magnetic anisotropy in Ni–Mn–Ga magnetic shape memory alloys,” *J. Magn. Magn. Mater.*, vol. 272–276, Part 3, pp. 2045–2046, May 2004.
[259] F. Nilsén, I. Aaltio, Y. Ge, T. Lindroos, and S. P. Hannula, “Characterization of Gas Atomized Ni-Mn-Ga Powders,” *Mater. Today Proc.*, vol. 2, pp. S879–S882, Jan. 2015.
[260] S. Vinodh Kumar, R. K. Singh, S. Seenithurai, S. Bysakh, M. Manivel Raja, and M. Mahendran, “Phase structure and magnetic properties of the annealed Mn-rich Ni–Mn–Ga ferromagnetic shape memory thin films,” *Mater. Res. Bull.*, vol. 61, pp. 95–100, Jan. 2015.
[261] M. Chmielus *et al.*, “Magnetic-field-induced recovery strain in polycrystalline Ni–Mn–Ga foam,” *J. Appl. Phys.*, vol. 108, no. 12, p. 123526, Dec. 2010.
[262] O. Heczko, “Determination of ordinary magnetostriction in Ni–Mn–Ga magnetic shape memory alloy,” *J. Magn. Magn. Mater.*, vol. 290, pp. 846–849, Apr. 2005.
[263] U. Gaitzsch *et al.*, “Processing Routes Toward Textured Polycrystals in Ferromagnetic Shape Memory Alloys,” *Adv. Eng. Mater.*, vol. 14, no. 8, pp. 636–652, Aug. 2012.
[264] R. A. Kellogg, A. B. Flatau, A. E. Clark, M. Wun-Fogle, and T. A. Lograsso, “Temperature and stress dependencies of the magnetic and magnetostrictive

properties of Fe0.81Ga0.19," *J. Appl. Phys.*, vol. 91, no. 10, pp. 7821–7823, May 2002.

[265] R. Techapiesancharoenkij, J. Kostamo, S. M. Allen, and R. C. O'Handley, "Frequency response of acoustic-assisted Ni–Mn–Ga ferromagnetic-shape-memory-alloy actuator," *J. Appl. Phys.*, vol. 105, no. 9, p. 093923, May 2009.

[266] H. E. Karaca, I. Karaman, B. Basaran, Y. I. Chumlyakov, and H. J. Maier, "Magnetic field and stress induced martensite reorientation in NiMnGa ferromagnetic shape memory alloy single crystals," *Acta Mater.*, vol. 54, no. 1, pp. 233–245, Jan. 2006.

Appendix

Appendix A – Image Copyright Clearances

The following images have been published previously: Figure 1.1, 1.2, Figure 1.3, Figure 2.1 and Figure 2.9. The novelty of the figures and any corresponding information is clearly acknowledged to the original authors in the text via referencing. Furthermore, to maintain legitimacy of copyrights, the above-mentioned images have been cleared for use in this dissertation document titled "4-Dimensional Printing and Characterization of Net-Shaped Porous Parts Made from Magnetic Ni-Mn-Ga Shape Memory Alloy Powders" authored by Matthew Caputo. The image copyright clearances are shown in this appendix. Furthermore, terms and conditions for the copyrights are organized by the figure numbers used in this document.

Figures 1.1 and 1.2

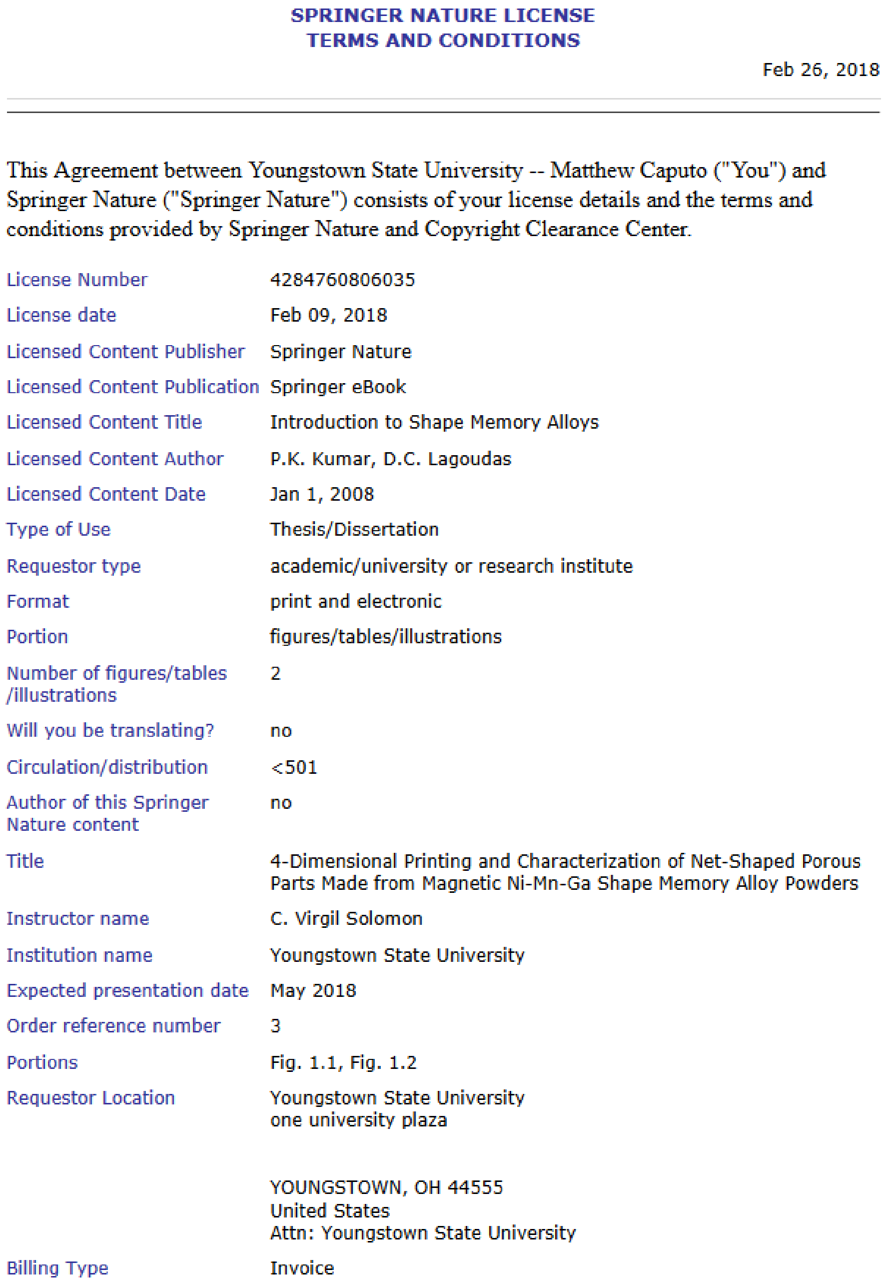

SPRINGER NATURE LICENSE
TERMS AND CONDITIONS

Feb 26, 2018

This Agreement between Youngstown State University -- Matthew Caputo ("You") and Springer Nature ("Springer Nature") consists of your license details and the terms and conditions provided by Springer Nature and Copyright Clearance Center.

License Number	4284760806035
License date	Feb 09, 2018
Licensed Content Publisher	Springer Nature
Licensed Content Publication	Springer eBook
Licensed Content Title	Introduction to Shape Memory Alloys
Licensed Content Author	P.K. Kumar, D.C. Lagoudas
Licensed Content Date	Jan 1, 2008
Type of Use	Thesis/Dissertation
Requestor type	academic/university or research institute
Format	print and electronic
Portion	figures/tables/illustrations
Number of figures/tables /illustrations	2
Will you be translating?	no
Circulation/distribution	<501
Author of this Springer Nature content	no
Title	4-Dimensional Printing and Characterization of Net-Shaped Porous Parts Made from Magnetic Ni-Mn-Ga Shape Memory Alloy Powders
Instructor name	C. Virgil Solomon
Institution name	Youngstown State University
Expected presentation date	May 2018
Order reference number	3
Portions	Fig. 1.1, Fig. 1.2
Requestor Location	Youngstown State University one university plaza YOUNGSTOWN, OH 44555 United States Attn: Youngstown State University
Billing Type	Invoice

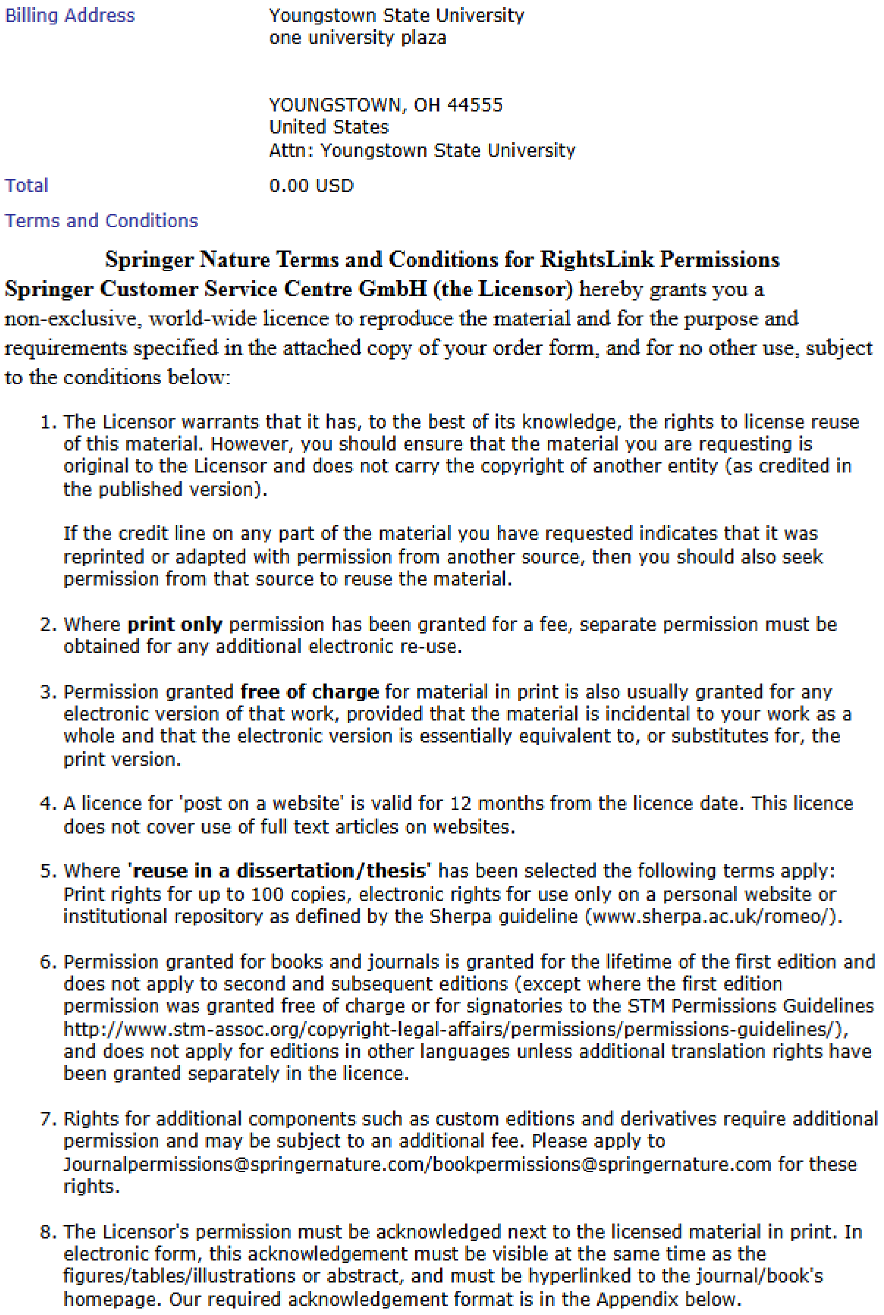

Billing Address
Youngstown State University
one university plaza

YOUNGSTOWN, OH 44555
United States
Attn: Youngstown State University

Total
0.00 USD

Terms and Conditions

Springer Nature Terms and Conditions for RightsLink Permissions

Springer Customer Service Centre GmbH (the Licensor) hereby grants you a non-exclusive, world-wide licence to reproduce the material and for the purpose and requirements specified in the attached copy of your order form, and for no other use, subject to the conditions below:

1. The Licensor warrants that it has, to the best of its knowledge, the rights to license reuse of this material. However, you should ensure that the material you are requesting is original to the Licensor and does not carry the copyright of another entity (as credited in the published version).

   If the credit line on any part of the material you have requested indicates that it was reprinted or adapted with permission from another source, then you should also seek permission from that source to reuse the material.

2. Where **print only** permission has been granted for a fee, separate permission must be obtained for any additional electronic re-use.
3. Permission granted **free of charge** for material in print is also usually granted for any electronic version of that work, provided that the material is incidental to your work as a whole and that the electronic version is essentially equivalent to, or substitutes for, the print version.
4. A licence for 'post on a website' is valid for 12 months from the licence date. This licence does not cover use of full text articles on websites.
5. Where **'reuse in a dissertation/thesis'** has been selected the following terms apply: Print rights for up to 100 copies, electronic rights for use only on a personal website or institutional repository as defined by the Sherpa guideline (www.sherpa.ac.uk/romeo/).
6. Permission granted for books and journals is granted for the lifetime of the first edition and does not apply to second and subsequent editions (except where the first edition permission was granted free of charge or for signatories to the STM Permissions Guidelines http://www.stm-assoc.org/copyright-legal-affairs/permissions/permissions-guidelines/), and does not apply for editions in other languages unless additional translation rights have been granted separately in the licence.
7. Rights for additional components such as custom editions and derivatives require additional permission and may be subject to an additional fee. Please apply to Journalpermissions@springernature.com/bookpermissions@springernature.com for these rights.
8. The Licensor's permission must be acknowledged next to the licensed material in print. In electronic form, this acknowledgement must be visible at the same time as the figures/tables/illustrations or abstract, and must be hyperlinked to the journal/book's homepage. Our required acknowledgement format is in the Appendix below.

9. Use of the material for incidental promotional use, minor editing privileges (this does not include cropping, adapting, omitting material or any other changes that affect the meaning, intention or moral rights of the author) and copies for the disabled are permitted under this licence.

10. Minor adaptations of single figures (changes of format, colour and style) do not require the Licensor's approval. However, the adaptation should be credited as shown in Appendix below.

Appendix — Acknowledgements:

For Journal Content:
Reprinted by permission from **[the Licensor]**: **[Journal Publisher** (e.g. Nature/Springer/Palgrave)] **[JOURNAL NAME] [REFERENCE CITATION** (Article name, Author(s) Name), **[COPYRIGHT]** (year of publication)

For **Advance Online Publication papers:**
Reprinted by permission from **[the Licensor]**: **[Journal Publisher** (e.g. Nature/Springer/Palgrave)] **[JOURNAL NAME] [REFERENCE CITATION** (Article name, Author(s) Name), **[COPYRIGHT]** (year of publication), advance online publication, day month year (doi: 10.1038/sj.[JOURNAL ACRONYM].)

For Adaptations/Translations:
Adapted/Translated by permission from **[the Licensor]**: **[Journal Publisher** (e.g. Nature/Springer/Palgrave)] **[JOURNAL NAME] [REFERENCE CITATION** (Article name, Author(s) Name), **[COPYRIGHT]** (year of publication)

Note: For any republication from the British Journal of Cancer, the following credit line style applies:

Reprinted/adapted/translated by permission from **[the Licensor]**: on behalf of Cancer Research UK: : **[Journal Publisher** (e.g. Nature/Springer/Palgrave)] **[JOURNAL NAME] [REFERENCE CITATION** (Article name, Author(s) Name), **[COPYRIGHT]** (year of publication)

For **Advance Online Publication** papers:
Reprinted by permission from The **[the Licensor]**: on behalf of Cancer Research UK: **[Journal Publisher** (e.g. Nature/Springer/Palgrave)] **[JOURNAL NAME] [REFERENCE CITATION** (Article name, Author(s) Name), **[COPYRIGHT]** (year of publication), advance online publication, day month year (doi: 10.1038/sj. [JOURNAL ACRONYM])

For Book content:
Reprinted/adapted by permission from **[the Licensor]**: **[Book Publisher** (e.g. Palgrave Macmillan, Springer etc) **[Book Title]** by **[Book author**(s)] **[COPYRIGHT]** (year of publication)

Other Conditions:

Figure 1.3

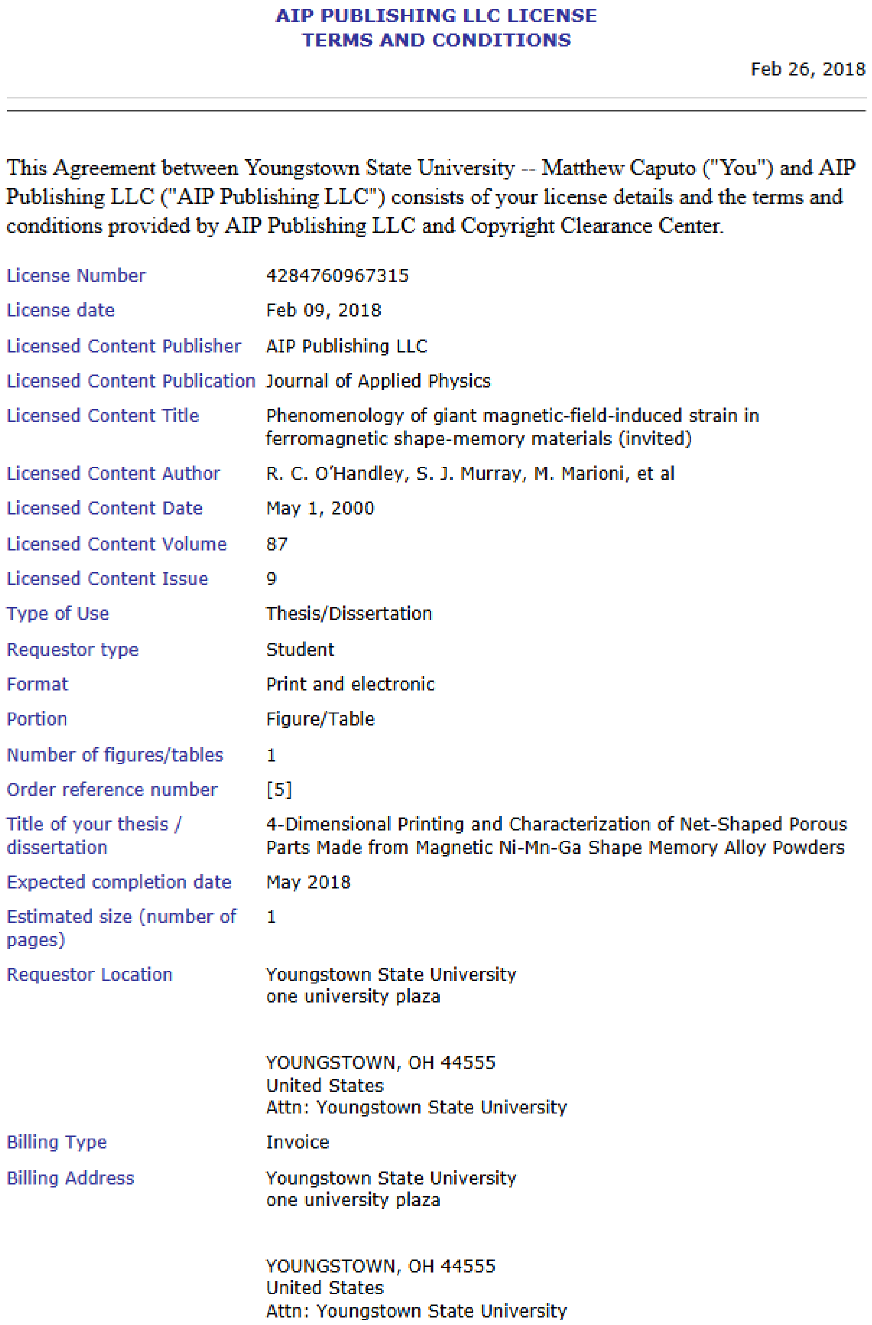

AIP PUBLISHING LLC LICENSE
TERMS AND CONDITIONS

Feb 26, 2018

This Agreement between Youngstown State University -- Matthew Caputo ("You") and AIP Publishing LLC ("AIP Publishing LLC") consists of your license details and the terms and conditions provided by AIP Publishing LLC and Copyright Clearance Center.

License Number	4284760967315
License date	Feb 09, 2018
Licensed Content Publisher	AIP Publishing LLC
Licensed Content Publication	Journal of Applied Physics
Licensed Content Title	Phenomenology of giant magnetic-field-induced strain in ferromagnetic shape-memory materials (invited)
Licensed Content Author	R. C. O'Handley, S. J. Murray, M. Marioni, et al
Licensed Content Date	May 1, 2000
Licensed Content Volume	87
Licensed Content Issue	9
Type of Use	Thesis/Dissertation
Requestor type	Student
Format	Print and electronic
Portion	Figure/Table
Number of figures/tables	1
Order reference number	[5]
Title of your thesis / dissertation	4-Dimensional Printing and Characterization of Net-Shaped Porous Parts Made from Magnetic Ni-Mn-Ga Shape Memory Alloy Powders
Expected completion date	May 2018
Estimated size (number of pages)	1
Requestor Location	Youngstown State University one university plaza YOUNGSTOWN, OH 44555 United States Attn: Youngstown State University
Billing Type	Invoice
Billing Address	Youngstown State University one university plaza YOUNGSTOWN, OH 44555 United States Attn: Youngstown State University

Terms and Conditions

AIP Publishing LLC -- Terms and Conditions: Permissions Uses

AIP Publishing hereby grants to you the non-exclusive right and license to use and/or distribute the Material according to the use specified in your order, on a one-time basis, for the specified term, with a maximum distribution equal to the number that you have ordered. Any links or other content accompanying the Material are not the subject of this license.

1. You agree to include the following copyright and permission notice with the reproduction of the Material:"Reprinted from [FULL CITATION], with the permission of AIP Publishing." For an article, the credit line and permission notice must be printed on the first page of the article or book chapter. For photographs, covers, or tables, the notice may appear with the Material, in a footnote, or in the reference list.
2. If you have licensed reuse of a figure, photograph, cover, or table, it is your responsibility to ensure that the material is original to AIP Publishing and does not contain the copyright of another entity, and that the copyright notice of the figure, photograph, cover, or table does not indicate that it was reprinted by AIP Publishing, with permission, from another source. Under no circumstances does AIP Publishing purport or intend to grant permission to reuse material to which it does not hold appropriate rights.
   You may not alter or modify the Material in any manner. You may translate the Material into another language only if you have licensed translation rights. You may not use the Material for promotional purposes.
3. The foregoing license shall not take effect unless and until AIP Publishing or its agent, Copyright Clearance Center, receives the Payment in accordance with Copyright Clearance Center Billing and Payment Terms and Conditions, which are incorporated herein by reference.
4. AIP Publishing or Copyright Clearance Center may, within two business days of granting this license, revoke the license for any reason whatsoever, with a full refund payable to you. Should you violate the terms of this license at any time, AIP Publishing, or Copyright Clearance Center may revoke the license with no refund to you. Notice of such revocation will be made using the contact information provided by you. Failure to receive such notice will not nullify the revocation.
5. AIP Publishing makes no representations or warranties with respect to the Material. You agree to indemnify and hold harmless AIP Publishing, and their officers, directors, employees or agents from and against any and all claims arising out of your use of the Material other than as specifically authorized herein.
6. The permission granted herein is personal to you and is not transferable or assignable without the prior written permission of AIP Publishing. This license may not be amended except in a writing signed by the party to be charged.
7. If purchase orders, acknowledgments or check endorsements are issued on any forms containing terms and conditions which are inconsistent with these provisions, such inconsistent terms and conditions shall be of no force and effect. This document, including the CCC Billing and Payment Terms and Conditions, shall be the entire agreement between the parties relating to the subject matter hereof.

This Agreement shall be governed by and construed in accordance with the laws of the State of New York. Both parties hereby submit to the jurisdiction of the courts of New York County for purposes of resolving any disputes that may arise hereunder.

V1.1

Questions? customercare@copyright.com or +1-855-239-3415 (toll free in the US) or +1-978-646-2777.

Figure 2.1

ELSEVIER LICENSE
TERMS AND CONDITIONS

Feb 26, 2018

This Agreement between Youngstown State University -- Matthew Caputo ("You") and Elsevier ("Elsevier") consists of your license details and the terms and conditions provided by Elsevier and Copyright Clearance Center.

License Number	4284761218341
License date	Feb 09, 2018
Licensed Content Publisher	Elsevier
Licensed Content Publication	Advances in Engineering Software
Licensed Content Title	A visual simulation technique for 3D printing
Licensed Content Author	H.J Jee,E Sachs
Licensed Content Date	Feb 1, 2000
Licensed Content Volume	31
Licensed Content Issue	2
Licensed Content Pages	10
Start Page	97
End Page	106
Type of Use	reuse in a thesis/dissertation
Intended publisher of new work	other
Portion	figures/tables/illustrations
Number of figures/tables /illustrations	1
Format	both print and electronic
Are you the author of this Elsevier article?	No
Will you be translating?	No
Order reference number	[37]
Original figure numbers	Fig. 2
Title of your thesis/dissertation	4-Dimensional Printing and Characterization of Net-Shaped Porous Parts Made from Magnetic Ni-Mn-Ga Shape Memory Alloy Powders
Publisher of new work	Youngstown State University
Author of new work	C. Virgil Solomon
Expected completion date	May 2018
Estimated size (number of pages)	1
Requestor Location	Youngstown State University one university plaza

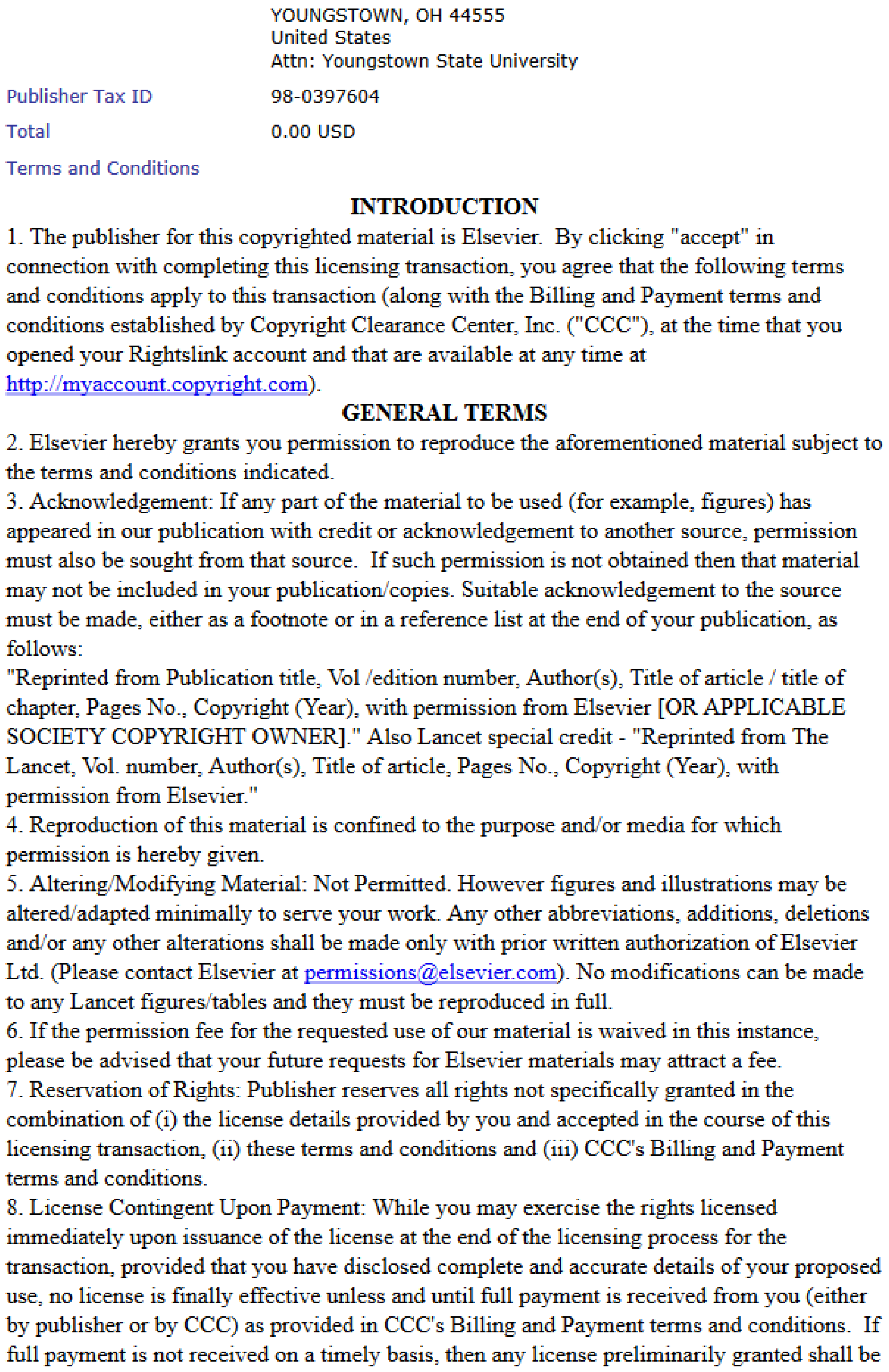

	YOUNGSTOWN, OH 44555 United States Attn: Youngstown State University
Publisher Tax ID	98-0397604
Total	0.00 USD

Terms and Conditions

INTRODUCTION

1. The publisher for this copyrighted material is Elsevier. By clicking "accept" in connection with completing this licensing transaction, you agree that the following terms and conditions apply to this transaction (along with the Billing and Payment terms and conditions established by Copyright Clearance Center, Inc. ("CCC"), at the time that you opened your Rightslink account and that are available at any time at http://myaccount.copyright.com).

GENERAL TERMS

2. Elsevier hereby grants you permission to reproduce the aforementioned material subject to the terms and conditions indicated.

3. Acknowledgement: If any part of the material to be used (for example, figures) has appeared in our publication with credit or acknowledgement to another source, permission must also be sought from that source. If such permission is not obtained then that material may not be included in your publication/copies. Suitable acknowledgement to the source must be made, either as a footnote or in a reference list at the end of your publication, as follows:

"Reprinted from Publication title, Vol /edition number, Author(s), Title of article / title of chapter, Pages No., Copyright (Year), with permission from Elsevier [OR APPLICABLE SOCIETY COPYRIGHT OWNER]." Also Lancet special credit - "Reprinted from The Lancet, Vol. number, Author(s), Title of article, Pages No., Copyright (Year), with permission from Elsevier."

4. Reproduction of this material is confined to the purpose and/or media for which permission is hereby given.

5. Altering/Modifying Material: Not Permitted. However figures and illustrations may be altered/adapted minimally to serve your work. Any other abbreviations, additions, deletions and/or any other alterations shall be made only with prior written authorization of Elsevier Ltd. (Please contact Elsevier at permissions@elsevier.com). No modifications can be made to any Lancet figures/tables and they must be reproduced in full.

6. If the permission fee for the requested use of our material is waived in this instance, please be advised that your future requests for Elsevier materials may attract a fee.

7. Reservation of Rights: Publisher reserves all rights not specifically granted in the combination of (i) the license details provided by you and accepted in the course of this licensing transaction, (ii) these terms and conditions and (iii) CCC's Billing and Payment terms and conditions.

8. License Contingent Upon Payment: While you may exercise the rights licensed immediately upon issuance of the license at the end of the licensing process for the transaction, provided that you have disclosed complete and accurate details of your proposed use, no license is finally effective unless and until full payment is received from you (either by publisher or by CCC) as provided in CCC's Billing and Payment terms and conditions. If full payment is not received on a timely basis, then any license preliminarily granted shall be

deemed automatically revoked and shall be void as if never granted. Further, in the event that you breach any of these terms and conditions or any of CCC's Billing and Payment terms and conditions, the license is automatically revoked and shall be void as if never granted. Use of materials as described in a revoked license, as well as any use of the materials beyond the scope of an unrevoked license, may constitute copyright infringement and publisher reserves the right to take any and all action to protect its copyright in the materials.

9. Warranties: Publisher makes no representations or warranties with respect to the licensed material.

10. Indemnity: You hereby indemnify and agree to hold harmless publisher and CCC, and their respective officers, directors, employees and agents, from and against any and all claims arising out of your use of the licensed material other than as specifically authorized pursuant to this license.

11. No Transfer of License: This license is personal to you and may not be sublicensed, assigned, or transferred by you to any other person without publisher's written permission.

12. No Amendment Except in Writing: This license may not be amended except in a writing signed by both parties (or, in the case of publisher, by CCC on publisher's behalf).

13. Objection to Contrary Terms: Publisher hereby objects to any terms contained in any purchase order, acknowledgment, check endorsement or other writing prepared by you, which terms are inconsistent with these terms and conditions or CCC's Billing and Payment terms and conditions. These terms and conditions, together with CCC's Billing and Payment terms and conditions (which are incorporated herein), comprise the entire agreement between you and publisher (and CCC) concerning this licensing transaction. In the event of any conflict between your obligations established by these terms and conditions and those established by CCC's Billing and Payment terms and conditions, these terms and conditions shall control.

14. Revocation: Elsevier or Copyright Clearance Center may deny the permissions described in this License at their sole discretion, for any reason or no reason, with a full refund payable to you. Notice of such denial will be made using the contact information provided by you. Failure to receive such notice will not alter or invalidate the denial. In no event will Elsevier or Copyright Clearance Center be responsible or liable for any costs, expenses or damage incurred by you as a result of a denial of your permission request, other than a refund of the amount(s) paid by you to Elsevier and/or Copyright Clearance Center for denied permissions.

LIMITED LICENSE

The following terms and conditions apply only to specific license types:

15. **Translation**: This permission is granted for non-exclusive world **English** rights only unless your license was granted for translation rights. If you licensed translation rights you may only translate this content into the languages you requested. A professional translator must perform all translations and reproduce the content word for word preserving the integrity of the article.

16. **Posting licensed content on any Website**: The following terms and conditions apply as follows: Licensing material from an Elsevier journal: All content posted to the web site must maintain the copyright information line on the bottom of each image; A hyper-text must be included to the Homepage of the journal from which you are licensing at http://www.sciencedirect.com/science/journal/xxxxx or the Elsevier homepage for books at http://www.elsevier.com; Central Storage: This license does not include permission for a

scanned version of the material to be stored in a central repository such as that provided by Heron/XanEdu.
Licensing material from an Elsevier book: A hyper-text link must be included to the Elsevier homepage at http://www.elsevier.com . All content posted to the web site must maintain the copyright information line on the bottom of each image.

Posting licensed content on Electronic reserve: In addition to the above the following clauses are applicable: The web site must be password-protected and made available only to bona fide students registered on a relevant course. This permission is granted for 1 year only. You may obtain a new license for future website posting.
17. **For journal authors:** the following clauses are applicable in addition to the above:
Preprints:
A preprint is an author's own write-up of research results and analysis, it has not been peer-reviewed, nor has it had any other value added to it by a publisher (such as formatting, copyright, technical enhancement etc.).
Authors can share their preprints anywhere at any time. Preprints should not be added to or enhanced in any way in order to appear more like, or to substitute for, the final versions of articles however authors can update their preprints on arXiv or RePEc with their Accepted Author Manuscript (see below).
If accepted for publication, we encourage authors to link from the preprint to their formal publication via its DOI. Millions of researchers have access to the formal publications on ScienceDirect, and so links will help users to find, access, cite and use the best available version. Please note that Cell Press, The Lancet and some society-owned have different preprint policies. Information on these policies is available on the journal homepage.
Accepted Author Manuscripts: An accepted author manuscript is the manuscript of an article that has been accepted for publication and which typically includes author-incorporated changes suggested during submission, peer review and editor-author communications.
Authors can share their accepted author manuscript:

- immediately
    - via their non-commercial person homepage or blog
    - by updating a preprint in arXiv or RePEc with the accepted manuscript
    - via their research institute or institutional repository for internal institutional uses or as part of an invitation-only research collaboration work-group
    - directly by providing copies to their students or to research collaborators for their personal use
    - for private scholarly sharing as part of an invitation-only work group on commercial sites with which Elsevier has an agreement
- After the embargo period
    - via non-commercial hosting platforms such as their institutional repository
    - via commercial sites with which Elsevier has an agreement

In all cases accepted manuscripts should:

- link to the formal publication via its DOI
- bear a CC-BY-NC-ND license - this is easy to do
- if aggregated with other manuscripts, for example in a repository or other site, be

shared in alignment with our hosting policy not be added to or enhanced in any way to appear more like, or to substitute for, the published journal article.

Published journal article (JPA): A published journal article (PJA) is the definitive final record of published research that appears or will appear in the journal and embodies all value-adding publishing activities including peer review co-ordination, copy-editing, formatting, (if relevant) pagination and online enrichment.
Policies for sharing publishing journal articles differ for subscription and gold open access articles:
Subscription Articles: If you are an author, please share a link to your article rather than the full-text. Millions of researchers have access to the formal publications on ScienceDirect, and so links will help your users to find, access, cite, and use the best available version. Theses and dissertations which contain embedded PJAs as part of the formal submission can be posted publicly by the awarding institution with DOI links back to the formal publications on ScienceDirect.
If you are affiliated with a library that subscribes to ScienceDirect you have additional private sharing rights for others' research accessed under that agreement. This includes use for classroom teaching and internal training at the institution (including use in course packs and courseware programs), and inclusion of the article for grant funding purposes.
Gold Open Access Articles: May be shared according to the author-selected end-user license and should contain a CrossMark logo, the end user license, and a DOI link to the formal publication on ScienceDirect.
Please refer to Elsevier's posting policy for further information.
18. **For book authors** the following clauses are applicable in addition to the above: Authors are permitted to place a brief summary of their work online only. You are not allowed to download and post the published electronic version of your chapter, nor may you scan the printed edition to create an electronic version. **Posting to a repository:** Authors are permitted to post a summary of their chapter only in their institution's repository.
19. **Thesis/Dissertation**: If your license is for use in a thesis/dissertation your thesis may be submitted to your institution in either print or electronic form. Should your thesis be published commercially, please reapply for permission. These requirements include permission for the Library and Archives of Canada to supply single copies, on demand, of the complete thesis and include permission for Proquest/UMI to supply single copies, on demand, of the complete thesis. Should your thesis be published commercially, please reapply for permission. Theses and dissertations which contain embedded PJAs as part of the formal submission can be posted publicly by the awarding institution with DOI links back to the formal publications on ScienceDirect.

Elsevier Open Access Terms and Conditions
You can publish open access with Elsevier in hundreds of open access journals or in nearly 2000 established subscription journals that support open access publishing. Permitted third party re-use of these open access articles is defined by the author's choice of Creative Commons user license. See our open access license policy for more information.
Terms & Conditions applicable to all Open Access articles published with Elsevier:
Any reuse of the article must not represent the author as endorsing the adaptation of the article nor should the article be modified in such a way as to damage the author's honour or reputation. If any changes have been made, such changes must be clearly indicated.

The author(s) must be appropriately credited and we ask that you include the end user license and a DOI link to the formal publication on ScienceDirect.
If any part of the material to be used (for example, figures) has appeared in our publication with credit or acknowledgement to another source it is the responsibility of the user to ensure their reuse complies with the terms and conditions determined by the rights holder.
Additional Terms & Conditions applicable to each Creative Commons user license:
CC BY: The CC-BY license allows users to copy, to create extracts, abstracts and new works from the Article, to alter and revise the Article and to make commercial use of the Article (including reuse and/or resale of the Article by commercial entities), provided the user gives appropriate credit (with a link to the formal publication through the relevant DOI), provides a link to the license, indicates if changes were made and the licensor is not represented as endorsing the use made of the work. The full details of the license are available at http://creativecommons.org/licenses/by/4.0.
CC BY NC SA: The CC BY-NC-SA license allows users to copy, to create extracts, abstracts and new works from the Article, to alter and revise the Article, provided this is not done for commercial purposes, and that the user gives appropriate credit (with a link to the formal publication through the relevant DOI), provides a link to the license, indicates if changes were made and the licensor is not represented as endorsing the use made of the work. Further, any new works must be made available on the same conditions. The full details of the license are available at http://creativecommons.org/licenses/by-nc-sa/4.0.
CC BY NC ND: The CC BY-NC-ND license allows users to copy and distribute the Article, provided this is not done for commercial purposes and further does not permit distribution of the Article if it is changed or edited in any way, and provided the user gives appropriate credit (with a link to the formal publication through the relevant DOI), provides a link to the license, and that the licensor is not represented as endorsing the use made of the work. The full details of the license are available at http://creativecommons.org/licenses/by-nc-nd/4.0.
Any commercial reuse of Open Access articles published with a CC BY NC SA or CC BY NC ND license requires permission from Elsevier and will be subject to a fee.
Commercial reuse includes:

- Associating advertising with the full text of the Article
- Charging fees for document delivery or access
- Article aggregation
- Systematic distribution via e-mail lists or share buttons

Posting or linking by commercial companies for use by customers of those companies.

20. **Other Conditions**:

Figure 2.9

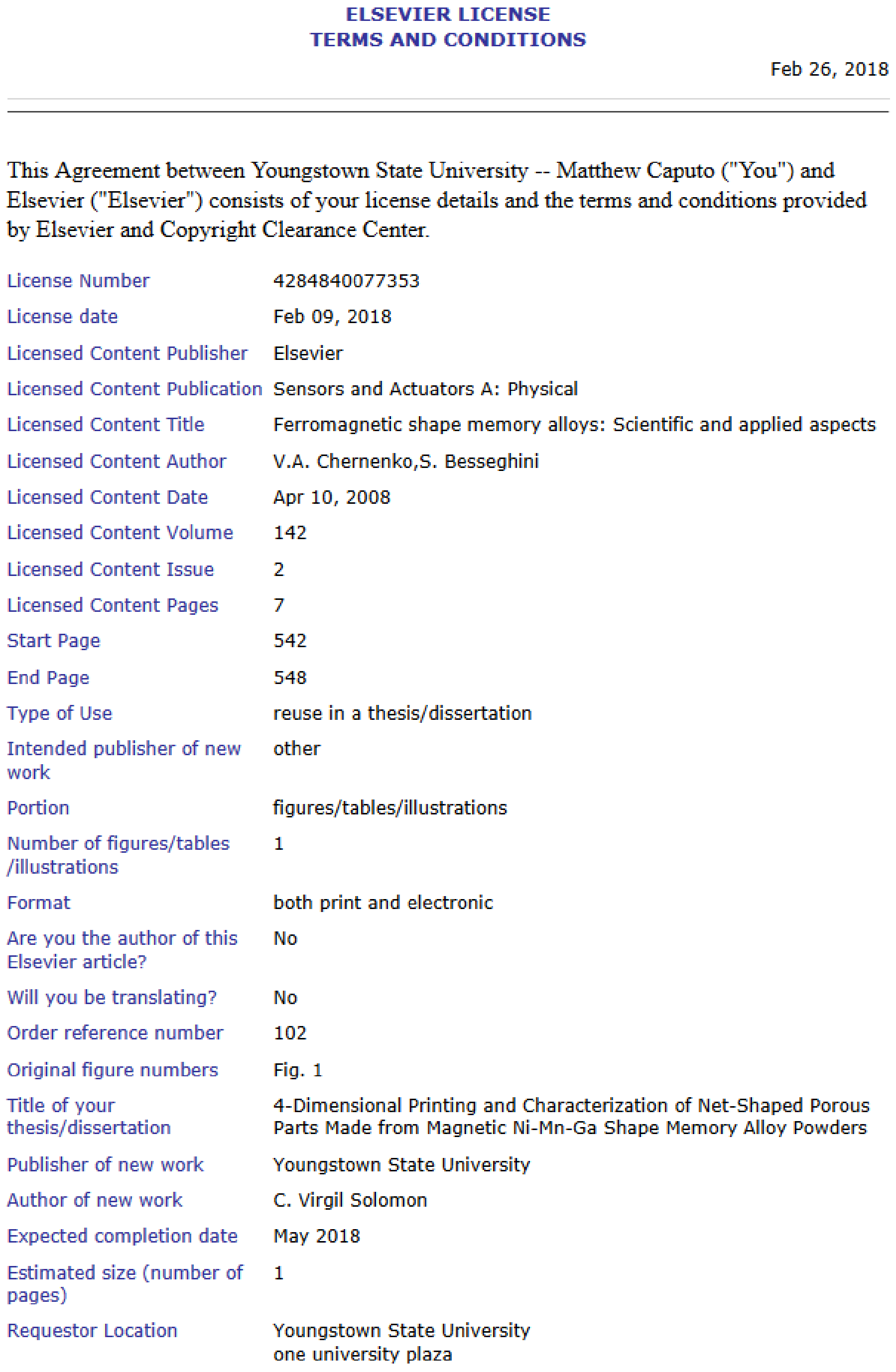

ELSEVIER LICENSE
TERMS AND CONDITIONS

Feb 26, 2018

This Agreement between Youngstown State University -- Matthew Caputo ("You") and Elsevier ("Elsevier") consists of your license details and the terms and conditions provided by Elsevier and Copyright Clearance Center.

License Number	4284840077353
License date	Feb 09, 2018
Licensed Content Publisher	Elsevier
Licensed Content Publication	Sensors and Actuators A: Physical
Licensed Content Title	Ferromagnetic shape memory alloys: Scientific and applied aspects
Licensed Content Author	V.A. Chernenko,S. Besseghini
Licensed Content Date	Apr 10, 2008
Licensed Content Volume	142
Licensed Content Issue	2
Licensed Content Pages	7
Start Page	542
End Page	548
Type of Use	reuse in a thesis/dissertation
Intended publisher of new work	other
Portion	figures/tables/illustrations
Number of figures/tables /illustrations	1
Format	both print and electronic
Are you the author of this Elsevier article?	No
Will you be translating?	No
Order reference number	102
Original figure numbers	Fig. 1
Title of your thesis/dissertation	4-Dimensional Printing and Characterization of Net-Shaped Porous Parts Made from Magnetic Ni-Mn-Ga Shape Memory Alloy Powders
Publisher of new work	Youngstown State University
Author of new work	C. Virgil Solomon
Expected completion date	May 2018
Estimated size (number of pages)	1
Requestor Location	Youngstown State University one university plaza

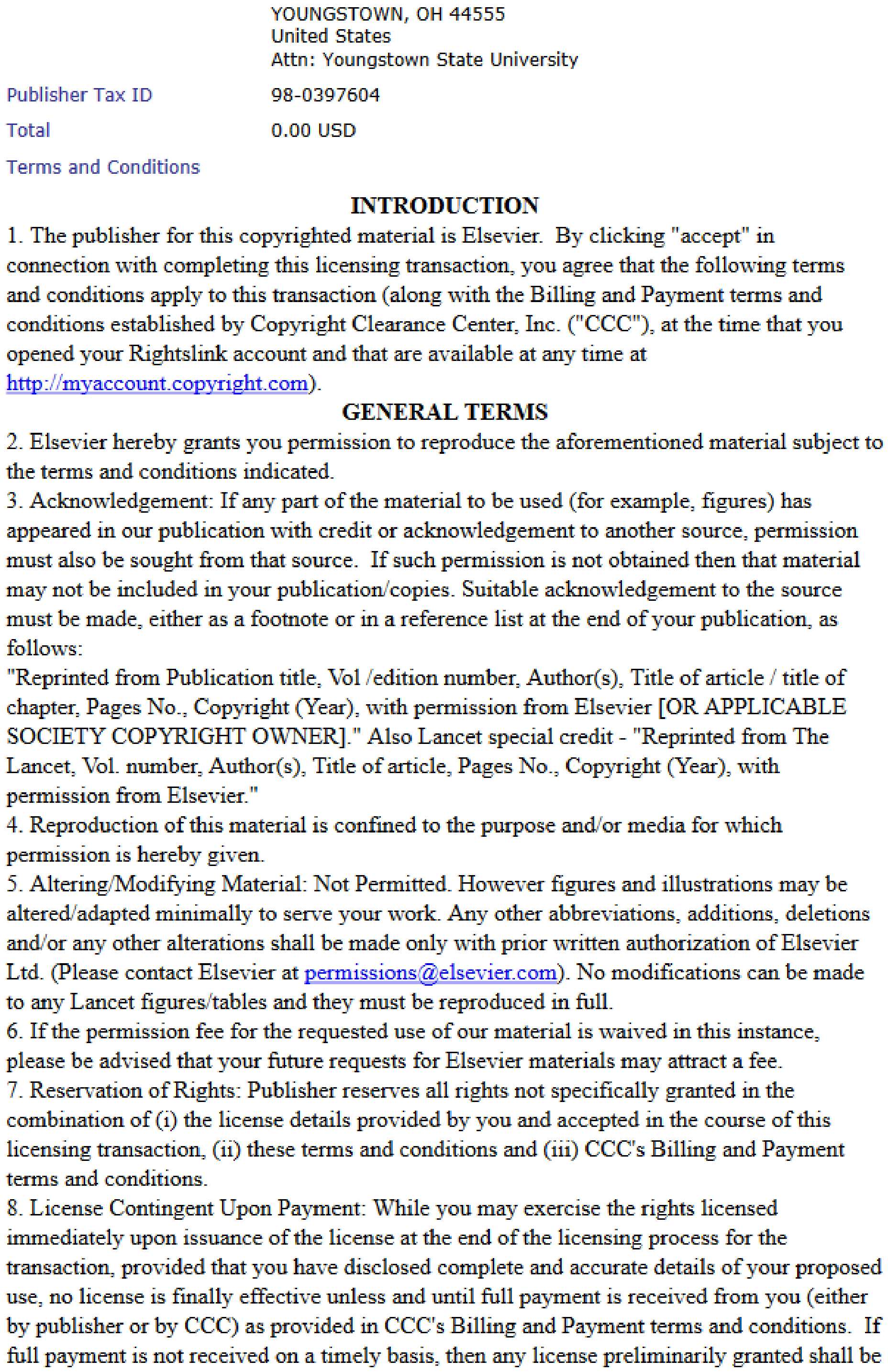

	YOUNGSTOWN, OH 44555 United States Attn: Youngstown State University
Publisher Tax ID	98-0397604
Total	0.00 USD
Terms and Conditions	

INTRODUCTION

1. The publisher for this copyrighted material is Elsevier. By clicking "accept" in connection with completing this licensing transaction, you agree that the following terms and conditions apply to this transaction (along with the Billing and Payment terms and conditions established by Copyright Clearance Center, Inc. ("CCC"), at the time that you opened your Rightslink account and that are available at any time at http://myaccount.copyright.com).

GENERAL TERMS

2. Elsevier hereby grants you permission to reproduce the aforementioned material subject to the terms and conditions indicated.

3. Acknowledgement: If any part of the material to be used (for example, figures) has appeared in our publication with credit or acknowledgement to another source, permission must also be sought from that source. If such permission is not obtained then that material may not be included in your publication/copies. Suitable acknowledgement to the source must be made, either as a footnote or in a reference list at the end of your publication, as follows:

"Reprinted from Publication title, Vol /edition number, Author(s), Title of article / title of chapter, Pages No., Copyright (Year), with permission from Elsevier [OR APPLICABLE SOCIETY COPYRIGHT OWNER]." Also Lancet special credit - "Reprinted from The Lancet, Vol. number, Author(s), Title of article, Pages No., Copyright (Year), with permission from Elsevier."

4. Reproduction of this material is confined to the purpose and/or media for which permission is hereby given.

5. Altering/Modifying Material: Not Permitted. However figures and illustrations may be altered/adapted minimally to serve your work. Any other abbreviations, additions, deletions and/or any other alterations shall be made only with prior written authorization of Elsevier Ltd. (Please contact Elsevier at permissions@elsevier.com). No modifications can be made to any Lancet figures/tables and they must be reproduced in full.

6. If the permission fee for the requested use of our material is waived in this instance, please be advised that your future requests for Elsevier materials may attract a fee.

7. Reservation of Rights: Publisher reserves all rights not specifically granted in the combination of (i) the license details provided by you and accepted in the course of this licensing transaction, (ii) these terms and conditions and (iii) CCC's Billing and Payment terms and conditions.

8. License Contingent Upon Payment: While you may exercise the rights licensed immediately upon issuance of the license at the end of the licensing process for the transaction, provided that you have disclosed complete and accurate details of your proposed use, no license is finally effective unless and until full payment is received from you (either by publisher or by CCC) as provided in CCC's Billing and Payment terms and conditions. If full payment is not received on a timely basis, then any license preliminarily granted shall be

deemed automatically revoked and shall be void as if never granted. Further, in the event that you breach any of these terms and conditions or any of CCC's Billing and Payment terms and conditions, the license is automatically revoked and shall be void as if never granted. Use of materials as described in a revoked license, as well as any use of the materials beyond the scope of an unrevoked license, may constitute copyright infringement and publisher reserves the right to take any and all action to protect its copyright in the materials.

9. Warranties: Publisher makes no representations or warranties with respect to the licensed material.

10. Indemnity: You hereby indemnify and agree to hold harmless publisher and CCC, and their respective officers, directors, employees and agents, from and against any and all claims arising out of your use of the licensed material other than as specifically authorized pursuant to this license.

11. No Transfer of License: This license is personal to you and may not be sublicensed, assigned, or transferred by you to any other person without publisher's written permission.

12. No Amendment Except in Writing: This license may not be amended except in a writing signed by both parties (or, in the case of publisher, by CCC on publisher's behalf).

13. Objection to Contrary Terms: Publisher hereby objects to any terms contained in any purchase order, acknowledgment, check endorsement or other writing prepared by you, which terms are inconsistent with these terms and conditions or CCC's Billing and Payment terms and conditions. These terms and conditions, together with CCC's Billing and Payment terms and conditions (which are incorporated herein), comprise the entire agreement between you and publisher (and CCC) concerning this licensing transaction. In the event of any conflict between your obligations established by these terms and conditions and those established by CCC's Billing and Payment terms and conditions, these terms and conditions shall control.

14. Revocation: Elsevier or Copyright Clearance Center may deny the permissions described in this License at their sole discretion, for any reason or no reason, with a full refund payable to you. Notice of such denial will be made using the contact information provided by you. Failure to receive such notice will not alter or invalidate the denial. In no event will Elsevier or Copyright Clearance Center be responsible or liable for any costs, expenses or damage incurred by you as a result of a denial of your permission request, other than a refund of the amount(s) paid by you to Elsevier and/or Copyright Clearance Center for denied permissions.

LIMITED LICENSE

The following terms and conditions apply only to specific license types:

15. **Translation**: This permission is granted for non-exclusive world **English** rights only unless your license was granted for translation rights. If you licensed translation rights you may only translate this content into the languages you requested. A professional translator must perform all translations and reproduce the content word for word preserving the integrity of the article.

16. **Posting licensed content on any Website**: The following terms and conditions apply as follows: Licensing material from an Elsevier journal: All content posted to the web site must maintain the copyright information line on the bottom of each image; A hyper-text must be included to the Homepage of the journal from which you are licensing at http://www.sciencedirect.com/science/journal/xxxxx or the Elsevier homepage for books at http://www.elsevier.com; Central Storage: This license does not include permission for a

scanned version of the material to be stored in a central repository such as that provided by Heron/XanEdu.
Licensing material from an Elsevier book: A hyper-text link must be included to the Elsevier homepage at http://www.elsevier.com . All content posted to the web site must maintain the copyright information line on the bottom of each image.

Posting licensed content on Electronic reserve: In addition to the above the following clauses are applicable: The web site must be password-protected and made available only to bona fide students registered on a relevant course. This permission is granted for 1 year only. You may obtain a new license for future website posting.
17. **For journal authors:** the following clauses are applicable in addition to the above:
Preprints:
A preprint is an author's own write-up of research results and analysis, it has not been peer-reviewed, nor has it had any other value added to it by a publisher (such as formatting, copyright, technical enhancement etc.).
Authors can share their preprints anywhere at any time. Preprints should not be added to or enhanced in any way in order to appear more like, or to substitute for, the final versions of articles however authors can update their preprints on arXiv or RePEc with their Accepted Author Manuscript (see below).
If accepted for publication, we encourage authors to link from the preprint to their formal publication via its DOI. Millions of researchers have access to the formal publications on ScienceDirect, and so links will help users to find, access, cite and use the best available version. Please note that Cell Press, The Lancet and some society-owned have different preprint policies. Information on these policies is available on the journal homepage.
Accepted Author Manuscripts: An accepted author manuscript is the manuscript of an article that has been accepted for publication and which typically includes author-incorporated changes suggested during submission, peer review and editor-author communications.
Authors can share their accepted author manuscript:

- immediately
  - via their non-commercial person homepage or blog
  - by updating a preprint in arXiv or RePEc with the accepted manuscript
  - via their research institute or institutional repository for internal institutional uses or as part of an invitation-only research collaboration work-group
  - directly by providing copies to their students or to research collaborators for their personal use
  - for private scholarly sharing as part of an invitation-only work group on commercial sites with which Elsevier has an agreement
- After the embargo period
  - via non-commercial hosting platforms such as their institutional repository
  - via commercial sites with which Elsevier has an agreement

In all cases accepted manuscripts should:

- link to the formal publication via its DOI
- bear a CC-BY-NC-ND license - this is easy to do
- if aggregated with other manuscripts, for example in a repository or other site, be

shared in alignment with our hosting policy not be added to or enhanced in any way to appear more like, or to substitute for, the published journal article.

Published journal article (JPA): A published journal article (PJA) is the definitive final record of published research that appears or will appear in the journal and embodies all value-adding publishing activities including peer review co-ordination, copy-editing, formatting, (if relevant) pagination and online enrichment.
Policies for sharing publishing journal articles differ for subscription and gold open access articles:
Subscription Articles: If you are an author, please share a link to your article rather than the full-text. Millions of researchers have access to the formal publications on ScienceDirect, and so links will help your users to find, access, cite, and use the best available version. Theses and dissertations which contain embedded PJAs as part of the formal submission can be posted publicly by the awarding institution with DOI links back to the formal publications on ScienceDirect.
If you are affiliated with a library that subscribes to ScienceDirect you have additional private sharing rights for others' research accessed under that agreement. This includes use for classroom teaching and internal training at the institution (including use in course packs and courseware programs), and inclusion of the article for grant funding purposes.
Gold Open Access Articles: May be shared according to the author-selected end-user license and should contain a CrossMark logo, the end user license, and a DOI link to the formal publication on ScienceDirect.
Please refer to Elsevier's posting policy for further information.
18. **For book authors** the following clauses are applicable in addition to the above: Authors are permitted to place a brief summary of their work online only. You are not allowed to download and post the published electronic version of your chapter, nor may you scan the printed edition to create an electronic version. **Posting to a repository:** Authors are permitted to post a summary of their chapter only in their institution's repository.
19. **Thesis/Dissertation**: If your license is for use in a thesis/dissertation your thesis may be submitted to your institution in either print or electronic form. Should your thesis be published commercially, please reapply for permission. These requirements include permission for the Library and Archives of Canada to supply single copies, on demand, of the complete thesis and include permission for Proquest/UMI to supply single copies, on demand, of the complete thesis. Should your thesis be published commercially, please reapply for permission. Theses and dissertations which contain embedded PJAs as part of the formal submission can be posted publicly by the awarding institution with DOI links back to the formal publications on ScienceDirect.

Elsevier Open Access Terms and Conditions
You can publish open access with Elsevier in hundreds of open access journals or in nearly 2000 established subscription journals that support open access publishing. Permitted third party re-use of these open access articles is defined by the author's choice of Creative Commons user license. See our open access license policy for more information.
Terms & Conditions applicable to all Open Access articles published with Elsevier:
Any reuse of the article must not represent the author as endorsing the adaptation of the article nor should the article be modified in such a way as to damage the author's honour or reputation. If any changes have been made, such changes must be clearly indicated.

The author(s) must be appropriately credited and we ask that you include the end user license and a DOI link to the formal publication on ScienceDirect.
If any part of the material to be used (for example, figures) has appeared in our publication with credit or acknowledgement to another source it is the responsibility of the user to ensure their reuse complies with the terms and conditions determined by the rights holder.
Additional Terms & Conditions applicable to each Creative Commons user license:
CC BY: The CC-BY license allows users to copy, to create extracts, abstracts and new works from the Article, to alter and revise the Article and to make commercial use of the Article (including reuse and/or resale of the Article by commercial entities), provided the user gives appropriate credit (with a link to the formal publication through the relevant DOI), provides a link to the license, indicates if changes were made and the licensor is not represented as endorsing the use made of the work. The full details of the license are available at http://creativecommons.org/licenses/by/4.0.
CC BY NC SA: The CC BY-NC-SA license allows users to copy, to create extracts, abstracts and new works from the Article, to alter and revise the Article, provided this is not done for commercial purposes, and that the user gives appropriate credit (with a link to the formal publication through the relevant DOI), provides a link to the license, indicates if changes were made and the licensor is not represented as endorsing the use made of the work. Further, any new works must be made available on the same conditions. The full details of the license are available at http://creativecommons.org/licenses/by-nc-sa/4.0.
CC BY NC ND: The CC BY-NC-ND license allows users to copy and distribute the Article, provided this is not done for commercial purposes and further does not permit distribution of the Article if it is changed or edited in any way, and provided the user gives appropriate credit (with a link to the formal publication through the relevant DOI), provides a link to the license, and that the licensor is not represented as endorsing the use made of the work. The full details of the license are available at http://creativecommons.org/licenses/by-nc-nd/4.0.
Any commercial reuse of Open Access articles published with a CC BY NC SA or CC BY NC ND license requires permission from Elsevier and will be subject to a fee.
Commercial reuse includes:

- Associating advertising with the full text of the Article
- Charging fees for document delivery or access
- Article aggregation
- Systematic distribution via e-mail lists or share buttons

Posting or linking by commercial companies for use by customers of those companies.

20. **Other Conditions**: